FATIGUE DAMAGE ACCUMULATION IN TITANIUM ALLOY IMI 834

By

Gavin James Baxter

Vol 2.

Thesis submitted for the degree of Doctor of Philosophy

Department of Engineering Materials

University of Sheffield

May 1994

VOLUME 2

FIGURES

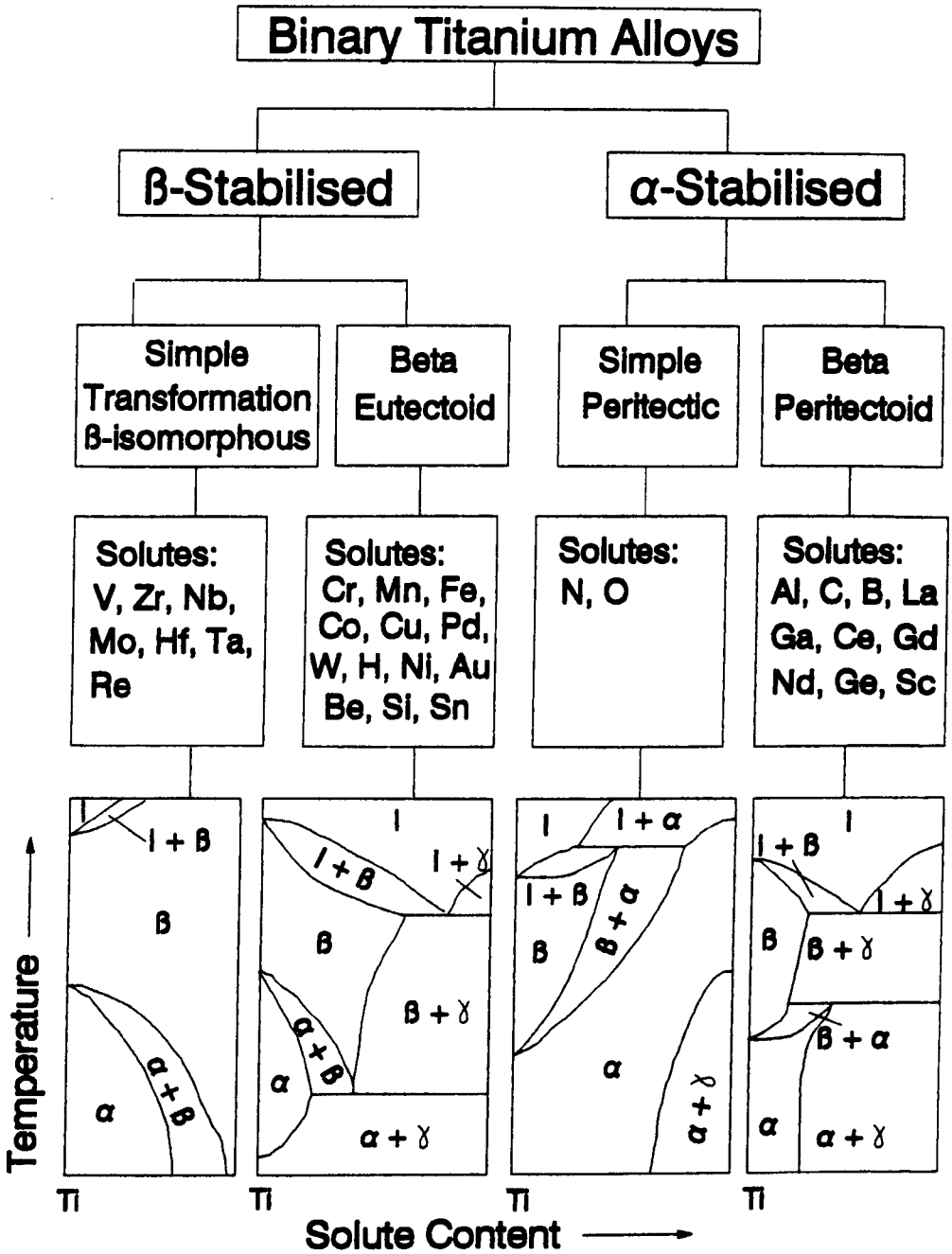

Figure 2.1 Classification scheme for binary titanium alloy phase diagrams [11].

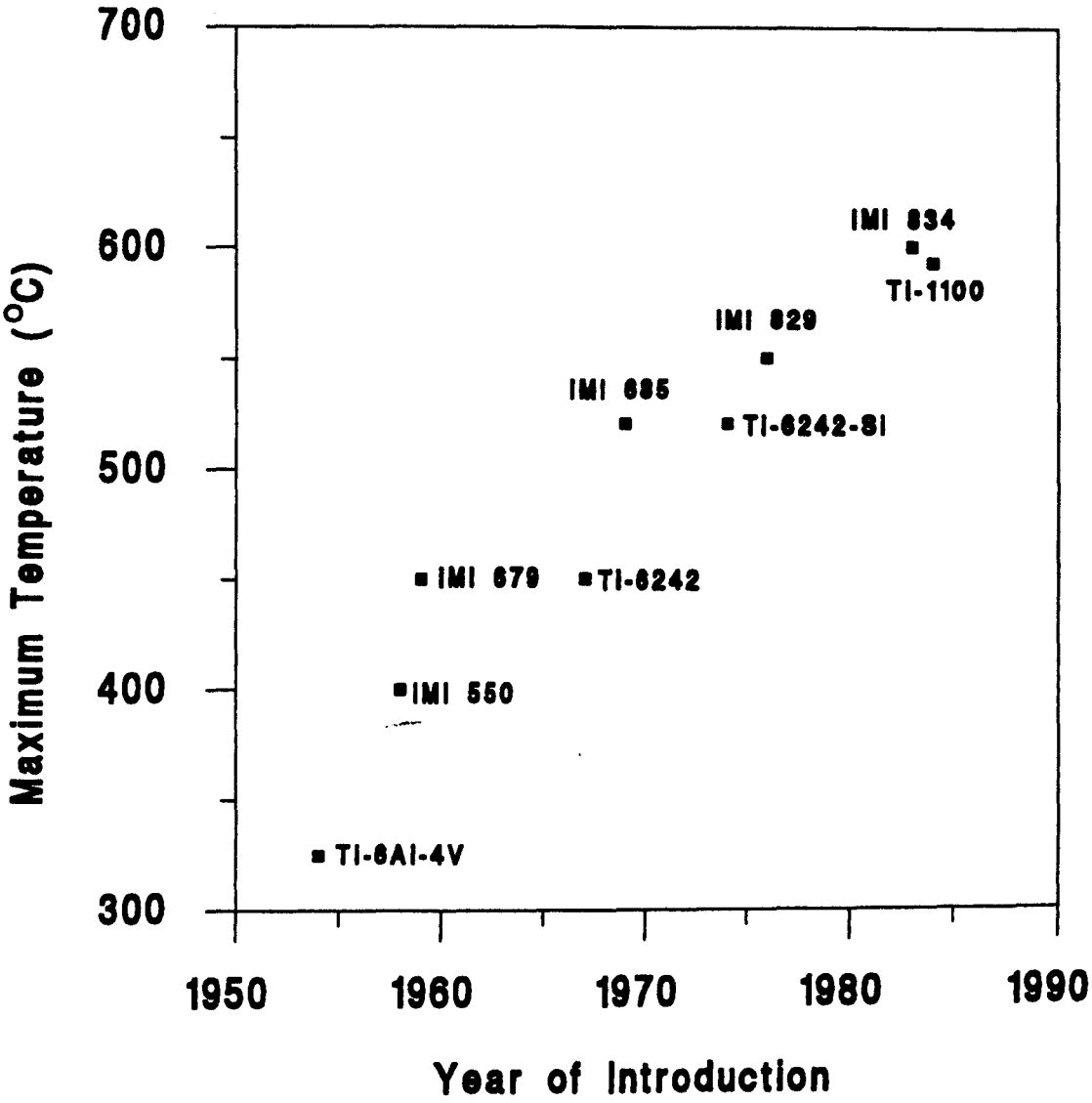

Figure 2.2 Improvements in the creep performance of high temperature titanium alloys [5].

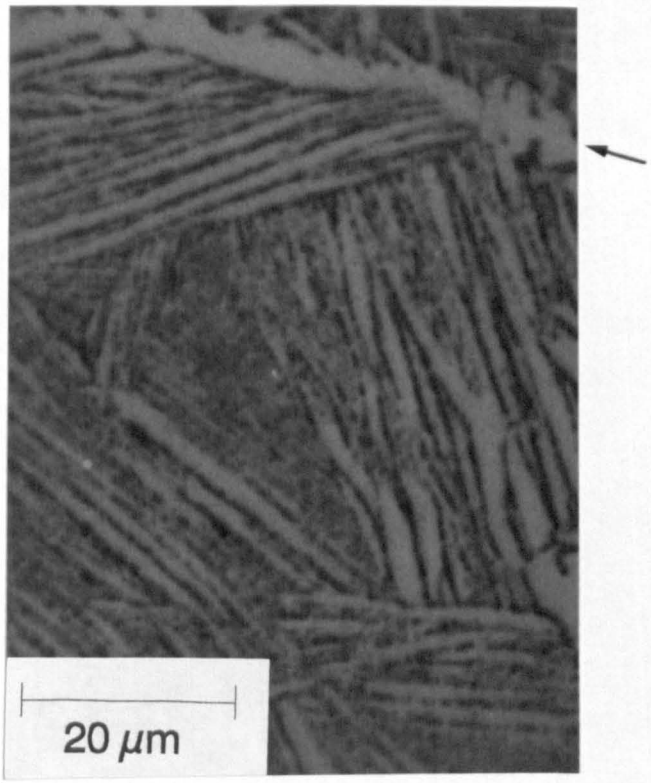

Figure 2.3 Optical microstructure showing acicular α-platelets in the transformed-β microstructure of titanium alloy IMI 834. Several colonies of similarly orientated α-platelets are nucleated in each prior-β grain. The grain boundaries are outlined by a thin layer of grain boundary α phase, one of which is indicated in the figure.

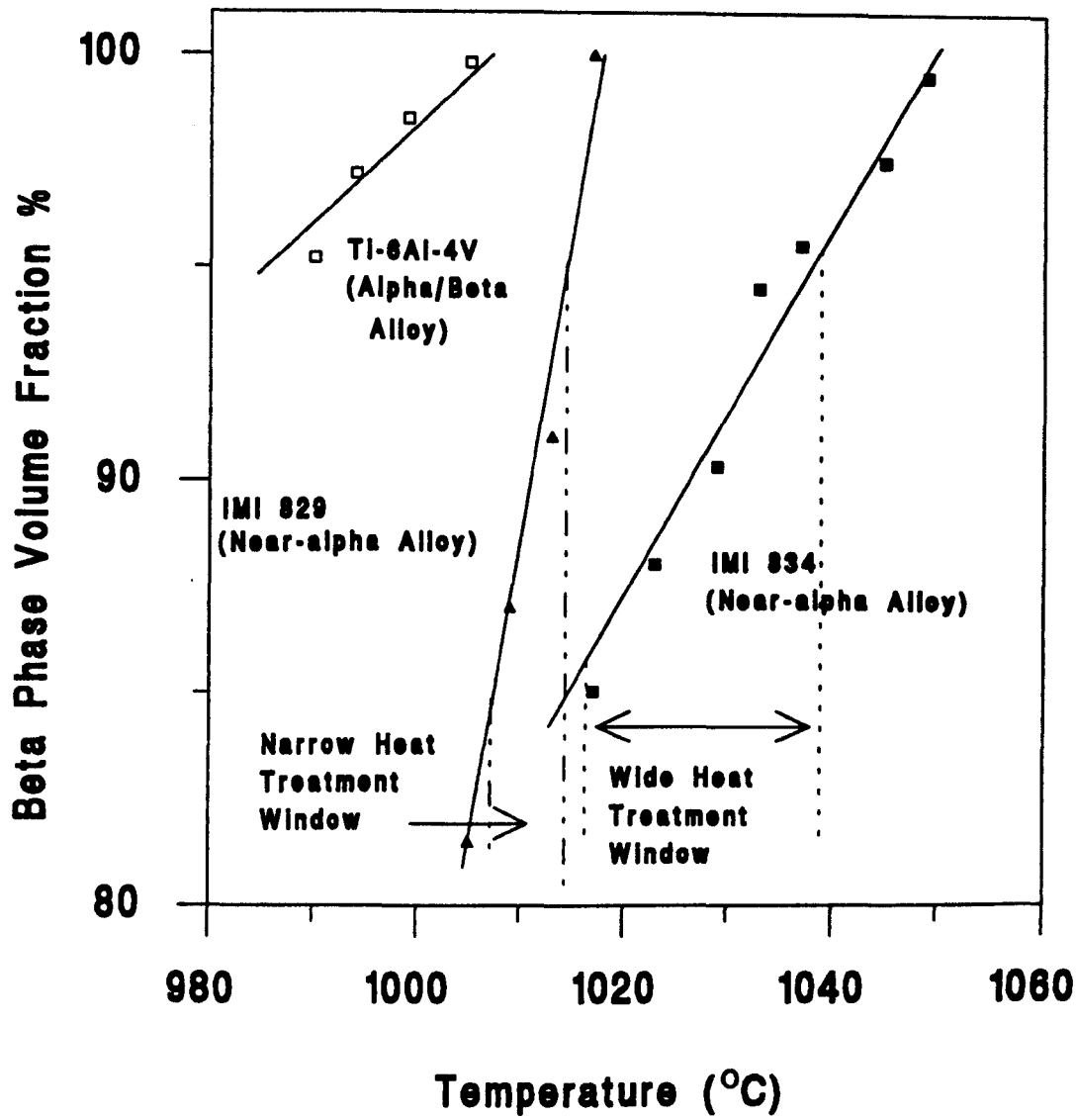

Figure 2.4 The effect of heat treatment on the volume fraction of primary beta phase; beta-transus approach curves for the alloys Ti-6Al-4V, IMI 829 and IMI 834 [31]. v/o of primary alpha = 100 minus v/o primary beta.

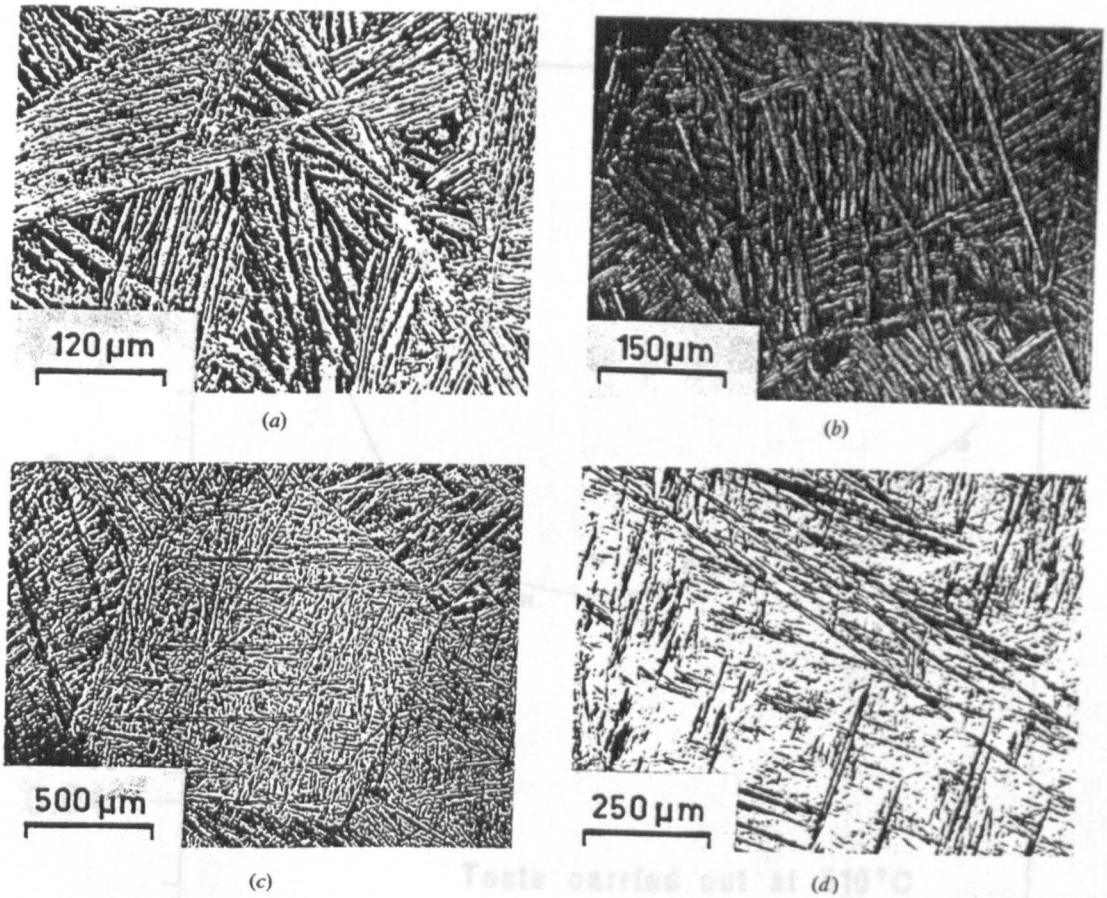

Figure 2.5 Optical micrographs showing the effect of cooling rate on the transformed-β microstructure of IMI 829 solution treated at 1050°C [34]. (a) Furnace cooled, (b) air cooled, (c) oil quenched and (d) water quenched. As the cooling rate is increased the microstructure becomes finer and a transition from a large colony microstructure (a) and (b) through a basketweave microstructure (c) to a martensitic microstructure (d) occurs.

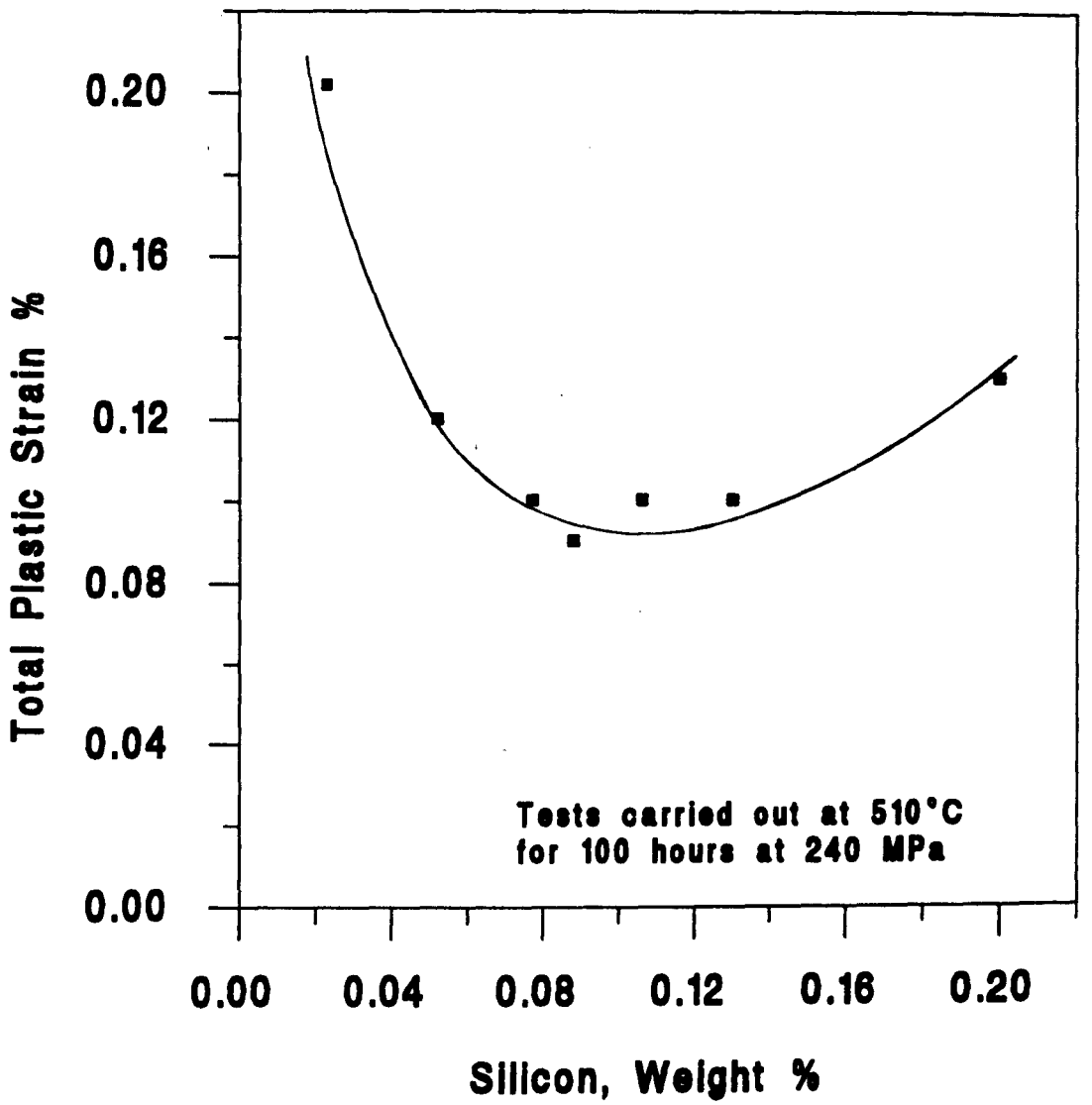

Figure 2.6 Effect of silicon on the creep strain in alloy Ti-6242 [53]. A minimum total plastic strain in the curve suggests that the best creep performance is obtained with the addition of 0.1 wt% silicon.

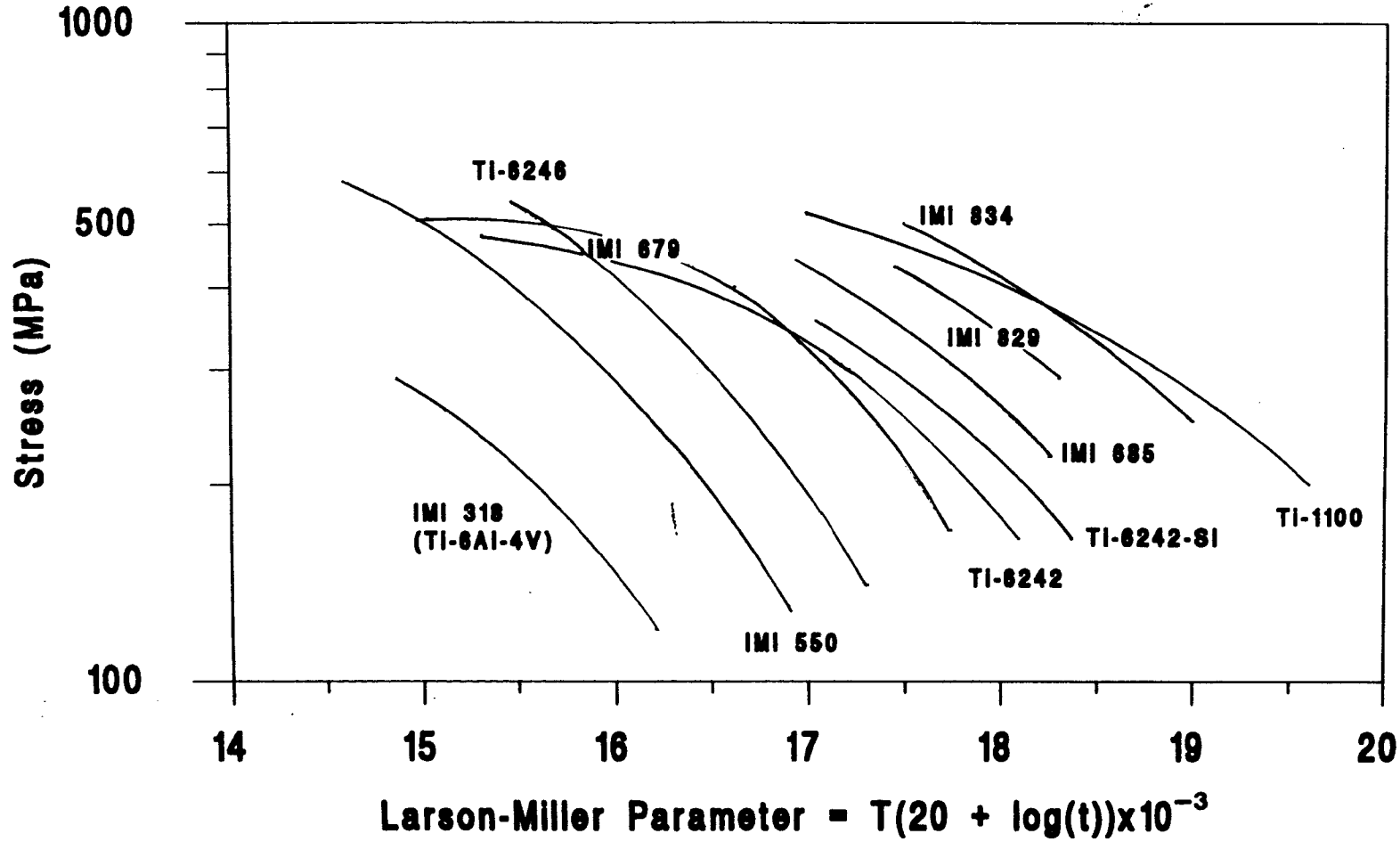

Figure 2.7 Larson-Miller 0.2% creep strain plot showing improvements over the last forty years [5, 28].

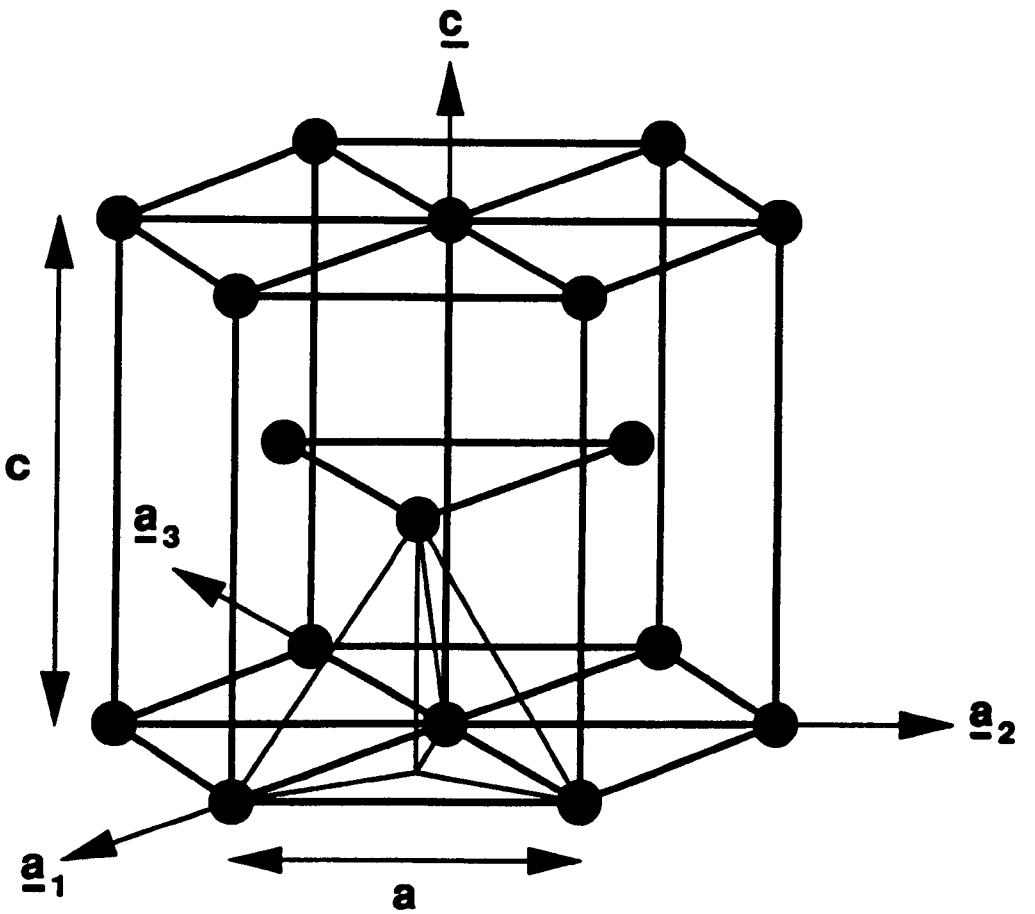

Figure 2.8 Hexagonal close packed crystal structure. Miller-Bravais indices for hcp materials [uvtw] and (hkil) are based on the vectors $\underline{a}_1$, $\underline{a}_2$, $\underline{a}_3$ and $\underline{c}$.

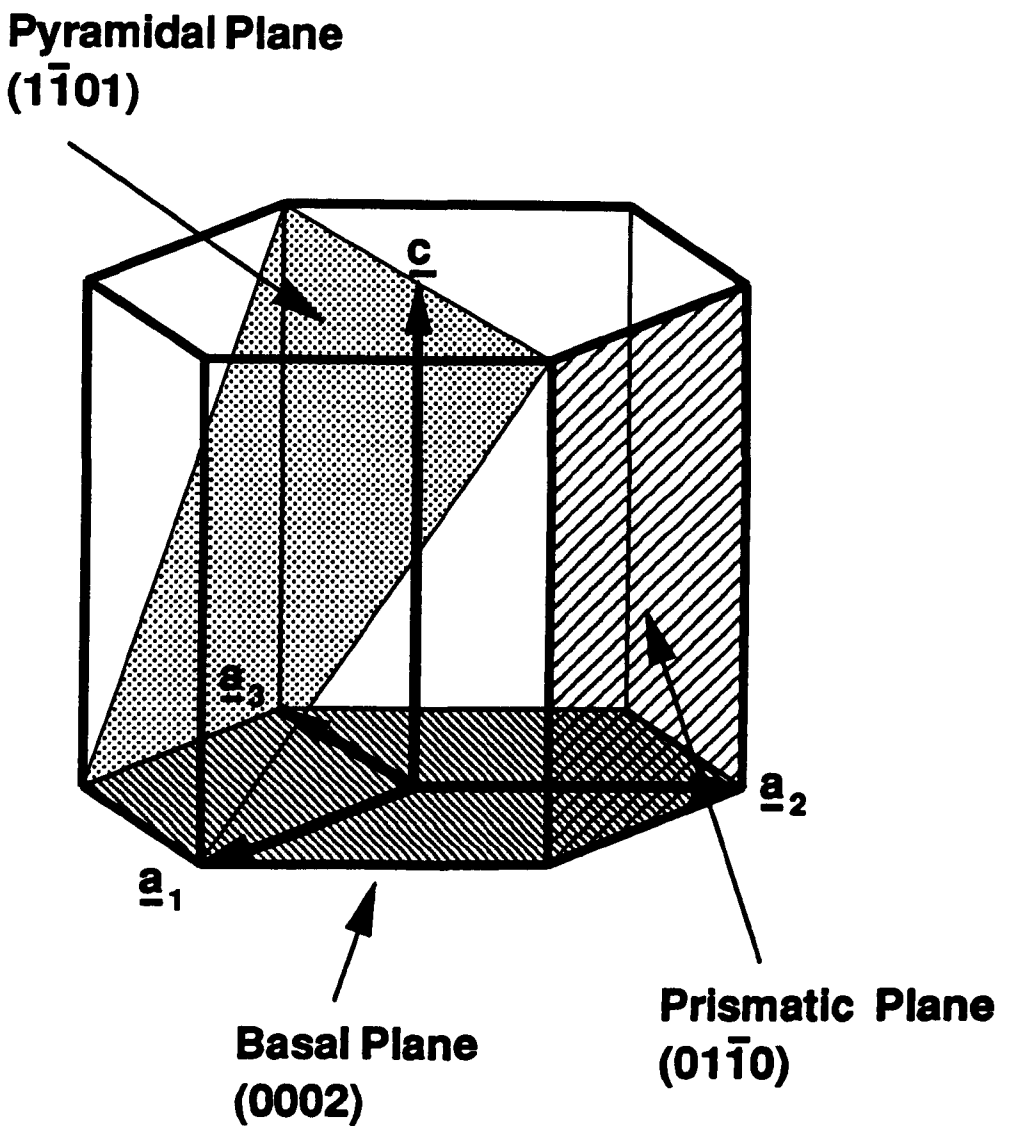

Figure 2.9 Major slip planes in titanium. Miller-Bravais indices are expressed as (a_1 a_2 a_3 c). The Burgers vector for slip on these planes is of the type $^1/_3$<11$\bar{2}$0>.

Figure 2.10 (a) Standard stereographic triangle (0001)-$(10\bar{1}0)$-$(11\bar{2}0)$ for a hcp metal. (b) Orientation dependence of the resolved shear stress for slip within the standard stereographic triangle (AOB) for a hcp metal [107]. The most highly stressed prism and basal slip systems are represented by areas $(01\bar{1}0)[2\bar{1}\bar{1}0]$ and $(0001)[11\bar{2}0]$, respectively. In basal slip, m reaches a maximum value of 0.5 when $\phi = \lambda = 45°$. Slip on the most highly stressed prism slip system is a maximum at E; 45° away from $(01\bar{1}0)$ and $(2\bar{1}\bar{1}0)$.

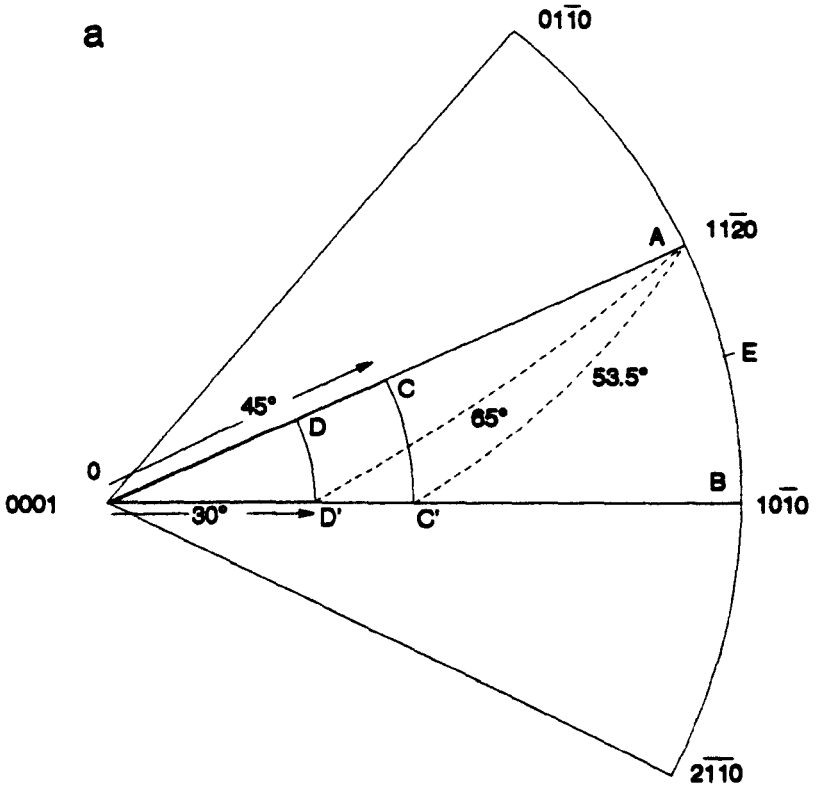
a
$01\bar{1}0$
$11\bar{2}0$
A
E
C
D
45°
53.5°
65°
0
0001
30°
D'
C'
B
$10\bar{1}0$
$2\bar{1}10$

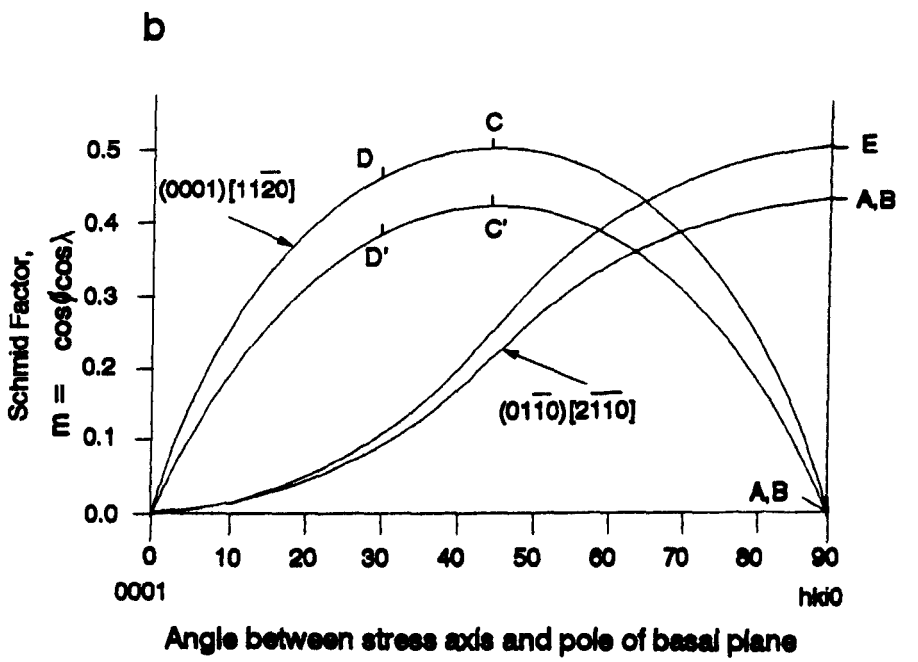
b
C
D
E
A,B
(0001)[11$\bar{2}$0]
C'
D'
(01$\bar{1}$0)[2$\bar{1}$10]
A,B
Schmid Factor,
m = cosϕcosλ
0.5
0.4
0.3
0.2
0.1
0.0
0
10
20
30
40
50
60
70
80
90
0001
hki0
Angle between stress axis and pole of basal plane

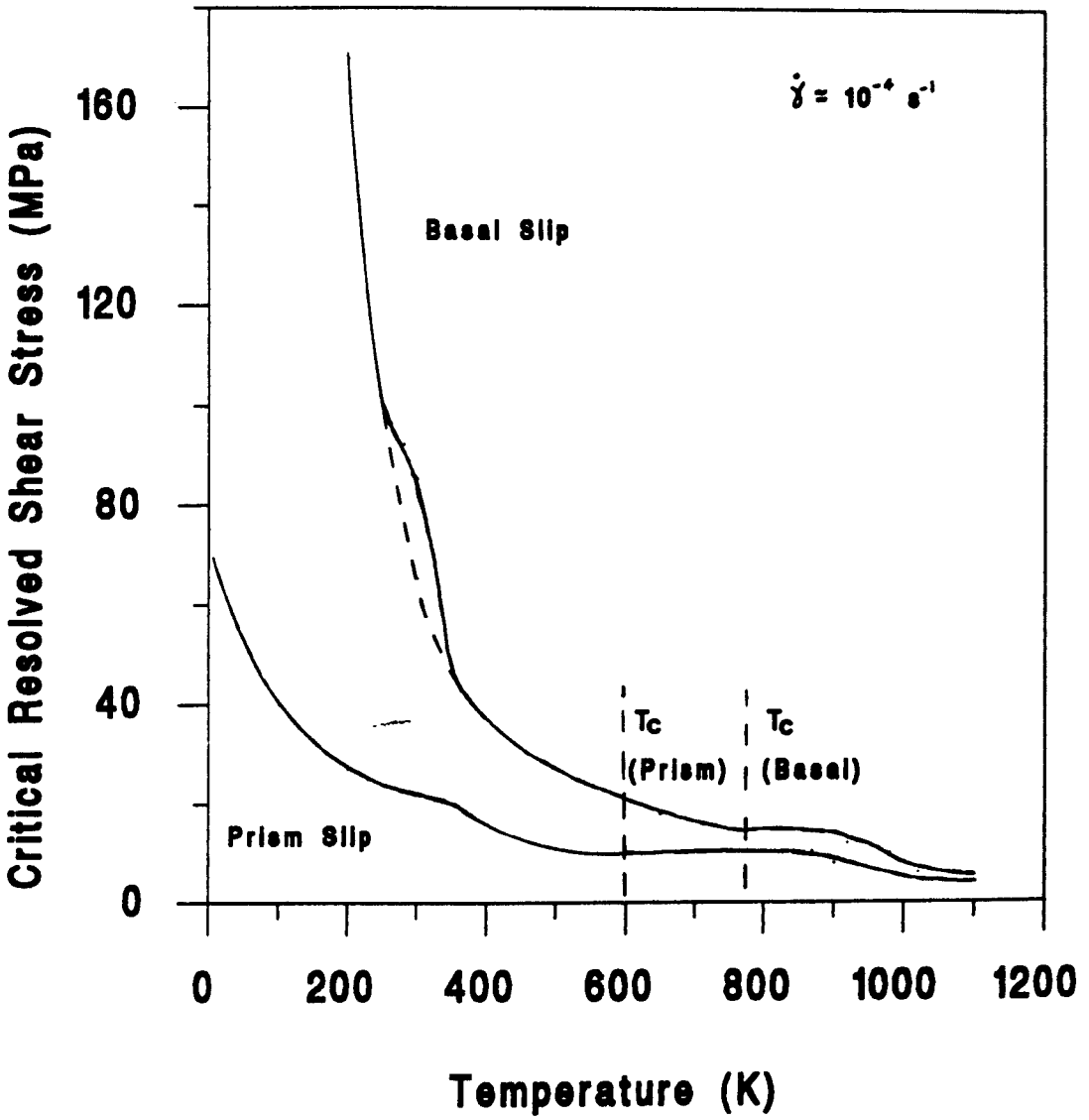

Figure 2.11 Effect of temperature on the critical resolved shear stress for basal and prism slip in titanium [100]. Interstitial content = 0.05 at %.

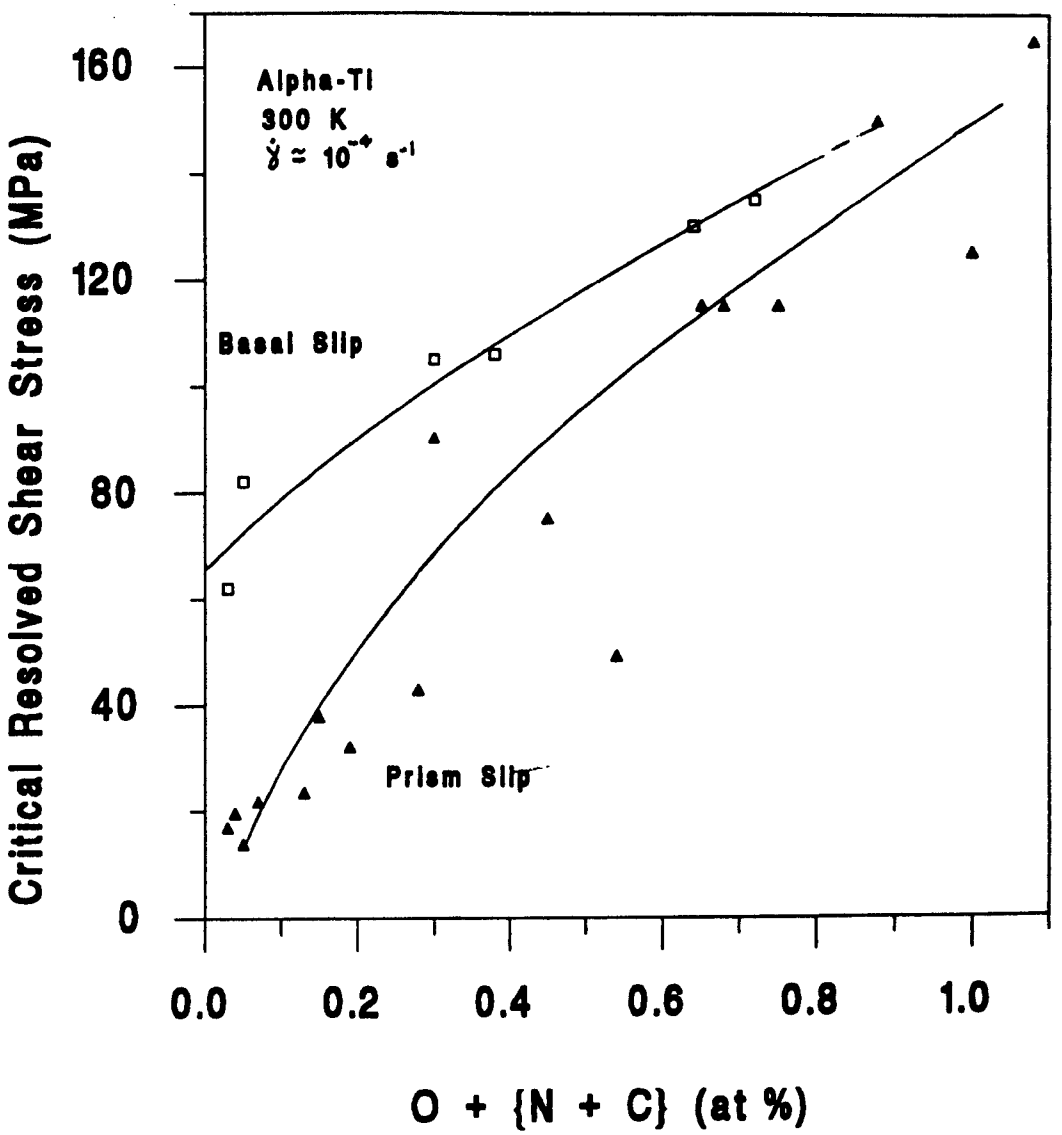

Figure 2.12 Effect of interstitial solute content on the critial resolved shear stress for basal and prism slip in titanium at 300 K [100].

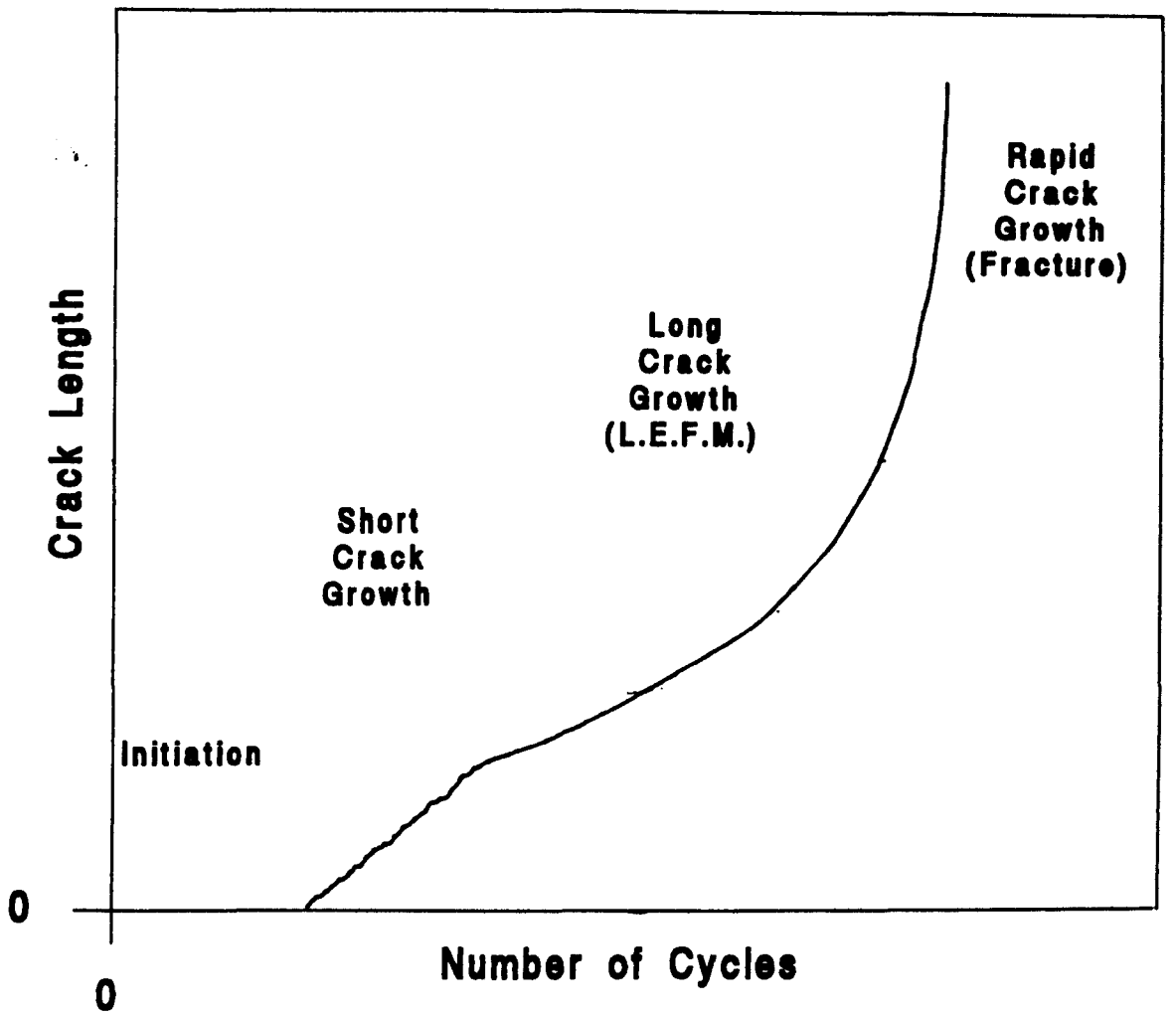

Figure 2.13 The stages of fatigue crack nucleation and crack growth [1].

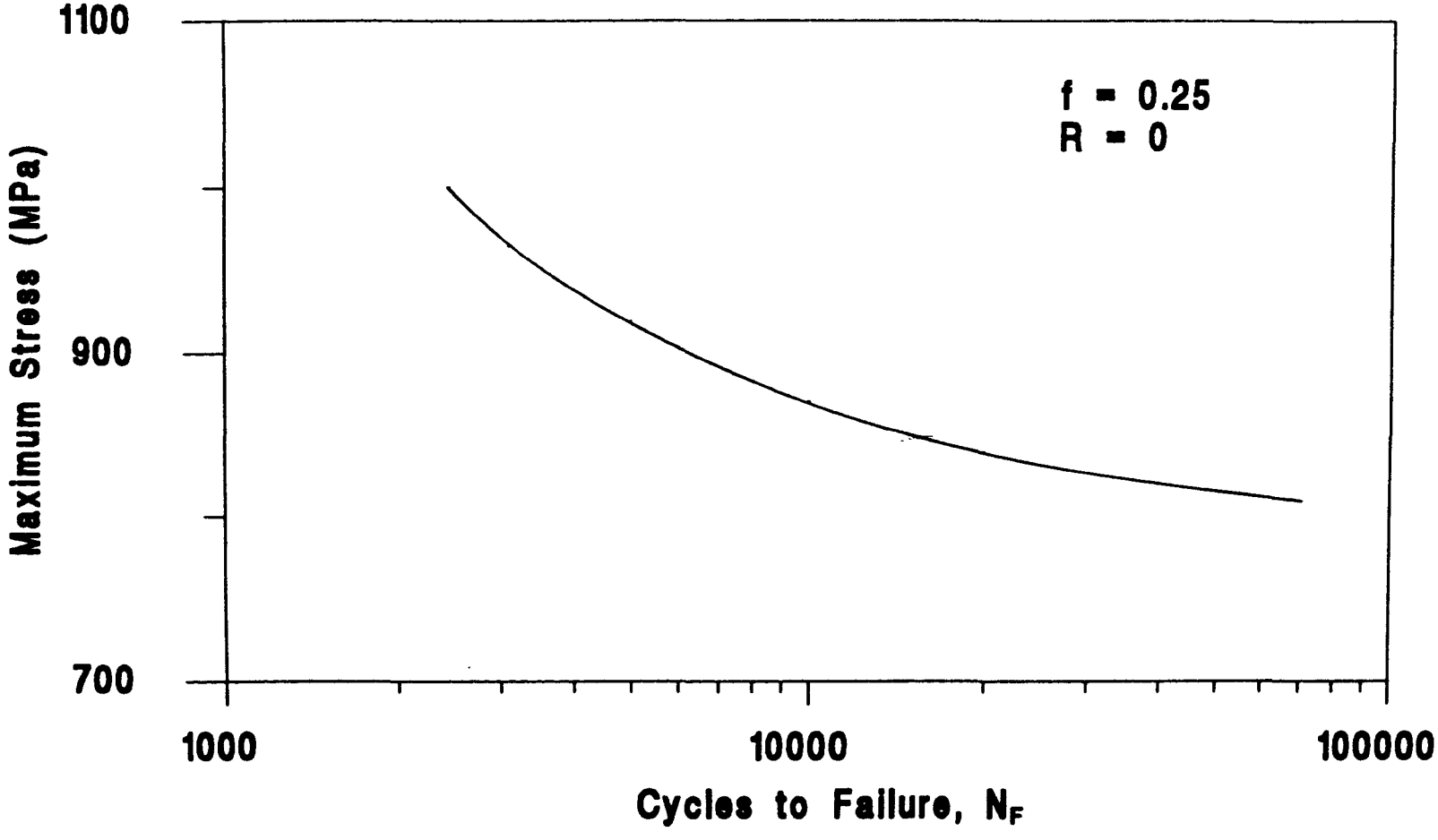

Figure 2.14 S-N curve for IMI 834 tested in low cycle fatigue at room temperature [131].

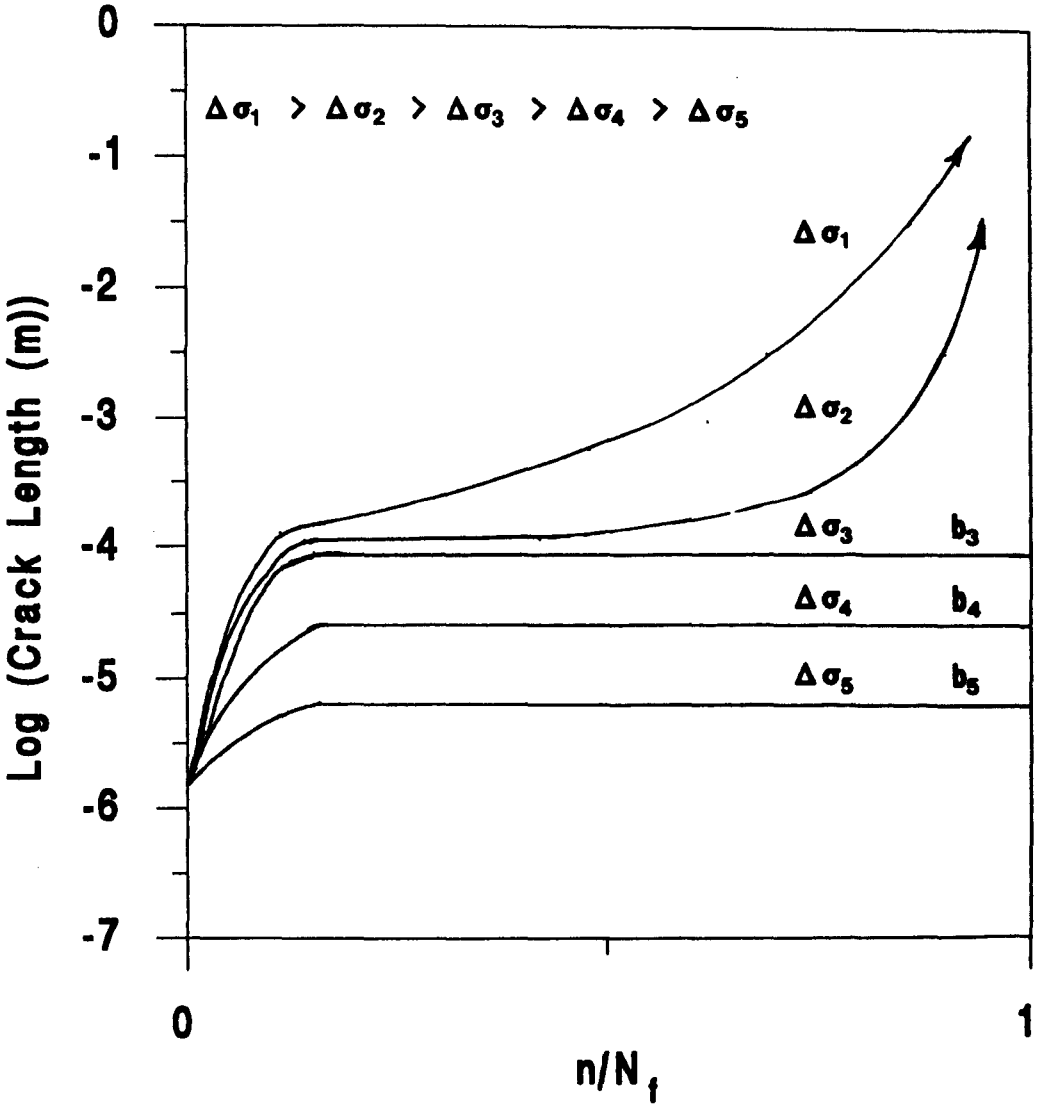

Figure 2.15 Short fatigue crack growth behaviour as influenced by microstructural barriers of different strengths and spacings [130].

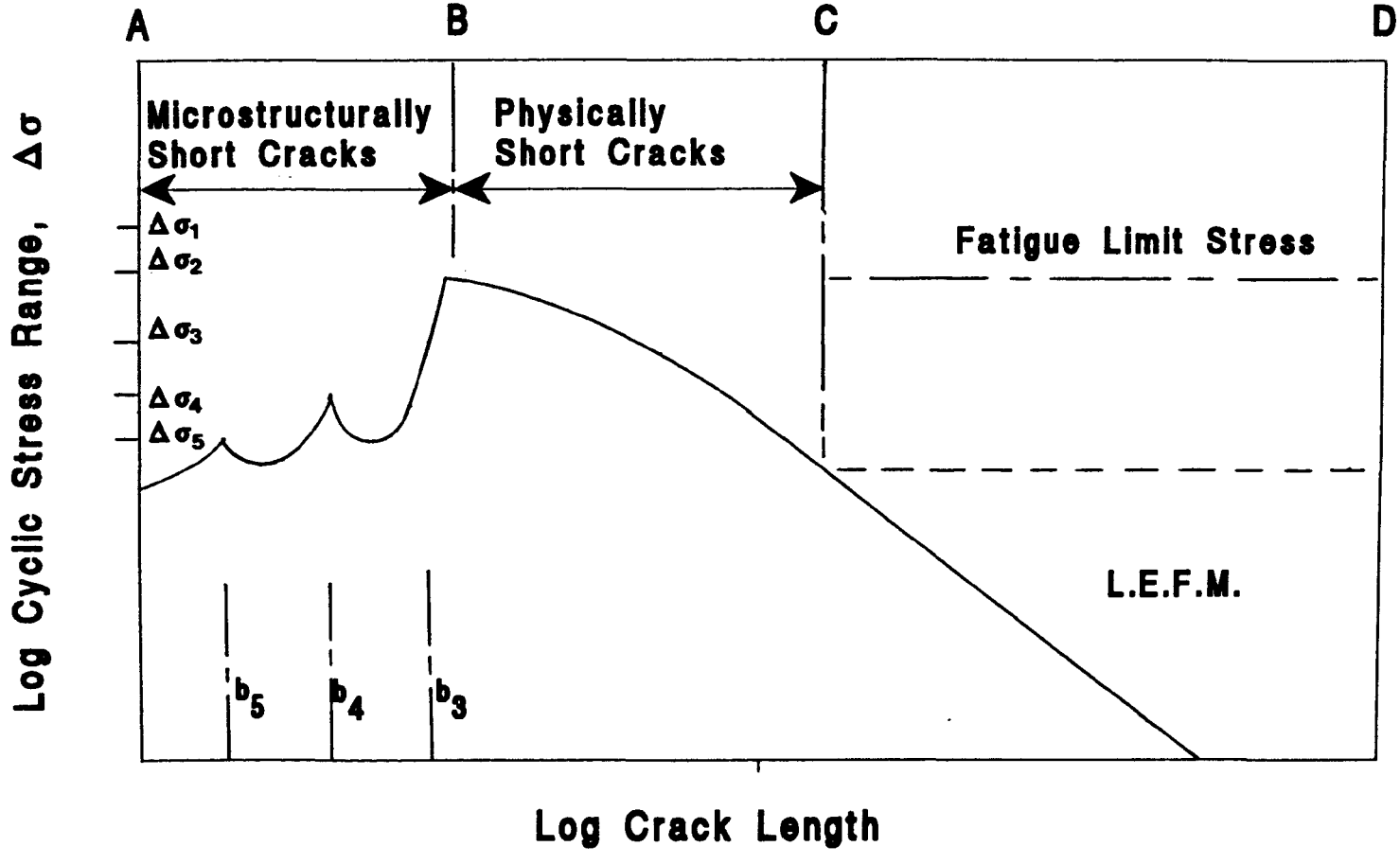

Figure 2.16 Fatigue limit dependency on crack length [130, 134].

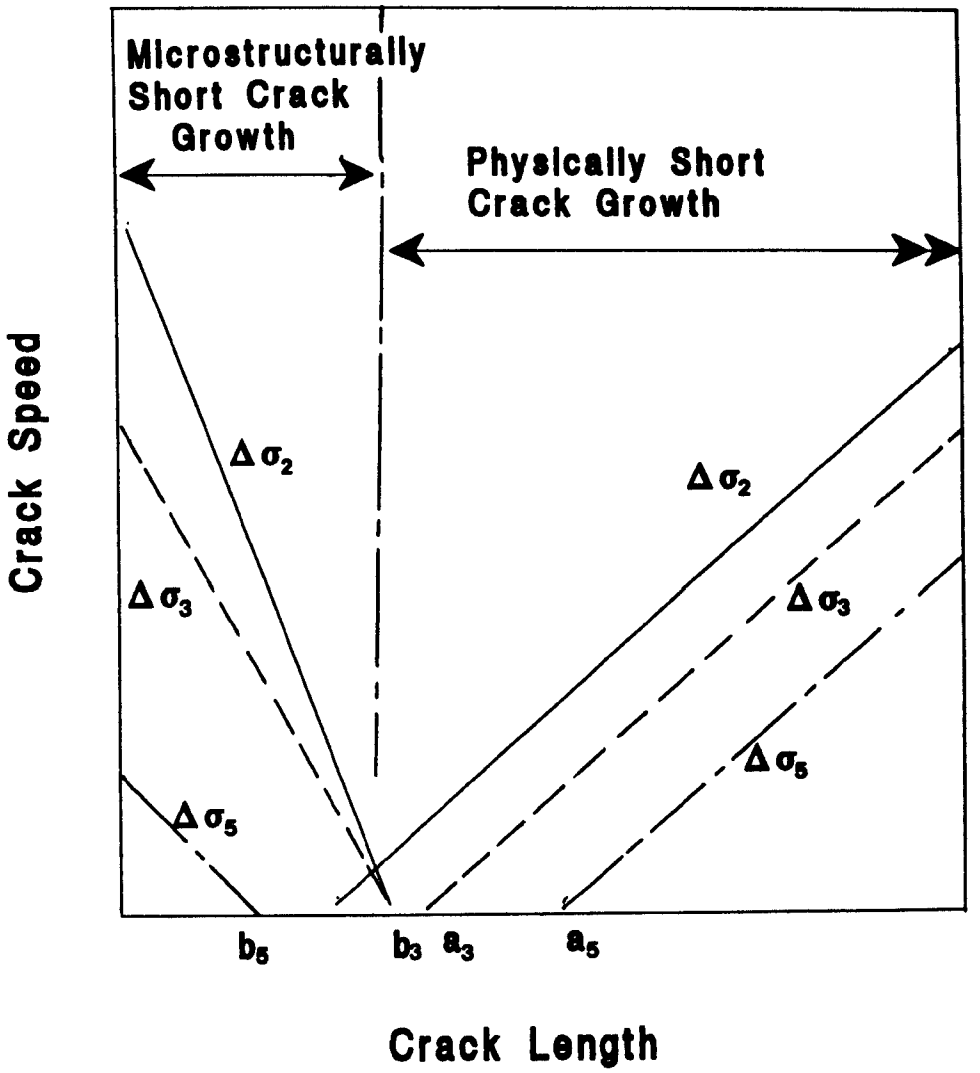

Figure 2.17 Effect of cyclic stress level and barrier strength on the propagation of a fatigue crack [130].

Figure 3.1 (A) to (F), Schematic diagrams illustrating the test specimen locations in the compressor disc section. All tangential specimens are designated by the letter T and all radial specimens by the letter R for identification. The letters A to E represent successive layers through the compressor disc as indicated in a cross-section of the disc section, Figure 3.1F. The letters I, M and O stand for Inner, Middle and Outer, respectively. Note the dimensions of all specimens are 10.0 x 10.0 x 80.0 mm.

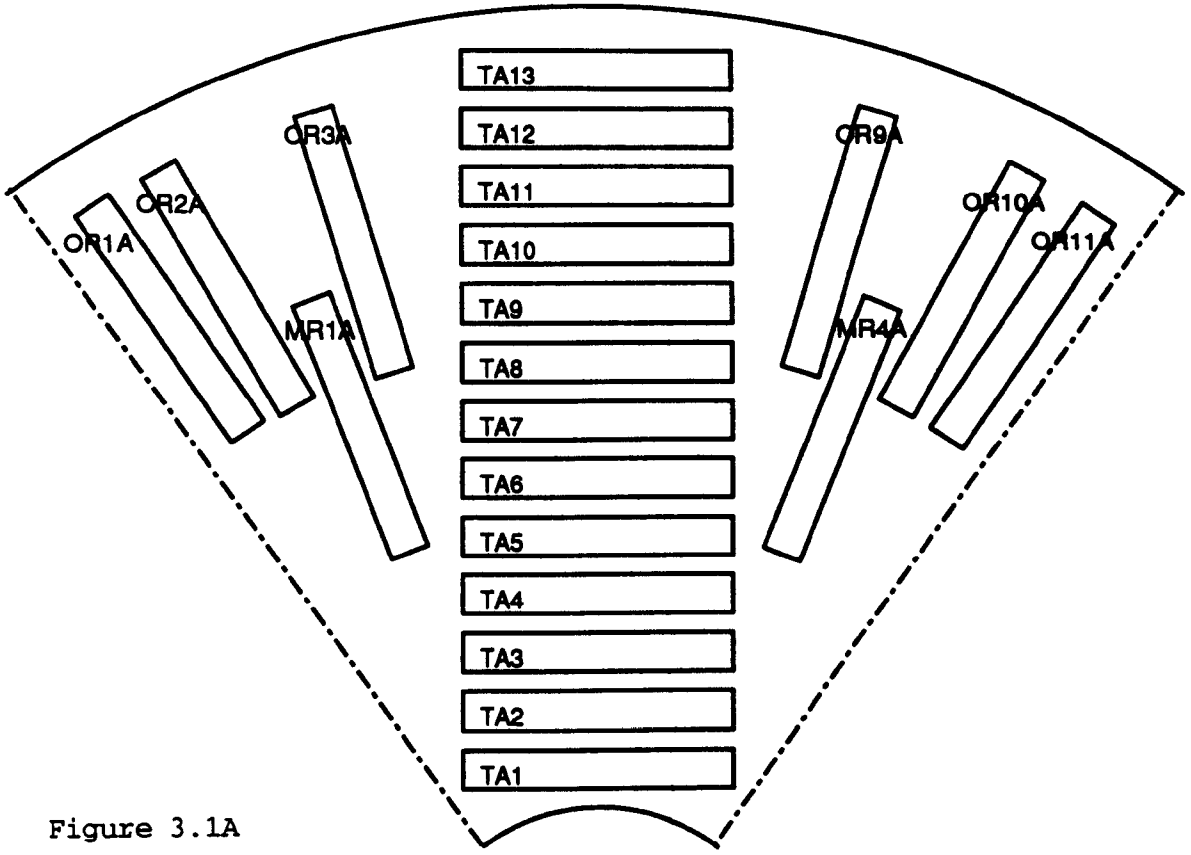

Figure 3.1A

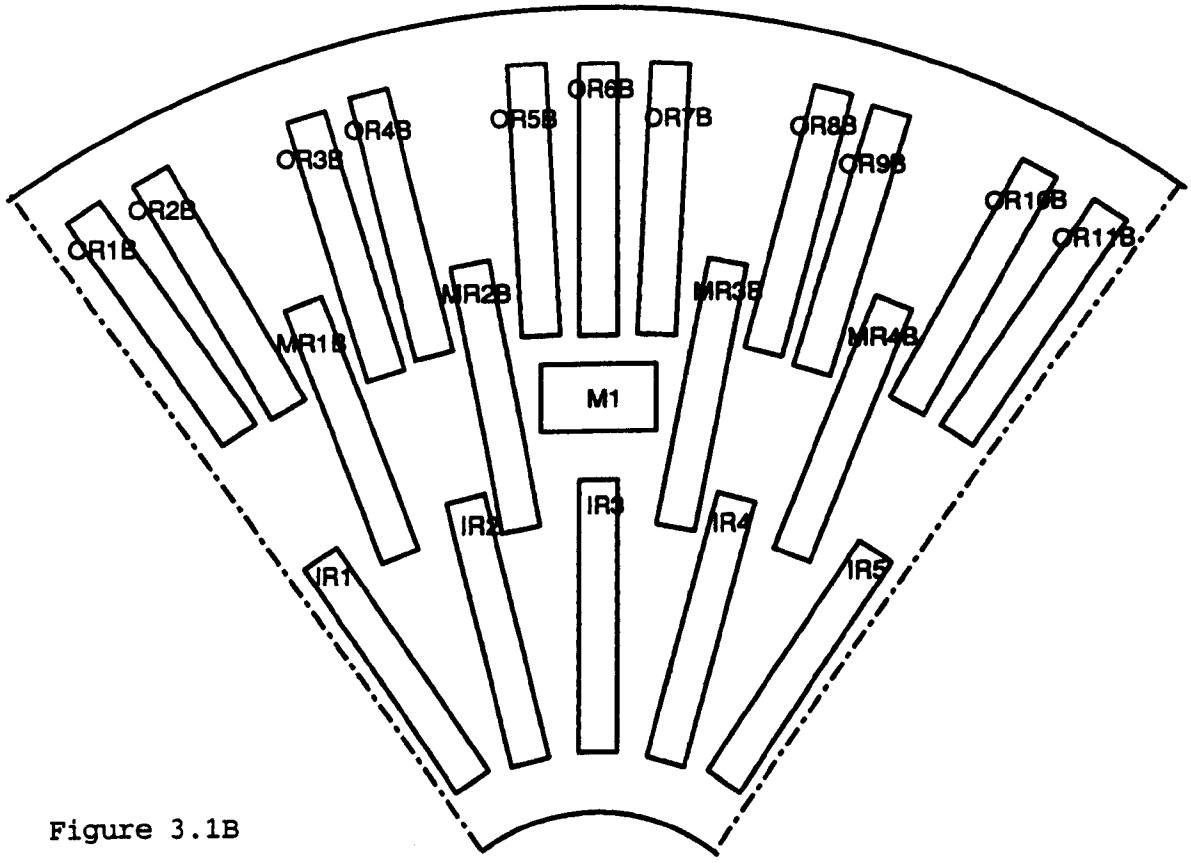

Figure 3.1B

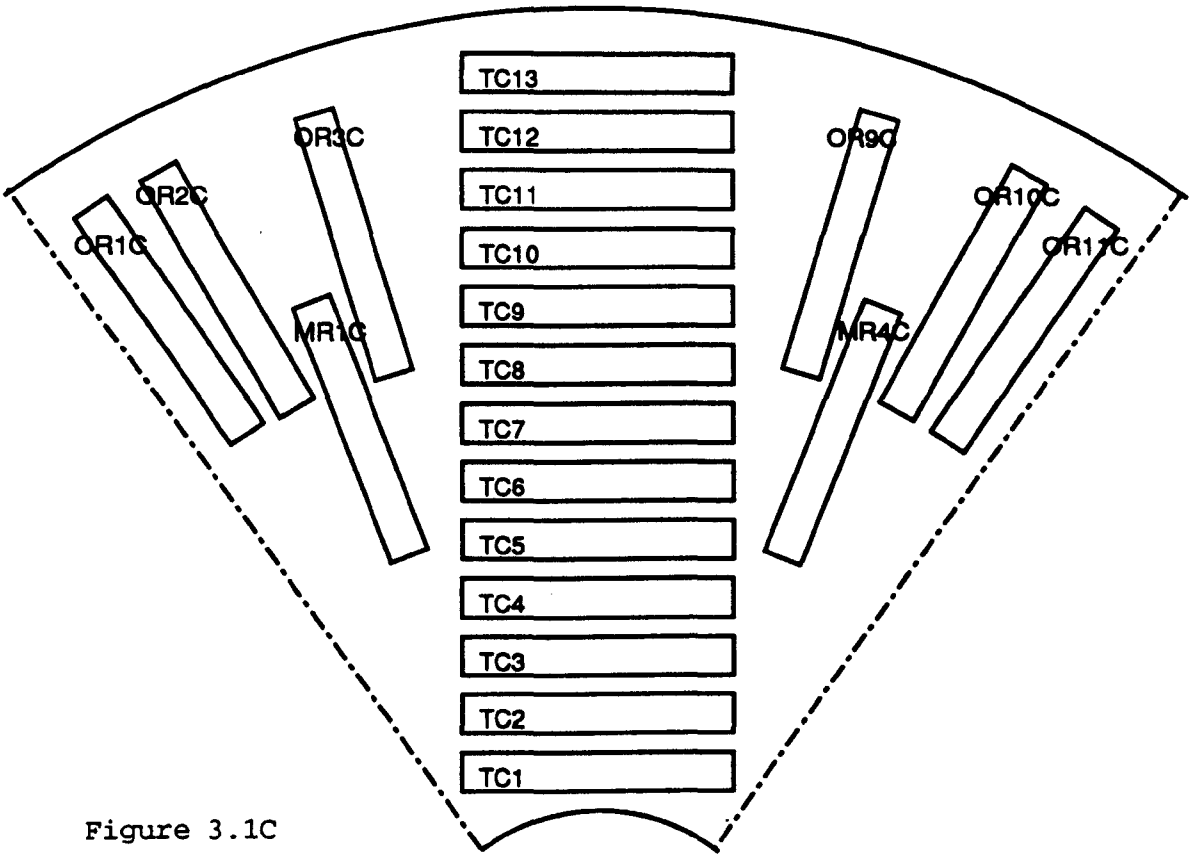

Figure 3.1C

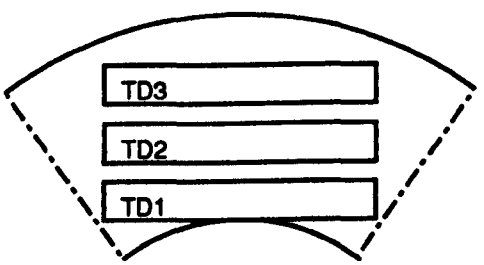

Figure 3.1D

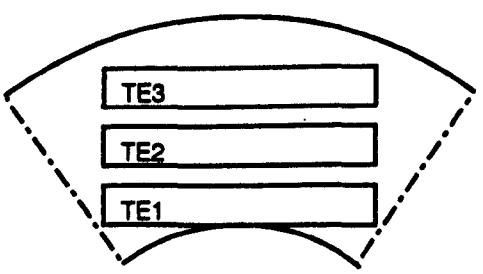

Figure 3.1E

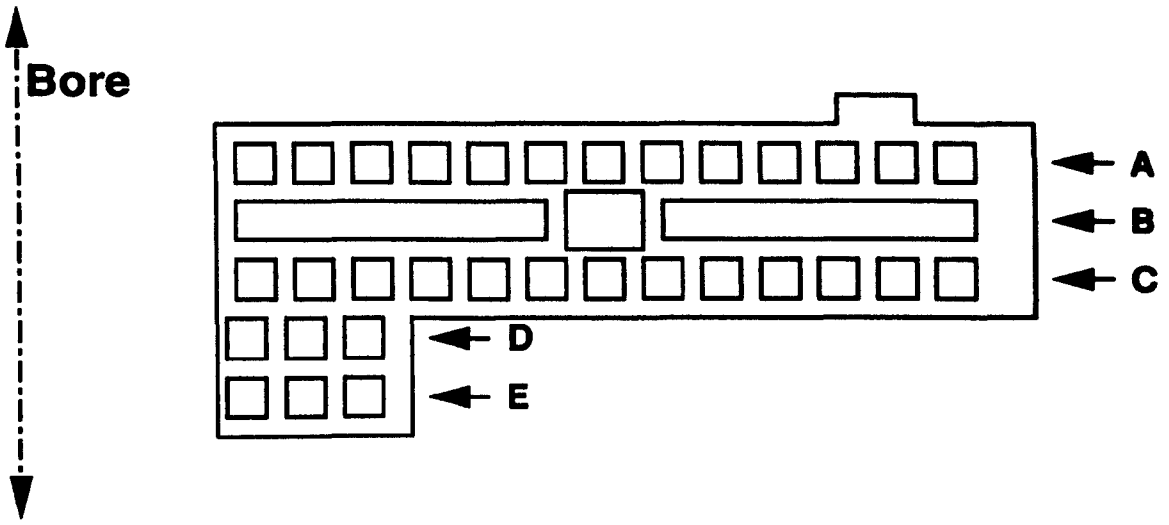

Figure 3.1F

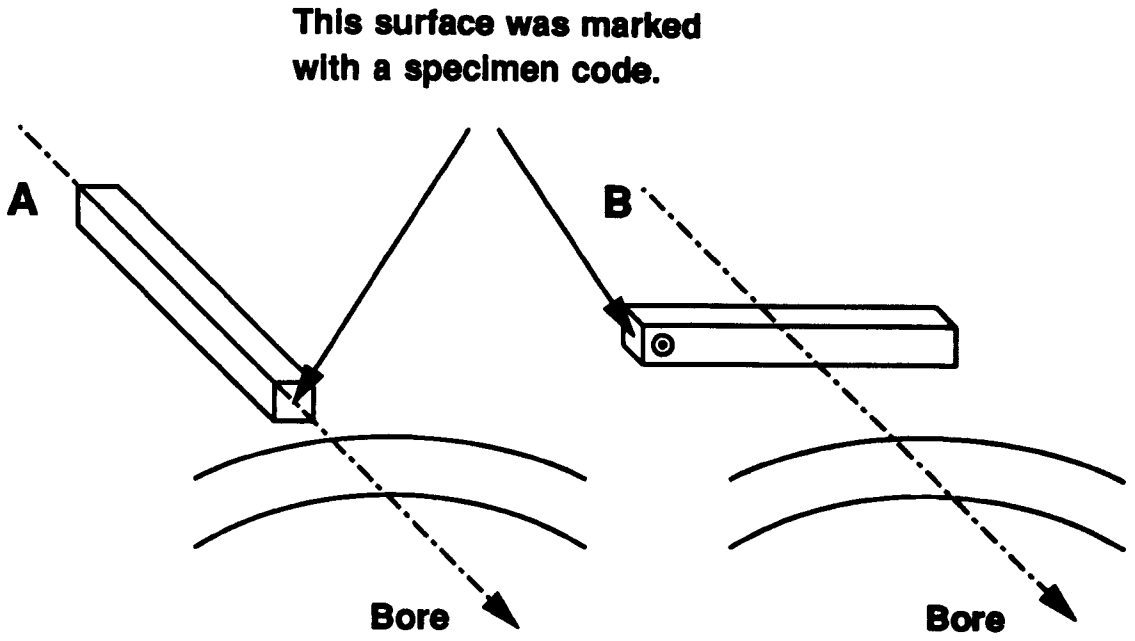

Figure 3.2 Diagram illustrating the surfaces and markings used to identify the position of (A) radial and (B) tangential specimens with respect to their original position within the compressor disc.
⊙ = surface facing the disc bore.

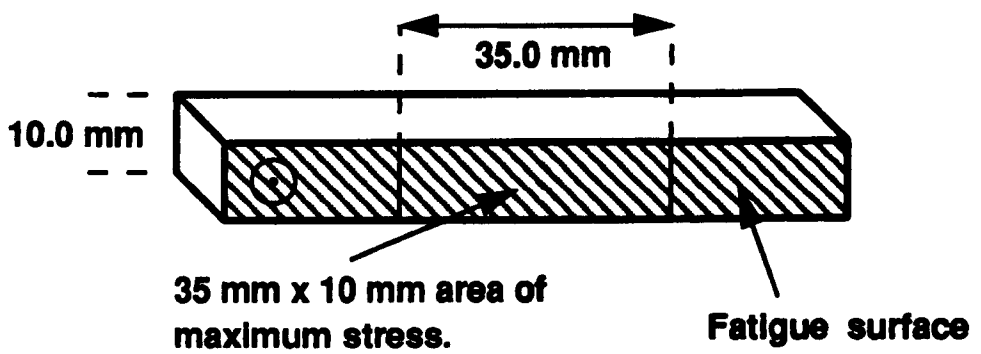

Figure 3.3 Position of the fatigue surface and surface of maximum stress on a tangential 4-point bend specimen.

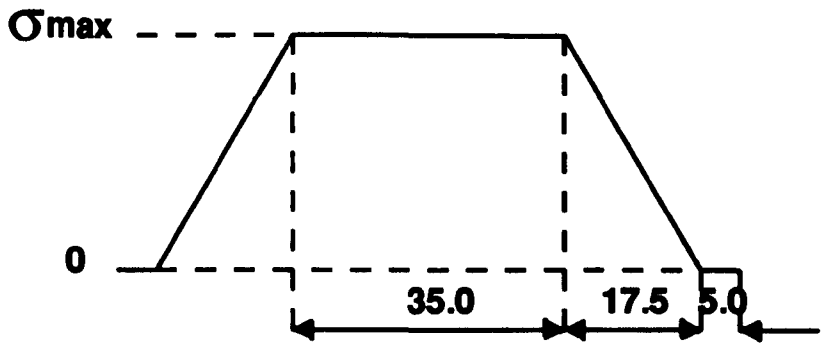

Figure 3.4 Bending moment diagram indicating the stress profile across the specimen length. All dimensions in millimetres.

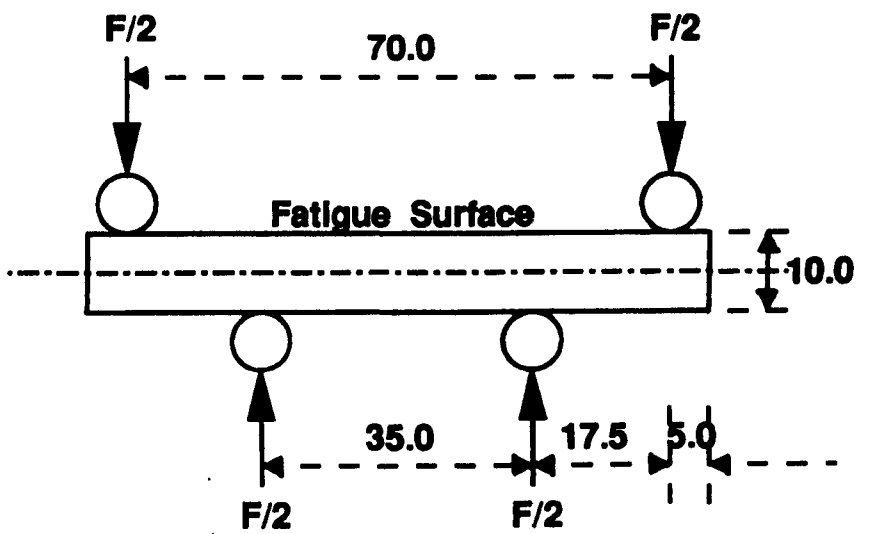

Figure 3.5 Four point bend test specimen configuration. All dimensions in millimetres.

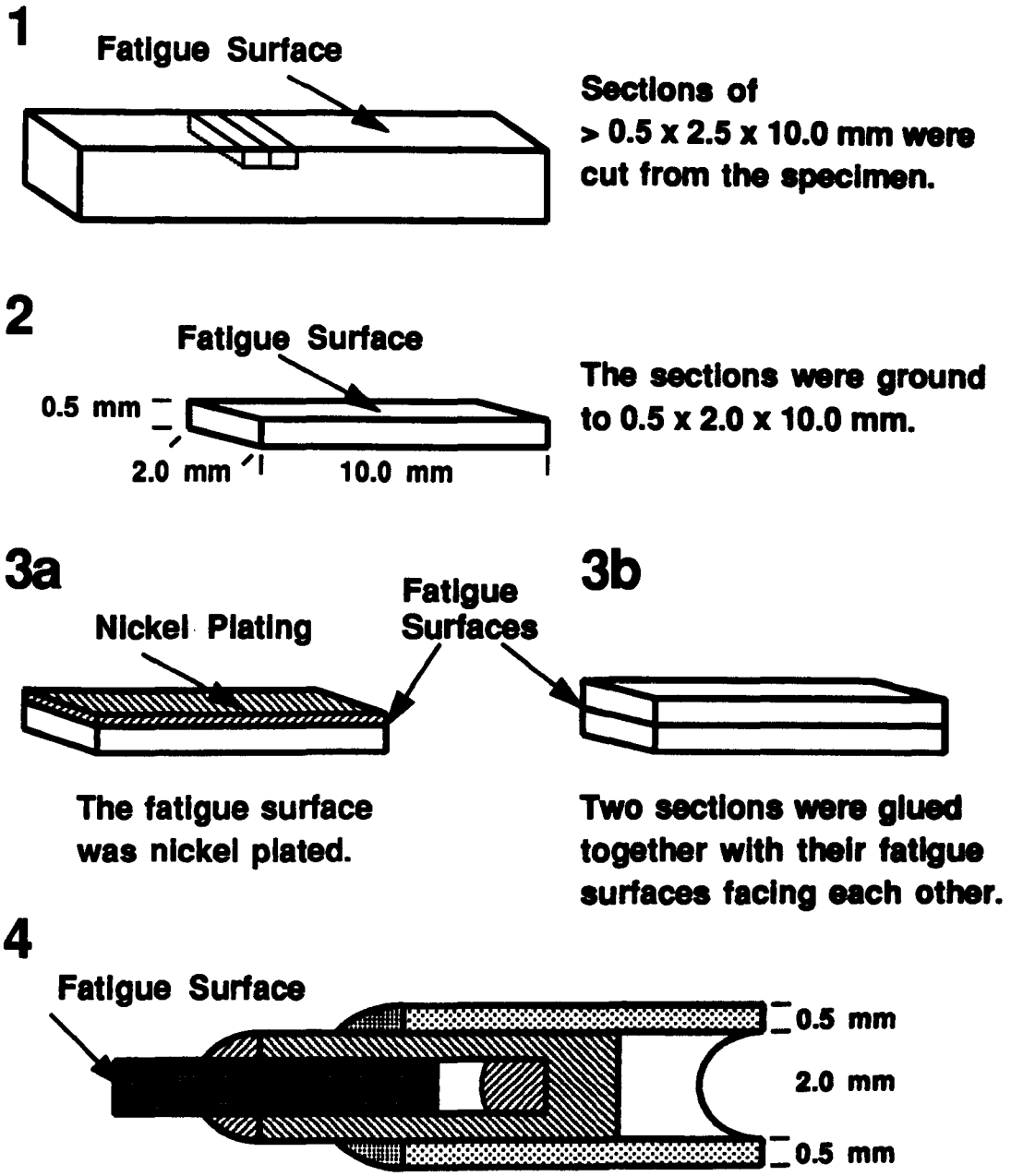

Figure 3.6A Cross-sectional thin foil preparation.

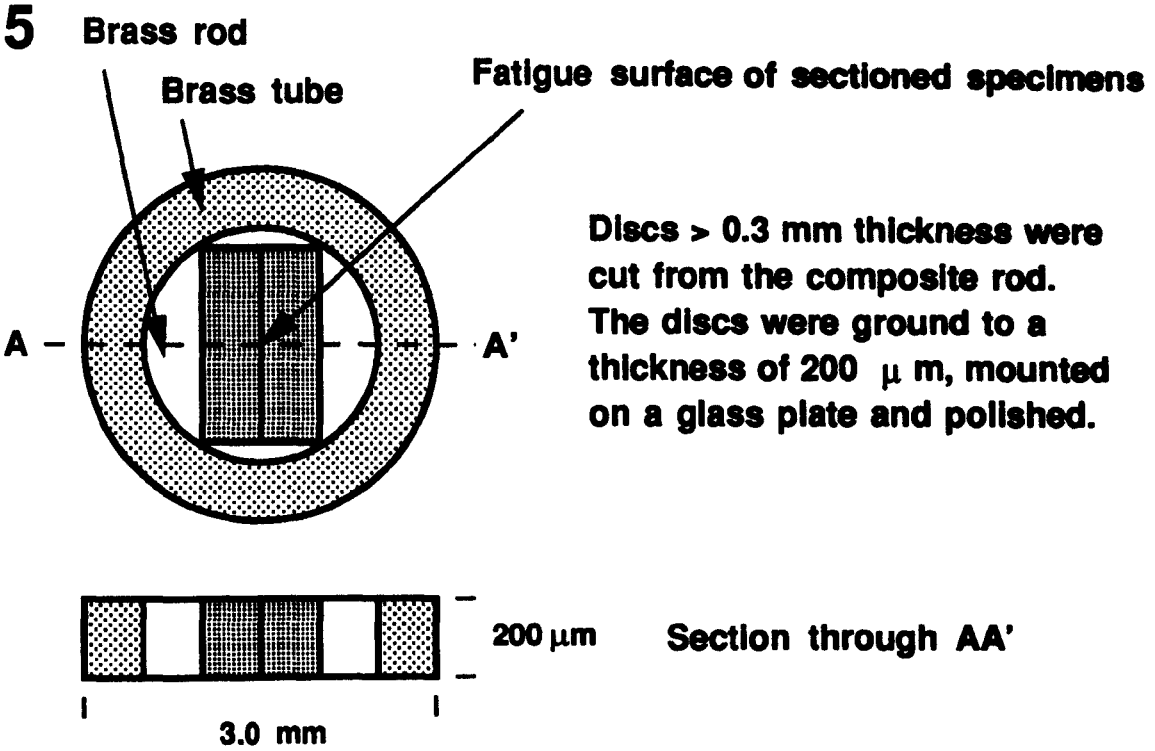

Figure 3.6B Cross-sectional thin foil preparation.

7

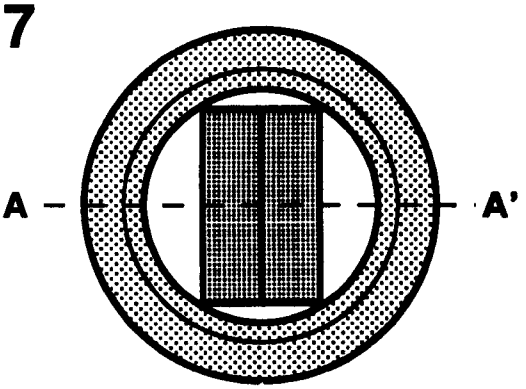

The surface without the copper grid was dimpled so that the remaining thickness of the disc was 80 μm. The dimpled surface was polished with colloidal silica.

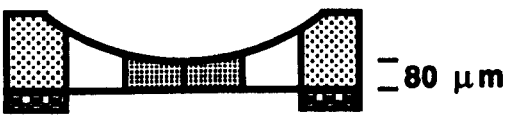

Section through AA'

8

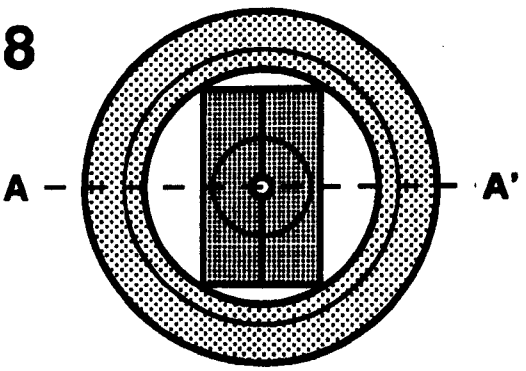

The disc was ion-beam milled to perforation from both sides at 6 kV and 0.5 mA. The angle of the ion beam was 16°.

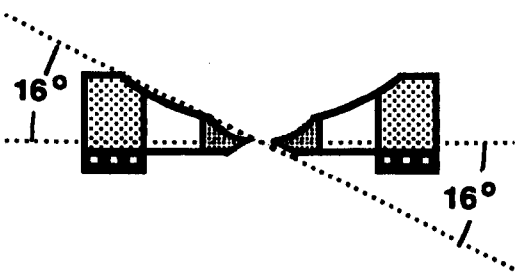

Section through AA'

Figure 3.6C Cross-sectional thin foil preparation.

A

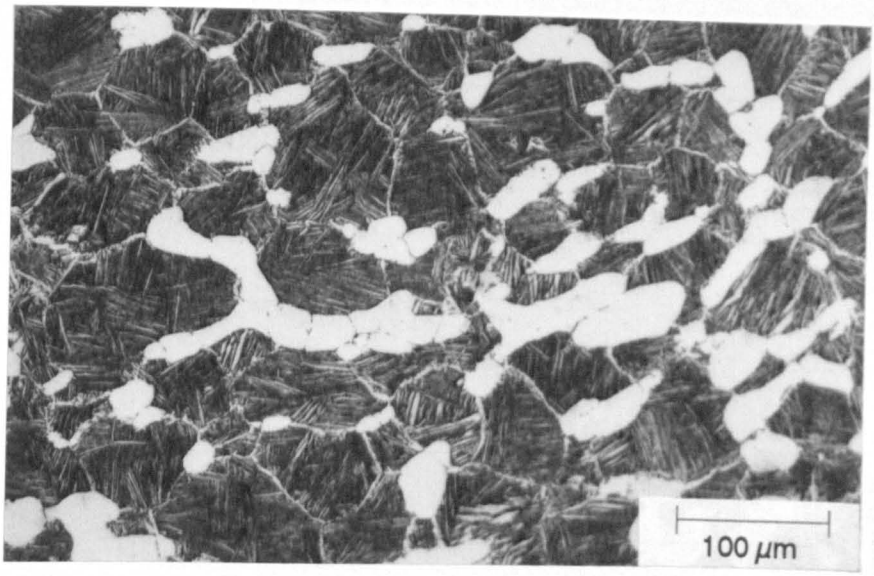

B

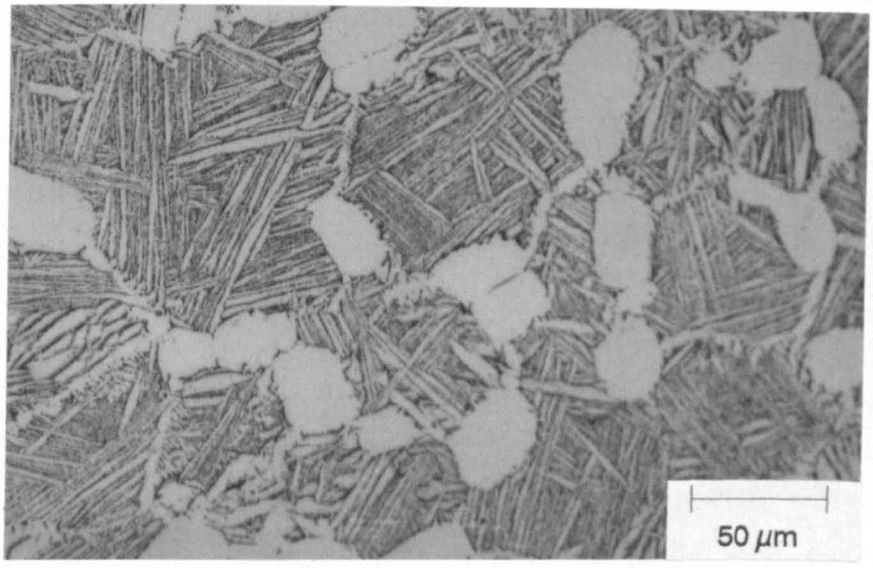

Figure 4.1 (A) and (B) Optical microstructure of IMI 834. Both micrographs clearly show the primary-α grains (white) at triple points in the grain boundaries of the transformed-β grains. The transformed-β grains are outlined by a thin layer of grain boundary alpha phase. Each transformed-β grain contains colonies of similarly orientated α-platelets.

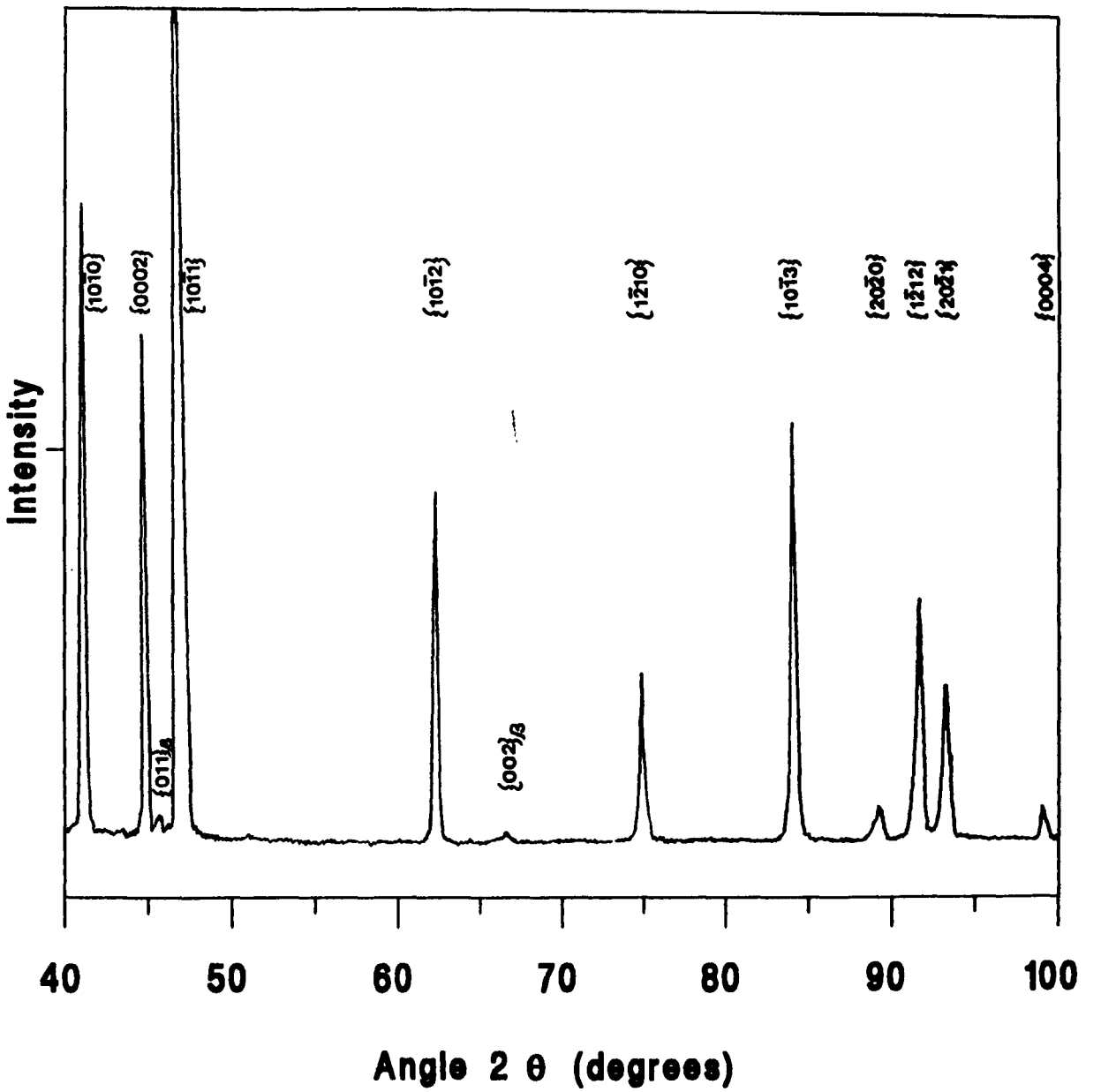

Figure 4.2 X-ray trace of IMI 834 showing the relative intensities of reflections from the alpha phase {hkil} and retained beta phase {hkl}.
(λ = 0.179021 nm).

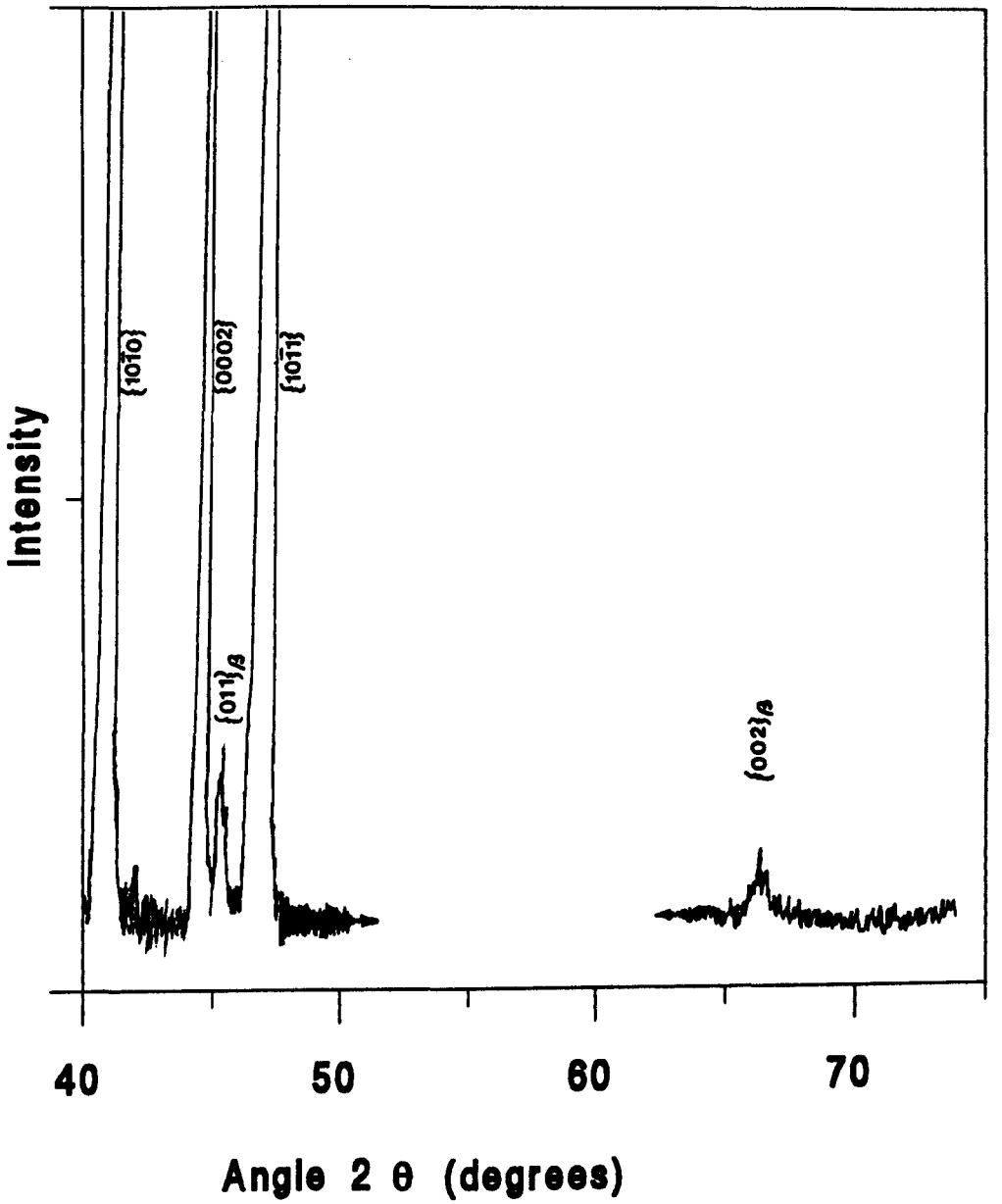

Figure 4.3 X-ray trace showing two peaks from the retained beta phase from which the lattice parameter was calculated. (λ = 0.179021 nm).

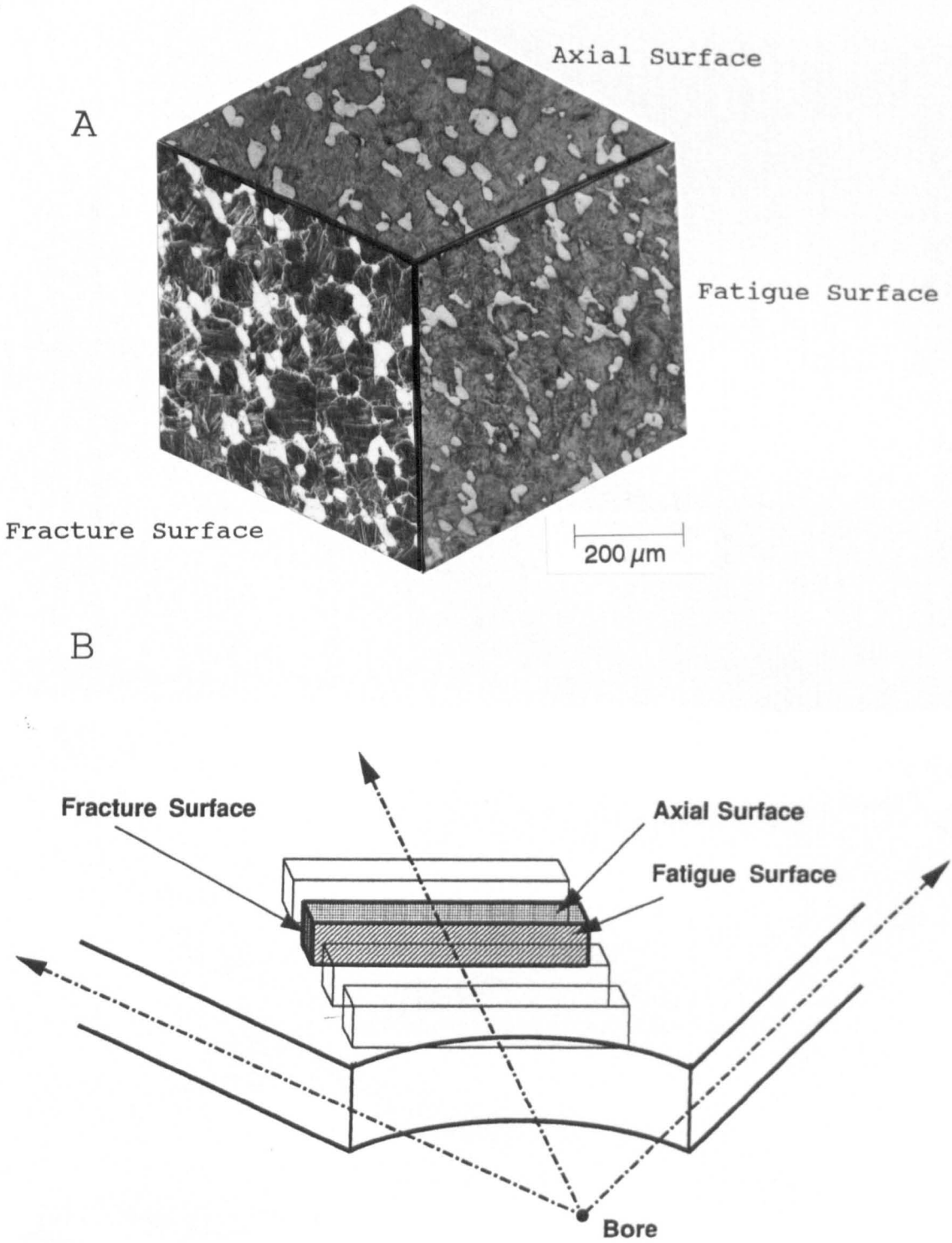

Figure 4.4 (A) Optical micrographs from the three orthogonal surfaces (indicated) of a tangential four point bend specimen. (B) Schematic diagram illustrating these surfaces in relation to the compressor disc geometry.

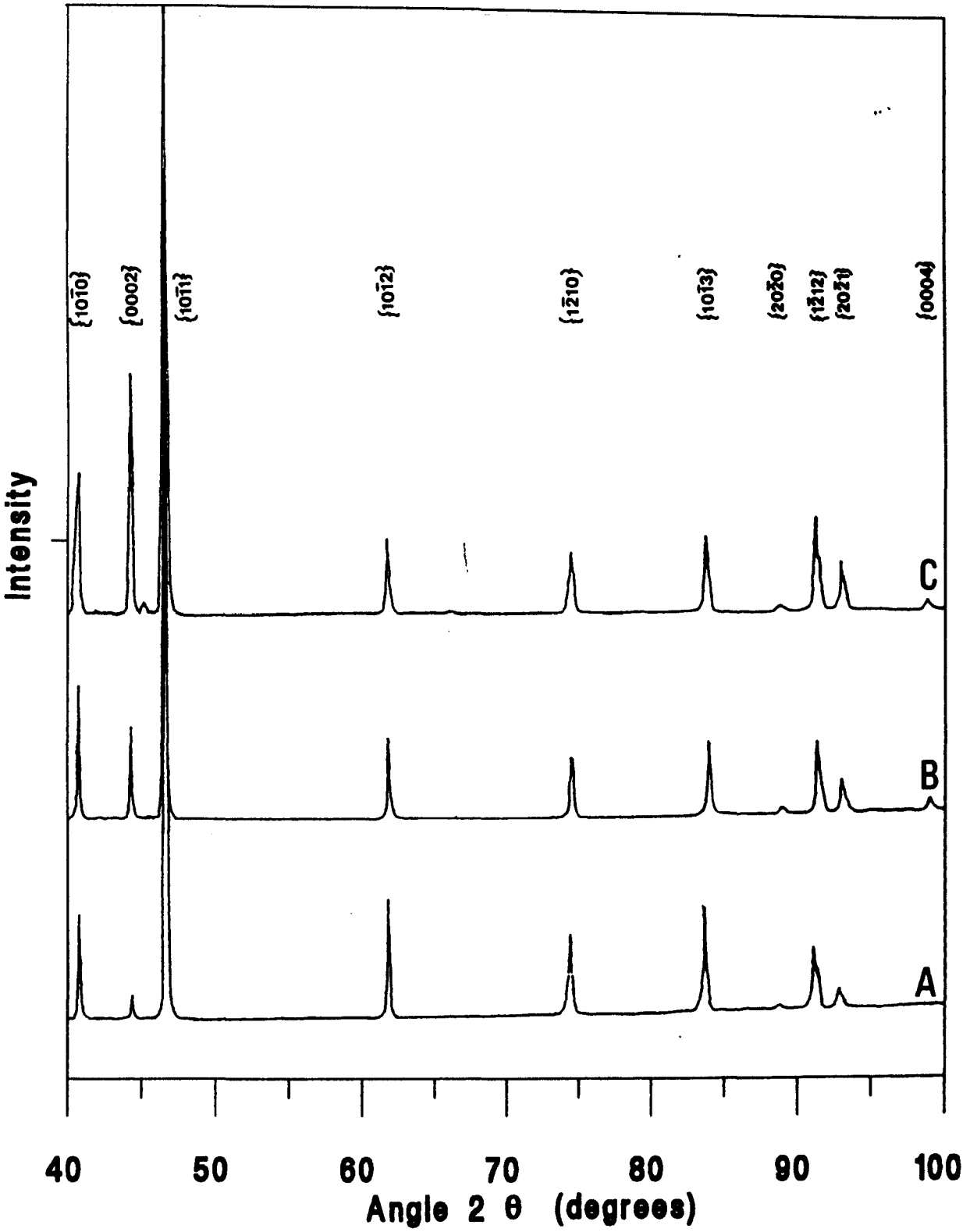

Figure 4.5 X-ray traces comparing the heights of reflections from the alpha phase from the three orthogonal surfaces. (A) Axial surface, (B) fatigue surface and (C) fracture surface. Of particular interest are the relative heights of the {0002} reflections. (λ = 0.179021 nm)

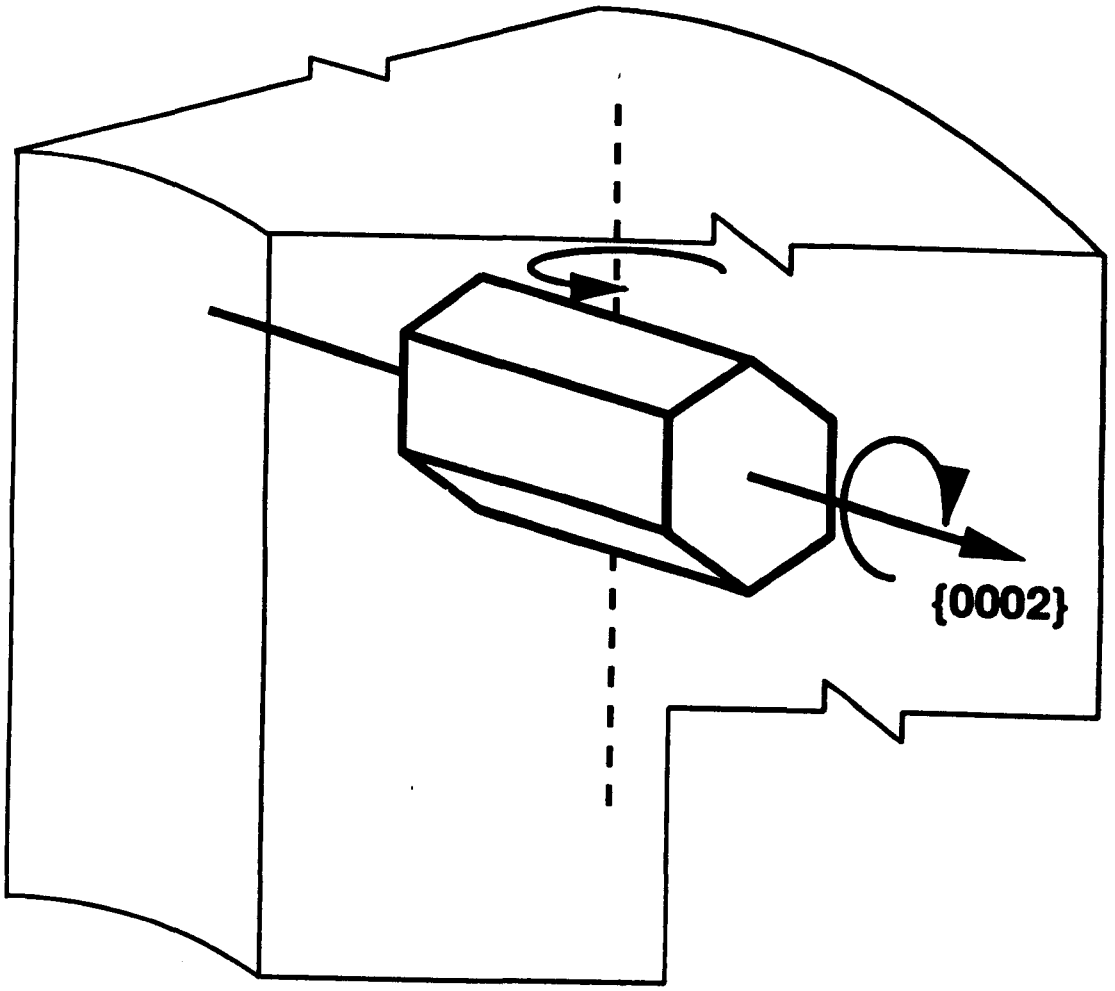

Figure 4.6 Schematic diagram illustrating the putative preferred hcp texture in the compressor disc section. The basal plane faces in the ‹0002› direction. The arrows represent the possible freedom of rotation of the crystal. {0002} reflections are favoured at or between the tangentially facing (fracture surface) and the radially facing (fatigue surface) directions.

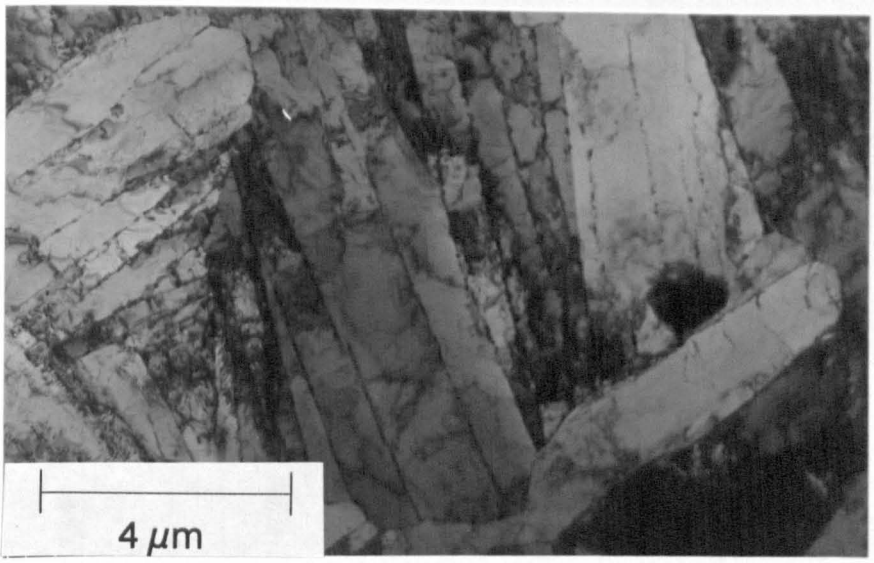

Figure 4.7 Low magnification T.E.M. micrograph showing the arrangement of α-platelets in adjacent colonies within a transformed-β grain. The α-platelet boundaries are generally linear, the other, less defined, bands are thickness fringes in the thin foil.

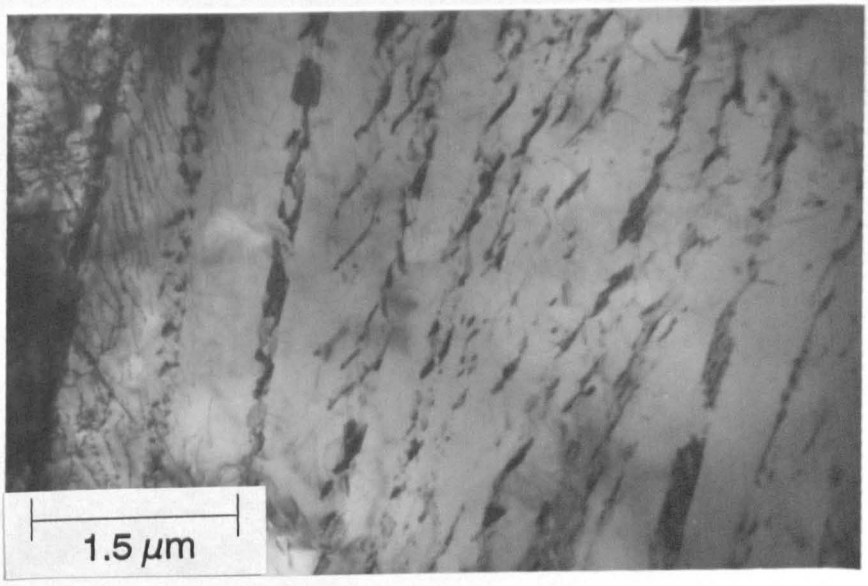

Figure 4.8 T.E.M. micrograph of part of a transformed-β colony showing retained-β phase (dark) along the boundaries of α-platelets.

A

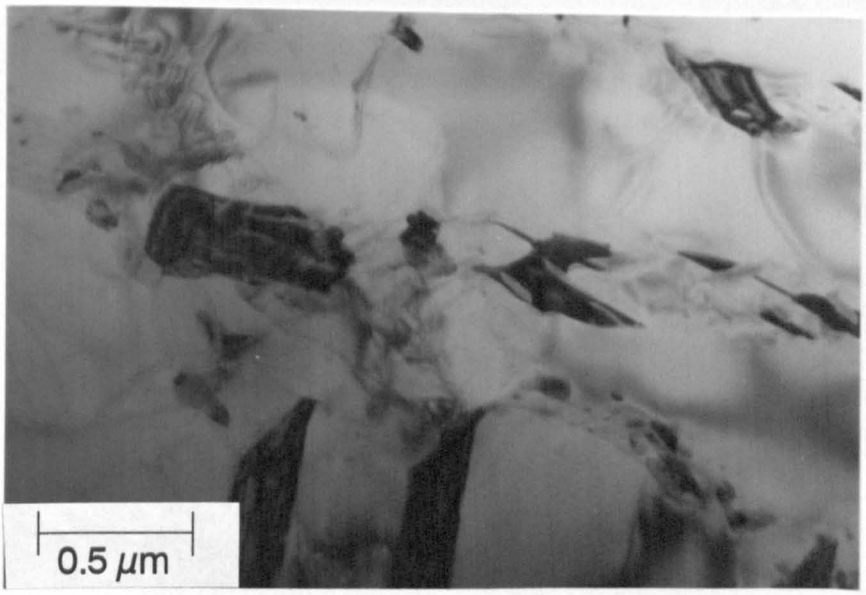

B

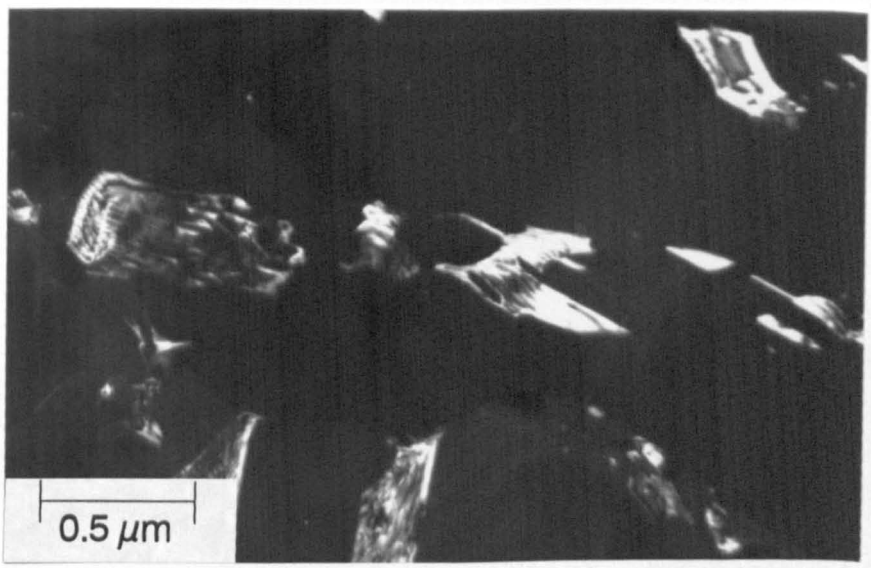

C

Figure 4.9 T.E.M. micrographs showing the retained-β phase along α-platelet boundaries; (A) bright field image, (B) dark field image, (C) corresponding diffraction pattern.

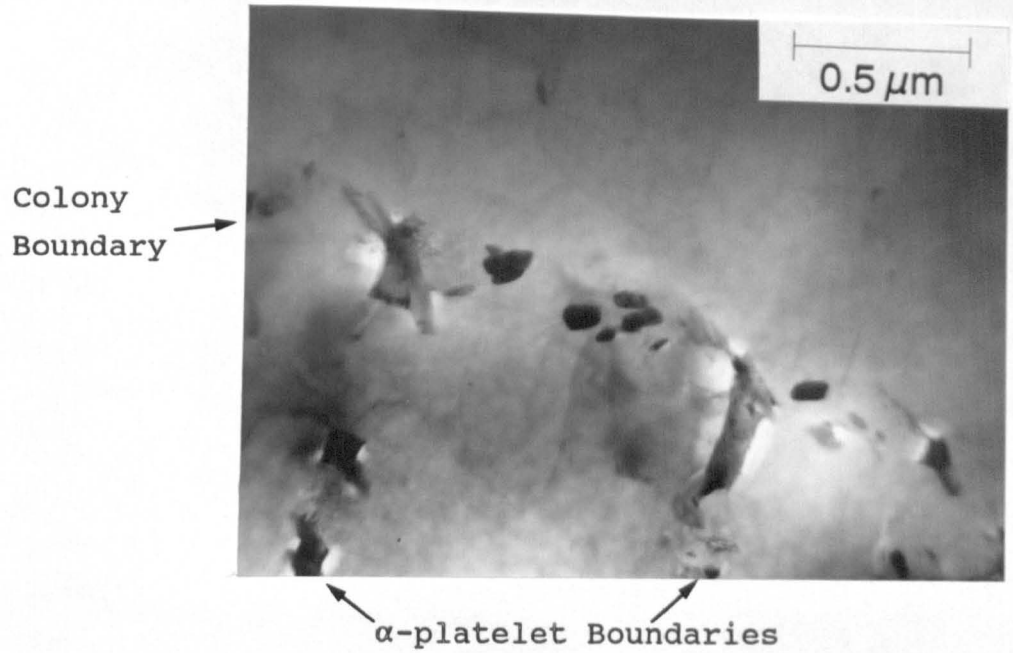

Figure 4.10 T.E.M. micrograph showing small silicide particles (black) along a colony boundary. Some retained-β phase is also present along the α-platelet boundaries (indicated).

Figure 4.11 (A) Dark field T.E.M. micrograph of silicides of approximately 0.05 - 0.3 μm in length in an α-platelet, (B) corresponding diffraction pattern. The ring in the diffraction pattern shows that the silicides are randomly orientated in this example.

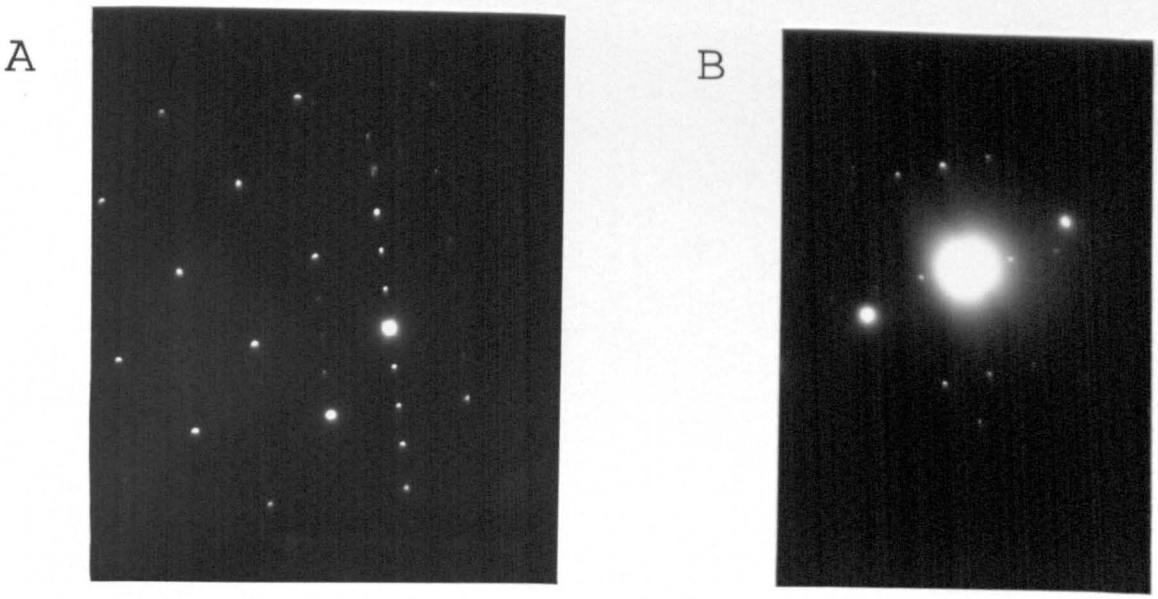

Figure 4.12 (A) and (B) diffraction patterns showing the reflections from silicide particles (less intense reflections) and the α phase. In (A) the orientation relationship $[01\bar{1}1]_\alpha // [\bar{2}110]_s$; $(\bar{2}110)_\alpha // (01\bar{1}0)_s$ holds (where s = silicide).

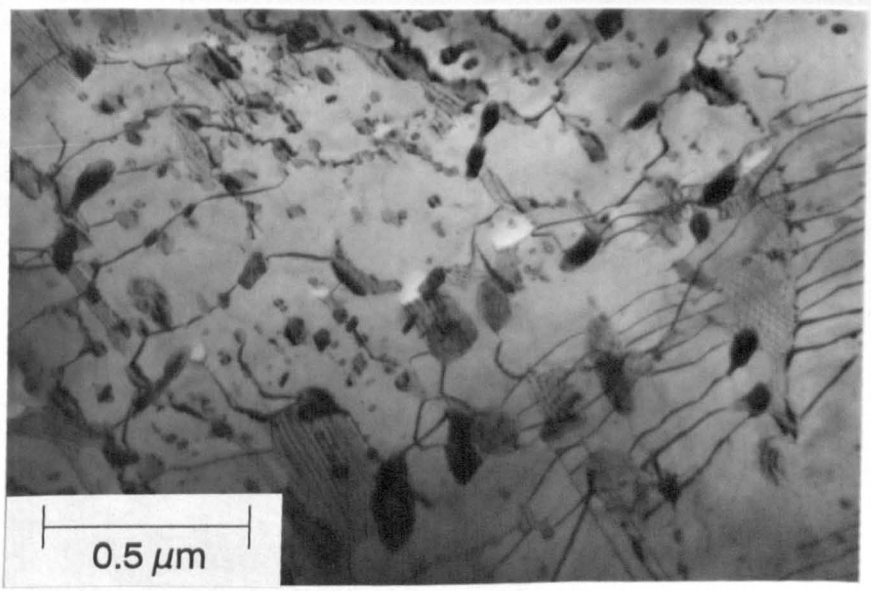

Figure 4.13 T.E.M. micrograph of interactions observed between dislocations, silicide particles and retained-β phase particles. Such interactions were observed when an α-platelet boundary occurred in the plane of the foil.

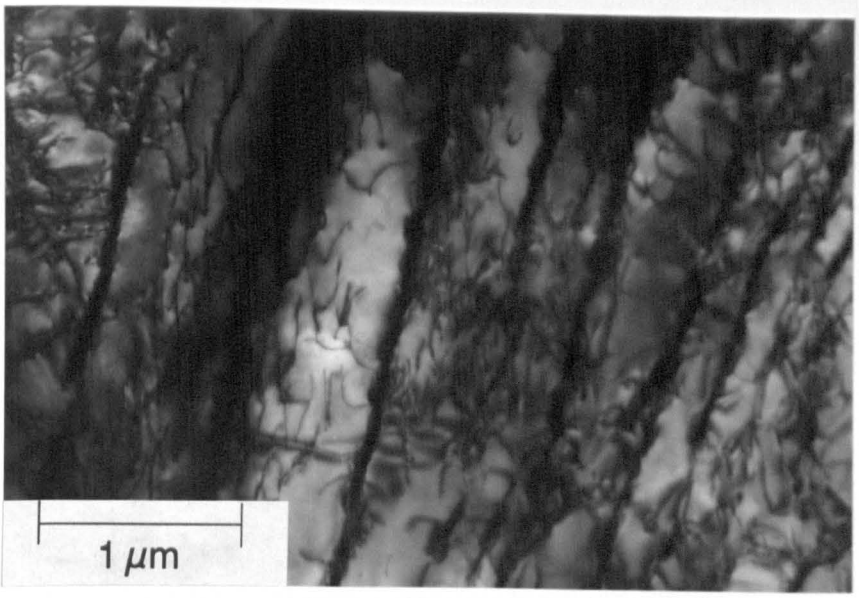

Figure 4.14 T.E.M. micrograph showing a high dislocation density within α-platelets. (Taken using multibeam conditions).

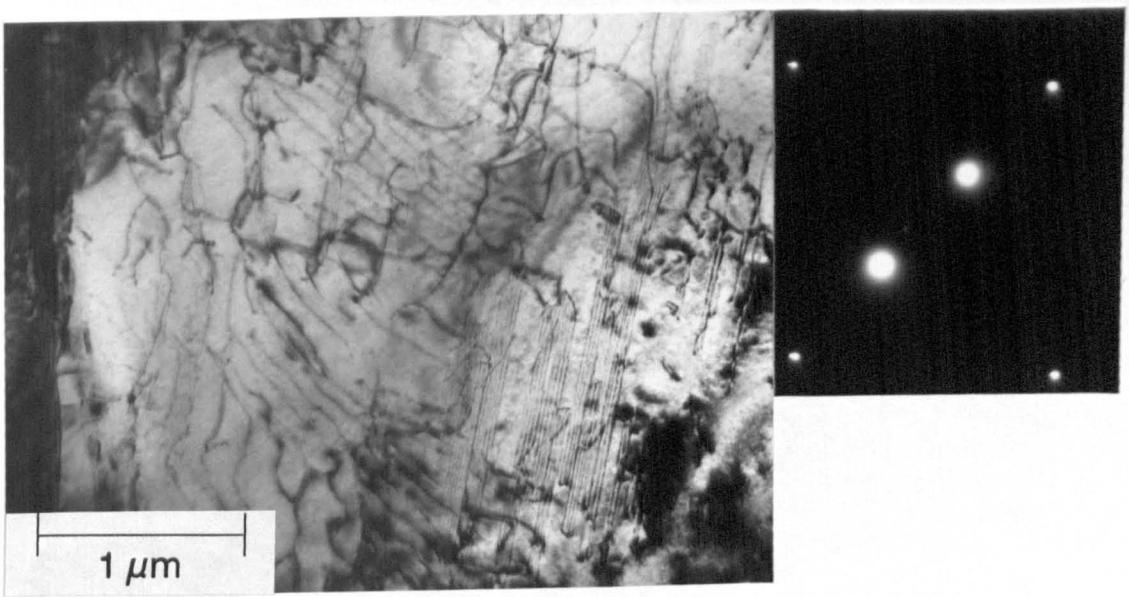

Figure 4.15 T.E.M. micrograph showing stacking faults (parallel fringes) in an α-platelet. The faults are bounded by partial dislocations. In the corresponding diffraction pattern, $\underline{g} = [01\bar{1}1]$, $B = [7\bar{2}\bar{5}3]$.

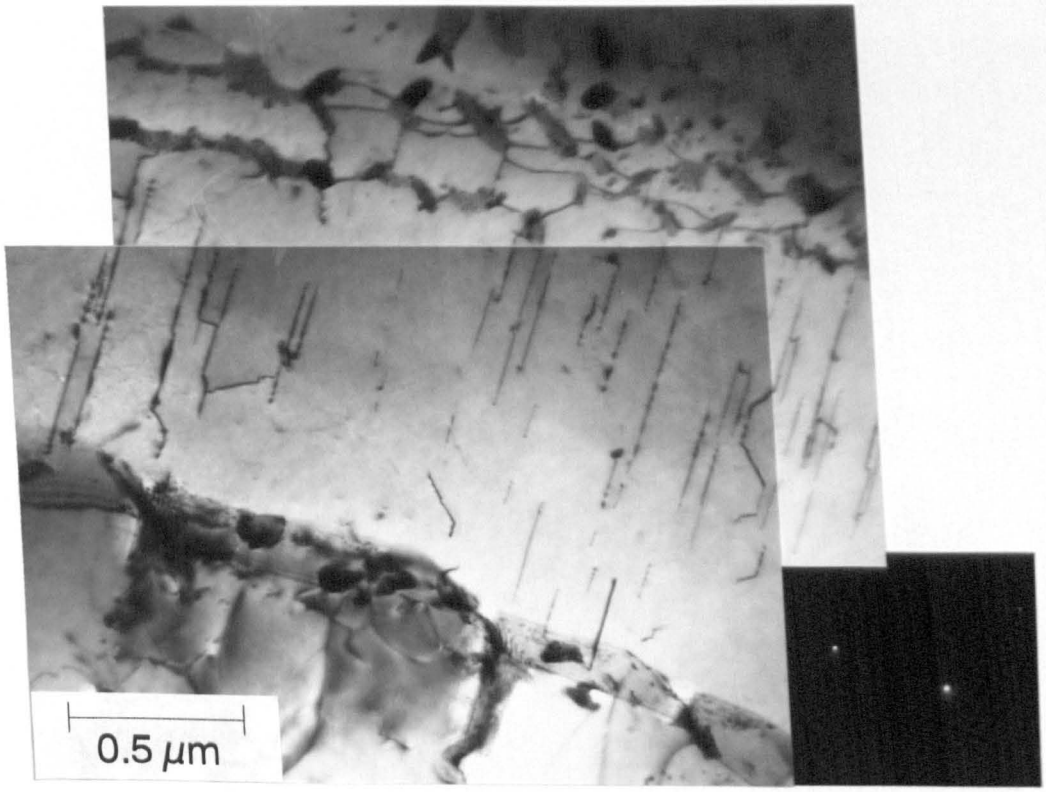

Figure 4.16 T.E.M. micrograph showing dislocations in contrast in the α-platelet and at 90° to g = [0002]. Some silicide precipitation has occurred on these dislocations.

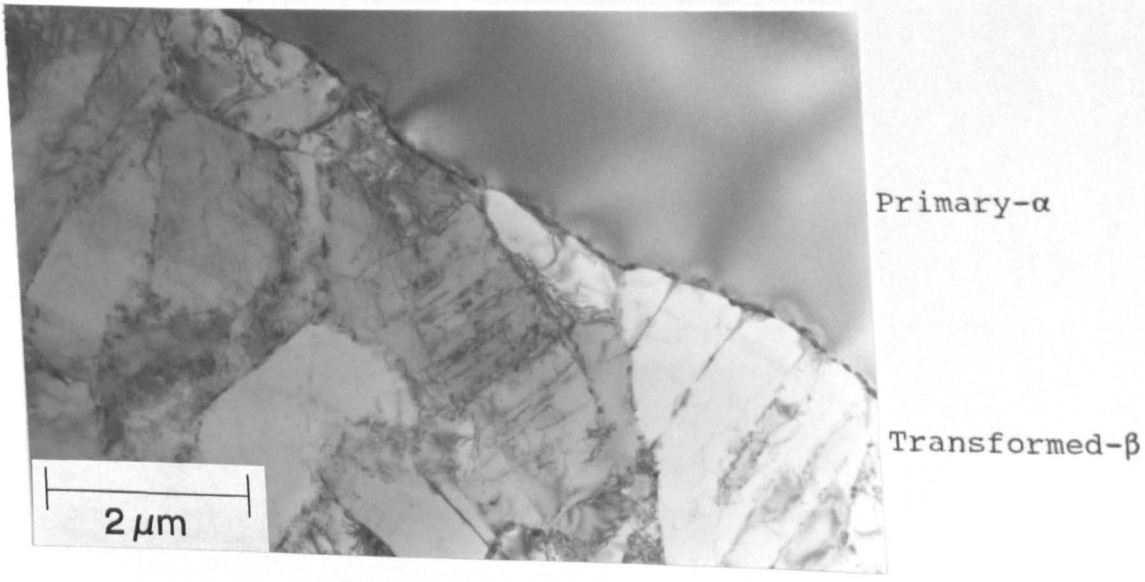

Figure 4.17 Low magnification T.E.M. micrograph showing the grain boundary between a primary-α grain and a transformed-β grain (taken under multibeam conditions).

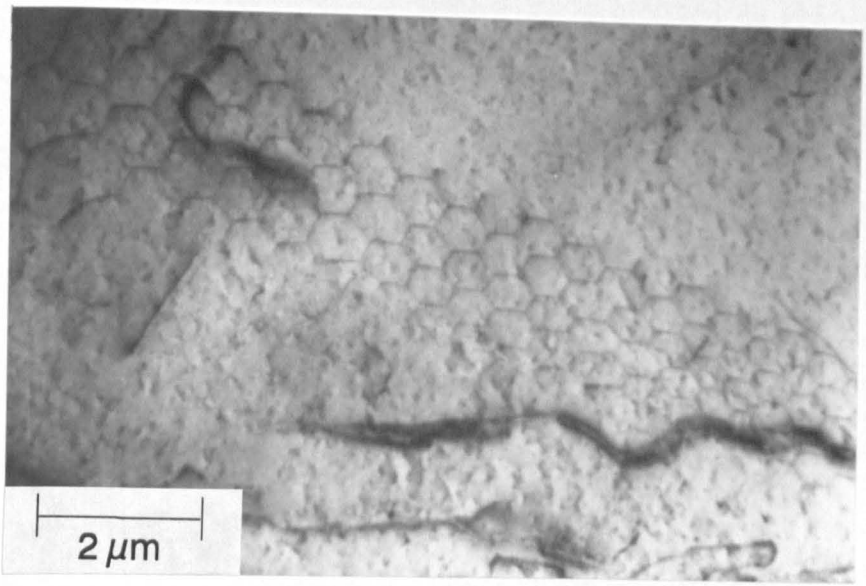

Figure 4.18 Bright field T.E.M. micrograph showing a hexagonal dislocation array. Such arrays occur at grain boundaries which separate two primary-α subgrains with a low misorientation.

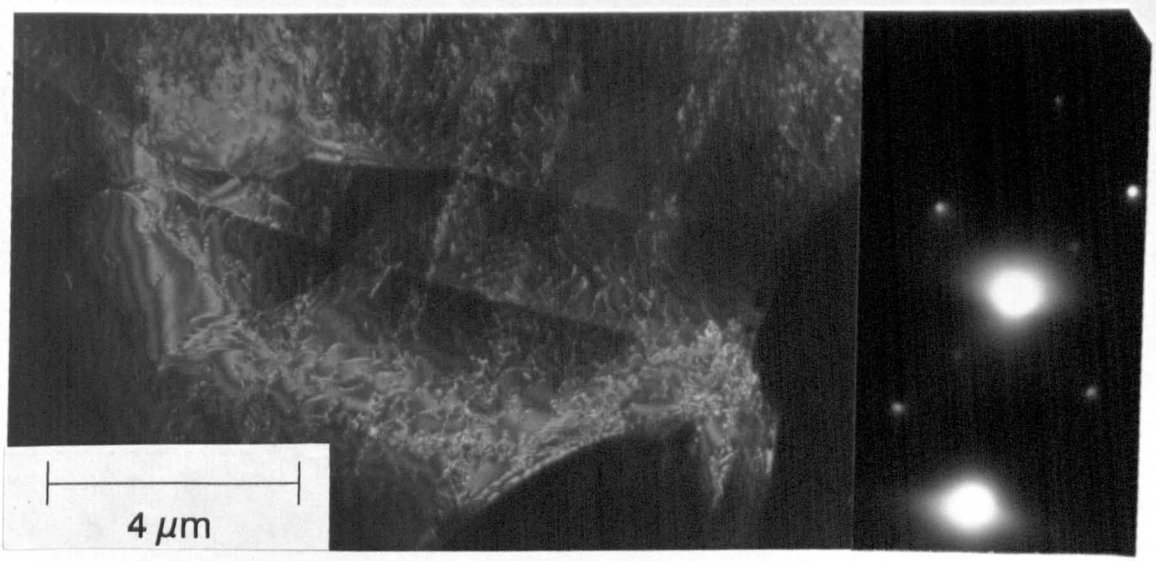

Figure 4.19 Low magnification dark field T.E.M. micrograph showing a high dislocation density contained within subgrains in the primary-α phase. B = close to $[1\bar{5}43]$, g = $[01\bar{1}3]$.

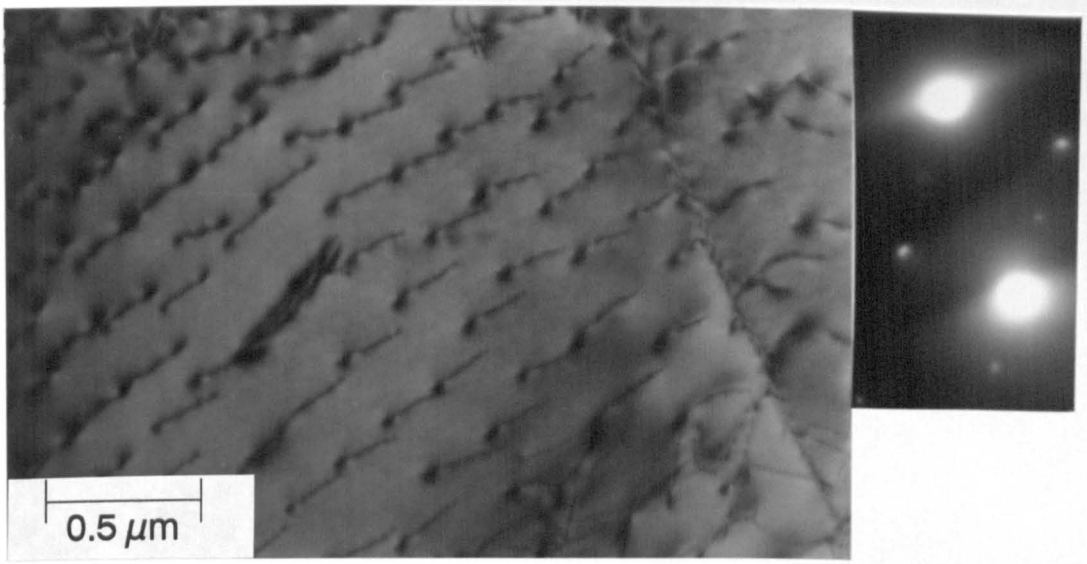

Figure 4.20 Bright field T.E.M. micrograph showing a network of dislocations contained in a primary-α subgrain. B = close to $[1\bar{5}43]$, g = $[01\bar{1}3]$.

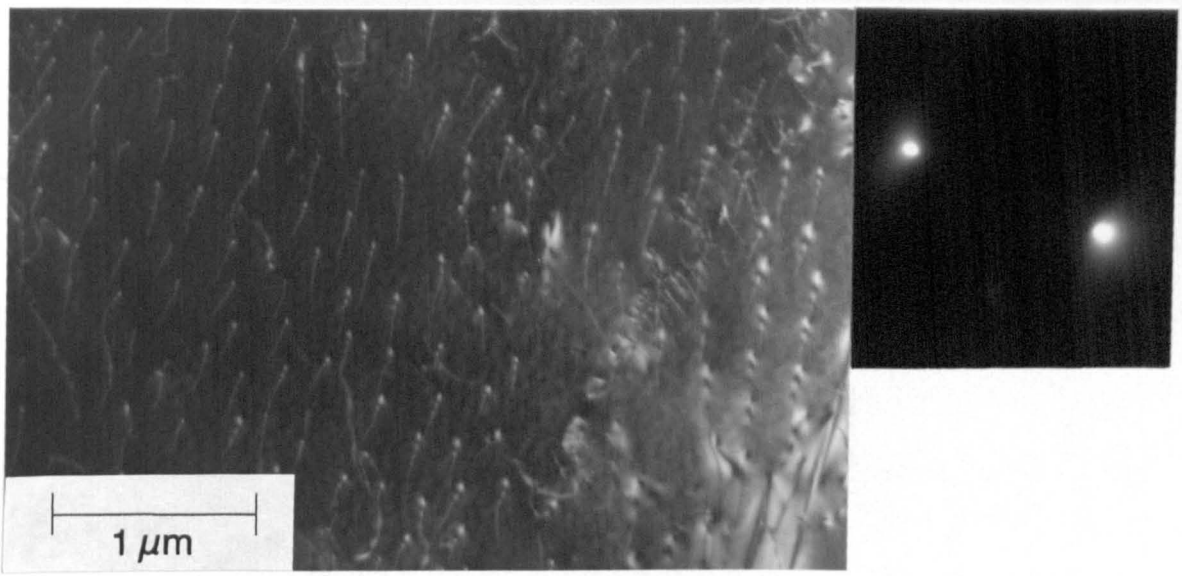

Figure 4.21 Dark field T.E.M. micrograph showing an example of the networks containing a high dislocation density which were observed in some primary-α grains. B = close to $[1\bar{5}43]$, g = $[01\bar{1}3]$.

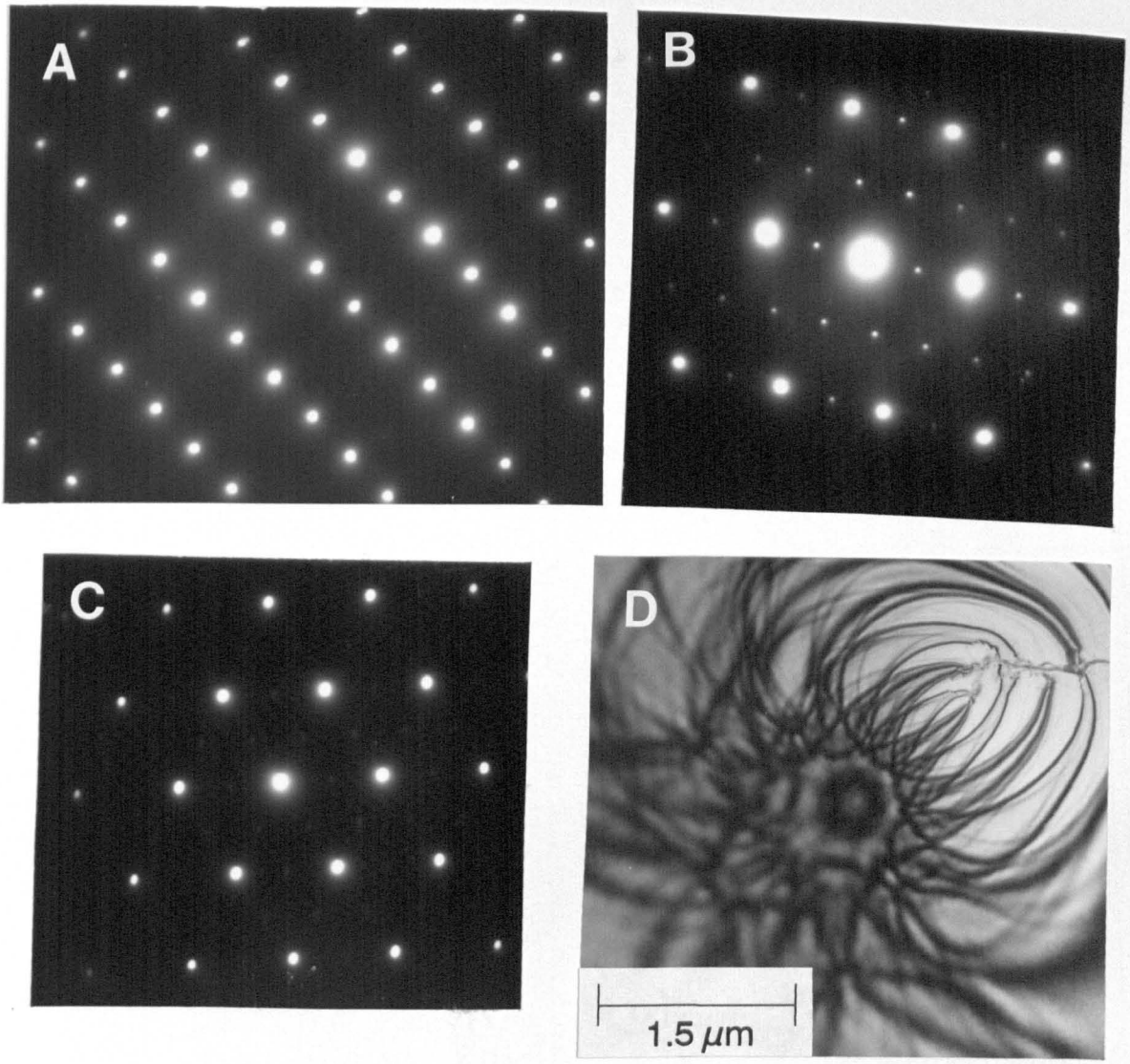

Figure 4.22 (A) to (C) Diffraction patterns from primary-α grains indicating the presence of Ti_3Al by additional reflections at half the distance of reflections from the primary-α phase. (A) B = $[1\bar{2}10]$, (B) B = $[2\bar{4}23]$, (C) B = [0001]. (D) Bright field T.E.M. micrograph of the bend centre from which diffraction pattern (C) was taken.

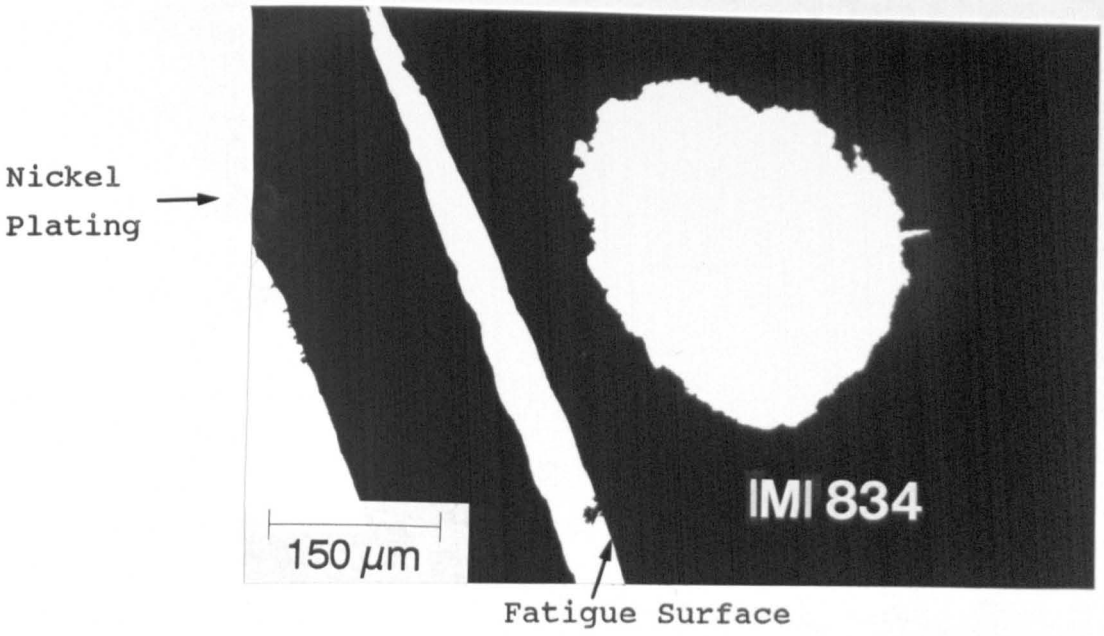

Figure 5.1 Low magnification T.E.M. micrograph showing the position of the thin area obtained from a nickel-plated cross-sectional thin foil. The fatigue surface and the nickel plating are indicated.

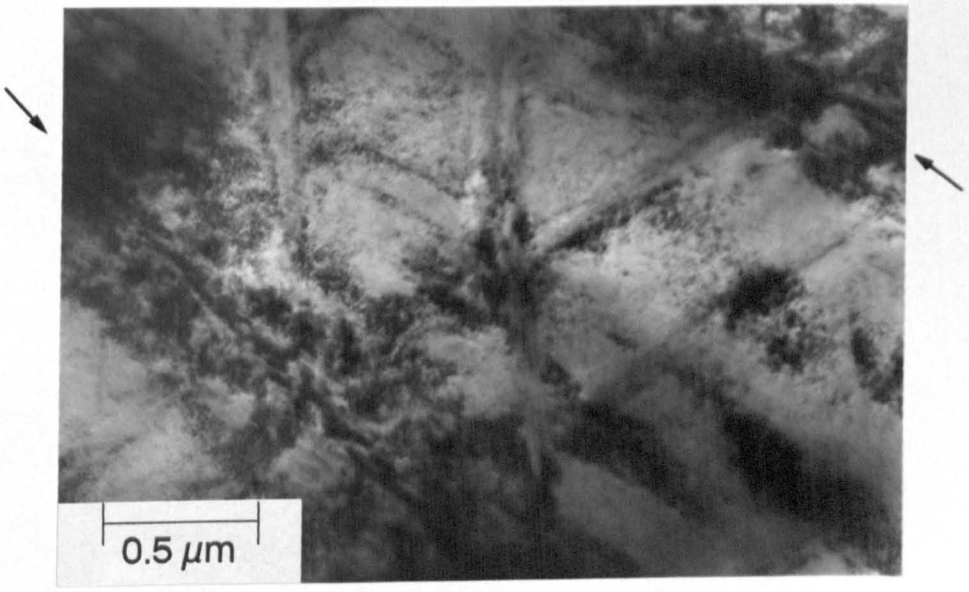

Figure 5.2 T.E.M. micrograph of the cross-sectional thin foil in Figure 5.1, showing the microstructure near to the fatigue surface. Two α-platelet boundaries which appear to have been transformed are arrowed. Note also the streaking between the α-platelet boundaries.

A

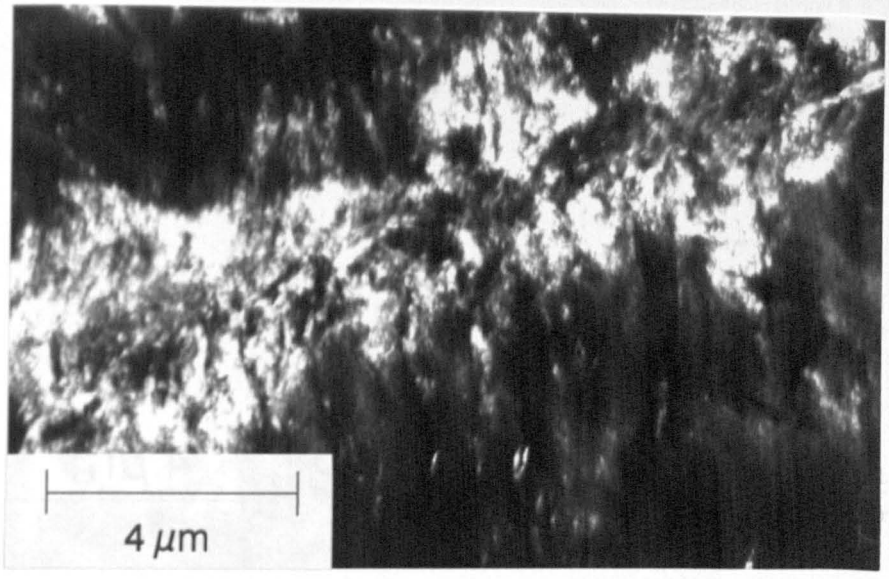

B

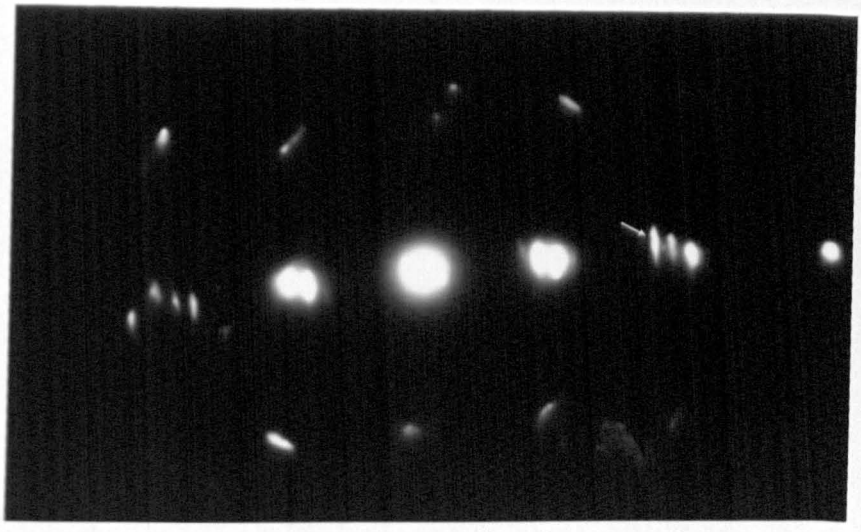

Figure 5.3 (A) Dark Field T.E.M. micrograph of an α-platelet boundary taken from approximately 100 μm from the fatigue surface of a nickel-plated cross-sectional thin foil using the reflection indicated in the corresponding diffraction pattern (B). A phase (bright) has formed along the α-platelet boundary and into the adjacent α-platelet.

A

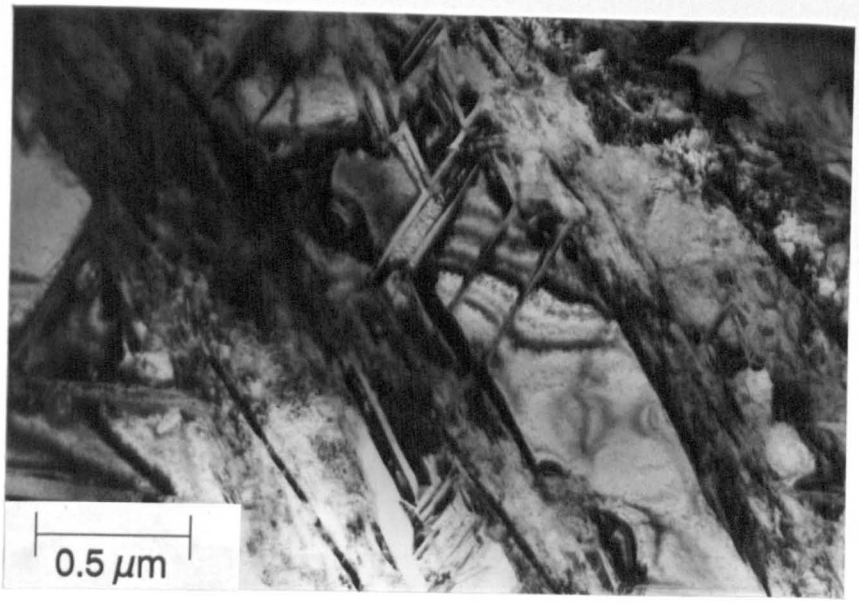

B

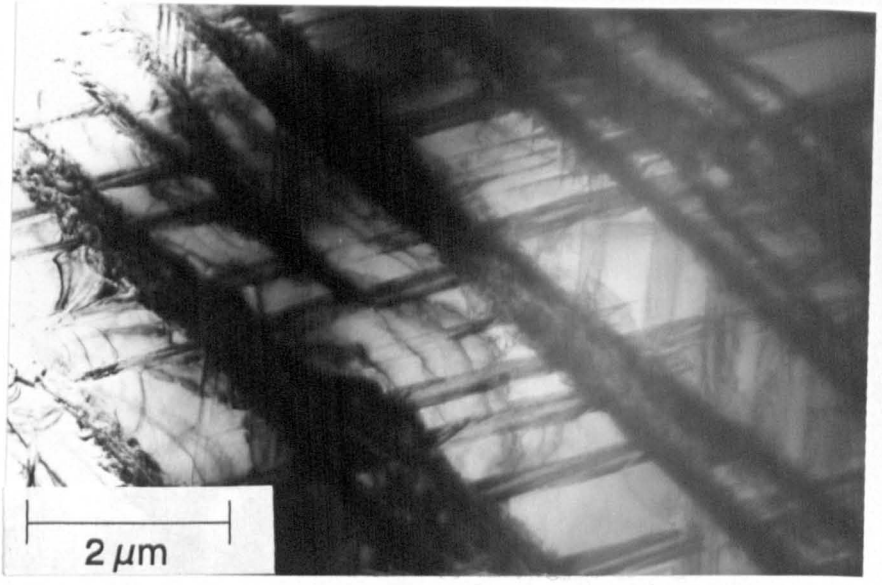

Figure 5.4 (A) and (B) Bright field T.E.M. micrographs showing examples of the thin foil microstructure at about 150 - 200 μm from the fatigue (nickel-plated) surface. Two phases have formed: One along the α-platelet boundaries and the second as acicular bands across the α-platelet widths.

C

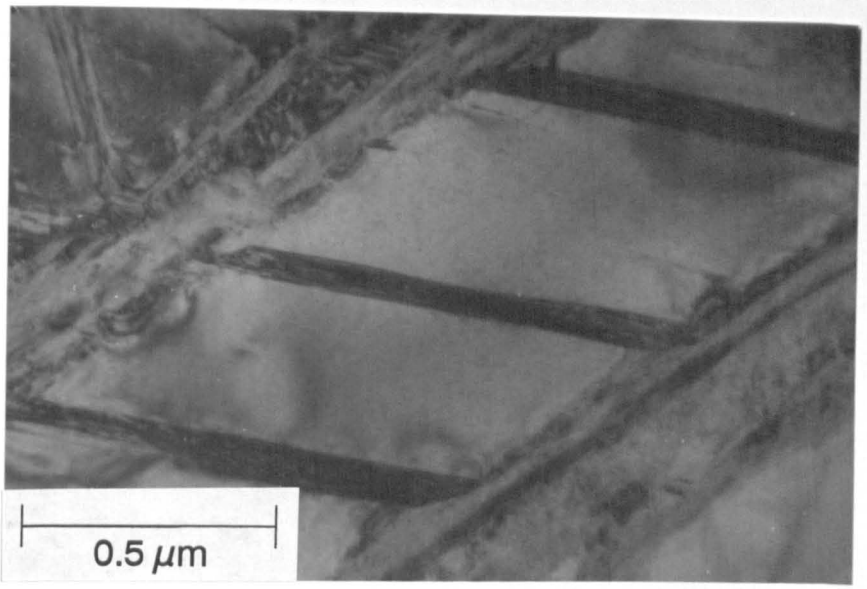

D

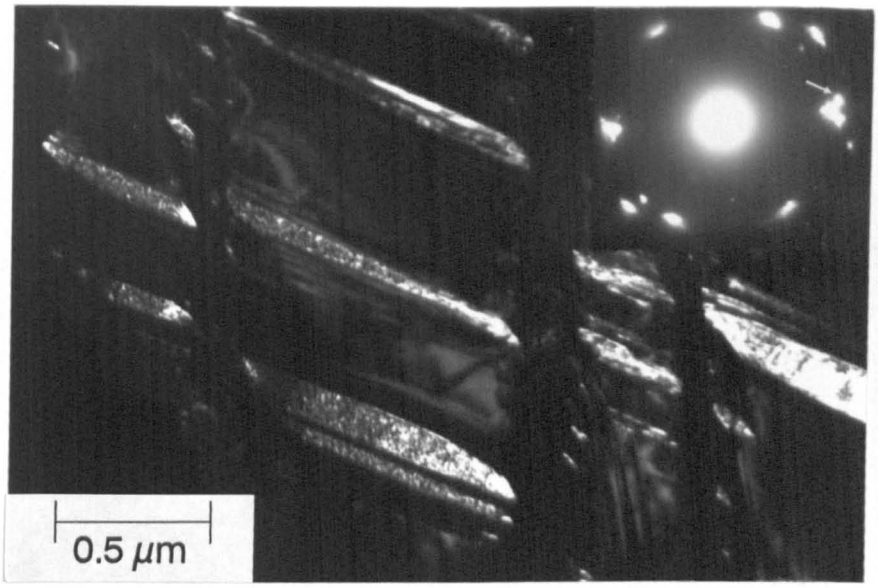

Figure 5.4 (C) Bright field and (D) dark field T.E.M. micrographs of the thin foil microstructure at about 150 - 200 μm from the fatigue (nickel-plated) surface of a cross-sectional foil. The acicular features in Figure 5.4D were imaged using the reflection indicated in the accompanying diffraction pattern.

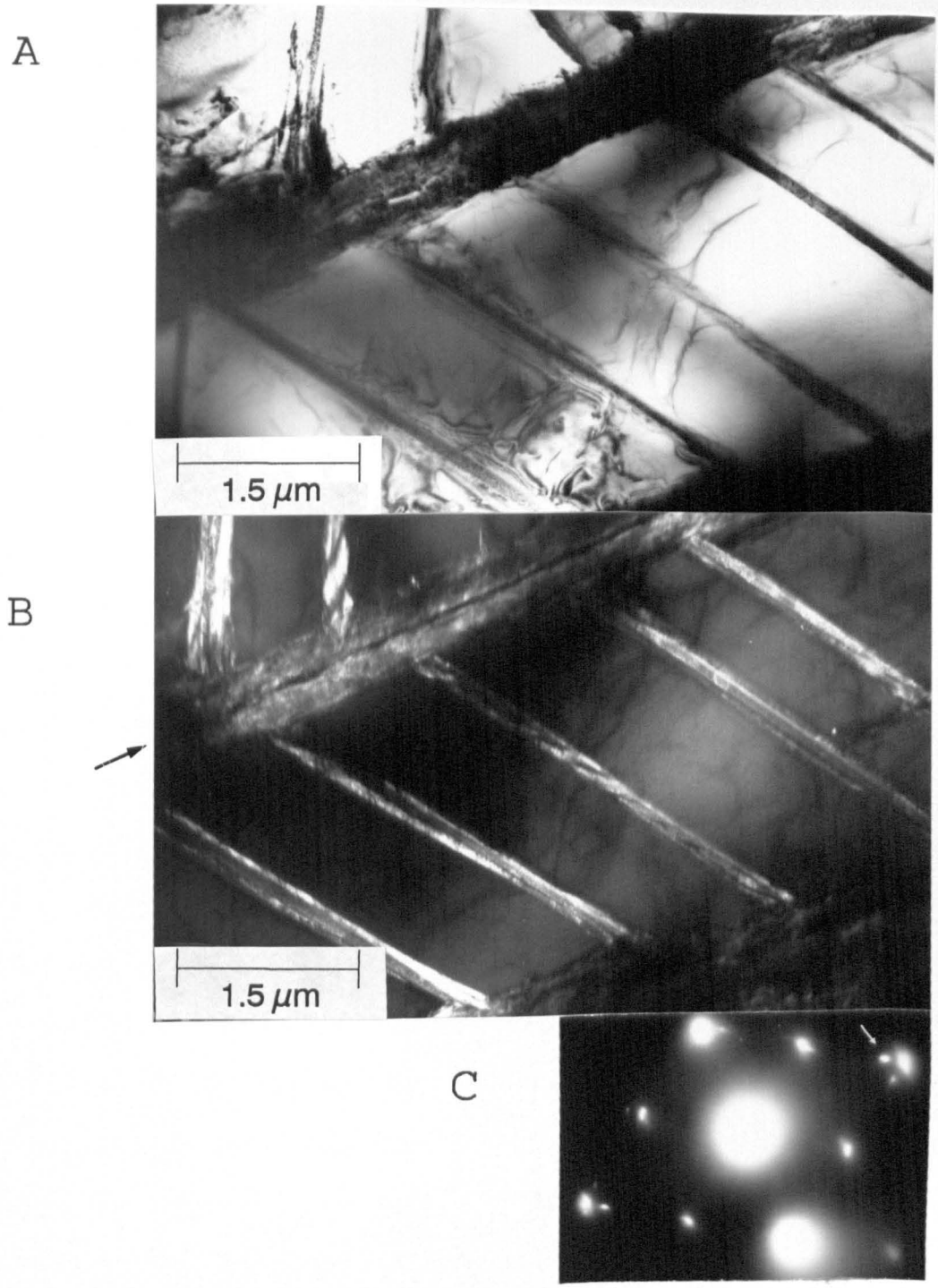

Figure 5.5 (A) Bright field and (B) dark field T.E.M. micrographs illustrating the phase along the α-platelet boundaries and the phase across the width of the α-platelets. Note the thin layer of retained-β phase along the centre of an α-platetet boundary in Figure 5.5B (arrowed). (C) Corresponding diffraction pattern indicating the reflection used to image the dark field micrograph.

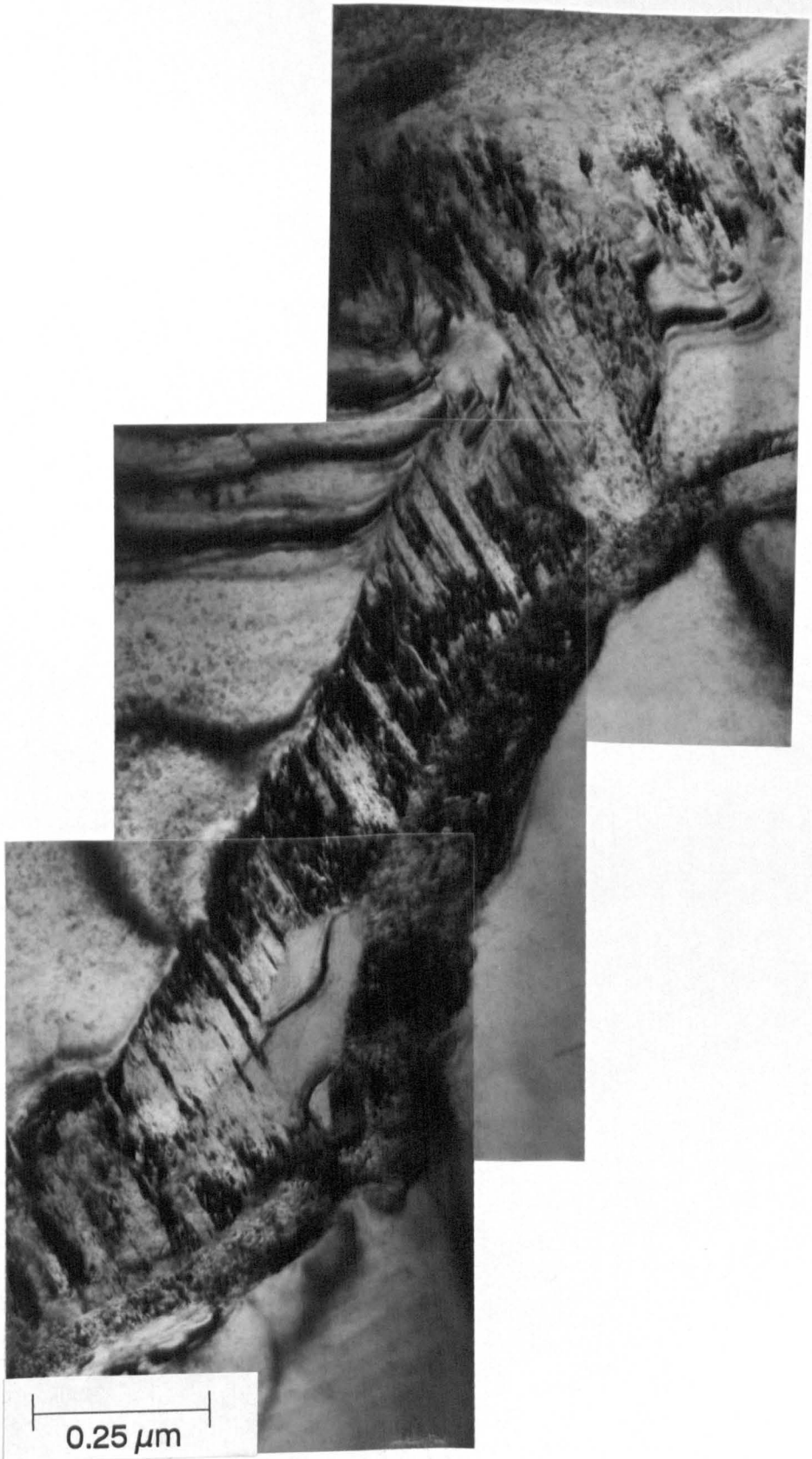

Figure 5.6 T.E.M. montage of an interface phase formed along an α-platelet boundary in a foil prepared by dimpling followed by ion-beam milling.

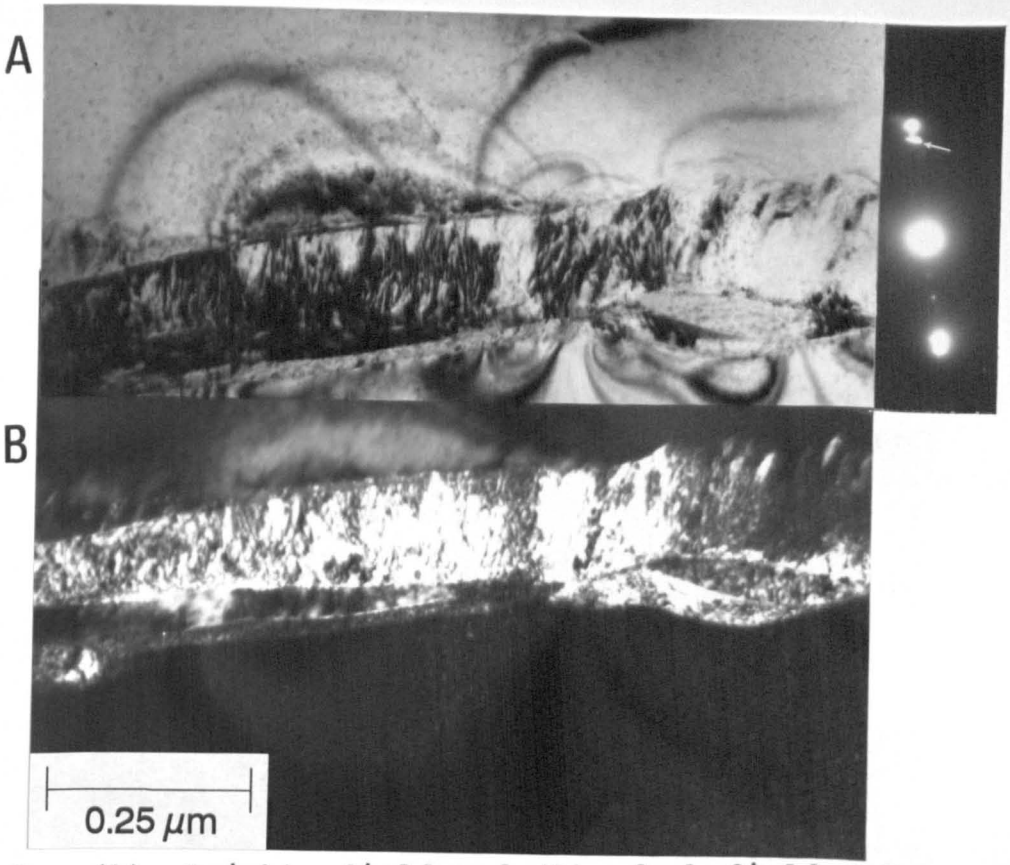

Figure 5.7 (A) Bright field and (B) dark field T.E.M. micrographs of a phase occurring along some of the α-platelet boundaries in a foil prepared by electropolishing and ion-beam milling. The reflection used to image (B) is indicated.

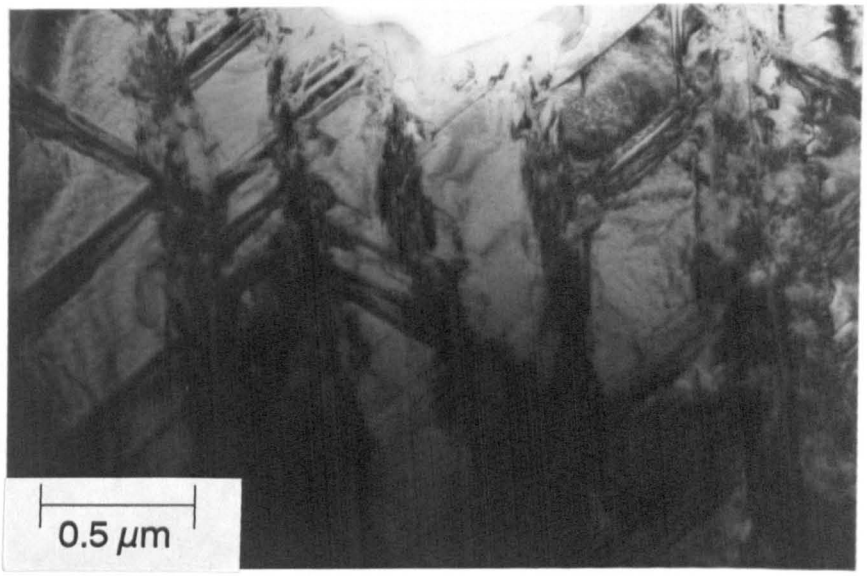

Figure 5.8 (A) Bright field T.E.M. micrograph of an area in a nickel-plated cross-sectional thin foil showing both the phases of interest.

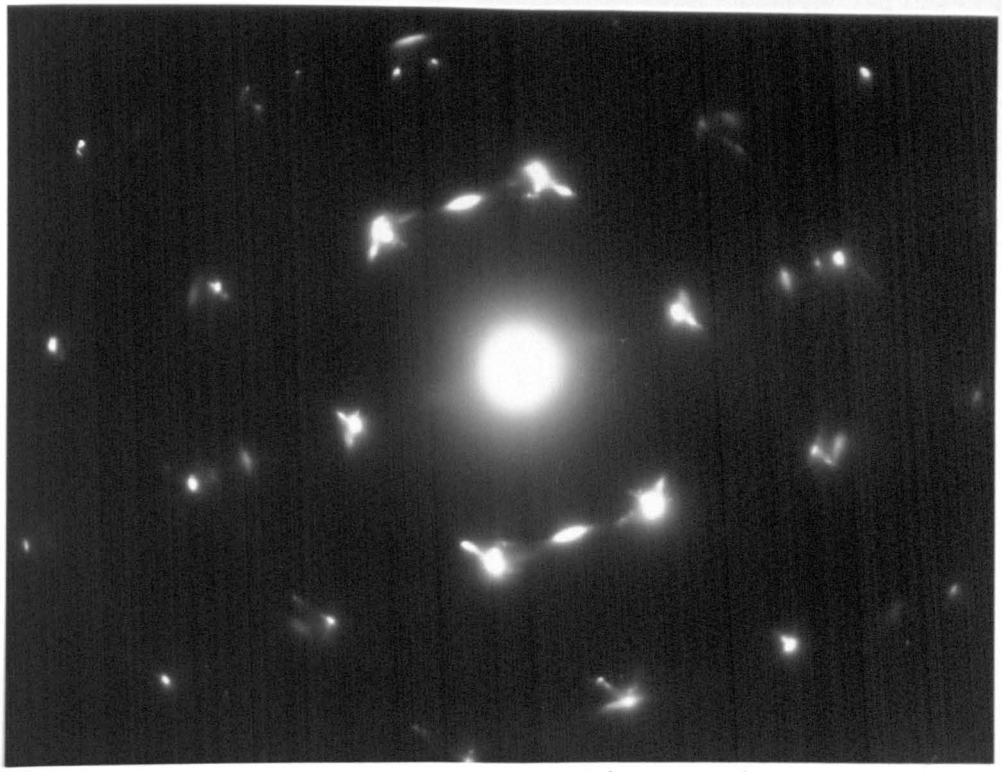

Figure 5.8 (B) Selected area diffraction pattern containing reflections from both phases of interest and reflections from a $[1\bar{2}13]_\alpha$ zone.

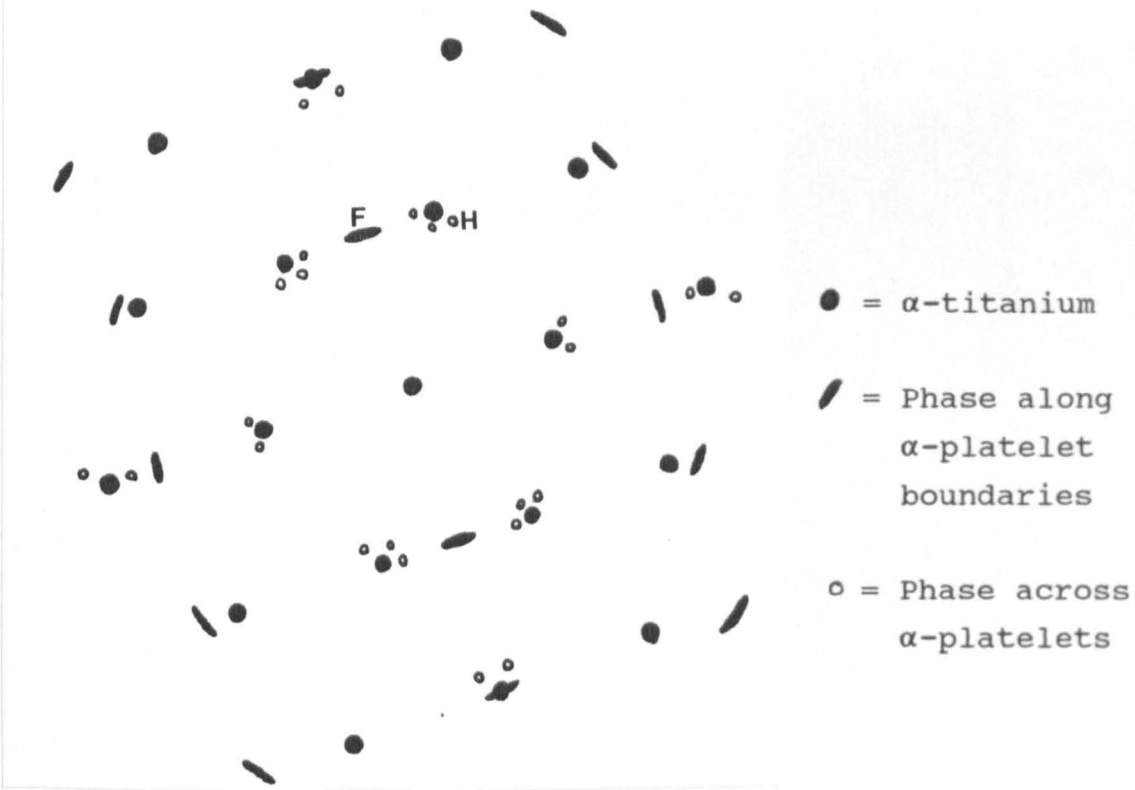

Figure 5.8 (C) Schematic representation of Figure 5.8B. Reflections marked F and H were used to image Figures 5.8D and 5.8E respectively.

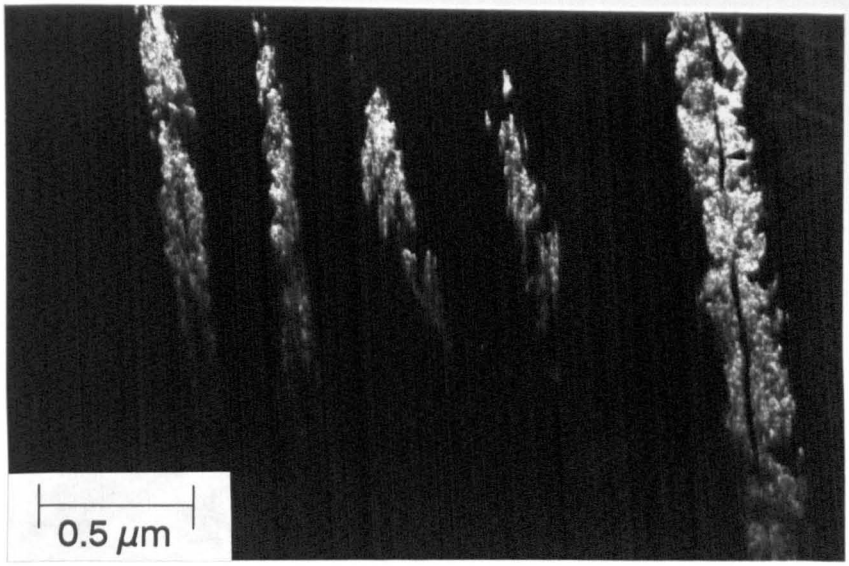

Figure 5.8 (D) Dark field T.E.M. micrograph of the phase present along the α-platelet boundaries imaged using the reflection marked F in Figure 5.8C. Note the thin films of retained-β present in some of the boundaries (indicated).

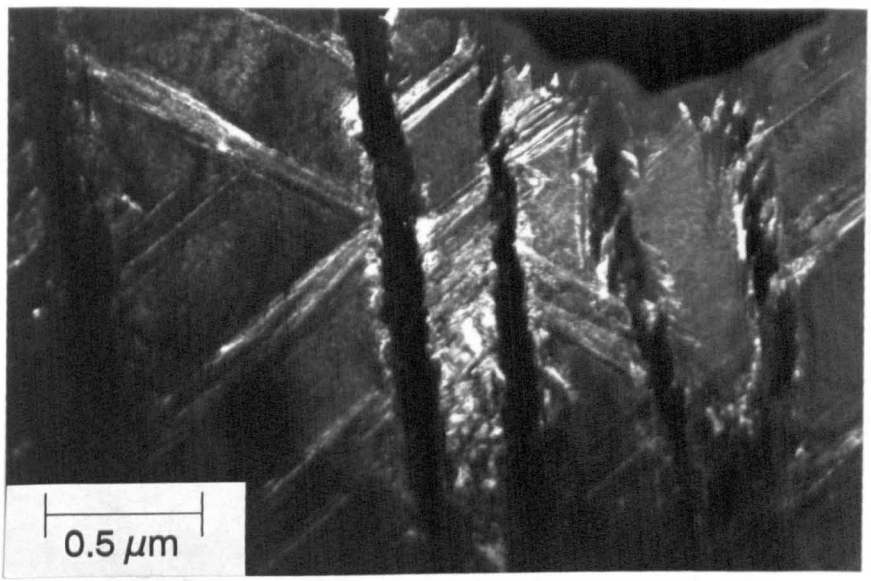

Figure 5.8 (E) Dark field T.E.M. micrograph of the acicular phase imaged using reflection H in Figure 5.8C. The phase occurs along the interface between the phase along the boundaries (Figure 5.8D) and the α-platelet phase, in addition to acicular bands which form across the α-platelets.

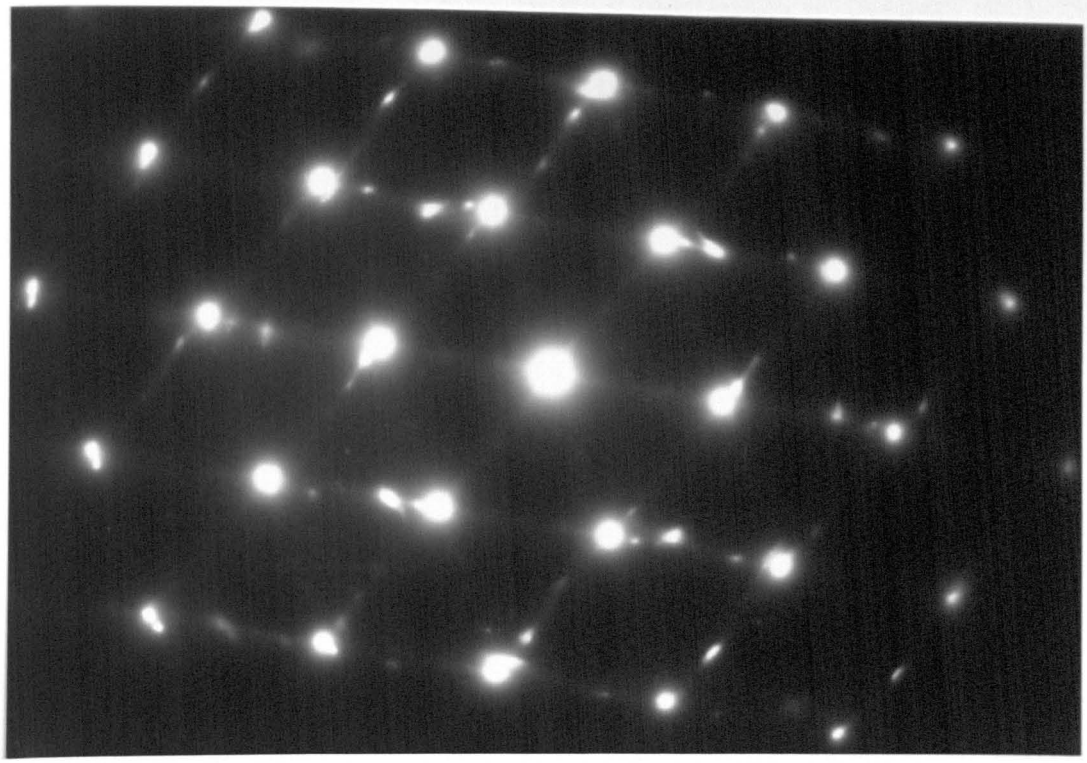

Figure 5.9 (A) Selected area diffraction pattern containing reflections from both phases of interest, an $[0001]_\alpha$ zone and an $[011]_\beta$ zone.

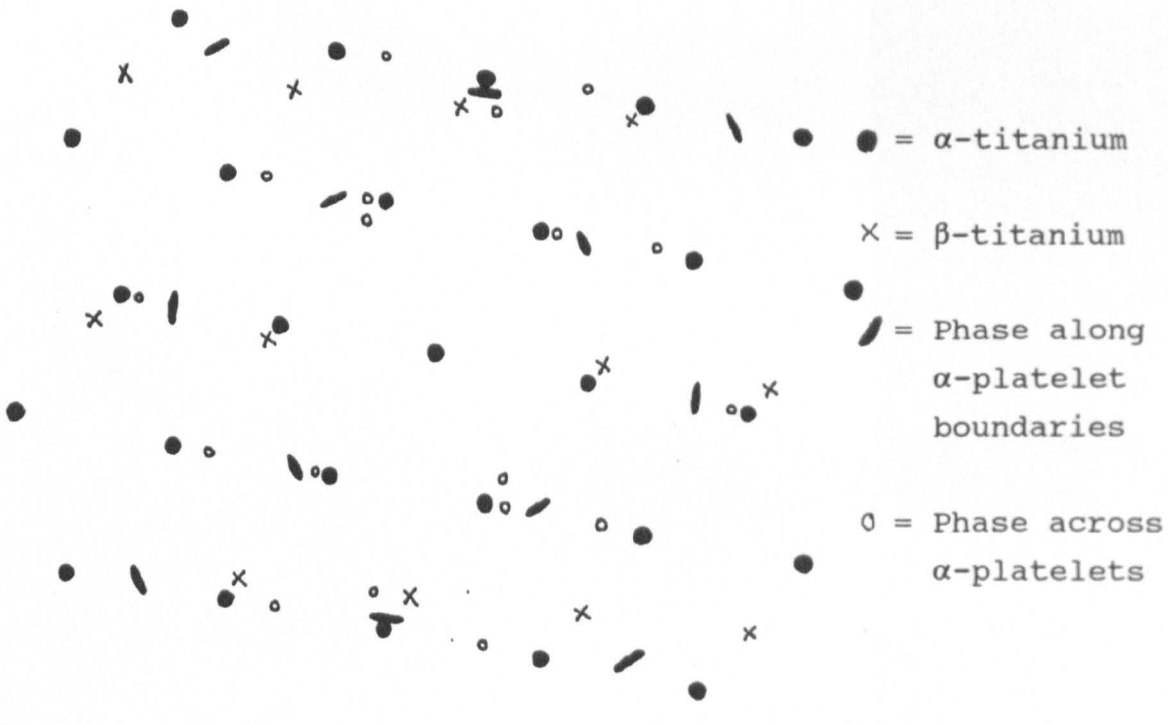

Figure 5.9 (B) Schematic representation of Figure 5.9A.

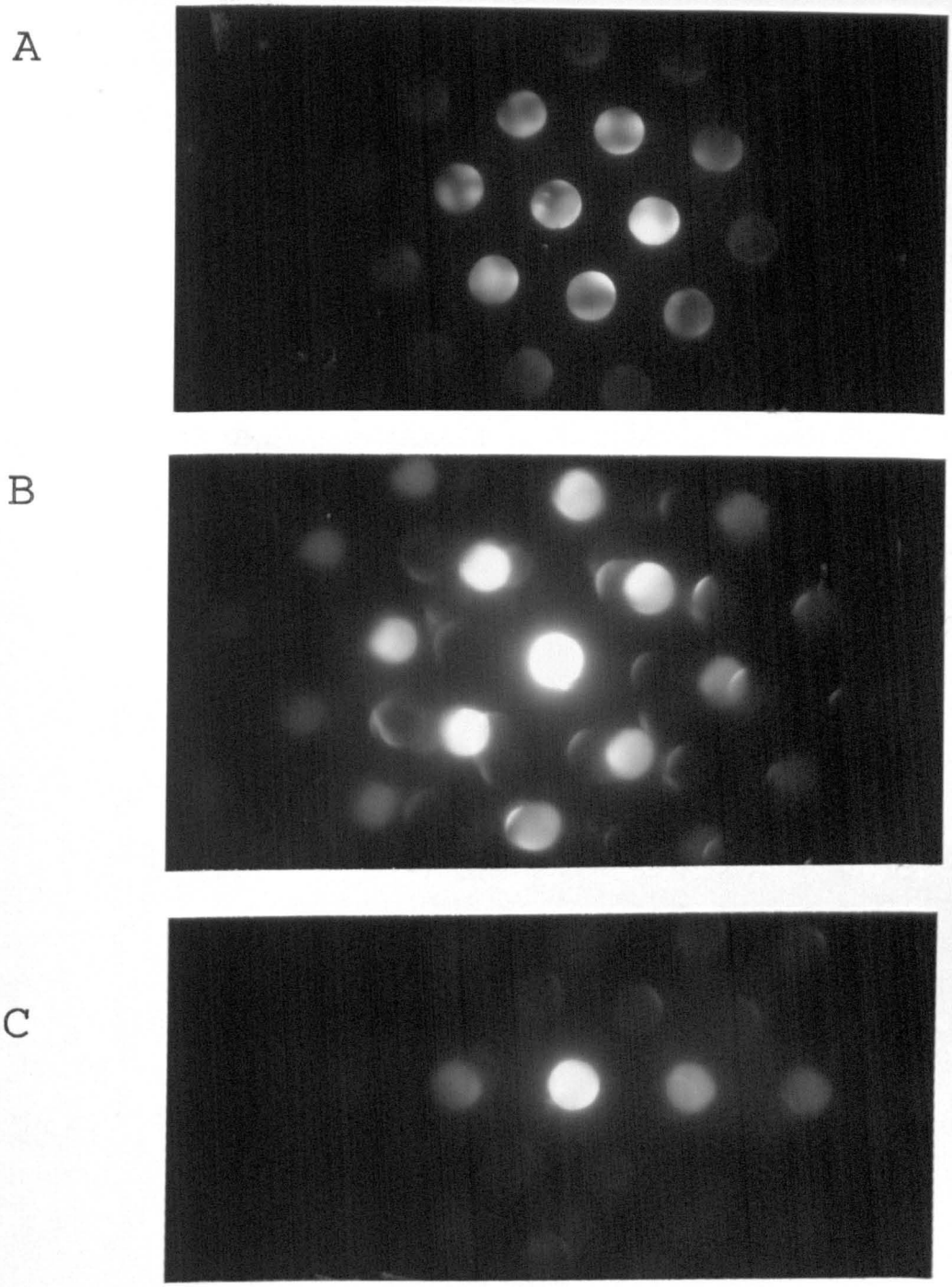

Figure 5.10 Convergent beam electron diffraction patterns from: (A) an [0001] zone of the α-phase. (B) A [112] zone of the phase along the boundaries. (C) The acicular phase across the α-platelets.

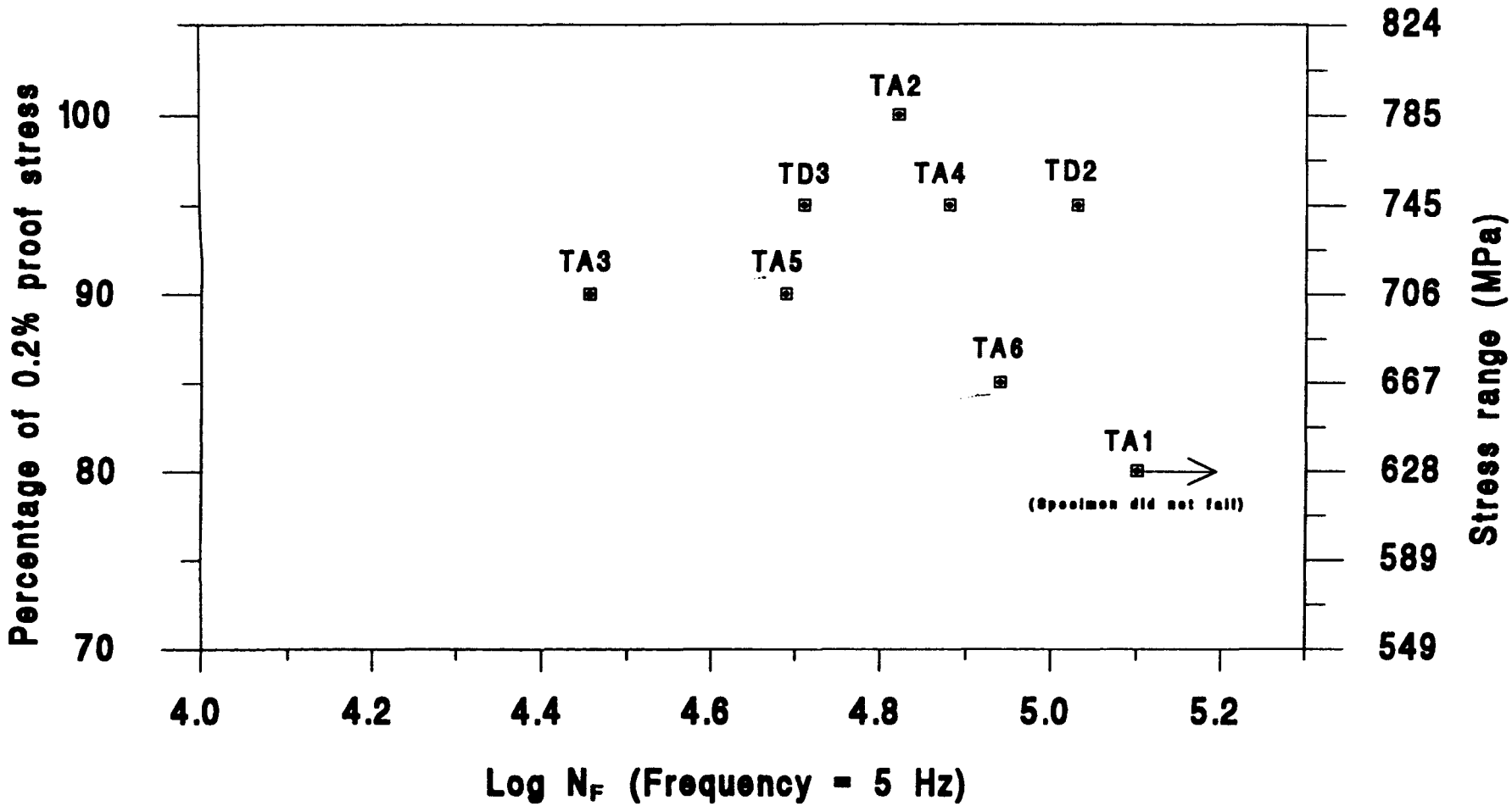

Figure 6.1 S-N data from tangential fatigue specimens. N = number of cycles, S = applied stress.

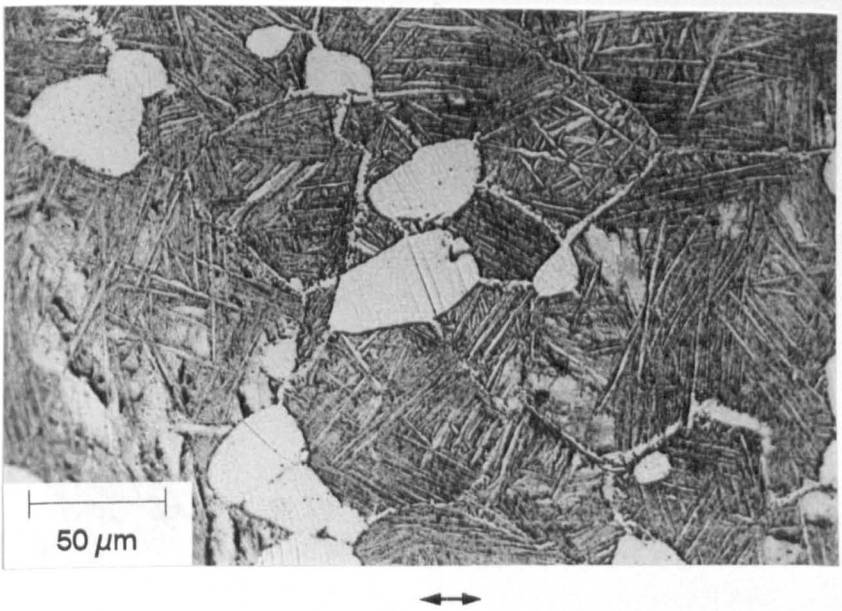

Figure 6.2 Optical micrograph showing slip bands in primary-α grains between 60° and 90° to the applied stress direction (arrowed). The specimen was fatigue tested to failure at 100% P.S. and etched to reveal the microstructure.

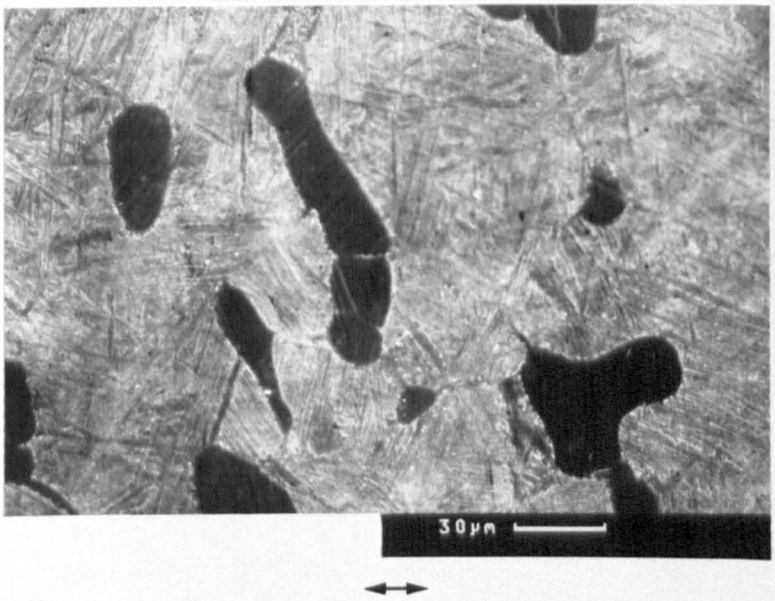

Figure 6.3 S.E.M. micrograph showing evidence of slip in primary-α grains between 45° and 70° to the applied stress direction (arrowed). The specimen was fatigue tested to failure at 100% P.S.

A

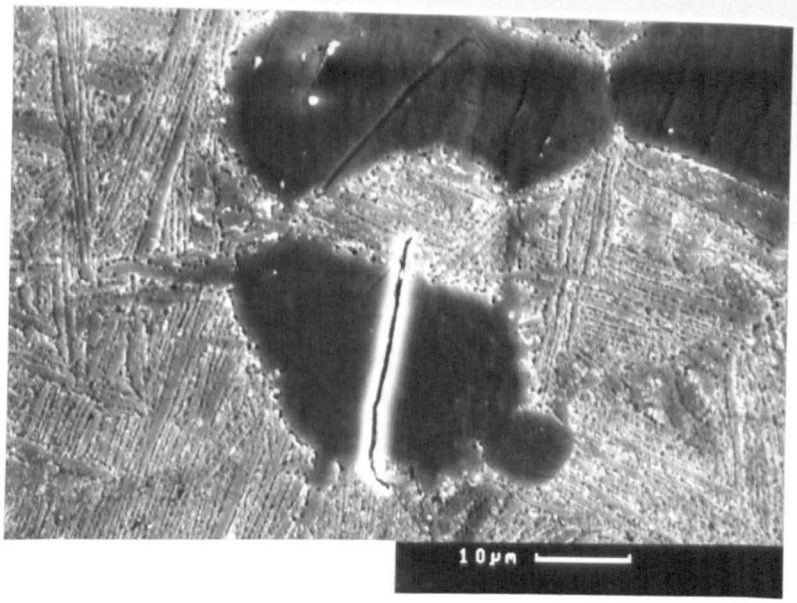

B

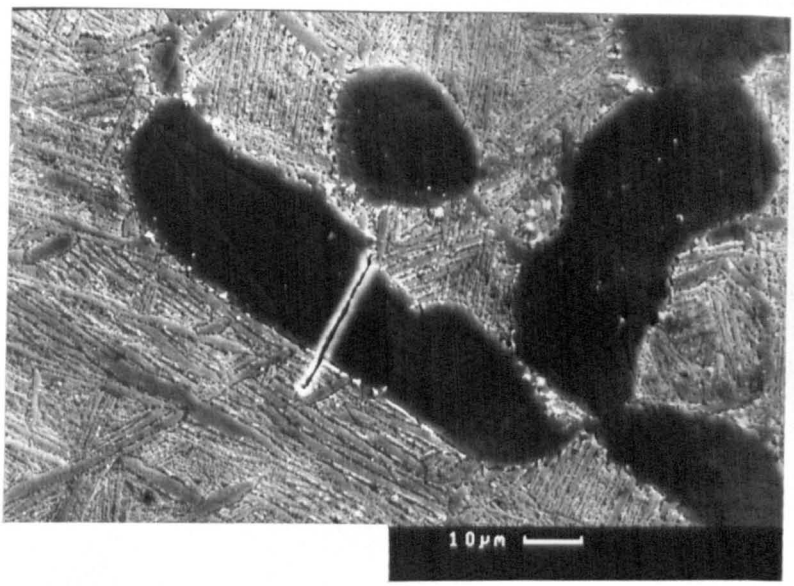

Figure 6.4 (A) and (B) S.E.M. micrographs showing examples of secondary cracks which have initiated parallel to slip bands in primary-α grains at (A) 81° and (B) 64° to the applied stress direction (arrowed). The examples were taken from a specimen which was fatigue tested to failure at 100% P.S.

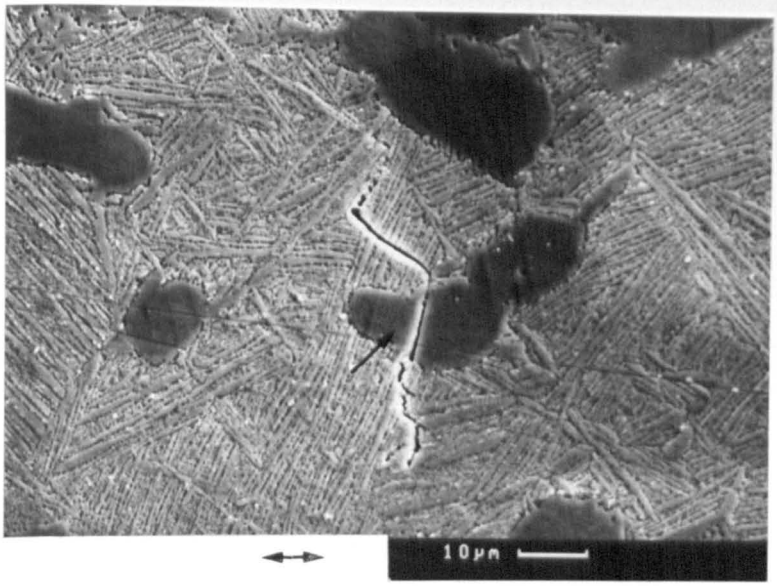

Figure 6.5 S.E.M. micrograph of a secondary crack, the origin of which occurred parallel to slip bands in the primary-α grain indicated. The specimen was fatigue tested to failure at 100% P.S. The initial crack occurred at 78° to the applied stress direction which is arrowed. The crack followed a path at 90° to the α-platelets in an adjacent transformed-β colony.

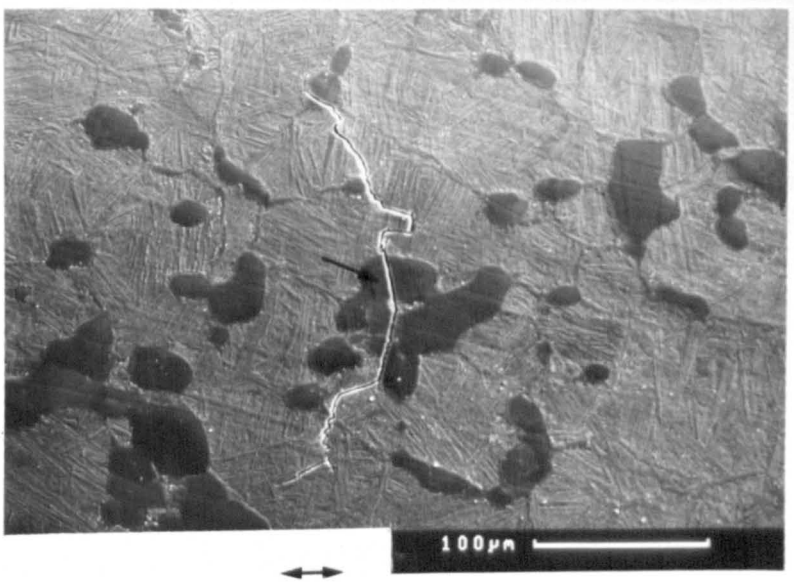

Figure 6.6 S.E.M. micrograph of a secondary crack, the origin of which was determined to be the primary-α grain indicated. The specimen was fatigue tested to failure at 100% P.S. The initial crack occurred at 78° to the applied stress direction which is arrowed.

Figure 6.7 (A) Optical montage of long secondary cracking (over 200 μm) in a specimen tested to failure at 100% P.S. The specimen was etched after fatigue testing to reveal the microstructure. The applied stress direction is arrowed. Some crack origins can be determined as primary-α grains, however, not all the crack origins are clearly identifiable. The propagating crack paths clearly show the tortuous and bifurcating nature of cracking in IMI 834. The arrows indicate short secondary crack paths at 90° to the direction of α-platelets.

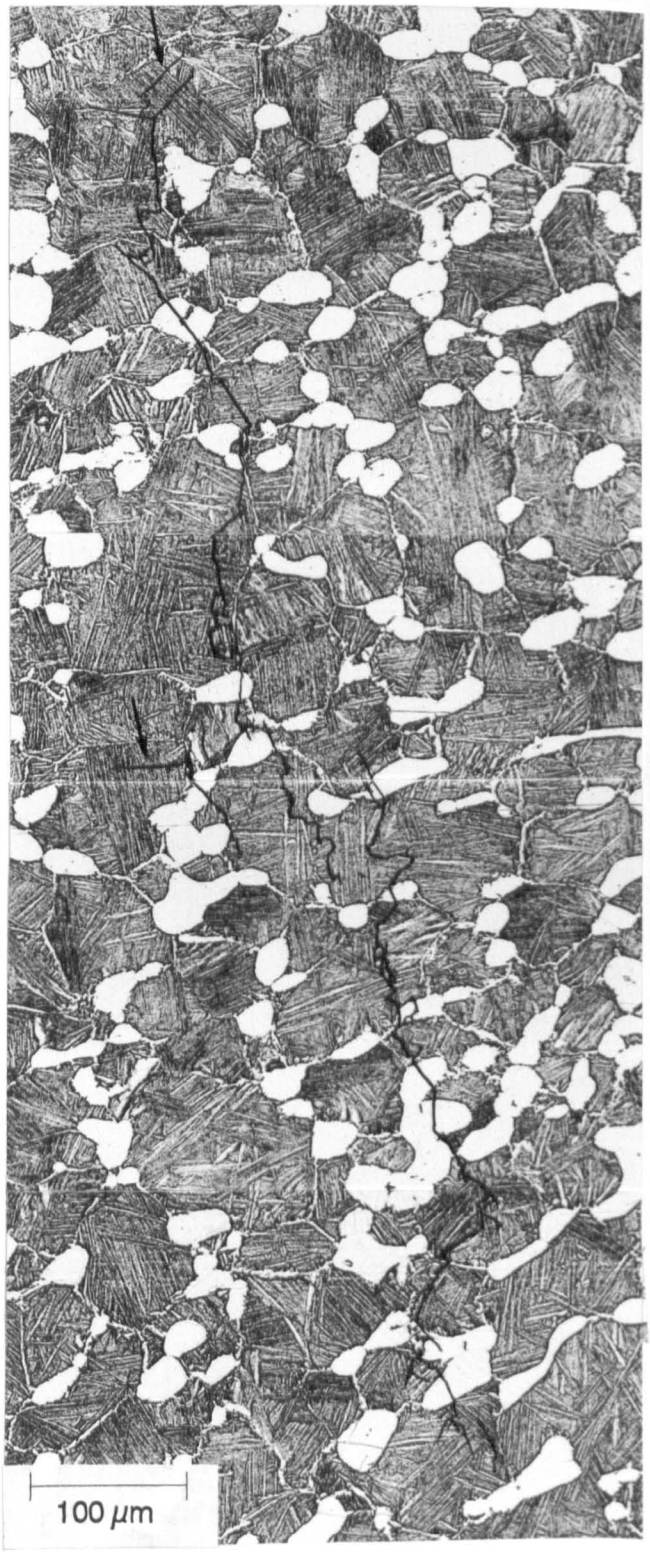
100 μm

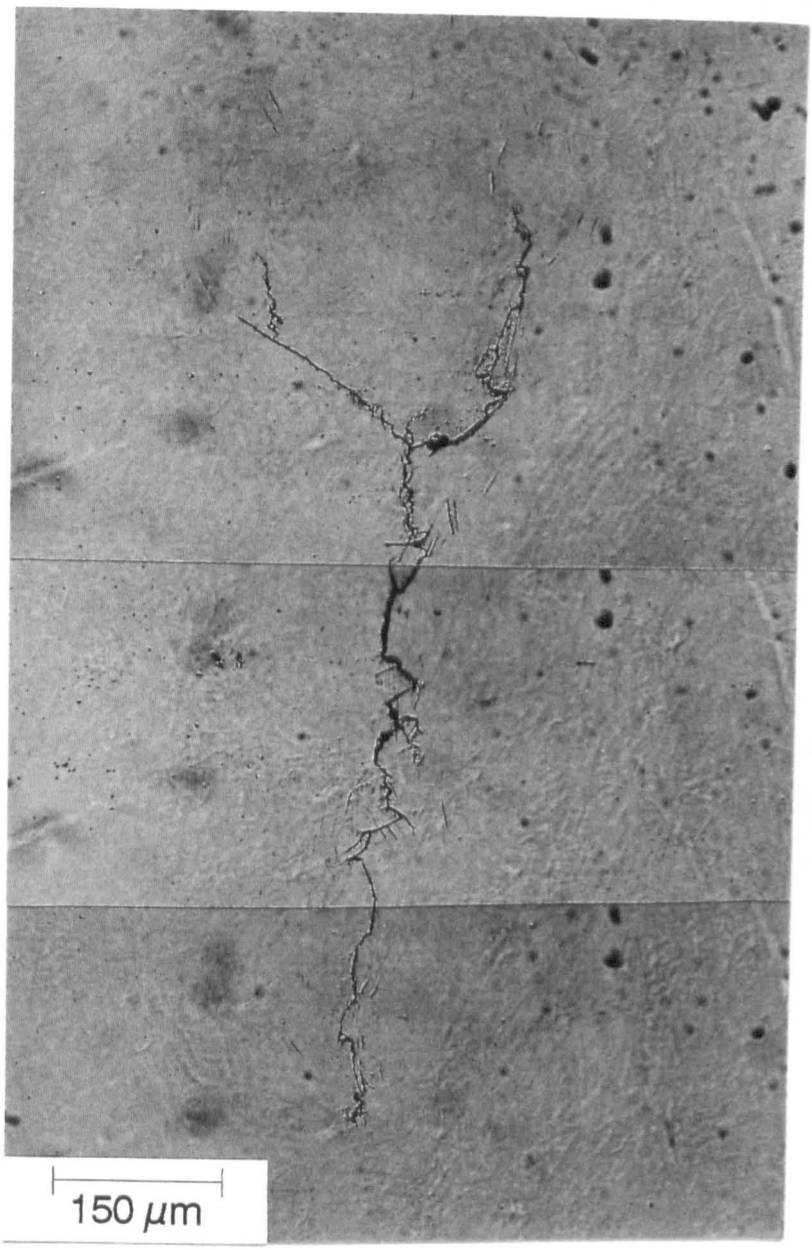

Figure 6.7 (B) Optical montage showing the tortuous and bifurcating nature of secondary cracks in a specimen fatigue tested to failure at 95% P.S. The applied stress direction is arrowed.

Figure 6.8 S.E.M. micrograph showing the detail of short crack propagation of the same secondary crack as in Figure 6.6. The initial crack occurred parallel to slip bands and at 78° to the fatigue surface in the primary-α grain, labelled A. Crack propagation in the adjacent transformed-β colony, B1, was initially restricted, as is evident from the crack bifurcation. When the boundary between colony B1 and colony B2 was reached, the path of the crack was interesting since it propagated at less than 10° to the applied stress direction but perpendicular to the α-platelet boundaries in B2. The path changed direction after approximately 10 μm to propagate along a colony boundary at a more expected angle close to 90° to the applied stress direction. The propagating crack turned again to follow a path at 90° to the α-platelet direction in B2 despite this being unfavourable with respect to the applied stress direction. A more expected crack path is followed at greater distances from the initiating primary-α grain (A).


B2
B1
A
10μm

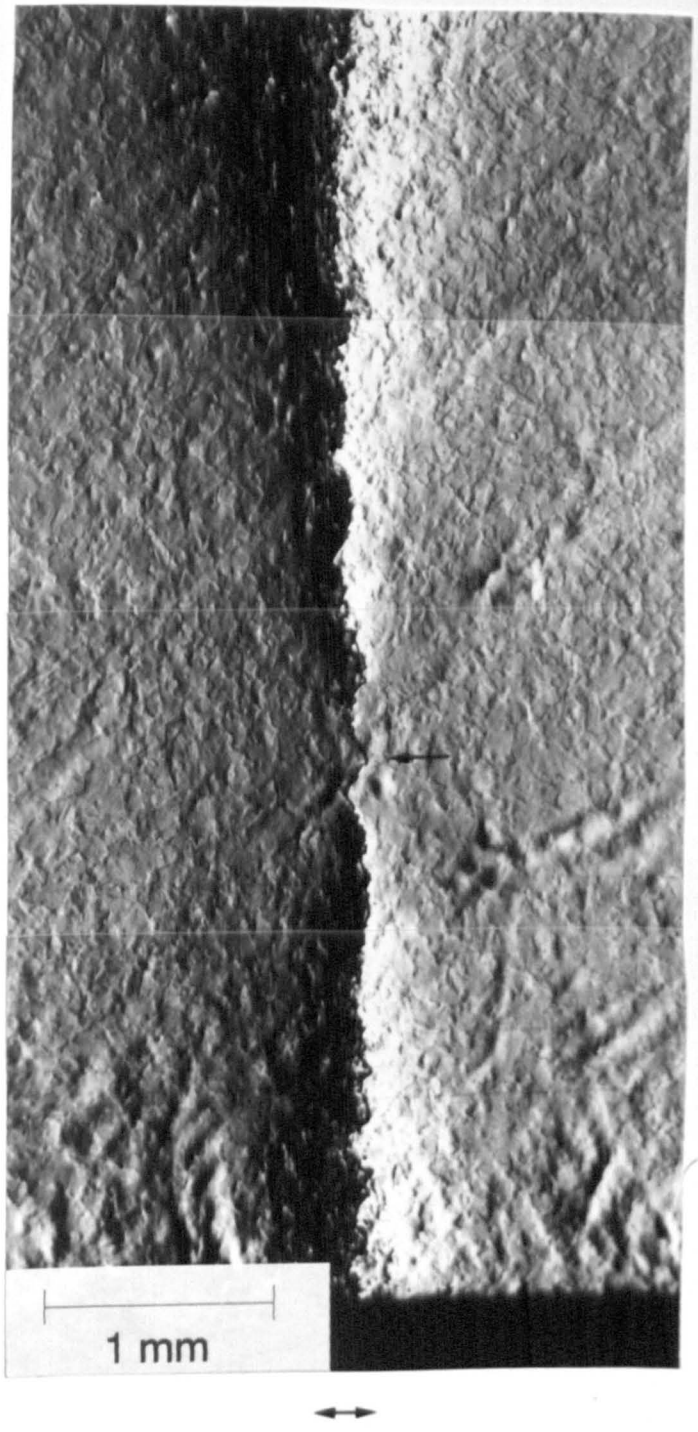

Figure 6.9 Low magnification optical montage taken using Nomarski interference, showing the path of the fatal crack in a specimen tested to just prior to failure at 100% P.S. Note the surface relief caused by the strain associated with the propagating crack. The applied stress direction and the region of crack origin are indicated by arrows.

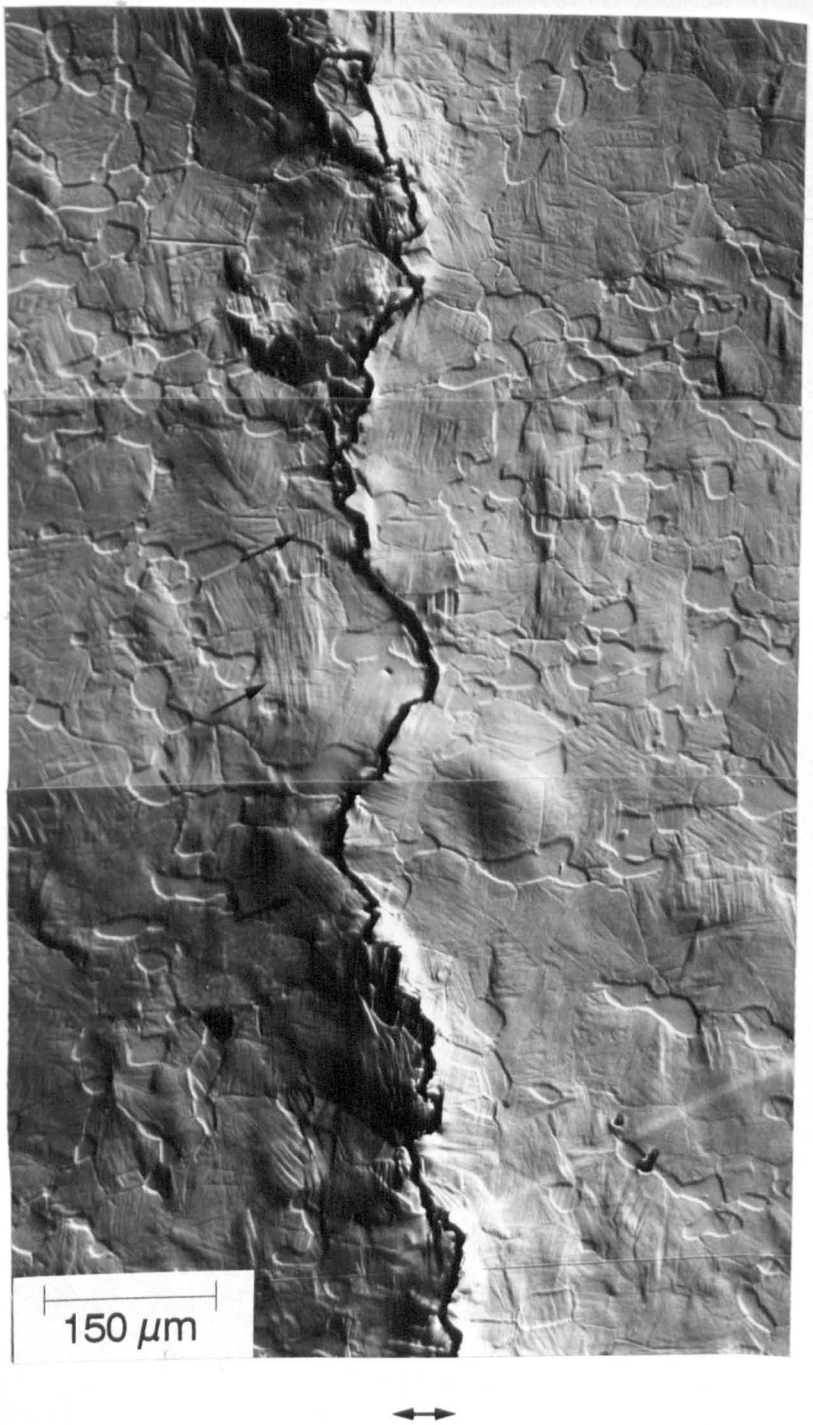

Figure 6.10 (A) Optical montage of the area containing the fatal crack origin in a specimen tested at 100% P.S., see also Figures 6.9 and 6.10B. The micrograph was taken using Nomarski interference. The applied stress direction and evidence of slip in transformed-β grains, are arrowed.

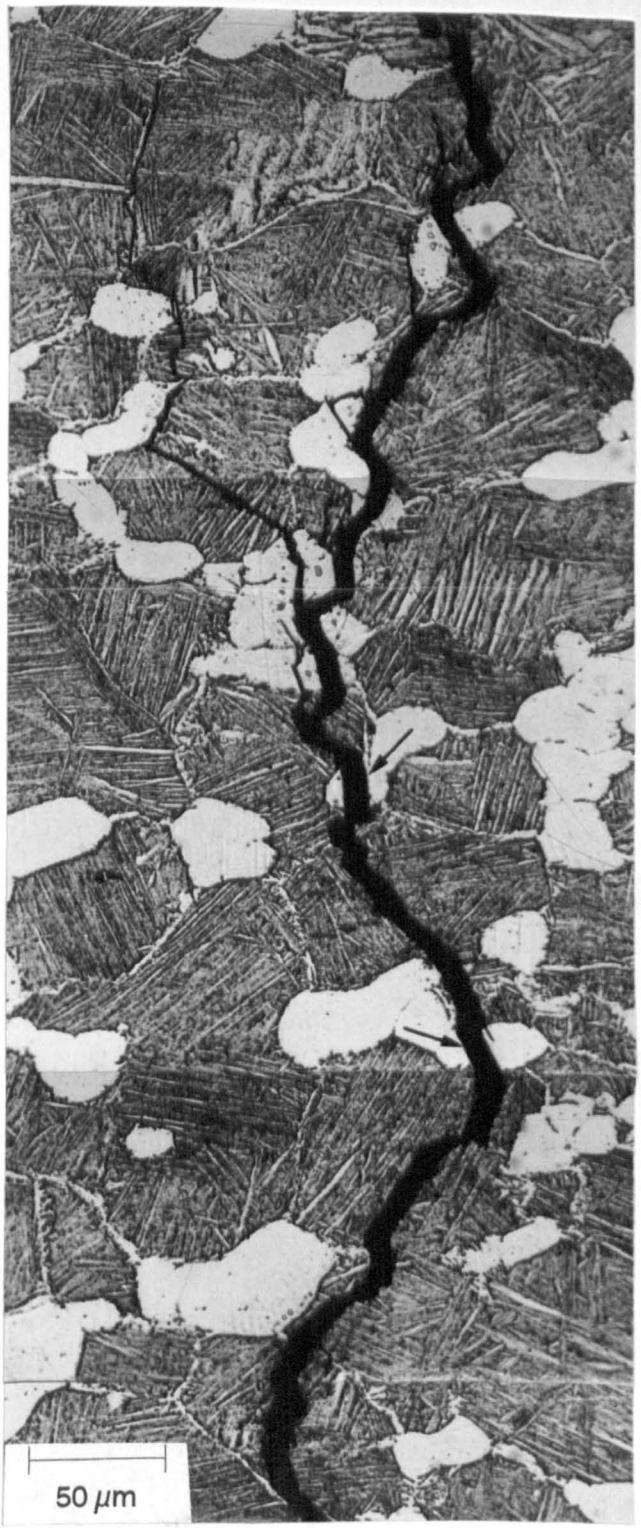

Figure 6.10 (B) Optical montage of the same fatal crack as shown in Figure 6.10A. The specimen was etched to reveal more detail in the microstructure. Two primary-α grains, where the crack occurs parallel to slip bands, are indicated as possible crack initiation sites. The applied stress direction is arrowed.

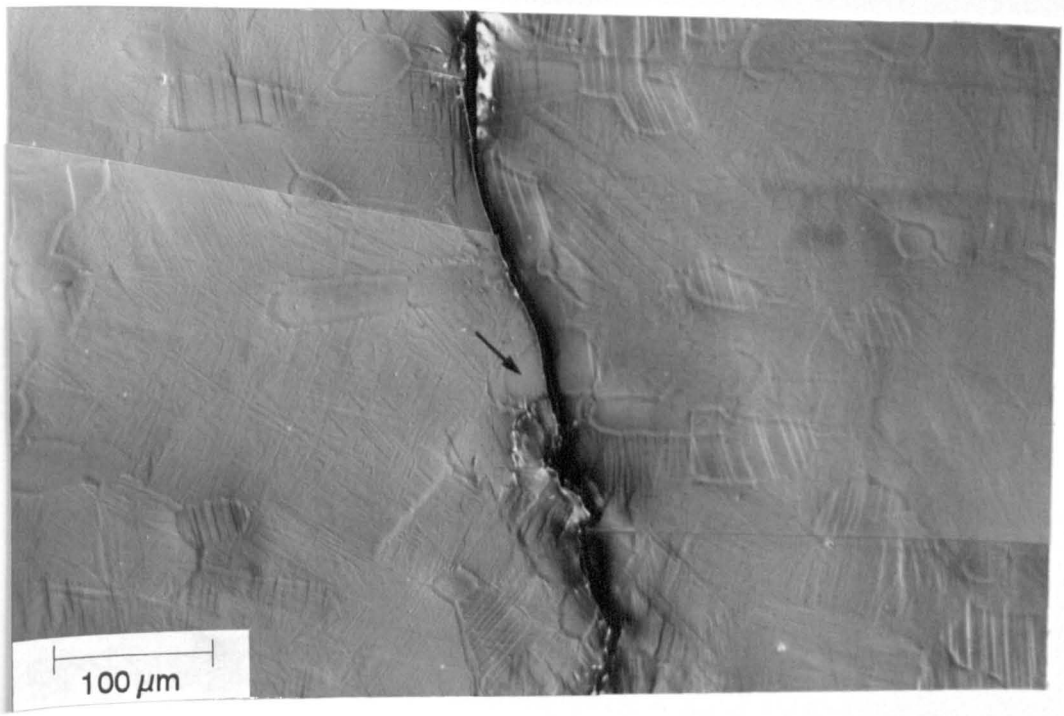

Figure 6.11 Optical montage of the two complementary fatigue surfaces of the fatal crack in a specimen tested to failure at 90% P.S. The applied stress direction and primary-α grain containing the crack origin (see also Figure 6.12) are arrowed. The initial crack occurred at 68° to the applied stress direction.

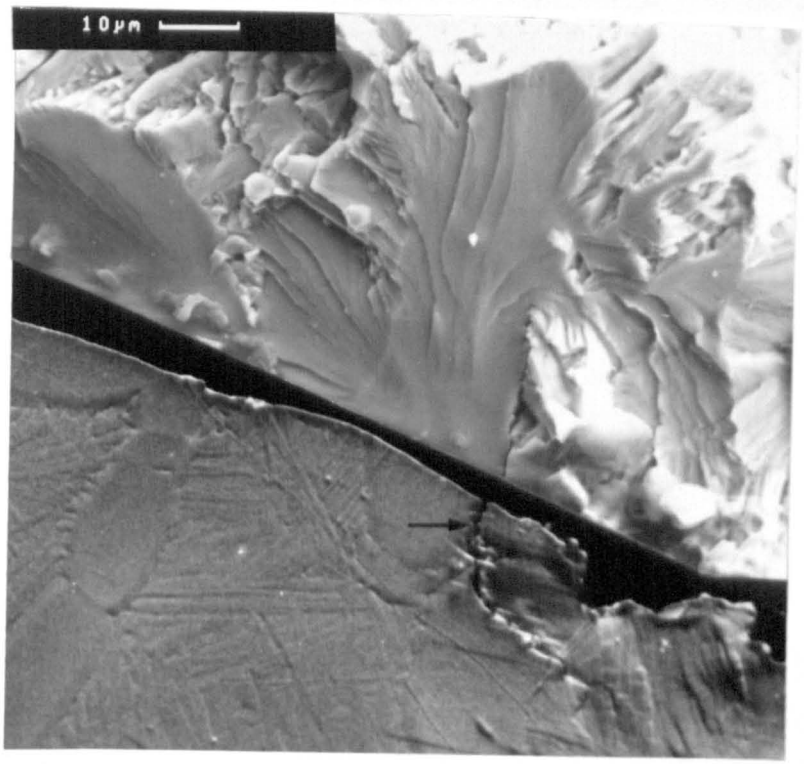

Figure 6.12 Comparison of the fatigue and fracture surfaces at the origin of the fatal crack in a specimen tested at 90% P.S. Note the grain boundary cracking (arrowed) and the elliptical feature at the centre of the smooth region in the initiating primary-α grain. The length of the initial slip band is effectively doubled since the adjacent primary-α grain has a similar orientation to the initial grain.

A

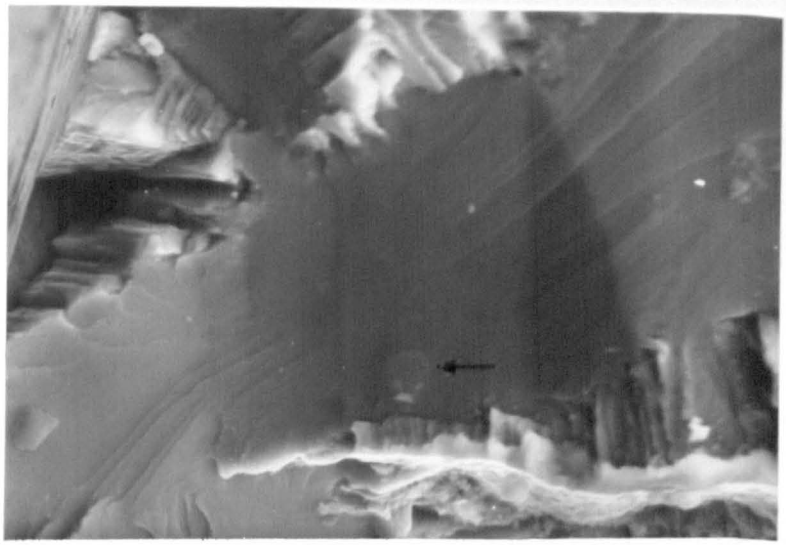

B

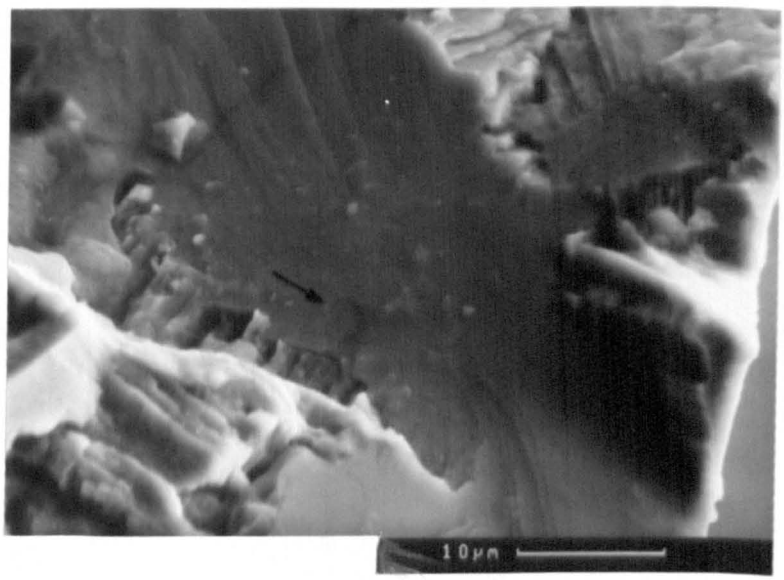

Figure 6.13 (A) and (B) S.E.M. micrographs of the complementary fracture surfaces taken from a sub-surface initiation site. The specimen was fatigue tested to failure at 95% P.S. The features associated with the primary-α grain containing the crack origin are similar to those in Figure 6.12. Note the small feature (arrowed) present on the complementary surfaces at the crack origin.

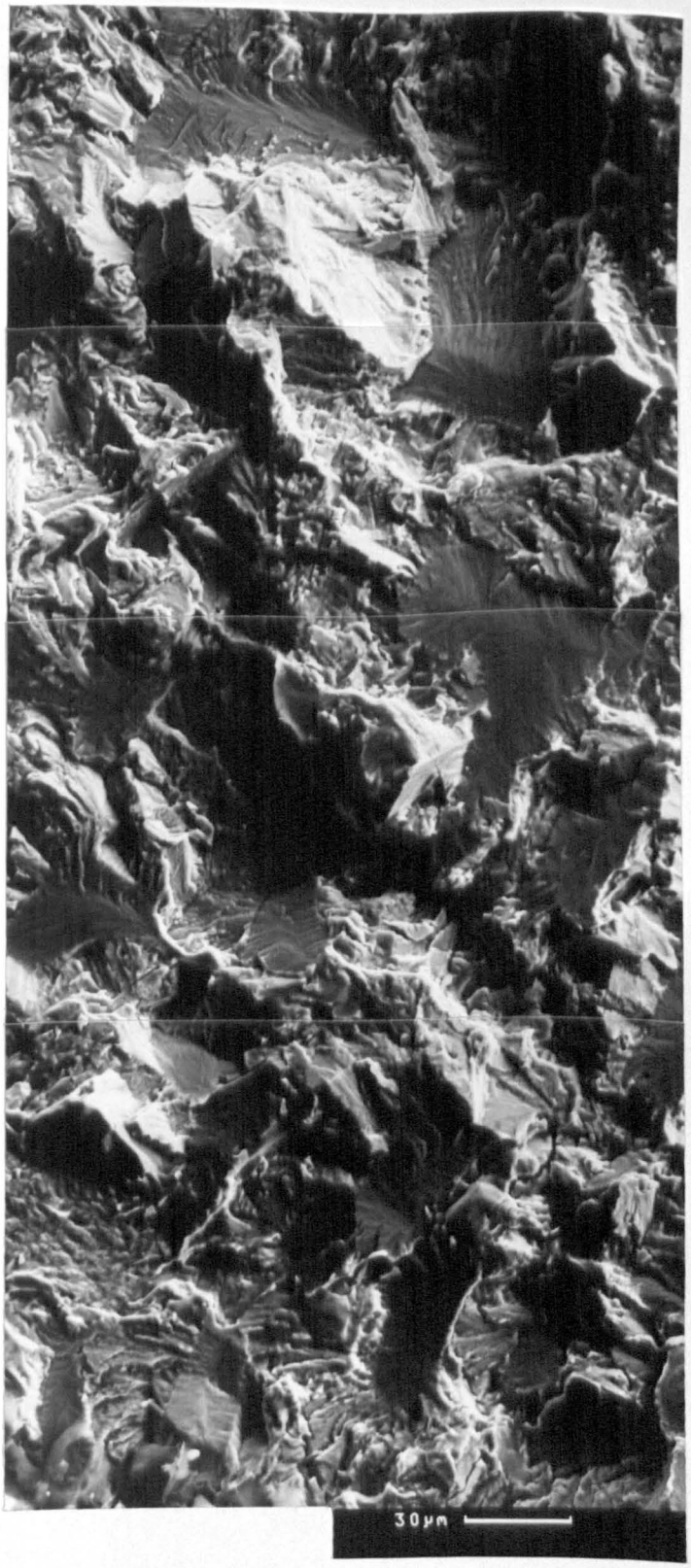

Figure 6.14 S.E.M. montage of an area of a fracture surface close to the crack origin. This clearly shows the facetting on the scale of the primary-α/transformed-β colonies associated with the area around the crack origin. The specimen was fatigue tested to failure at 95% P.S.

Figure 6.15 (A) to (C) Features associated with long crack propagation. (A) and (B) show fluting and (C) shows a transformed-β colony cut at 90° to the α-platelets.

A

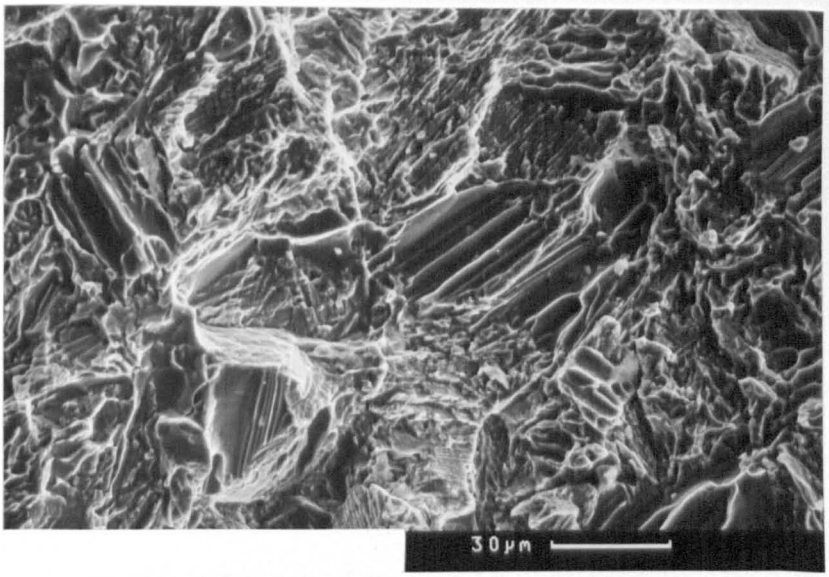

B

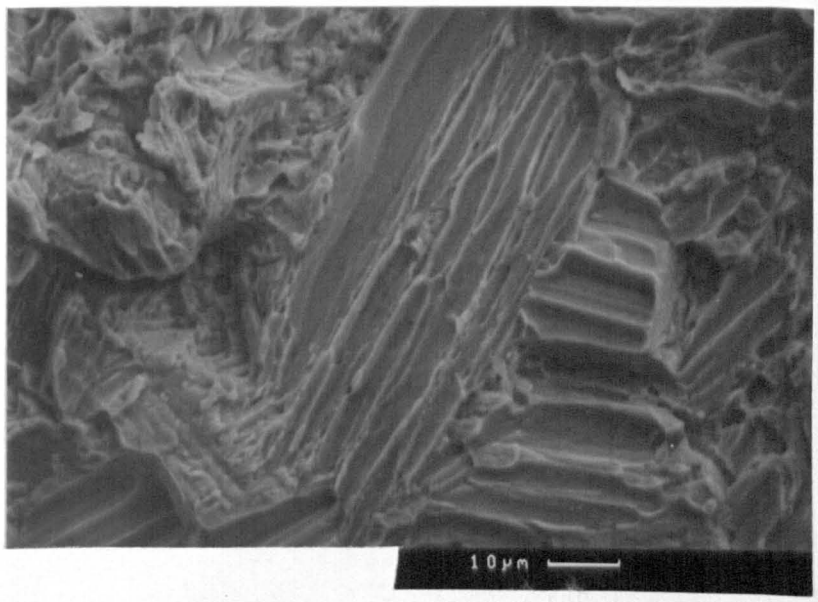

C

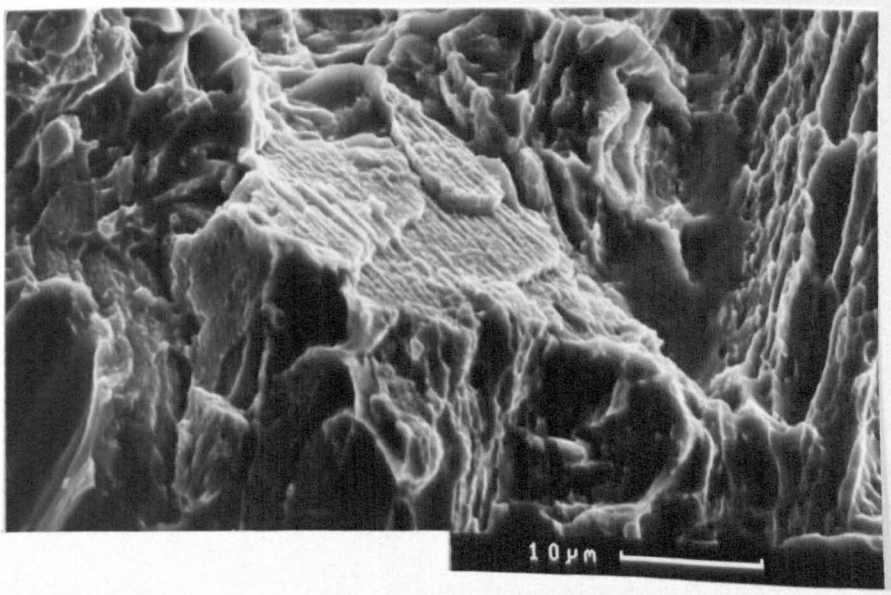

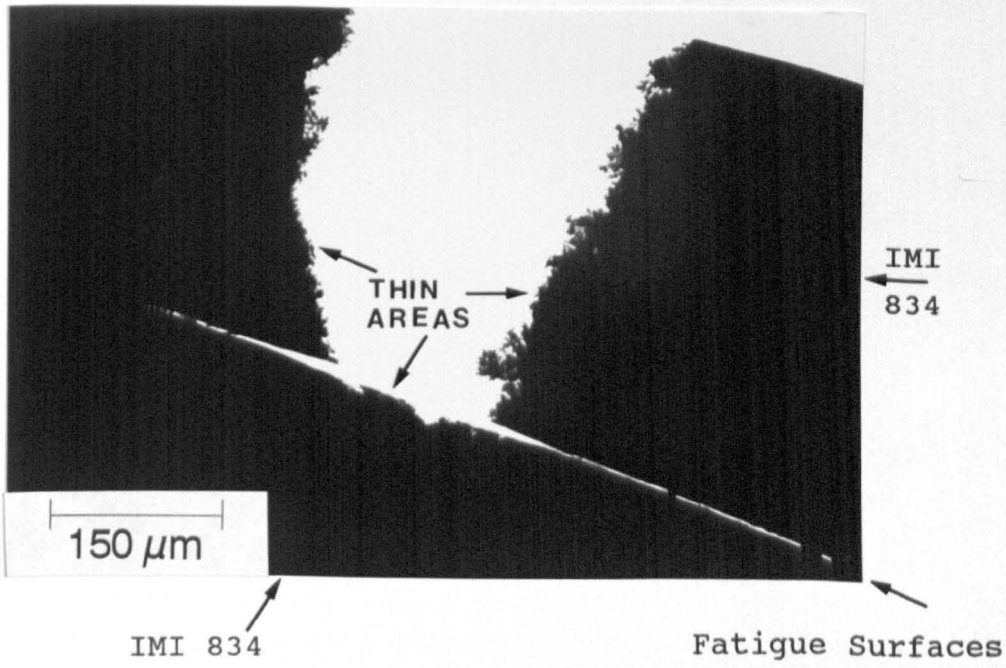

Figure 6.16 Low magnification T.E.M. micrograph showing an example of the thin areas obtained from a cross-sectional thin foil.

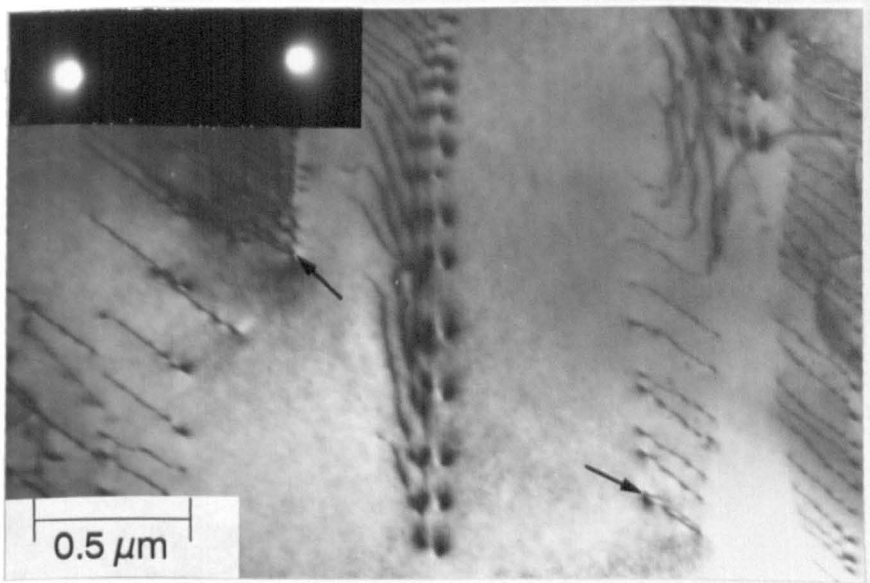

Figure 6.17 T.E.M. micrograph of intense planar slip bands in a primary-α grain. Note the pairing of dislocations in some bands (indicated). B = close to $[3\bar{3}02]$, $\underline{g} = [11\bar{2}0]$.

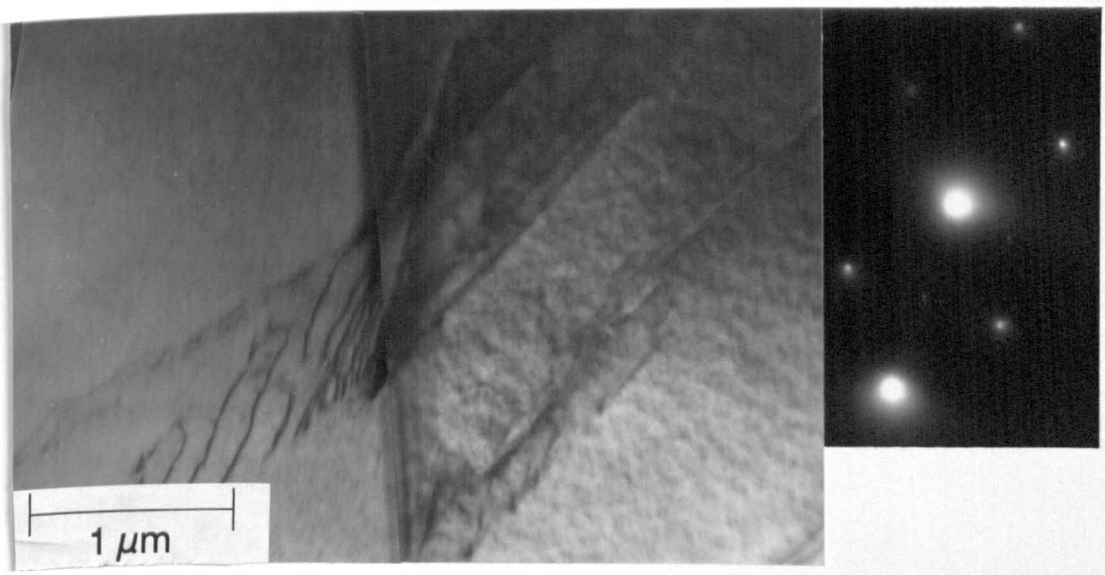

Figure 6.18 T.E.M. montage of slip bands in adjacent primary-α grains. The slip bands change direction at the boundary between the grains. The misorientation of the primary-α grains is approximately 9°. B = close to $[01\bar{1}1]$, g = $[\bar{2}110]$.

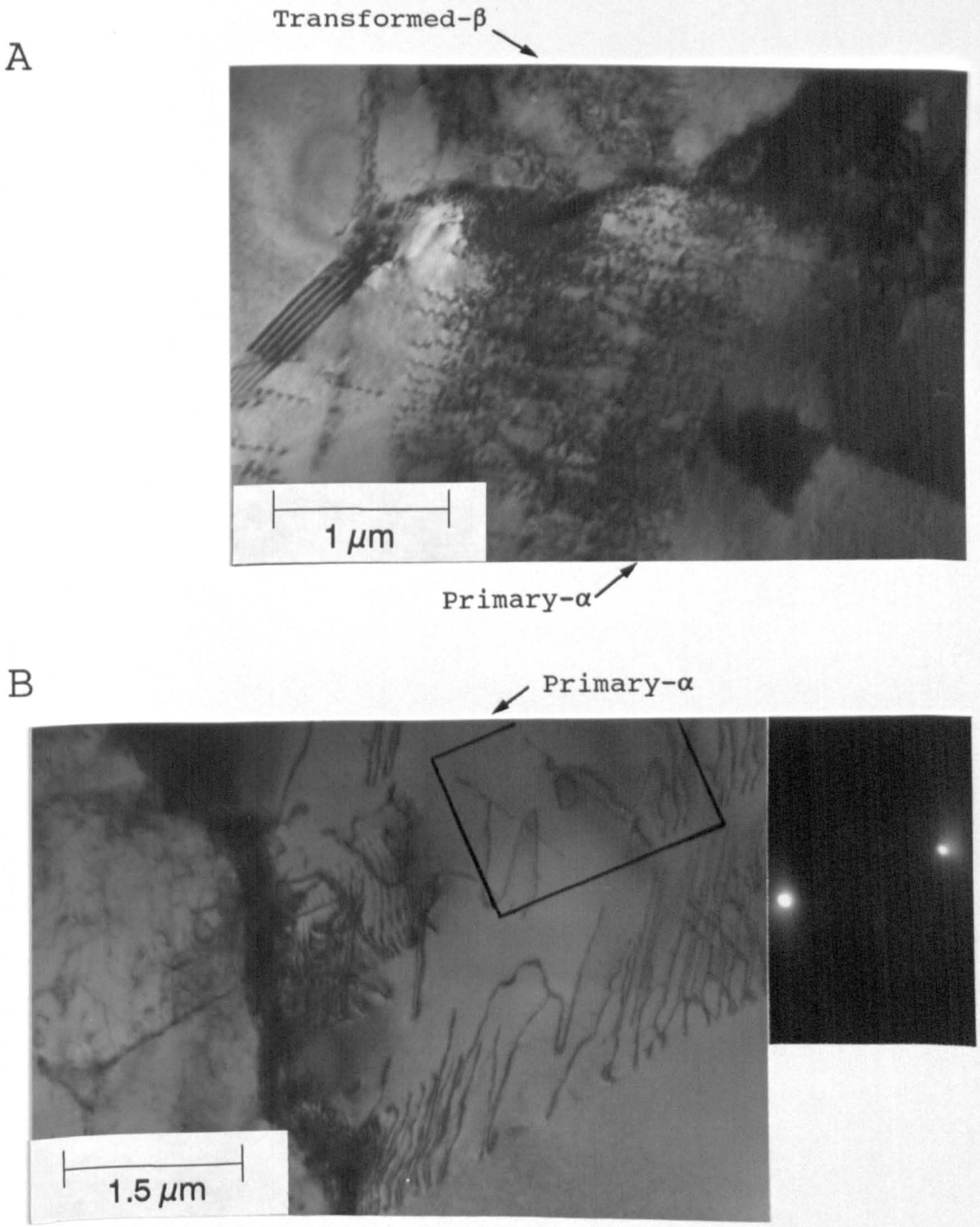

Figure 6.19 (A) and (B). T.E.M. micrographs showing dislocations in slip bands in primary-α grains piling up at the boundary with an adjacent transformed-β grain. (A) Taken under multibeam conditions. (B) B = close to [0001], $\underline{g} = [2\bar{1}\bar{1}0]$. The boxed region in (B) is imaged in more detail and under different two beam conditions in Figures 6.20A to F (see also Table 6.4).

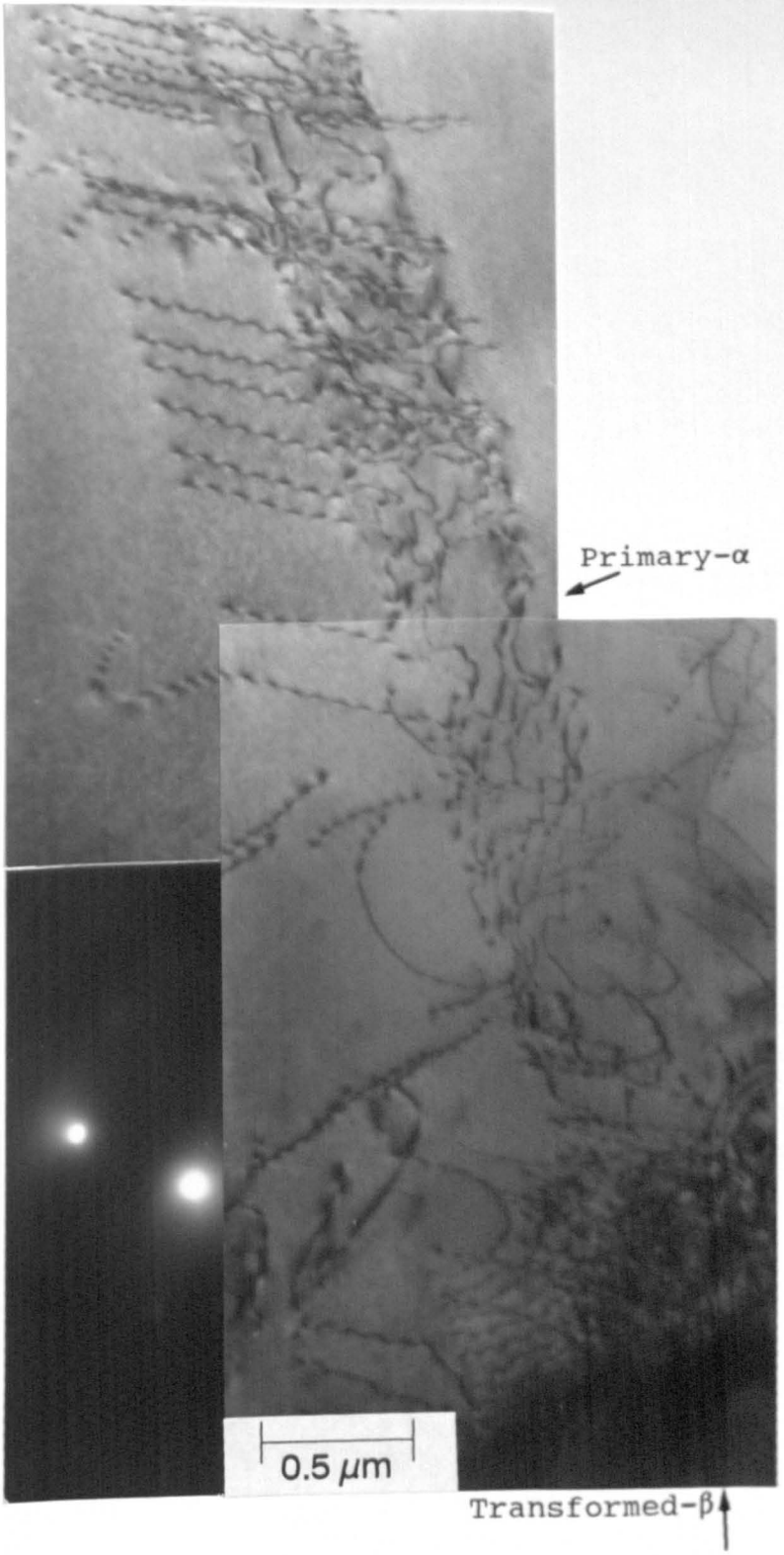

Figure 6.19 (C) T.E.M. montage showing a dislocation pile-up in a primary-α grain at the boundary of an adjacent transformed-β grain. B = close to $[0\bar{1}11]$, g = $[10\bar{1}1]$.

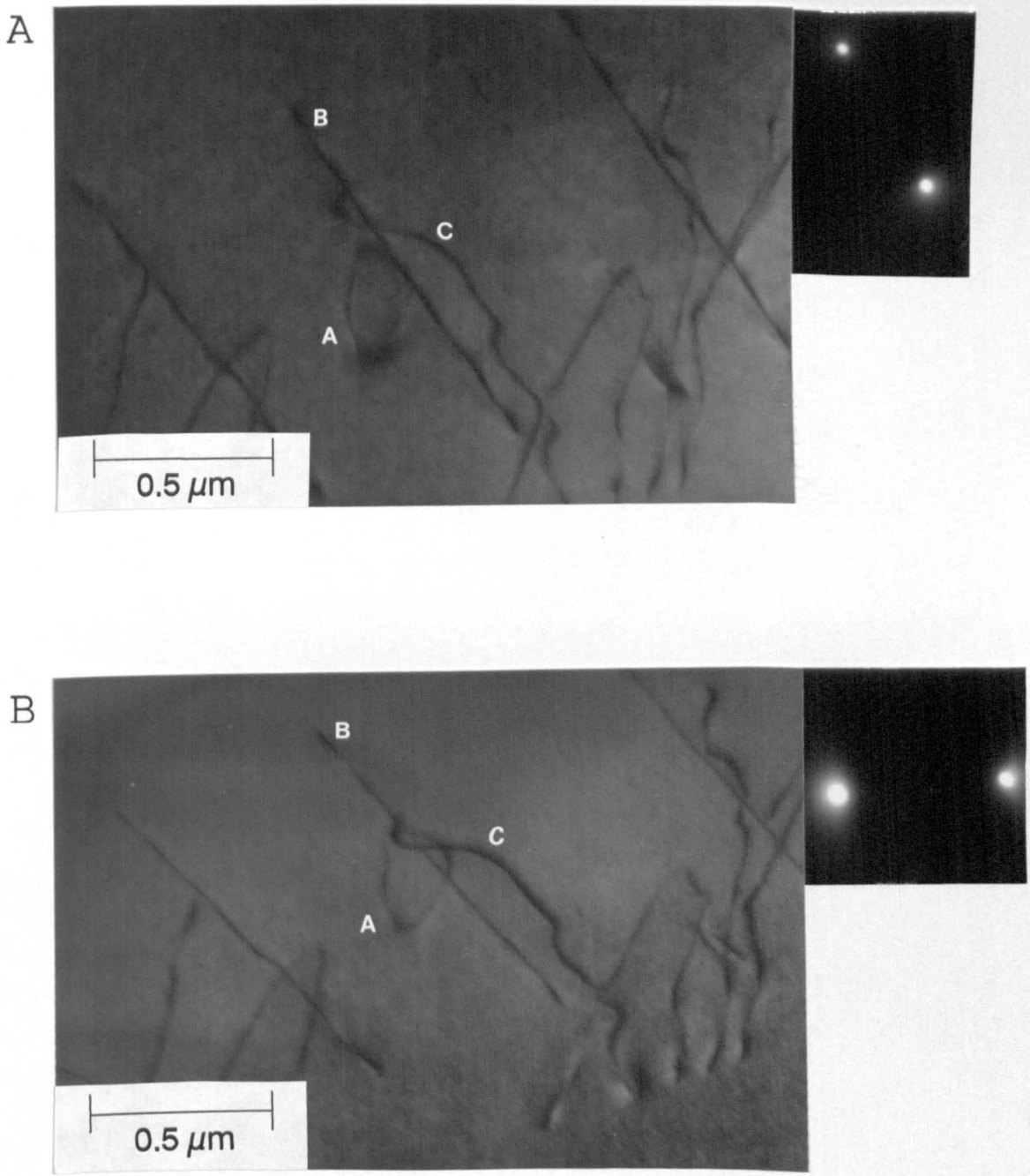

Figure 6.20 (A) and (B) T.E.M. micrographs showing part of a slip band corresponding to the boxed region indicated in Figure 6.19B. Dislocations labelled A, B and C are imaged under the diffraction conditions listed in Table 6.4. (A) B = close to [0001], $\underline{g}$ = $[1\bar{2}10]$, (B) B = close to $[0\bar{1}12]$, $\underline{g}$ = $[\bar{2}110]$. See also Figures 6.20C to 6.20F.

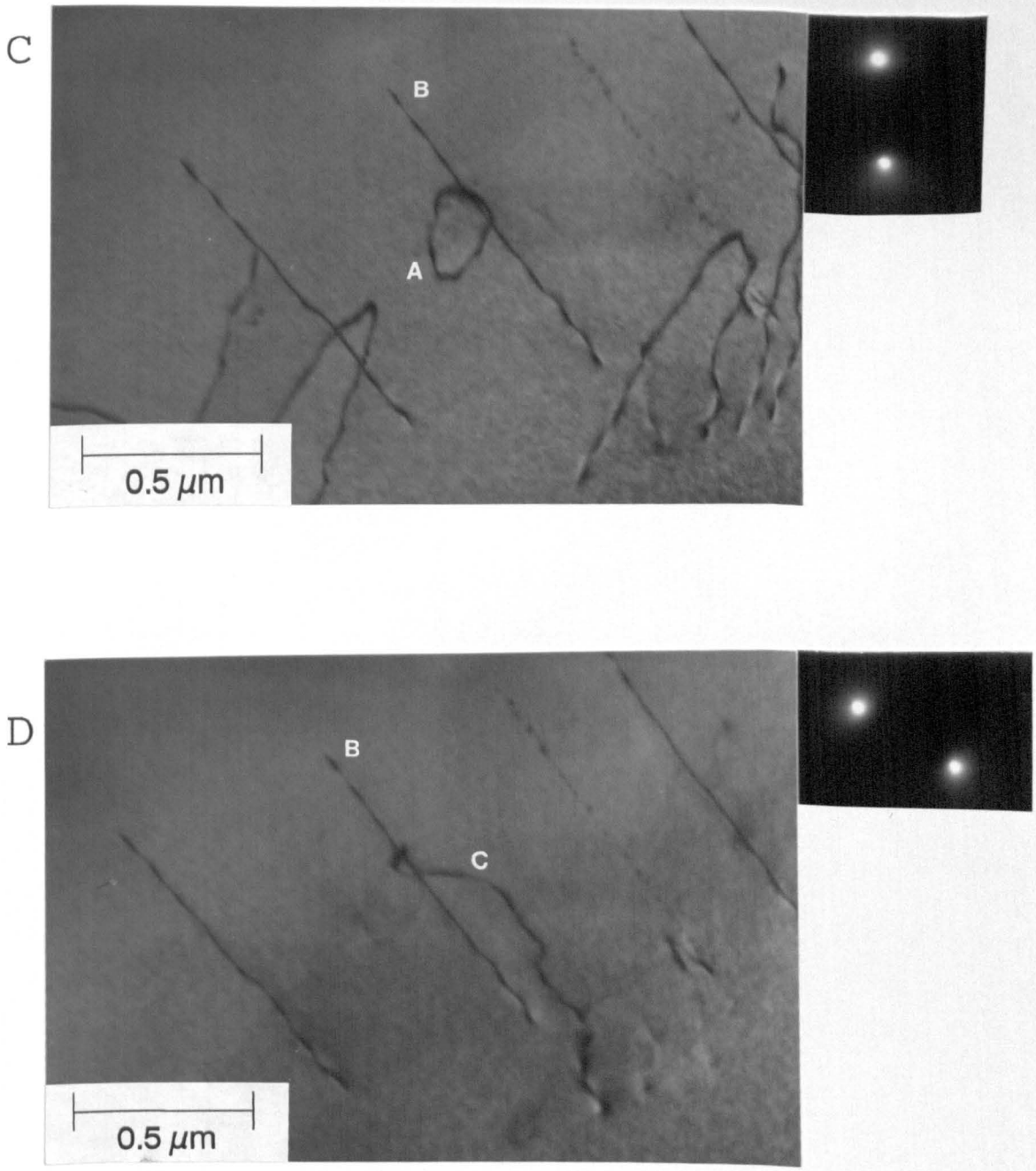

Figure 6.20 (C) and (D) T.E.M. micrographs showing part of a slip band corresponding to the boxed region indicated in Figure 6.19B. Dislocations labelled A, B and C are imaged under the diffraction conditions listed in Table 6.4. (C) B = close to $[1\bar{2}13]$, $\underline{g}$ = $[01\bar{1}1]$. (D) B = close to $[1\bar{2}13]$, $\underline{g}$ = $[1\bar{1}0\bar{1}]$. See also Figures 6.20A, 6.20B, 6.20E and 6.20F.

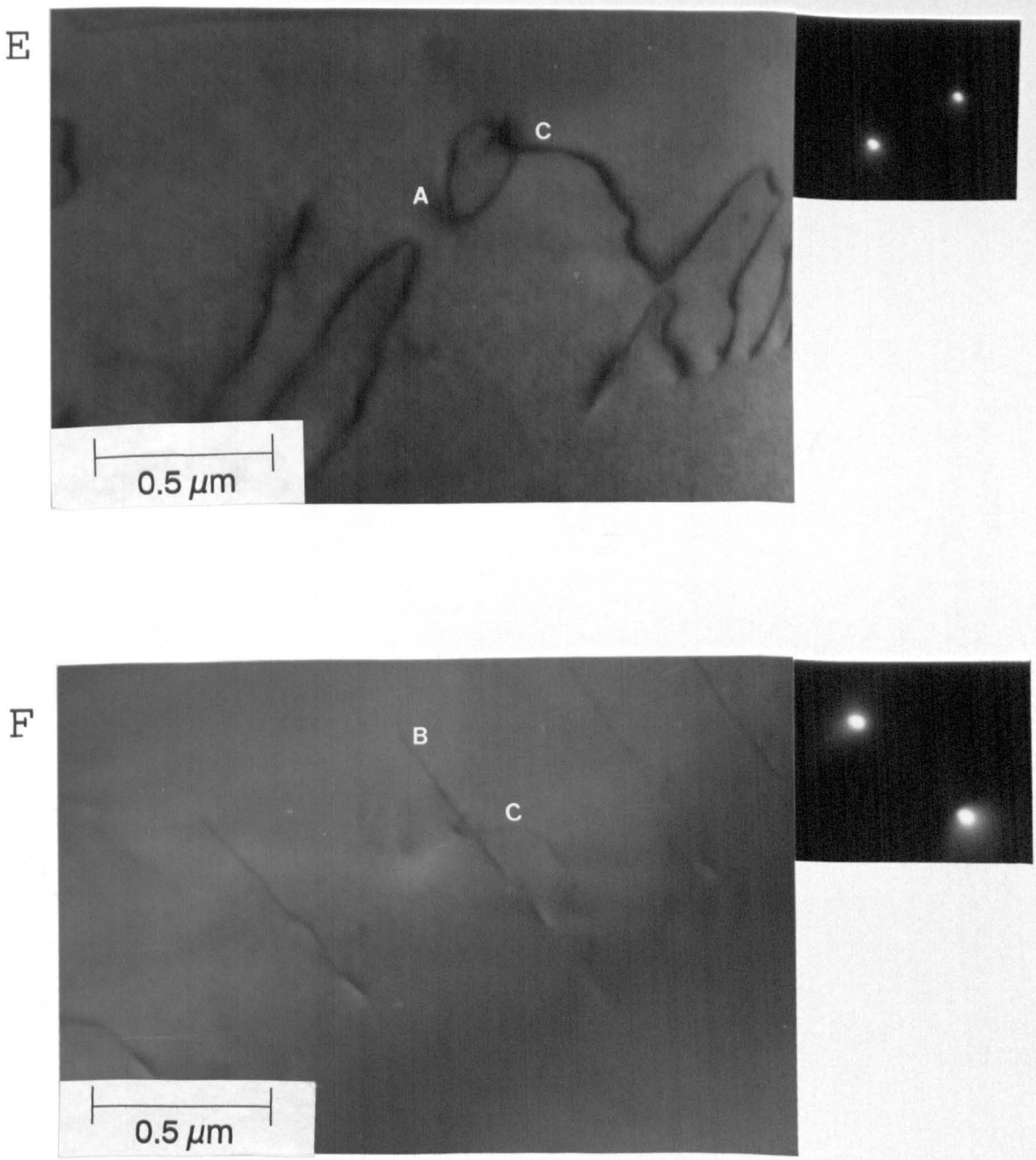

Figure 6.20 (E) and (F) T.E.M. micrographs showing part of a slip band corresponding to the boxed region indicated in Figure 6.19B. Dislocations labelled A, B and C are imaged under the diffraction conditions listed in Table 6.4. (E) B = close to $[1\bar{2}13]$, $\underline{g}$ = $[10\bar{1}0]$. (F) B = close to $[2\bar{4}23]$, $\underline{g}$ = $[\bar{1}102]$. See also Figures 6.20A to 6.20D.

Figure 6.21 Stereographic projection using trace analysis to show that the line sense, U, of the dislocation marked B in Figures 6.20A to 6.20F is between $[1\bar{2}10]$ and $[1\bar{1}00]$ and lies on the basal plane. Table 6.4 gives the corresponding values for ϕ. It is also shown that the dislocations (marked B) are close to screw in orientation since U is close to the Burgers vector, $\underline{b}$, of $1/3[1\bar{2}10]$.

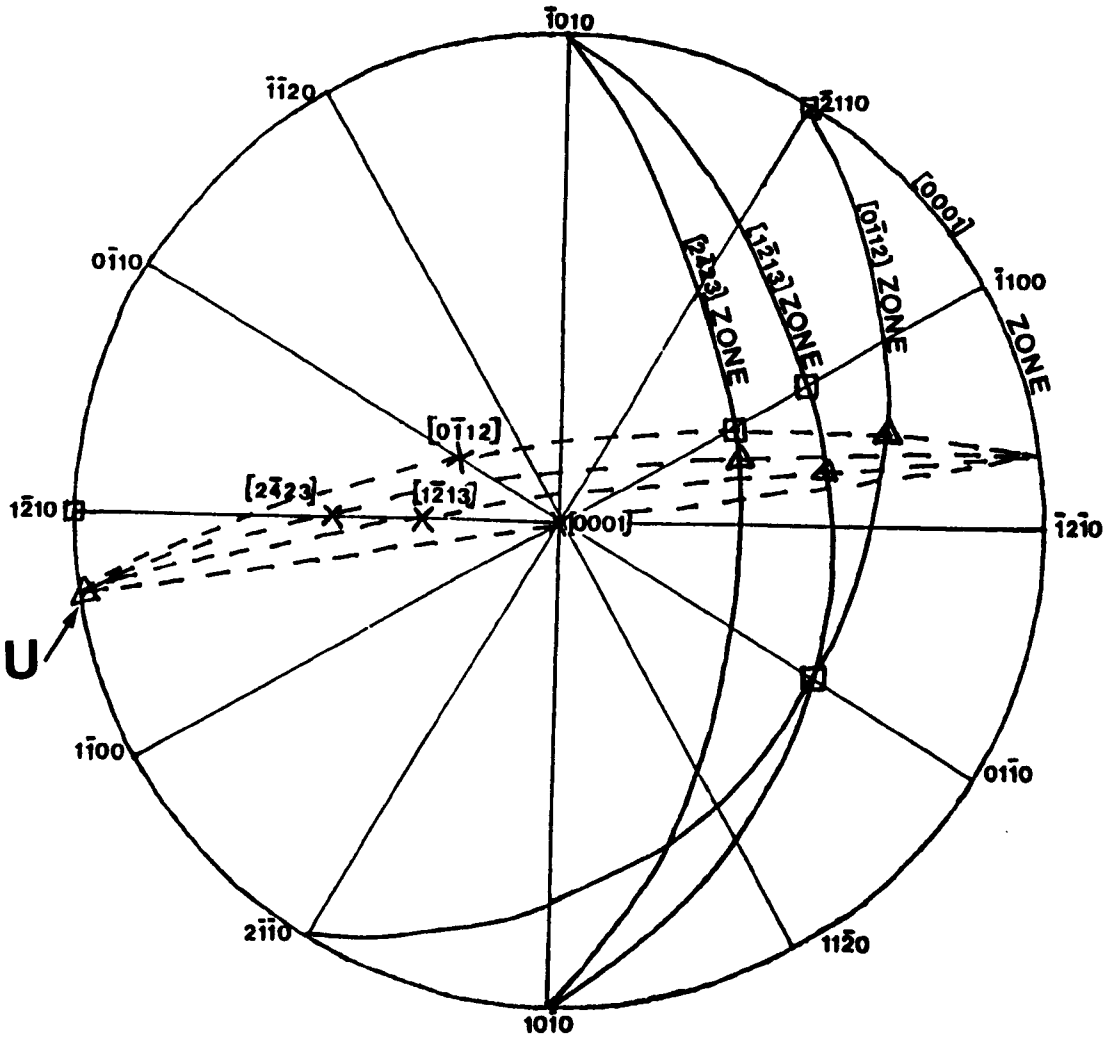

X = zone axis of beam directions, B, marked as zones on the stereographic projection.

□ = the g vector(s) on each zone (see Table 6.4).

△ = u′, the projected direction of the dislocation which is $\phi°$ away from the corresponding g vector.

U = Line sense of the dislocation marked B (Figures 6.20A to F), which must lie on the true slip plane.

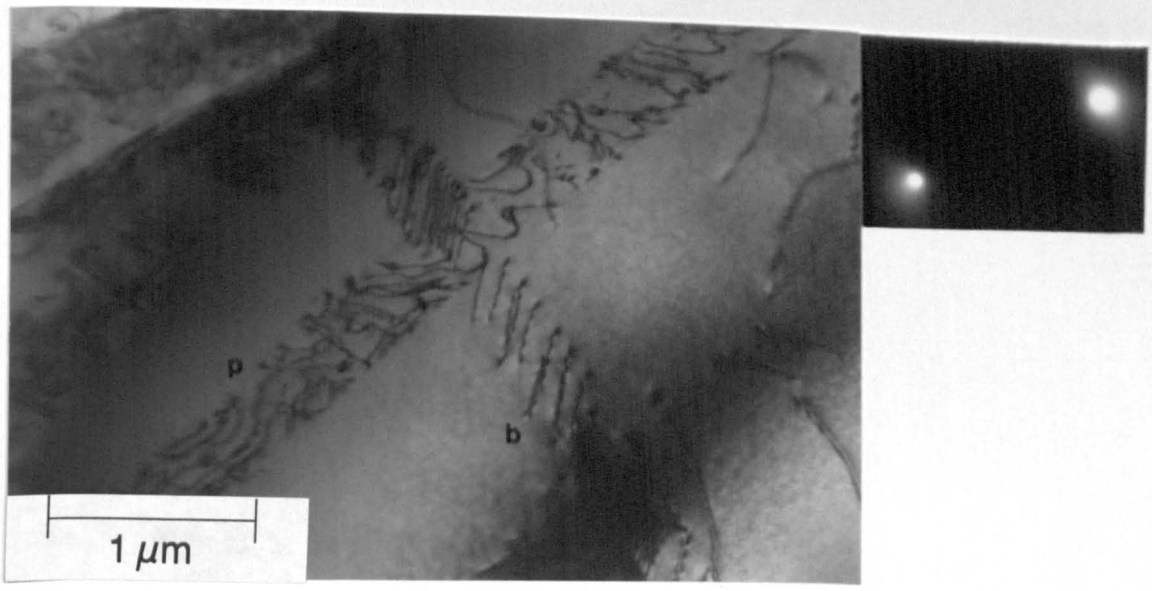

Figure 6.22 T.E.M. micrograph taken from a back-thinned foil, showing an example of slip on a basal plane, marked b, and a prism plane, marked p, which occur in the same primary-α grain. Note the pairing of dislocations in the basal plane. B = close to $[0\bar{3}32]$, $\underline{g}$ = $[0\bar{1}13]$.

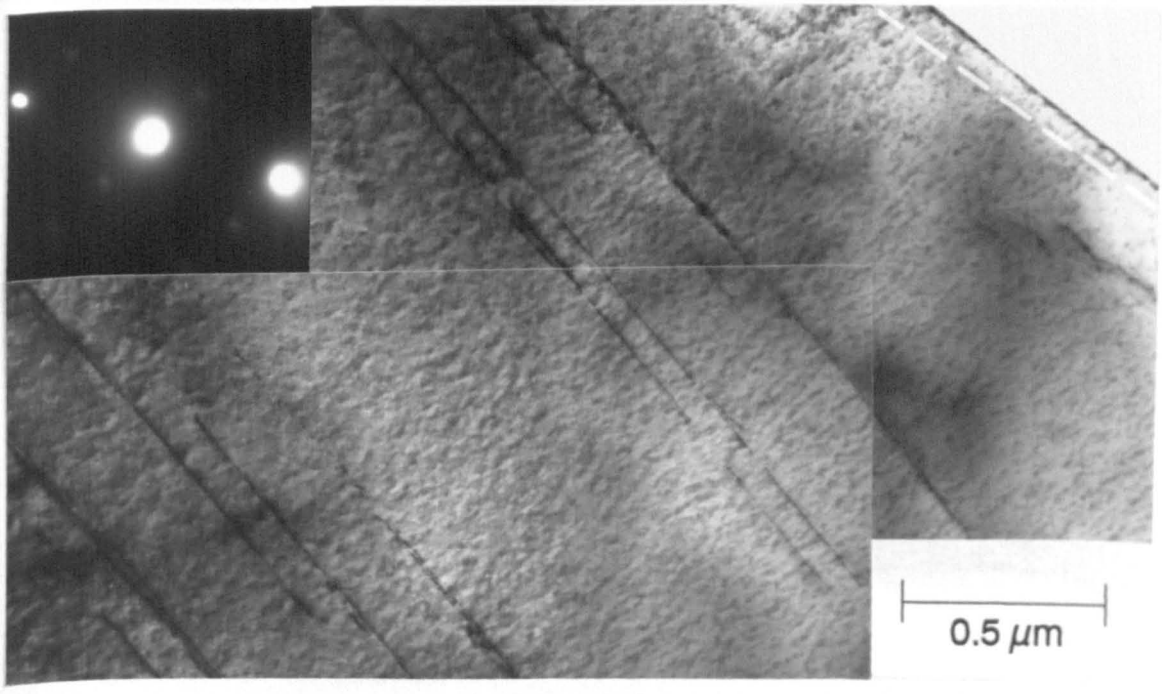

Figure 6.23 T.E.M. micrograph from a cross-sectional thin foil showing a primary-α grain adjacent to the fatigue surface. Slip bands have occurred on the basal plane at 20° to the fatigue surface, the angle of which is indicated. B = close to $[11\bar{2}0]$, $\underline{g}$ = $[1\bar{1}01]$.

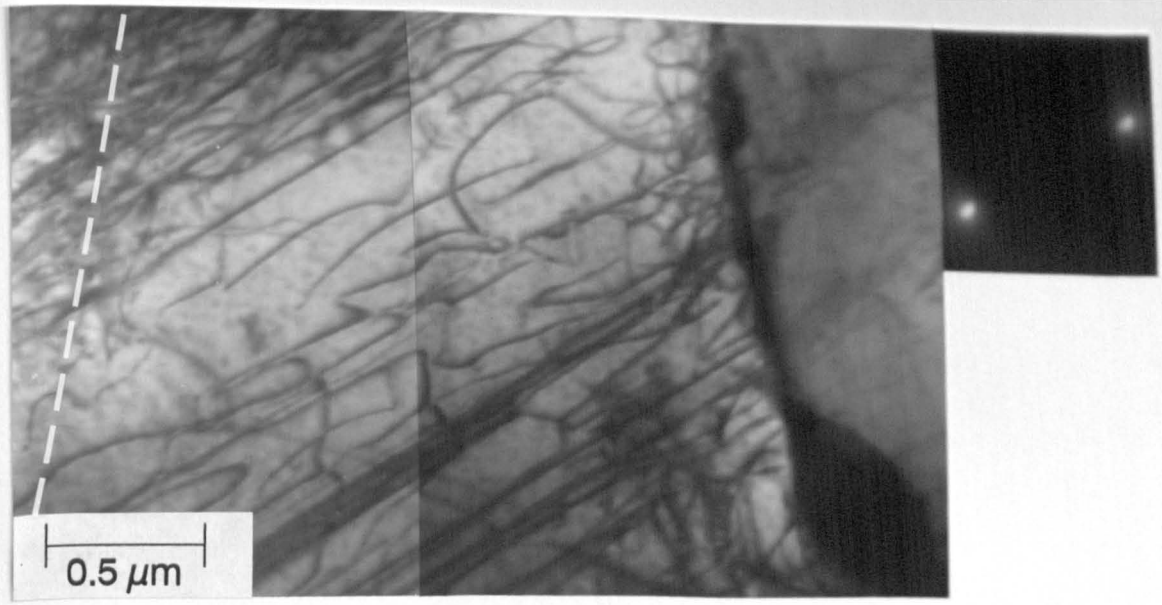

Figure 6.24 T.E.M. micrograph showing a primary-α grain in which slip on the basal plane occurred at 45° to the fatigue surface, the angle of which is indicated. B = close to $[0\bar{2}21]$, g = $[\bar{2}110]$.

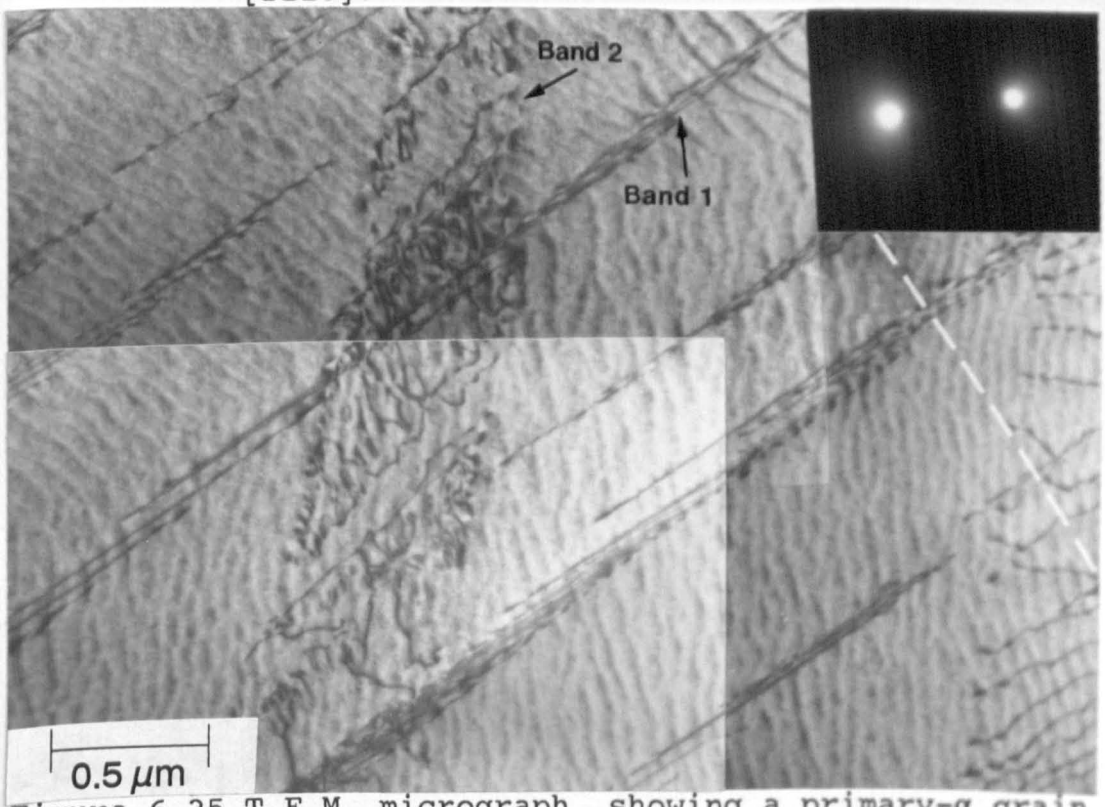

Figure 6.25 T.E.M. micrograph showing a primary-α grain adjacent to the fatigue surface. Slip occurred on two planes at 90° (band 1) and 40° (band 2) to the fatigue surface, the angle of which is indicated. B = close to $[1\bar{2}10]$, g = $[10\bar{1}1]$.

Figure 6.26 (A) to (C) T.E.M. micrographs showing slip on two planes in a primary-α grain adjacent to the fatigue surface in a cross-sectional thin foil. (A) B = close to $[1\bar{2}13]$, $\underline{g}$ = $[10\bar{1}0]$, (B) B = close to $[0\bar{1}12]$, $\underline{g}$ = $[2\bar{1}\bar{1}0]$, (C) B = close to $[1\bar{1}00]$, $\underline{g}$ = $[11\bar{2}0]$. (see Figure 6.25 and Table 6.5). The angle of the fatigue surface is indicated by a dashed line in each micrograph.

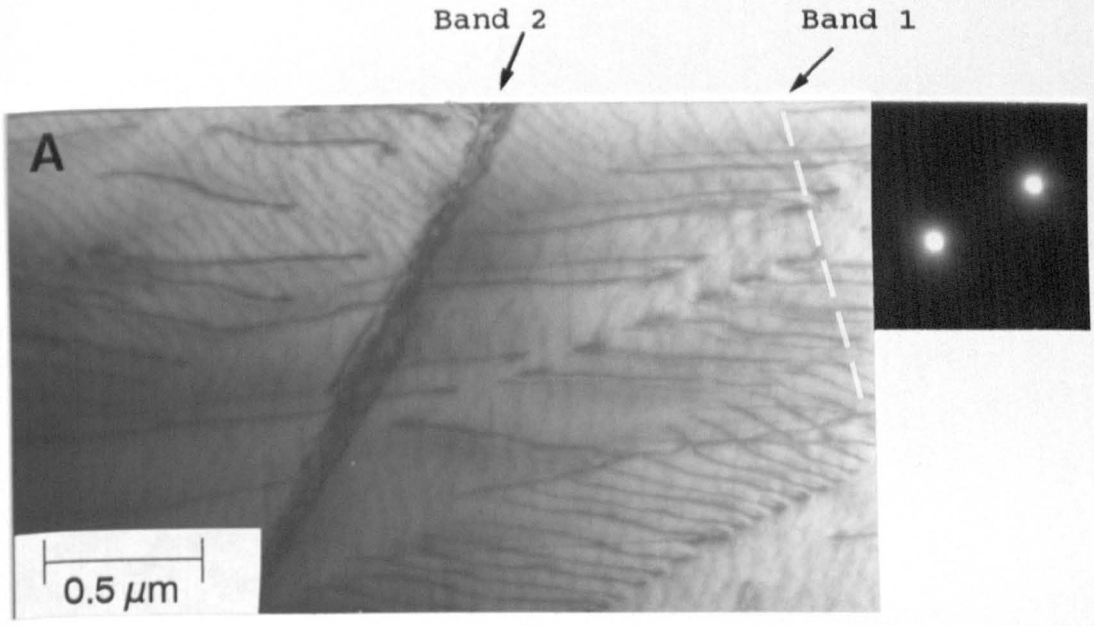
Band 2
Band 1
A
0.5 μm

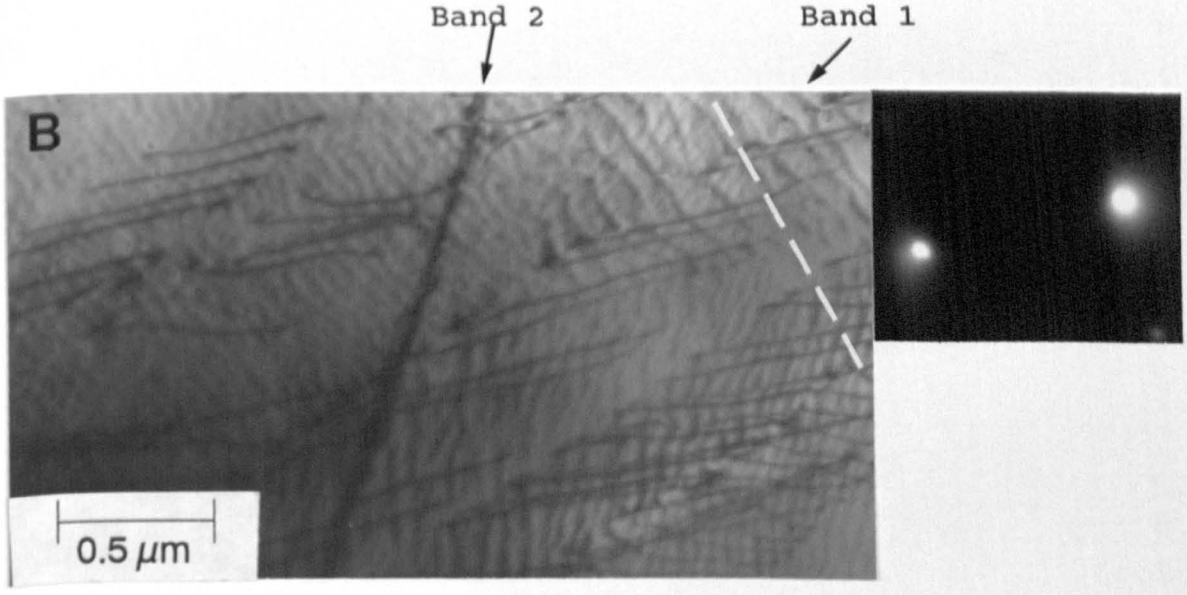
Band 2
Band 1
B
0.5 μm

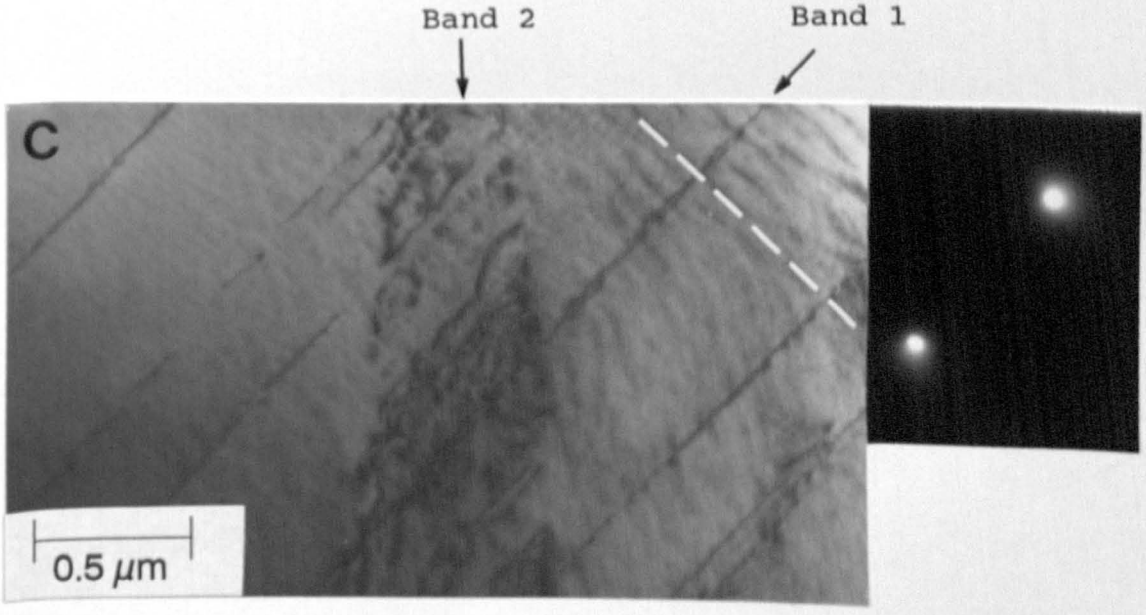
Band 2
Band 1
C
0.5 μm

Figure 6.27 Stereographic projection using trace analysis to show that the line sense, U, of slip band 1 in Figures 6.25 and 6.26A to C lies on the basal plane (*i.e.* 90° from (0001)). Table 6.5 lists the corresponding values for ϕ_1 (the angle between the g vector and direction of the slip band) and the thickness of the slip band at each zone analysed.

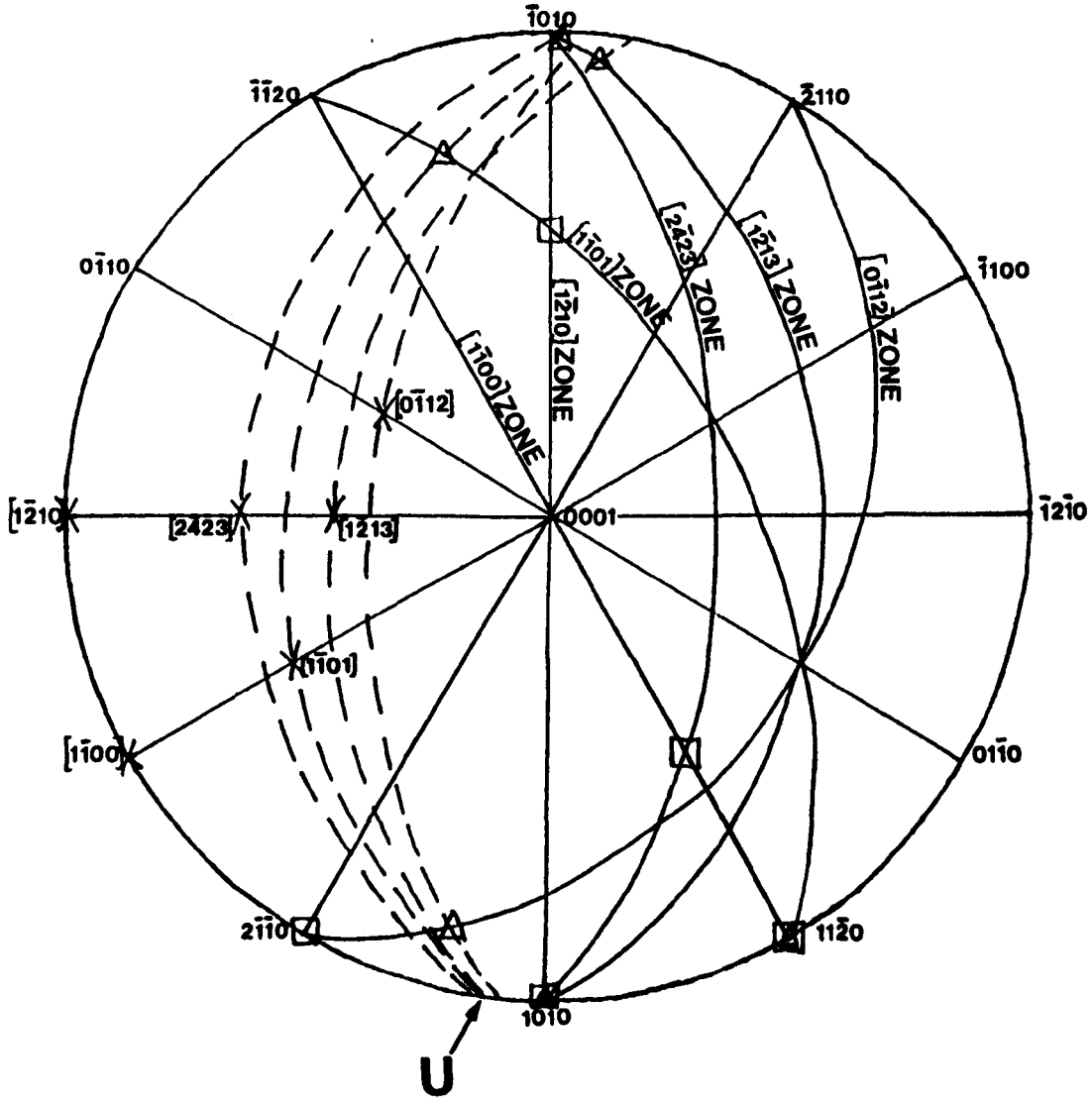

X = zone axis of beam directions, B, marked as zones.

□ = g vector(s) used to image the slip band on each zone (see Table 6.5).

△ = u′, the projected direction of slip band 2 (see Table 6.5) which is $\phi_1°$ away from the corresponding g vector.

U = Line sense of slip band 1 which must lie on the true slip plane.

Figure 6.28 (A) Stereographic projection showing the traces of zones, zone axes, X, and the projected directions, u', of slip band 2 in Figures 6.25 and 6.26A to C. See Table 6.5 and Figures 6.28B and 6.28C for the determination of U, the line sense of slip band 2, which must lie on the true slip plane.

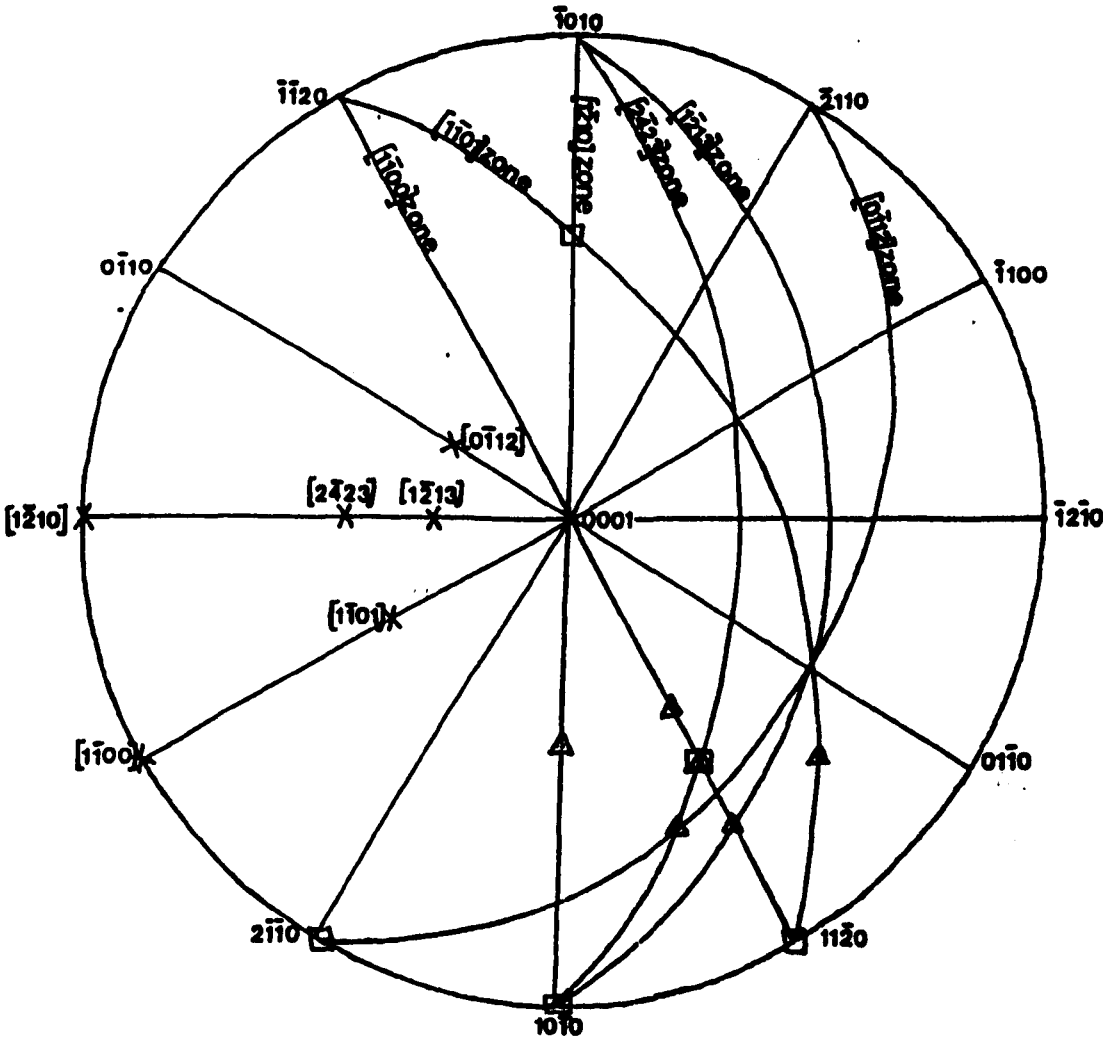

X = zone axis of beam directions, B, marked as zones.

□ = g vector(s) used to image the slip band on each zone (see Table 6.5).

△ = u′, the projected direction of slip band 2 (see Table 6.5) which is ϕ_2° away from the corresponding g vector.

Figure 6.28 (B) Stereographic projection using trace analysis to indicate the line sense, U, of slip band 2 in Figures 6.25 and Figures 6.26A to C. The traces of zones and zone axes (X) are identified in Figure 6.28A.

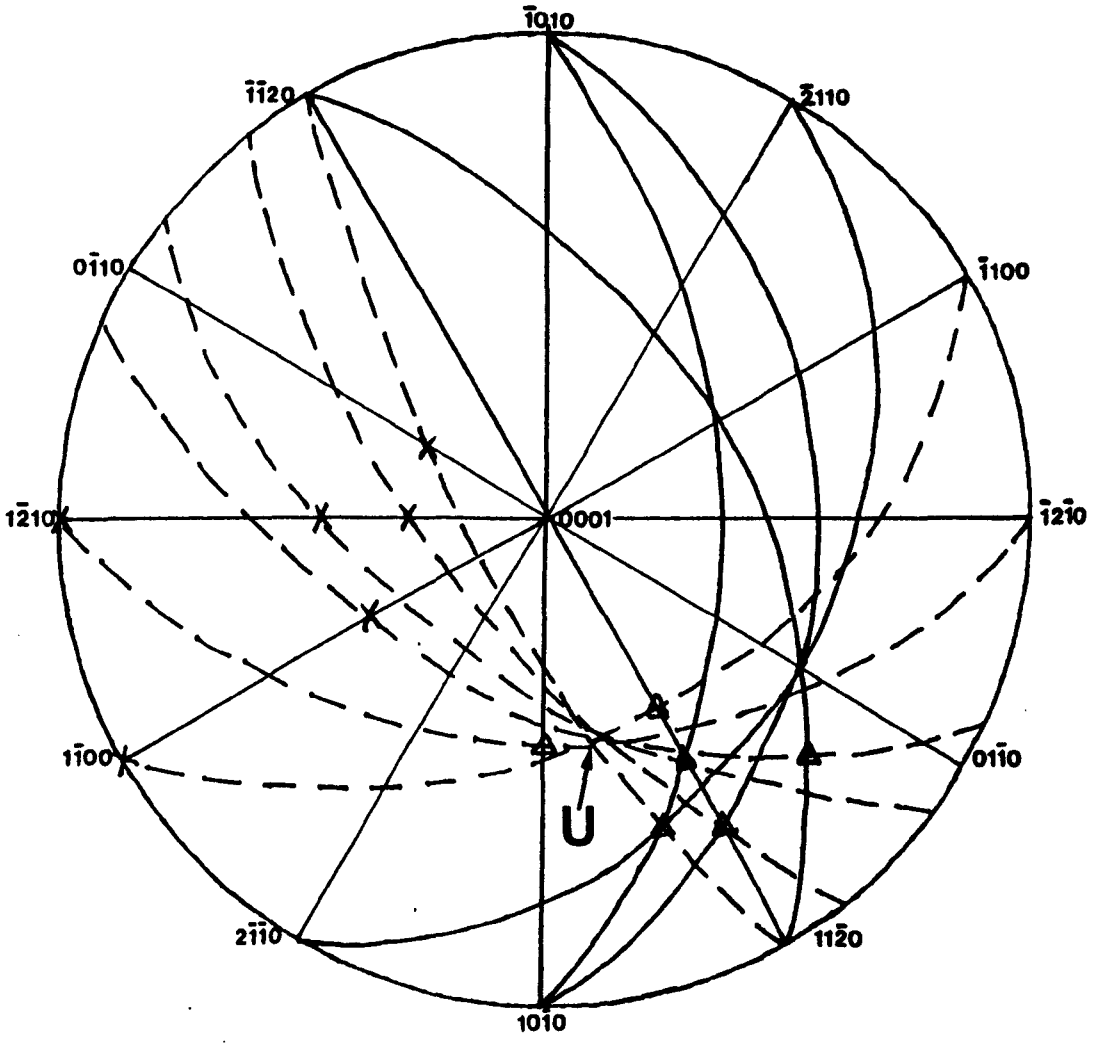

X = zone axis of beam directions, B, marked as zones.

△ = u′, the projected direction of slip band 2 which is ϕ_2° away from the corresponding g vector (see Table 6.5).

U = Line sense of slip band 2 which must lie on the true slip plane.

Figure 6.28 (C) Stereographic projection using trace analysis to identify the trace of the slip plane on which slip band 2 occurred (see Figures 6.25, 6.26A to C, 6.28A and 6.28B and Table 6.5). The pole of slip plane ($\bar{1}101$) lies on a great circle at 90° from U. Also indicated are the measured thicknesses (μm) of slip band 2 at each zone imaged (see Table 6.5). These show that the slip band is imaged at close to edge on (0.00 μm) at the $[0\bar{1}12]$ and $[1\bar{2}13]$ zones and that the thickness increases with the distance from the slip plane, as expected.

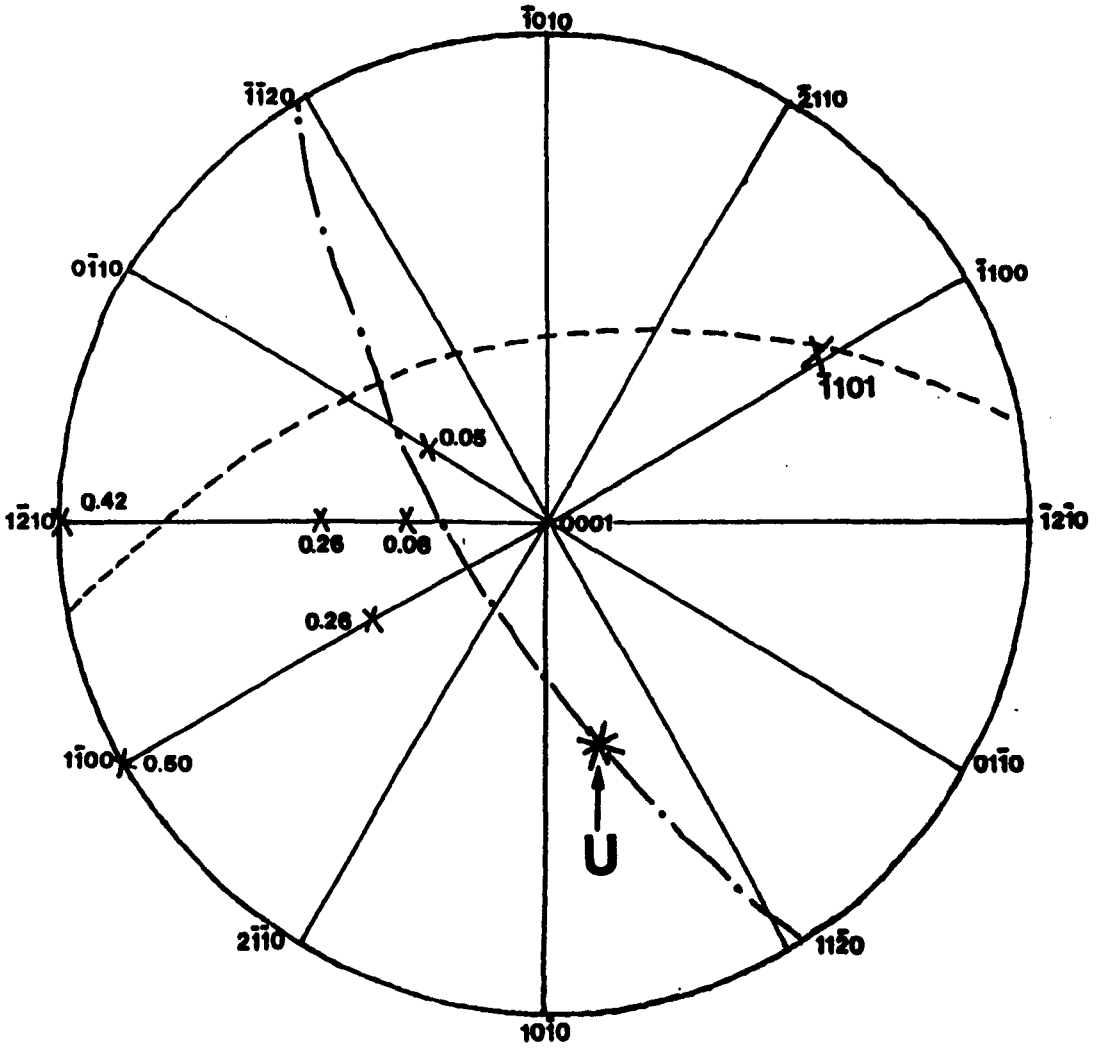

U = Line sense of slip band 2 which must lie on the true slip plane.

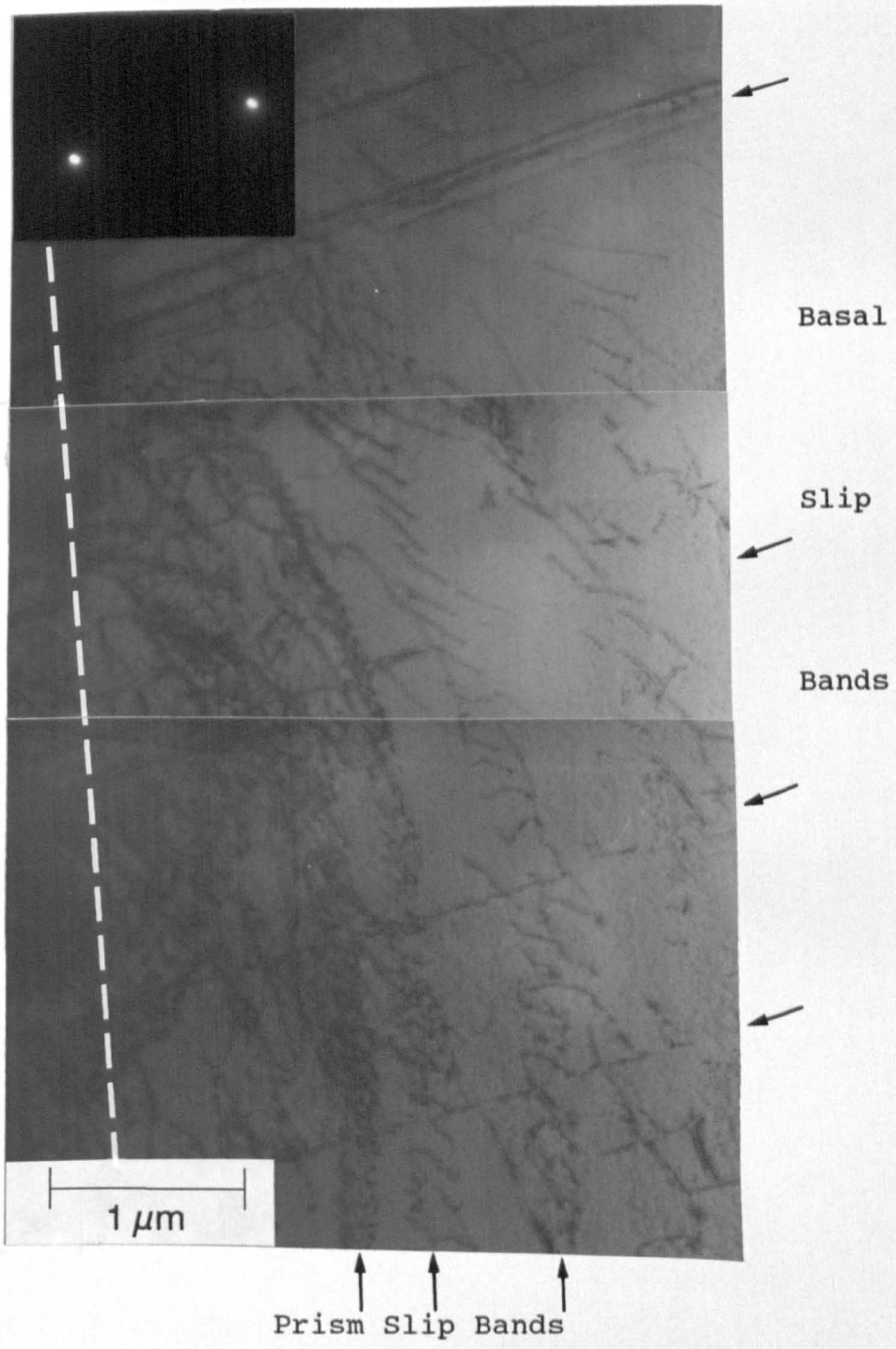

Figure 6.29 T.E.M montage showing two slip systems in a primary-α grain at 15° and 75° to the fatigue surface, the angle of which is indicated by a dashed line. B = close to $[1\bar{1}00]$, g = $[11\bar{2}0]$.

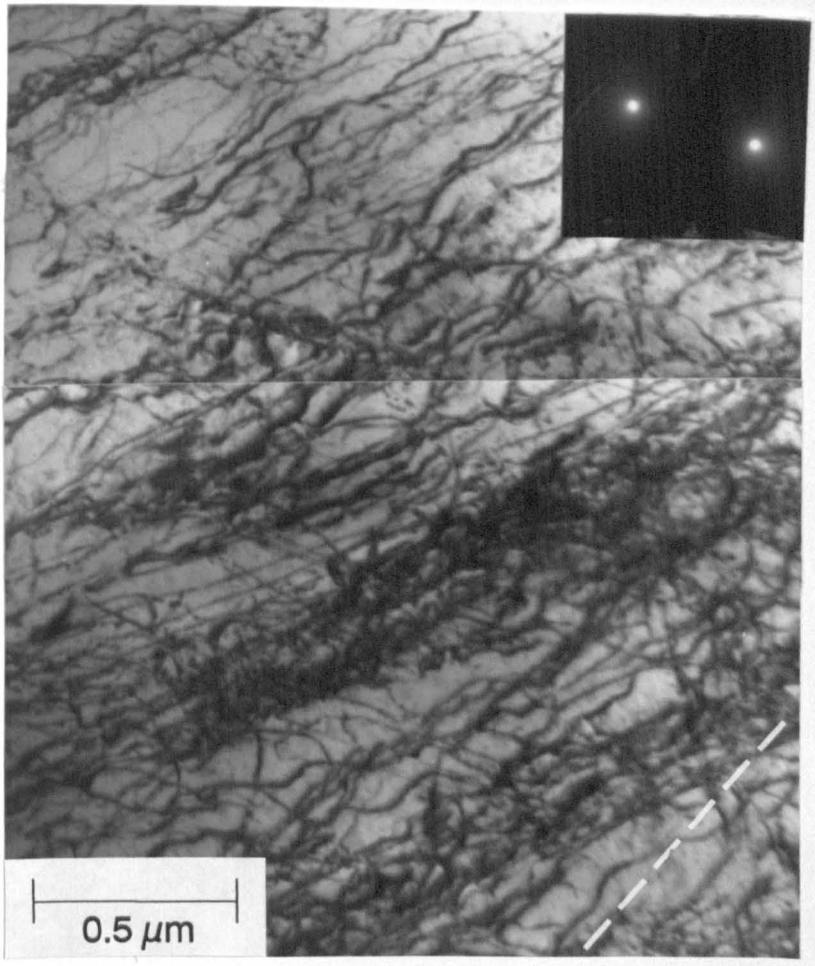

Figure 6.30 (A) T.E.M. montage showing the high dislocation density which occurred in a primary-α grain adjacent to the fatigue surface in a cross-sectional foil. Basal slip is present at 20° to the fatigue surface, the angle of which is indicated. Dislocations with a <c + a> type Burgers vector are also present. The <c + a> type dislocations are wave-like and tangled in appearance. B = close to $[0\bar{1}11]$, g = $[10\bar{1}1]$. See also Figure 6.30B.

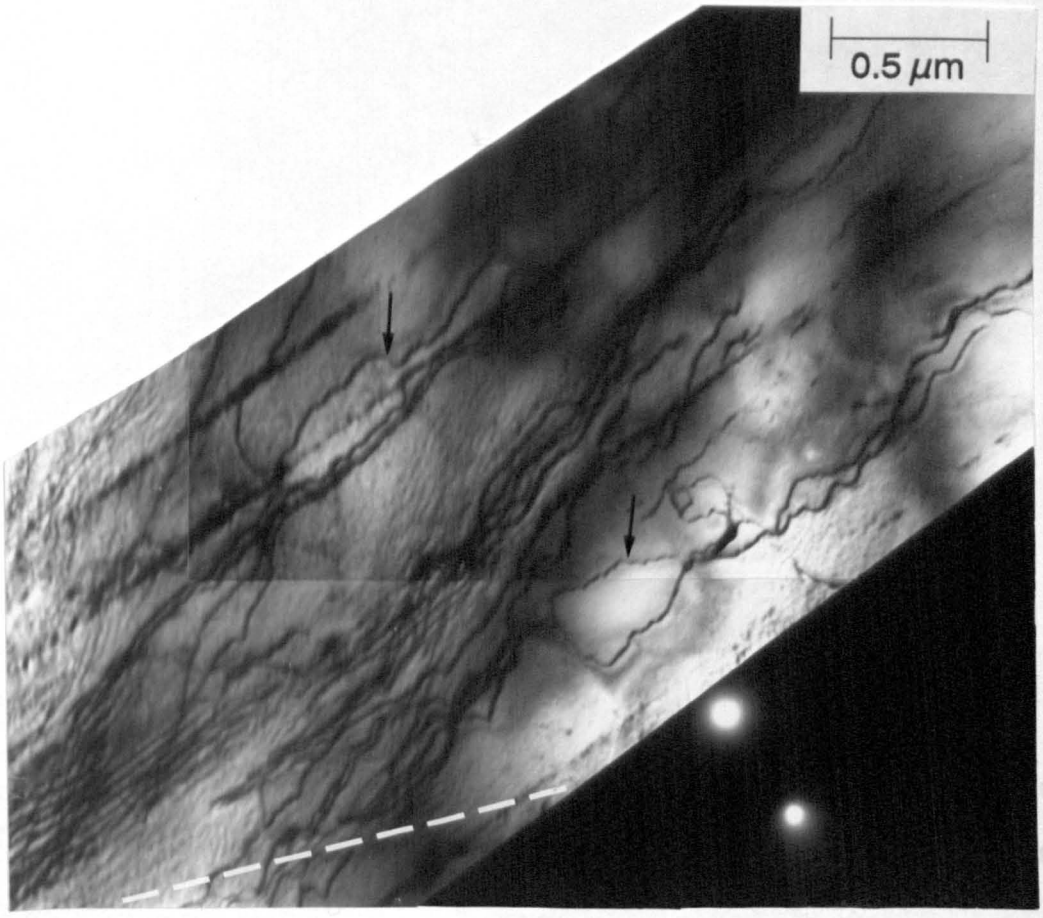

Figure 6.30 (B) T.E.M. montage showing the high dislocation density which occurred in a primary-α grain adjacent to the fatigue surface in a cross-sectional foil. Under the condition $\underline{g}$ = [0002], basal slip can be seen with residual contrast. The basal slip occurs at 20° to the fatigue surface, the angle of which is indicated. Dislocations with Burgers vectors of the $\langle \underline{c} + \underline{a} \rangle$ type are in contrast under this condition. These appear tangled and wave-like in nature and are often paired (see arrowed dislocations). B = close to $[1\bar{2}10]$, $\underline{g}$ = [0002].

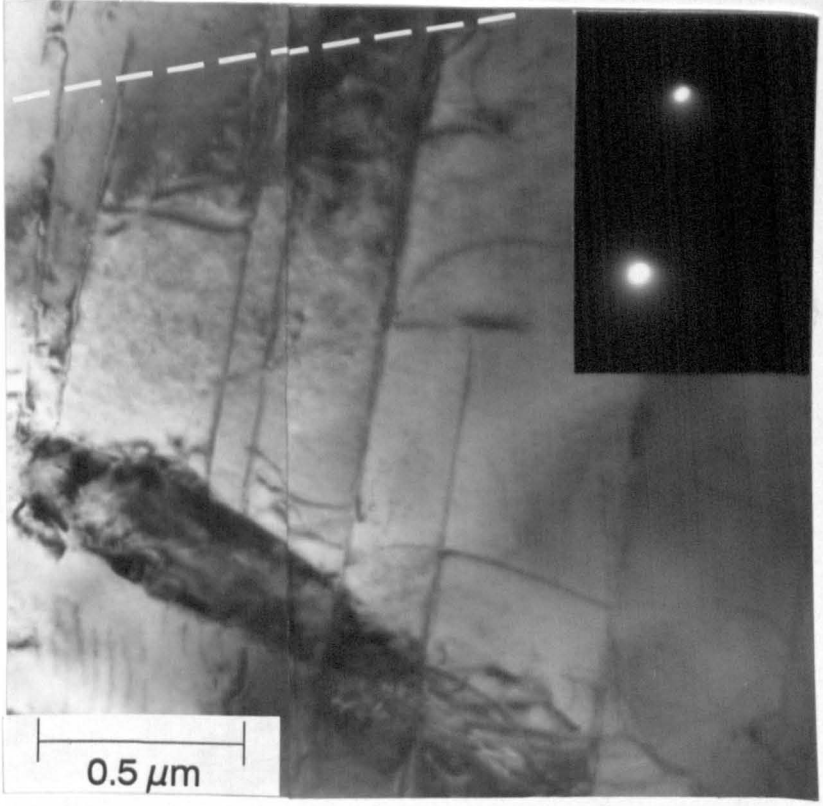

Figure 6.31 T.E.M. montage showing basal slip at 75° to the fatigue surface (indicated). The slip was arrested at a particle on a low angle boundary between two primary-α grains. B = close to $[01\bar{1}0]$, g = $[\bar{2}110]$.

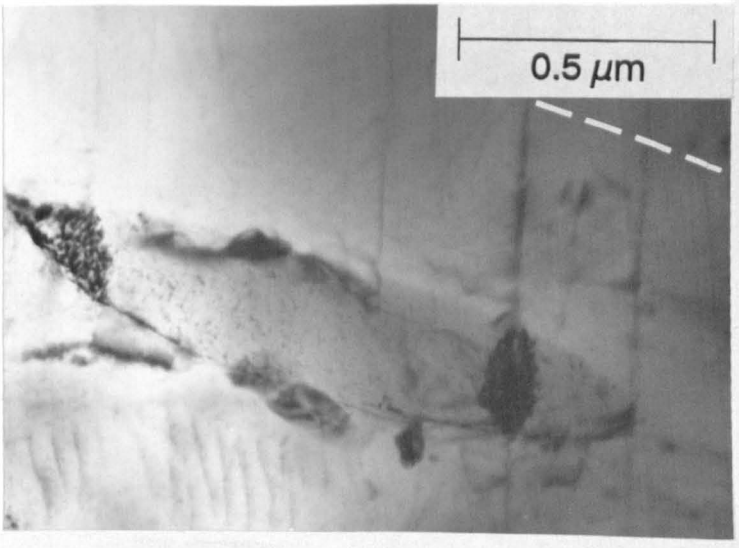

Figure 6.32 T.E.M. micrograph taken under multibeam conditions, showing the slip-band interactions with the particle and the silicide particles associated with the β. The angle of the fatigue surface is indicated.

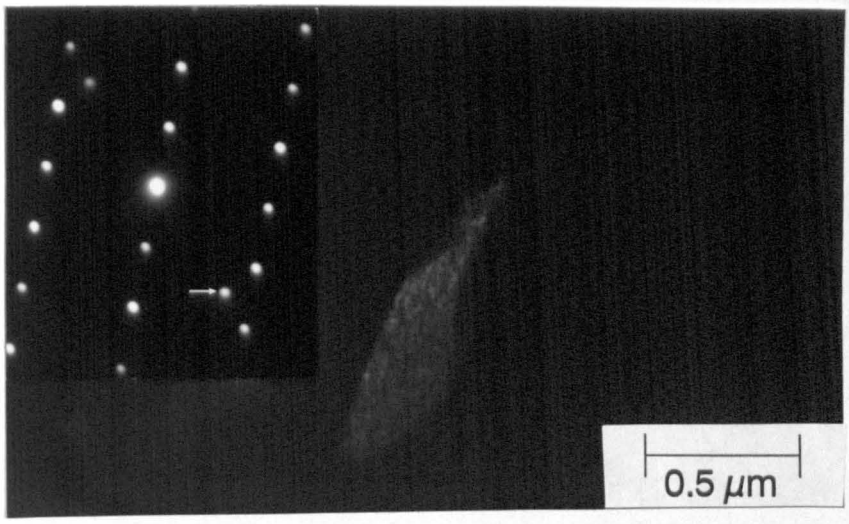

Figure 6.33 (A) Dark field T.E.M. micrograph of the particle, identified as a β particle from (B) a selected area diffraction pattern using $\underline{g} = [011]_{\beta}$ (arrowed).

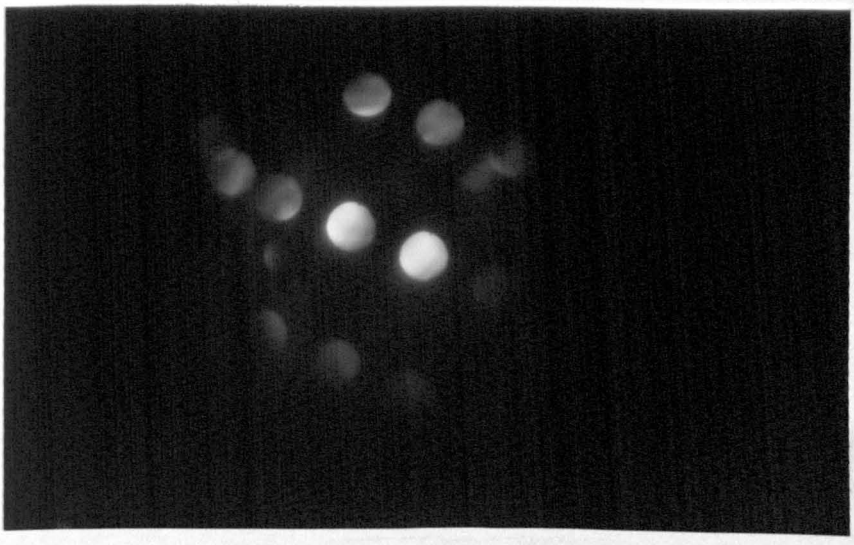

Figure 6.34 Convergent beam electron diffraction pattern taken from the β particle. $B = [113]_{\beta}$.

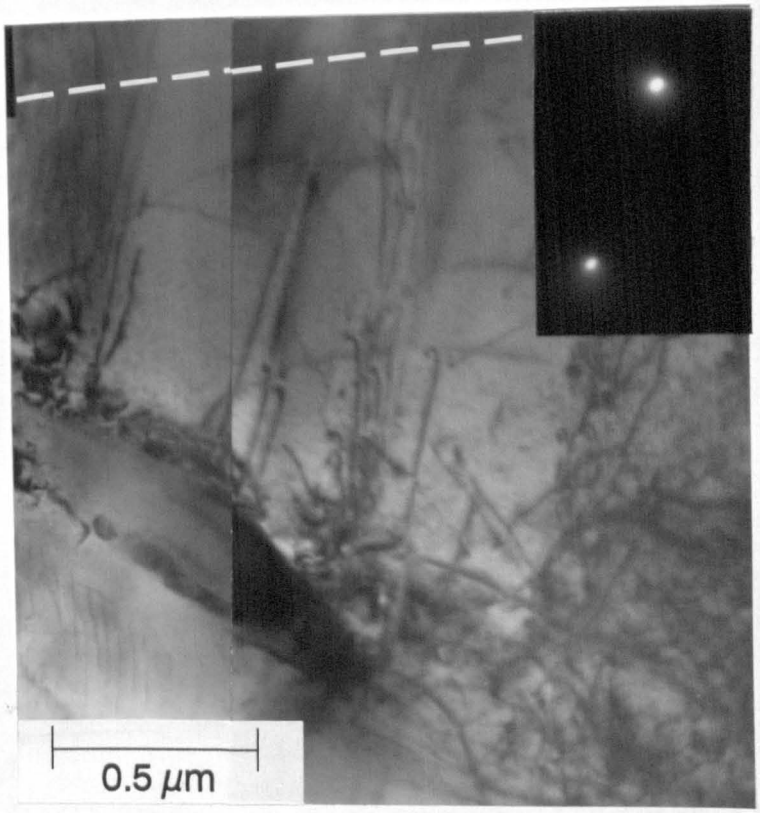

Figure 6.35 T.E.M. montage showing the same region as Figures 6.31 and 6.32. The slip band interactions with the β phase particle are imaged under the condition B = close to $[0\bar{3}32]$, g = $[\bar{2}110]$. The angle of the fatigue surface is indicated.

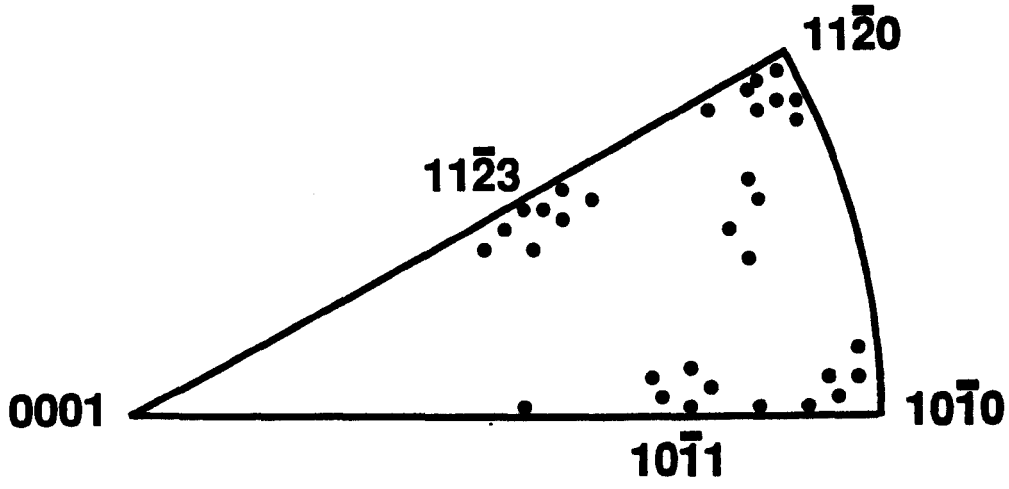

Figure 6.36 Standard stereographic triangle (0001) - (10$\bar{1}$0) - (11$\bar{2}$0) for titanium. Grain orientations taken from near the fatigue surface in cross-sectional thin foils at 0° tilt.

A

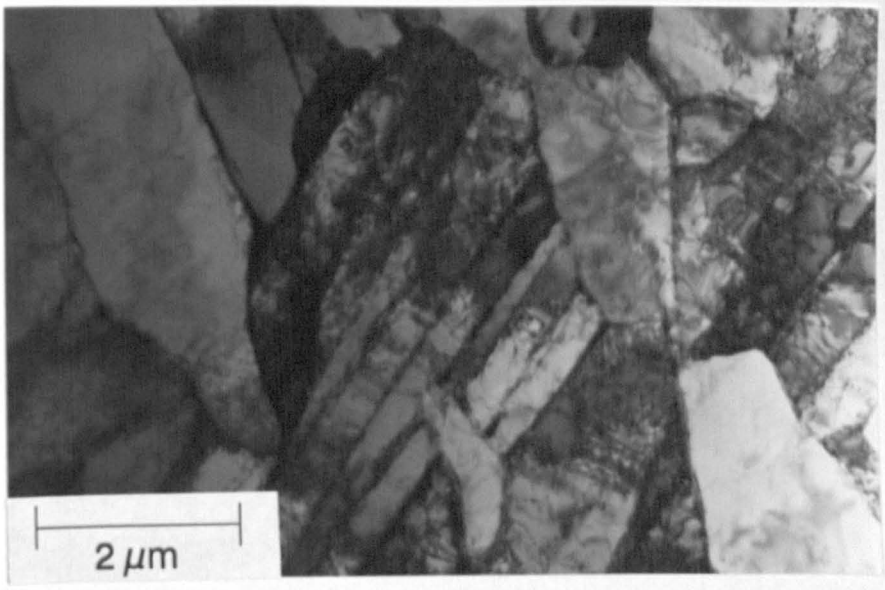

B

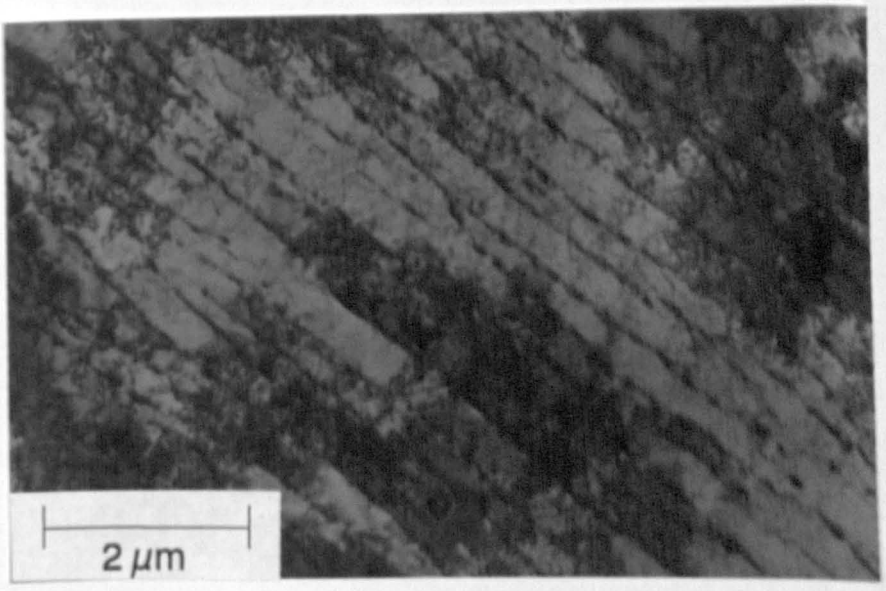

Figure 6.37 (A) and (B) Low magnification T.E.M. micrographs of transformed-β taken from a back-thinned foil. These show the more homogeneous nature of damage in the transformed-β grains compared to that found in primary-α grains.

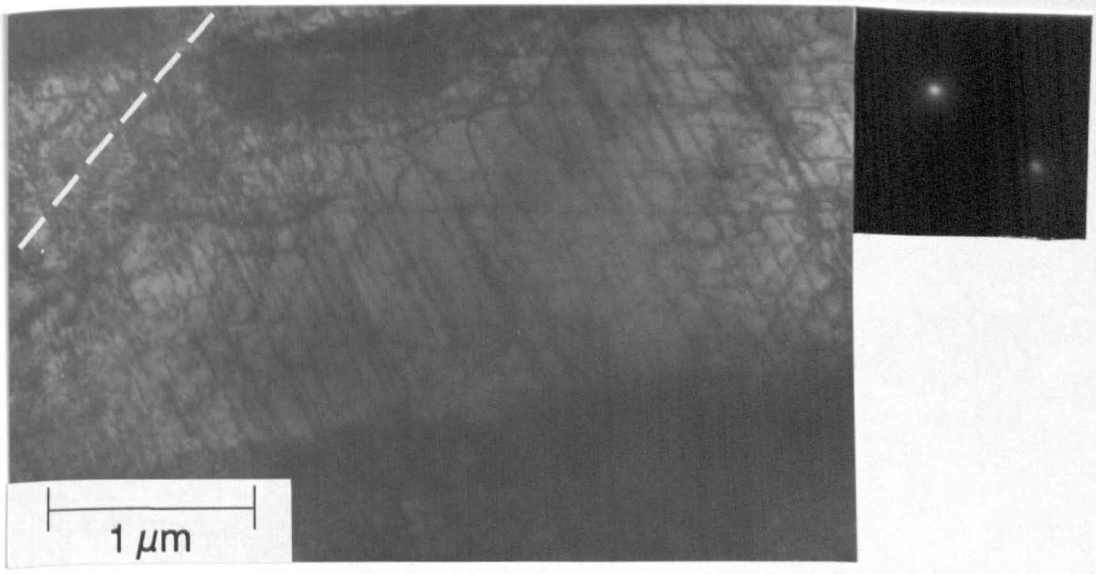

Figure 6.38 Low magnification T.E.M. micrograph of slip in transformed-β. B = close to $[1\bar{2}13]$, g = $[10\bar{1}1]$. The angle of the fatigue surface is indicated.

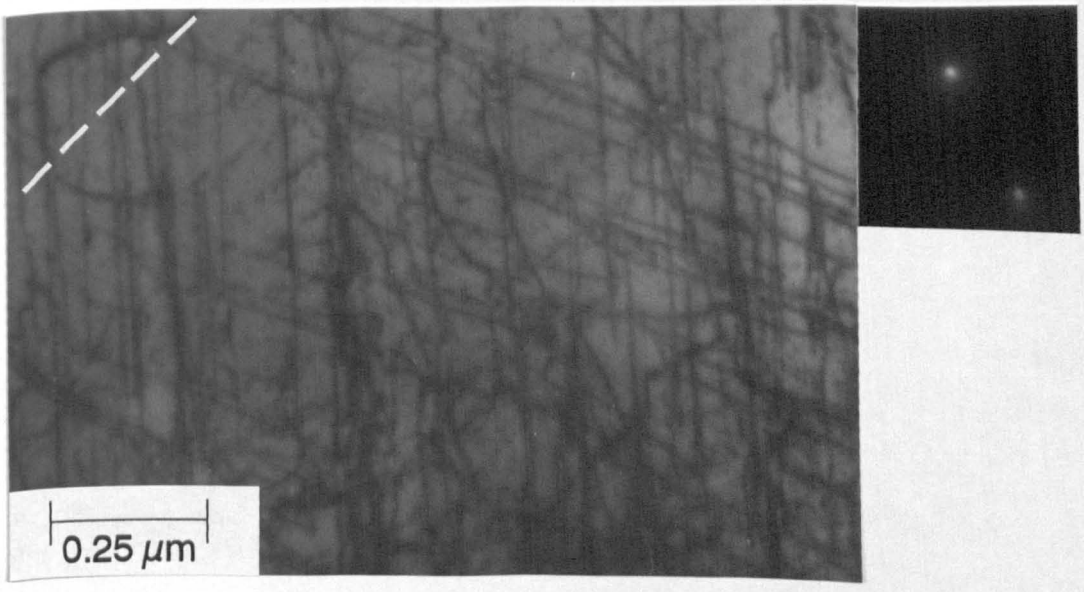

Figure 6.39 High magnification T.E.M. micrograph of slip in transformed-β. B = close to $[1\bar{2}13]$, g = $[10\bar{1}1]$. The angle of the fatigue surface is indicated.

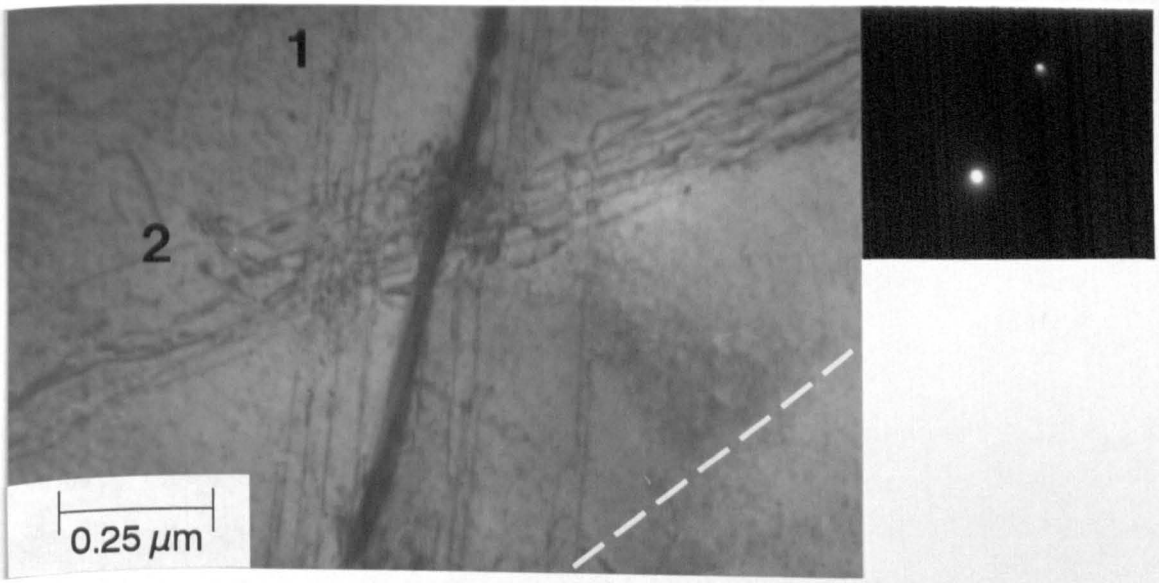

Figure 6.40 T.E.M. micrograph of two slip bands (1 and 2) which occurred nearly parallel to and at about 60° to an α-platelet boundary in the transformed-β. The area imaged occurred approximately 10 μm below the fatigue surface. B = close to $[1\bar{2}13]$, g = $[10\bar{1}1]$. The angle of the fatigue surface is indicated. See also Figures 6.41A and B and Table 6.8.

A

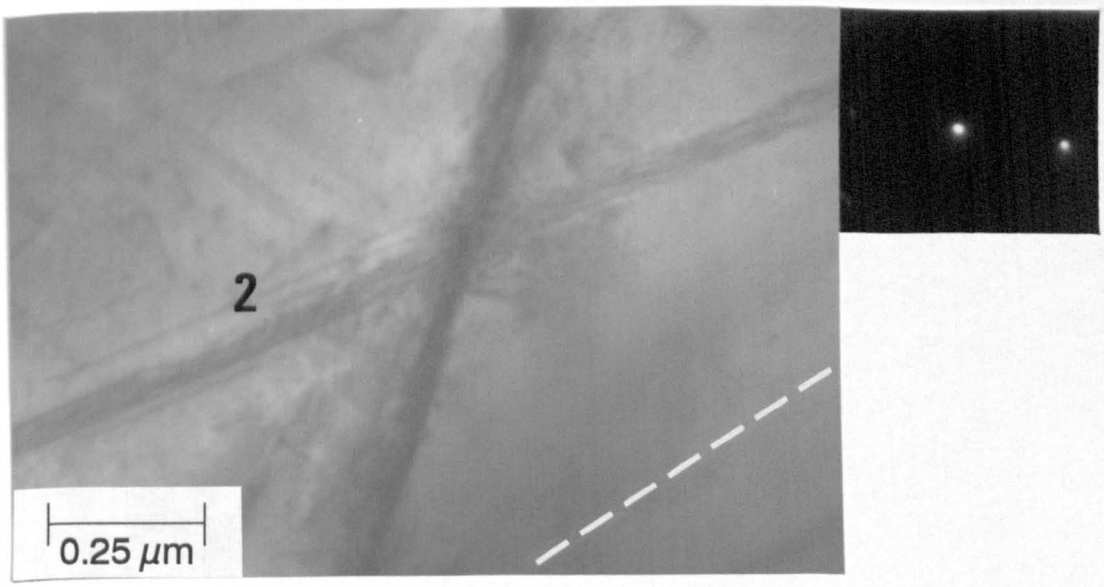

B

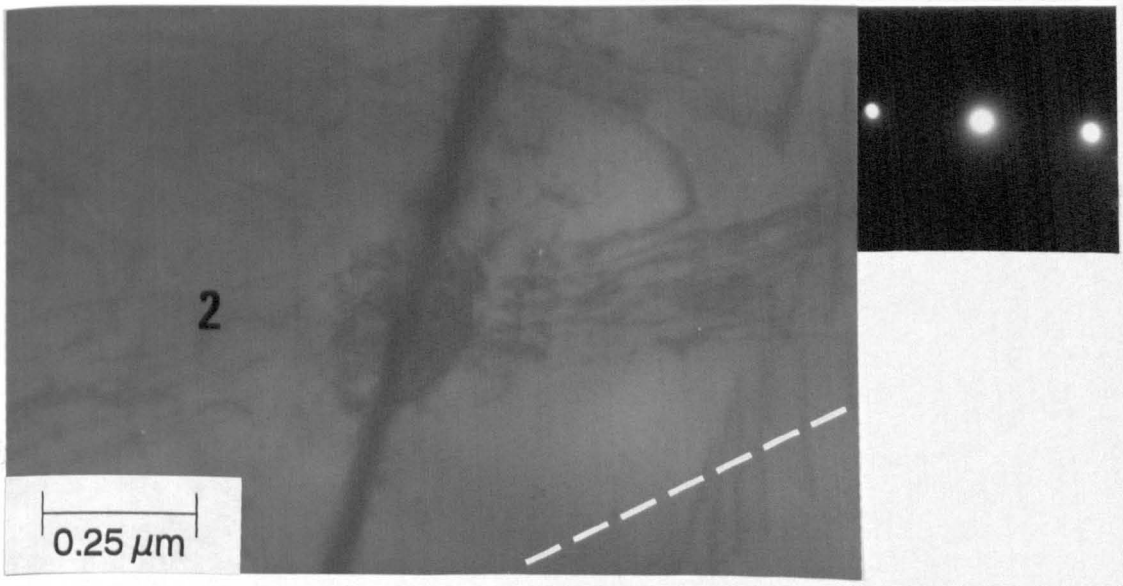

Figure 6.41 T.E.M. micrographs of the same area as that in Figure 6.40, taken under (A) B = close to [0001], g = [$10\bar{1}0$] and (B) B = close to [$2\bar{4}23$], g = [$10\bar{1}0$]. Note the accumulation of damage at the α-platelet boundary in Figure 6.41B. The angle of the fatigue surface is indicated. Table 6.8 lists the conditions under which this region was imaged.

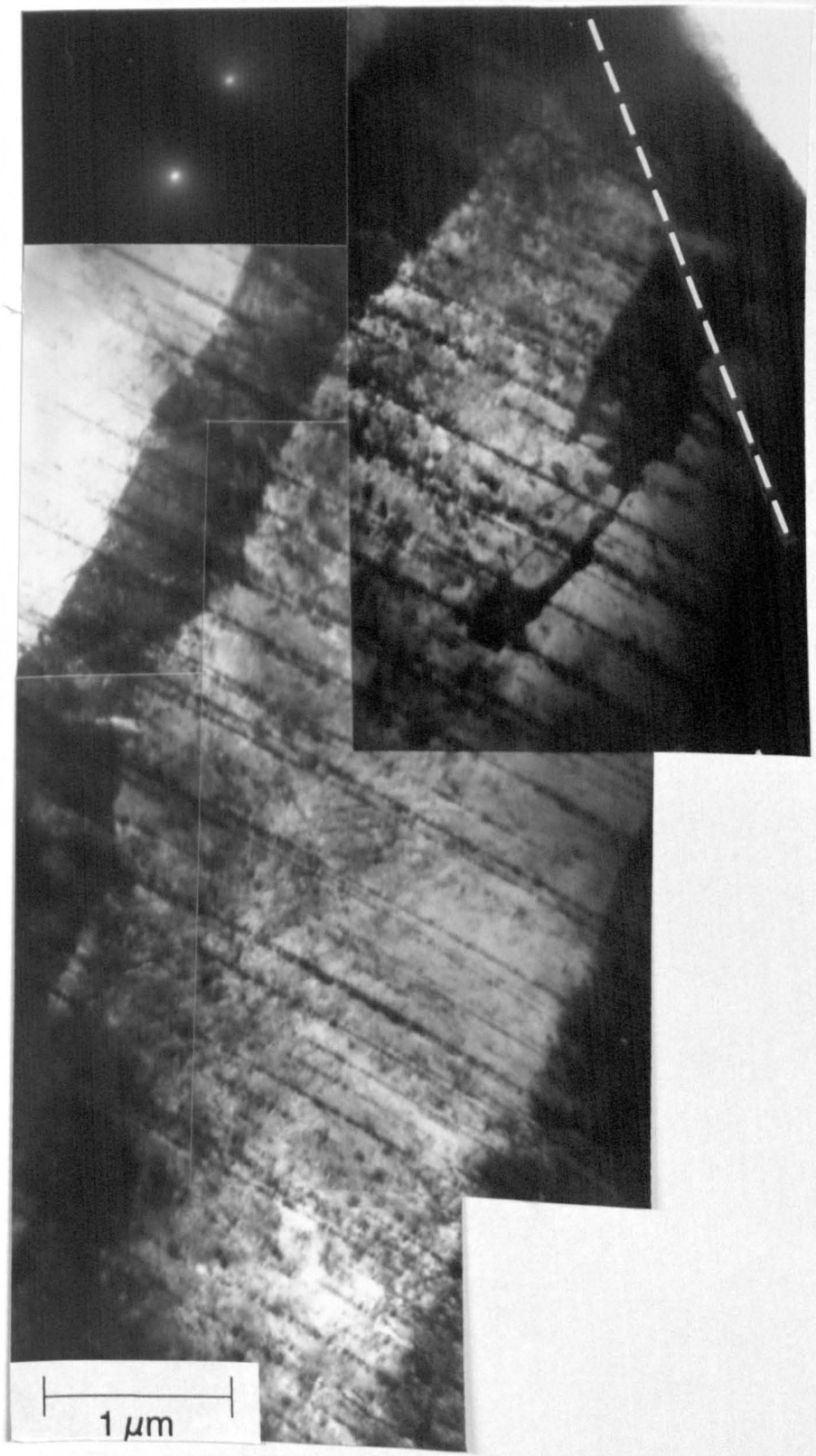

Figure 6.42 T.E.M. montage of basal slip in transformed-β which occurred at 45° to the fatigue surface. B = close to $[1\bar{2}10]$, $\underline{g}$ = [0002]. The angle of the fatigue surface is indicated.

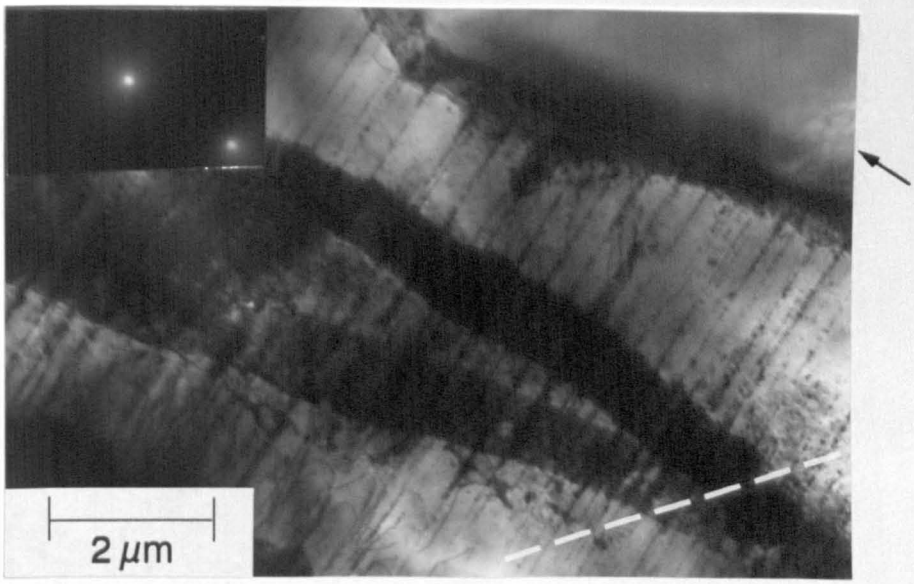

Figure 6.43 T.E.M. micrograph showing that the basal slip was arrested at the boundary between the transformed-β and an adjacent primary-α grain, arrowed. B = close to $[1\bar{2}10]$, g = [0002]. The angle of the fatigue surface is indicated.

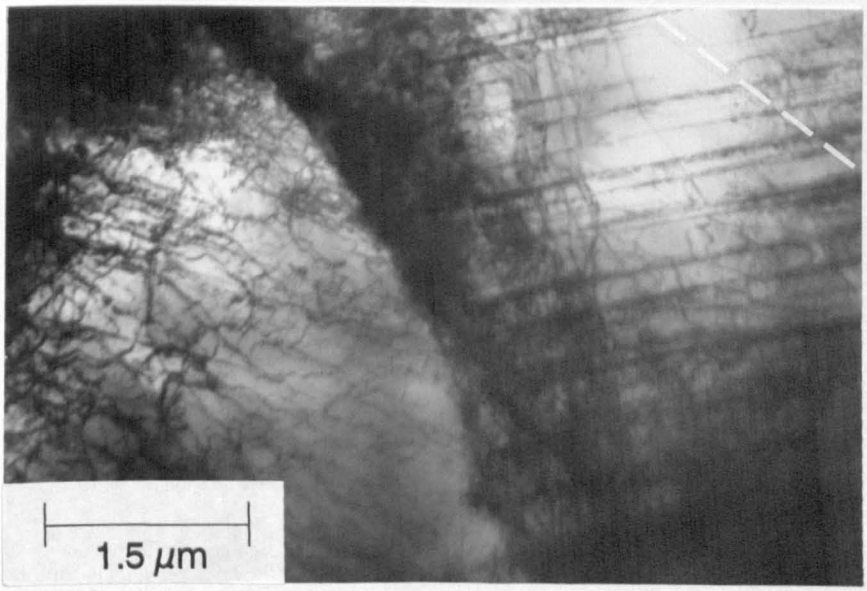

Figure 6.44 T.E.M. micrograph showing that a primary-α grain, which is adjacent to the transformed-β grain illustrated in Figures 6.43 and 6.44, contains a high dislocation density. Dislocations with Burgers vectors of the type $1/3\langle 11\bar{2}3\rangle$ are identified in the primary-α (see Figure 6.30A). The angle of fatigue surface is indicated.

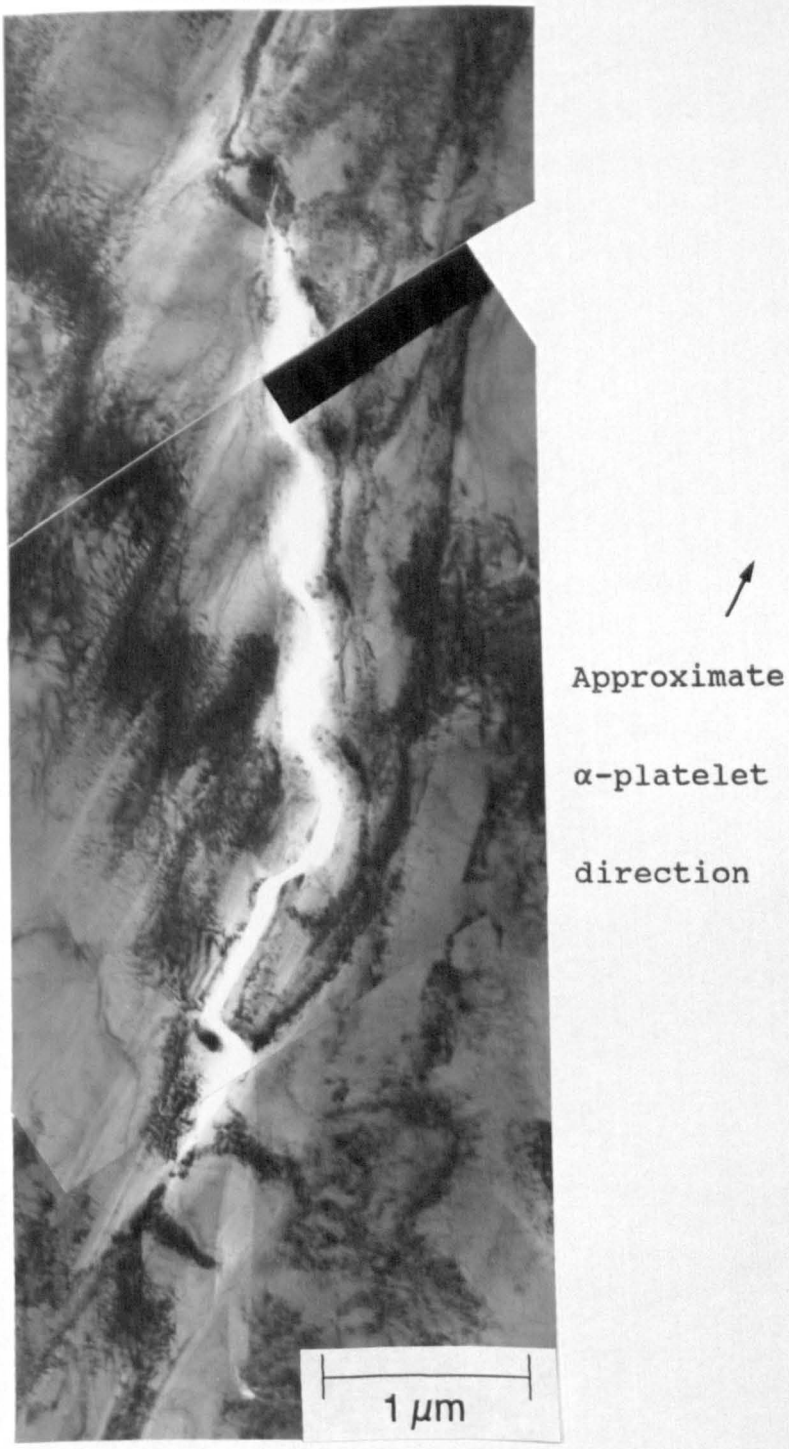

Figure 6.45 T.E.M. montage of cracking in a transformed-β grain in a back-thinned foil. The crack followed a zig-zag path along an α-platelet or colony boundary. The approximate α-platelet direction is arrowed, however, it is difficult to distinguish this due to the high amount of deformation associated with the cracking.

Figure 6.46 T.E.M. montage of crack in transformed-β showing damage associated with the crack in both the transformed-β and an adjacent primary-α grain (top). The microcrack is labelled with an arrow. Approximate α-platelet direction is also indicated.

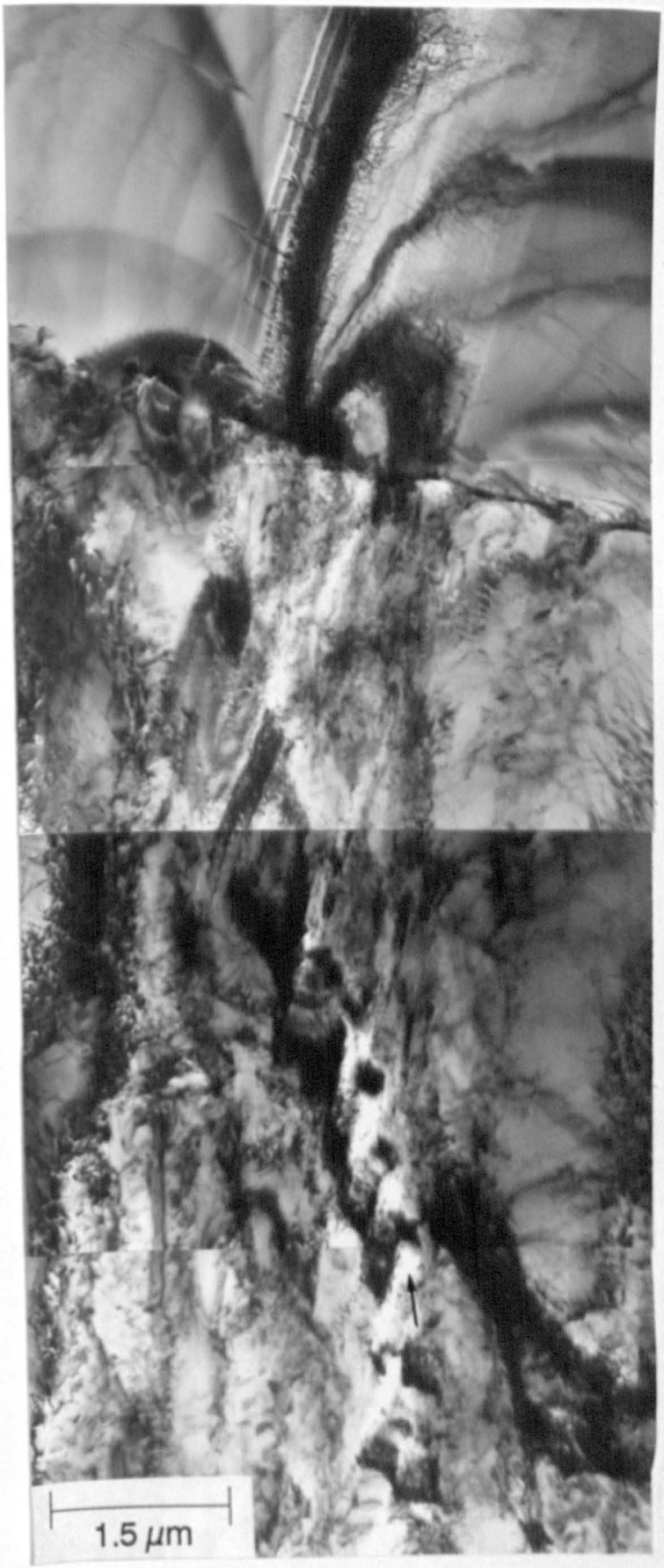
Primary-α
Approximate
α-platelet
direction
1.5 μm

Figure 6.47 T.E.M. montage taken from region ahead of the microcrack illustrated in Figure 6.46, this montage shows the variation in dislocation density associated with the plastic zone and adjacent transformed-β.

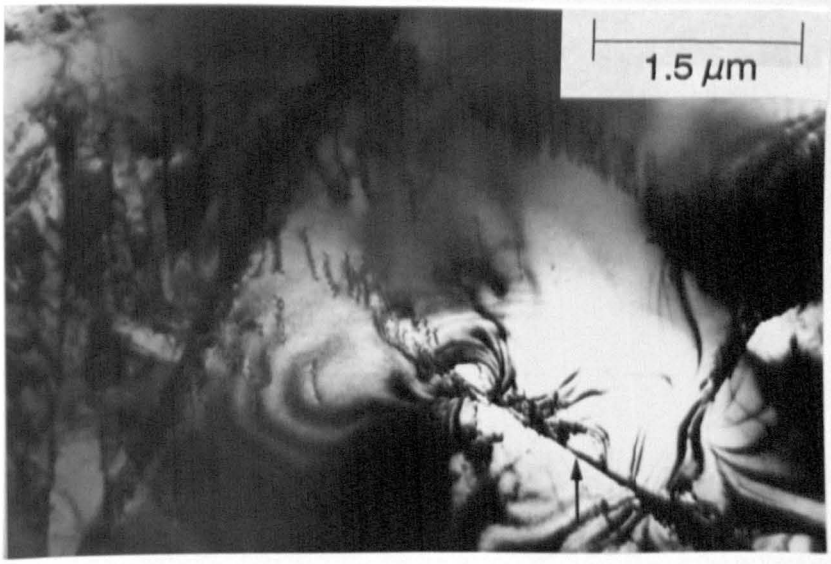

Figure 6.48 Low magnification T.E.M. micrograph from a back-thinned foil showing a crack (arrowed) in a primary-α grain and its position in relation to the nearby grain boundary and slip bands.

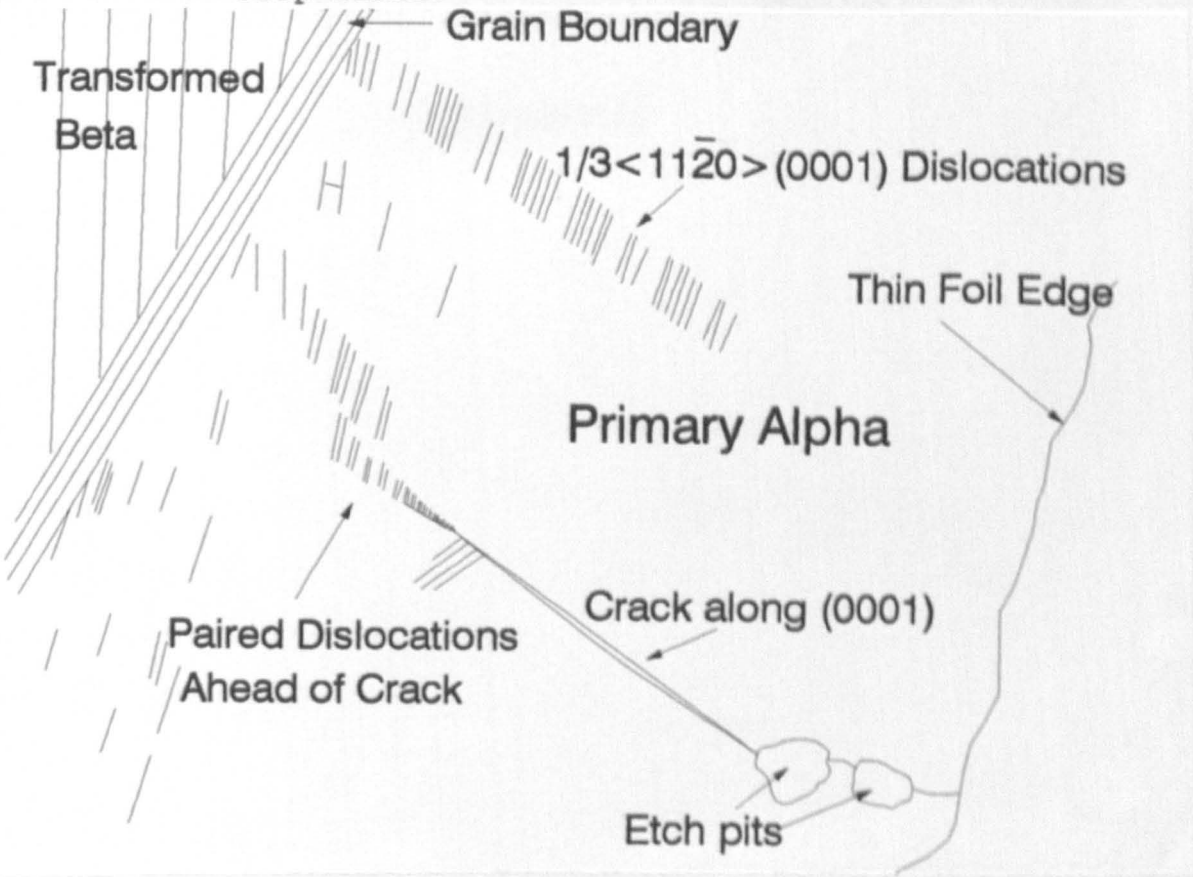

Figure 6.49 Sketch of Figure 6.48 illustrating the microstructure around the crack in the primary-α.

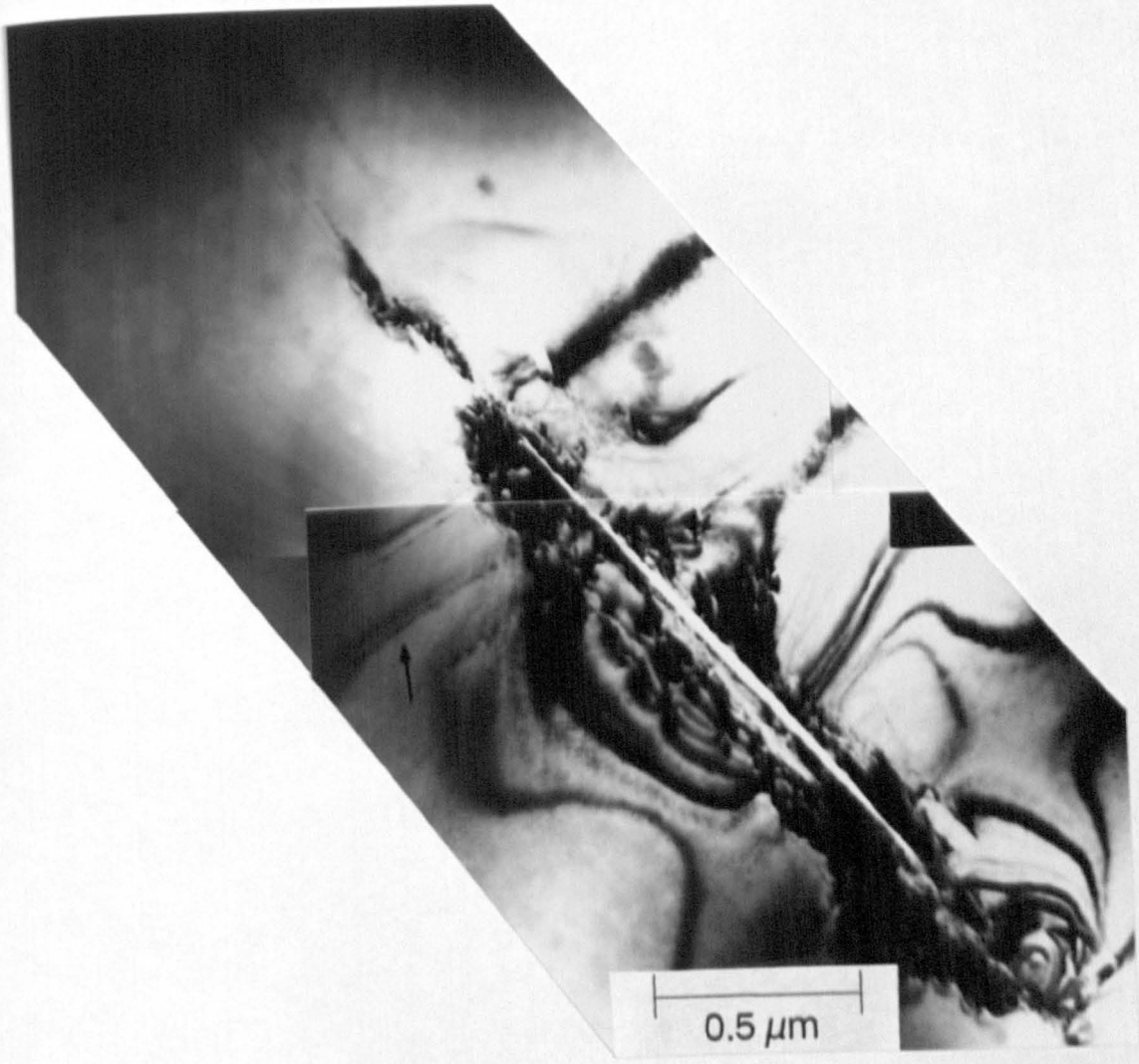

Figure 6.50 Low magnification T.E.M. micrograph of crack in primary-α grain. Note deformation at edge of crack and bands of dislocations (arrowed) near the crack tip, occurring at 90° to the direction of the crack.

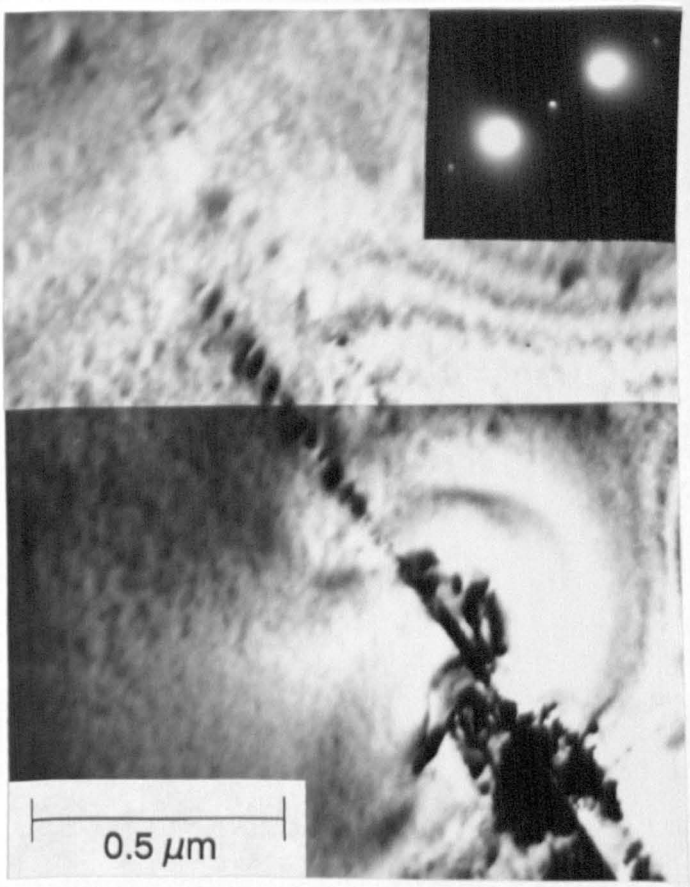

Figure 6.51 T.E.M. montage taken using B = close to [1$\bar{2}$10], g = [0002]. The dislocations ahead of the crack tip are out of contrast and occur at 90° to g = [0002] and are therefore <a> type dislocations on the basal plane.

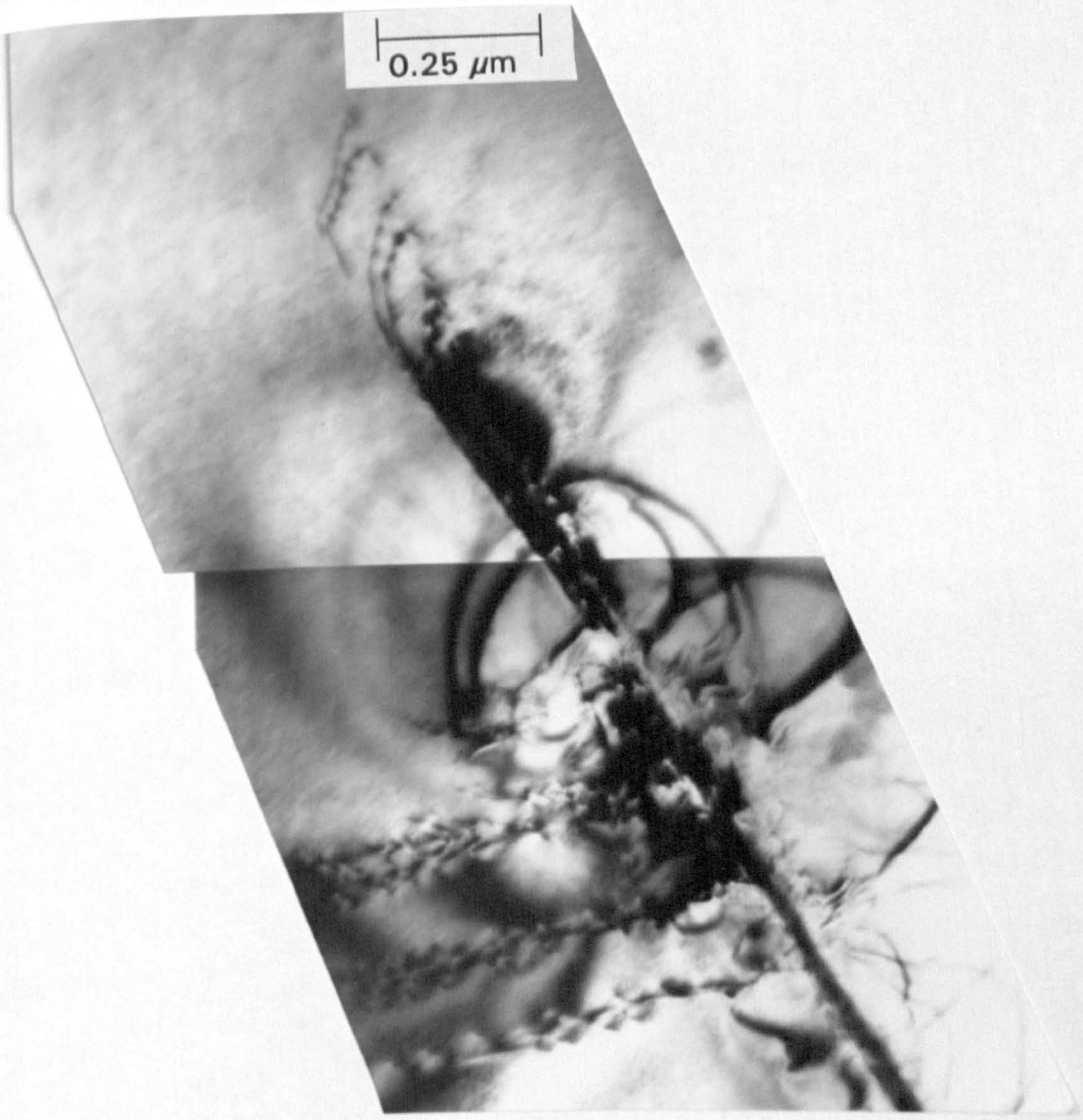

Figure 6.52 T.E.M. montage illustrating the strain around the crack tip highlighted by the thickness fringes. Note the paired dislocations on the basal slip plane ahead of the crack tip.

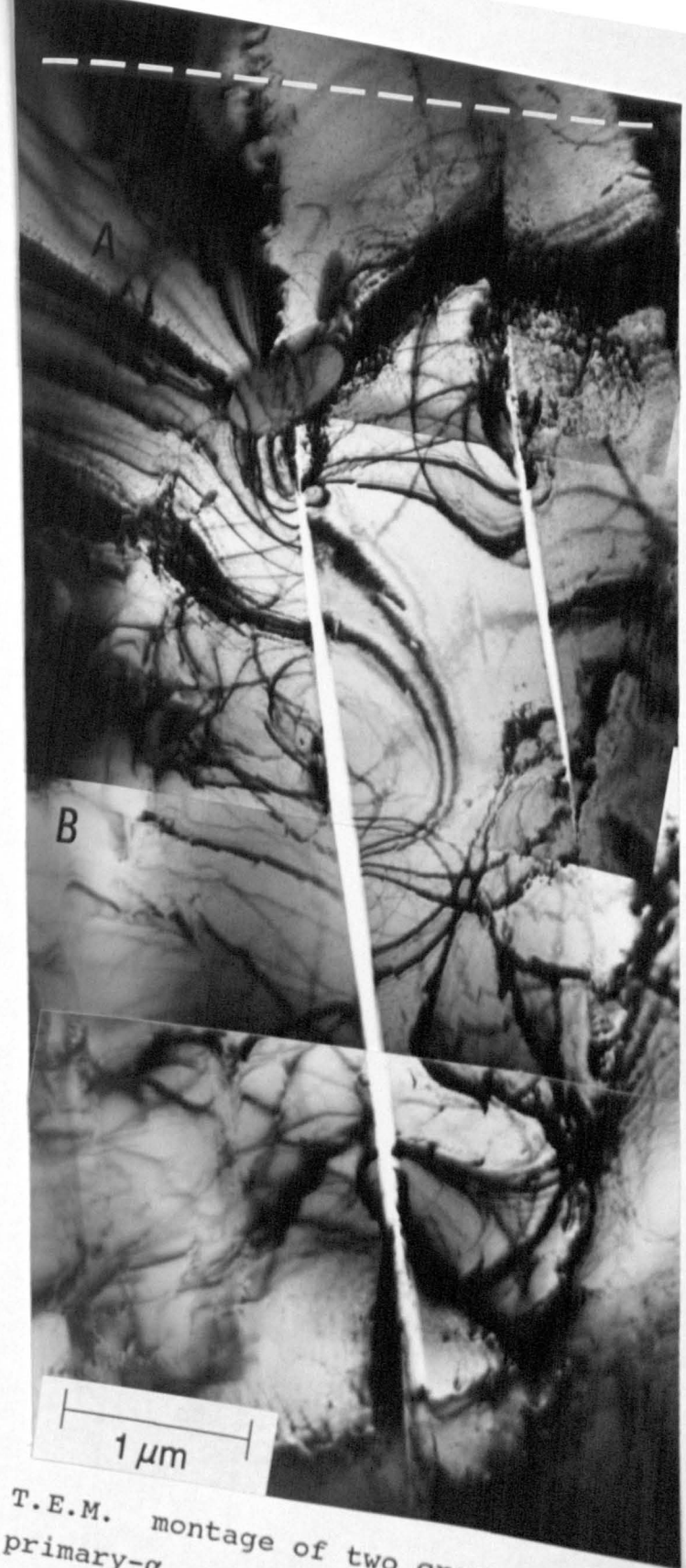

igure 6.53 T.E.M. montage of two cracks initiated in a primary-α grain about 15 μm below the fatigue surface. The cracks are parallel and the longer of the two is bounded by a particle at the tip closest to the fatigue surface.

A

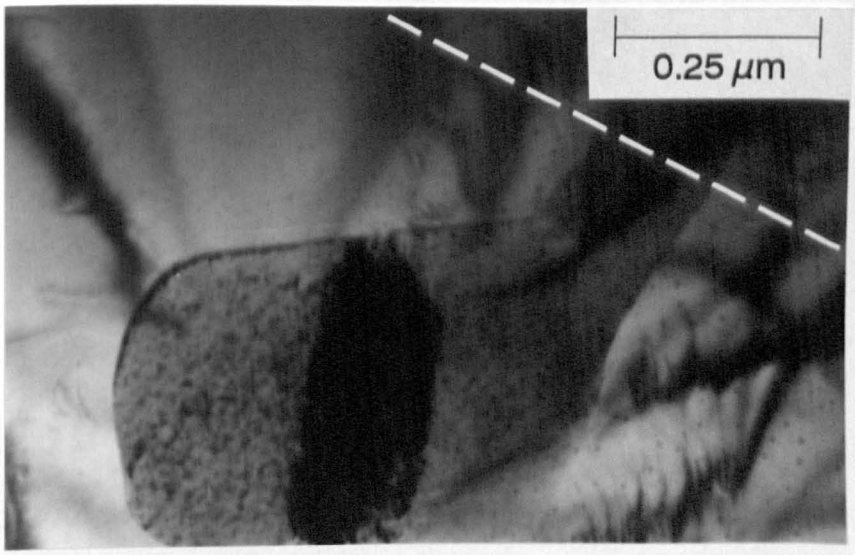

B

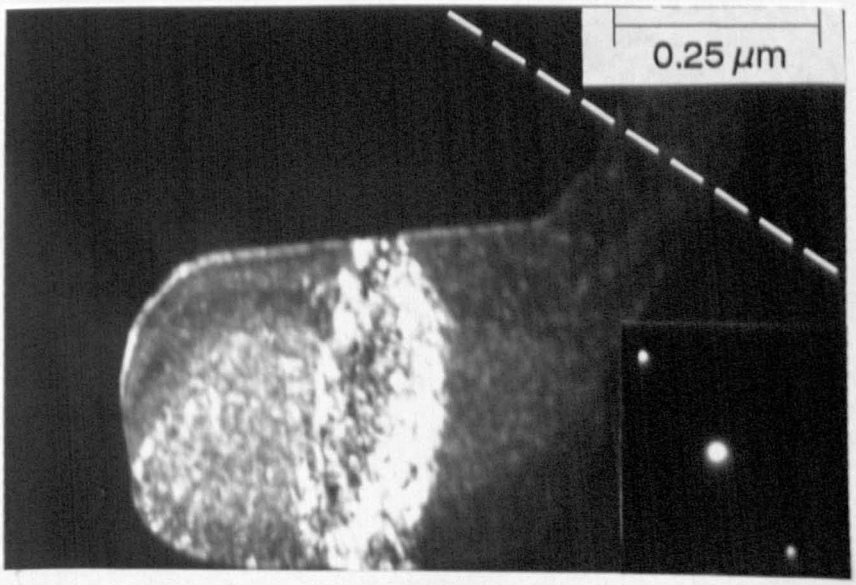

Figure 6.54 (A) Bright field micrograph, (B) dark field T.E.M. micrograph and corresponding diffraction pattern of the β particle. These micrographs show that a relatively high density of damage has occurred in the β-particle along a region which is parallel to the slip band and microcracking in the adjacent primary-α grains. $\underline{g} = [011]_{\beta}$. The angle of the fatigue surface is indicated.

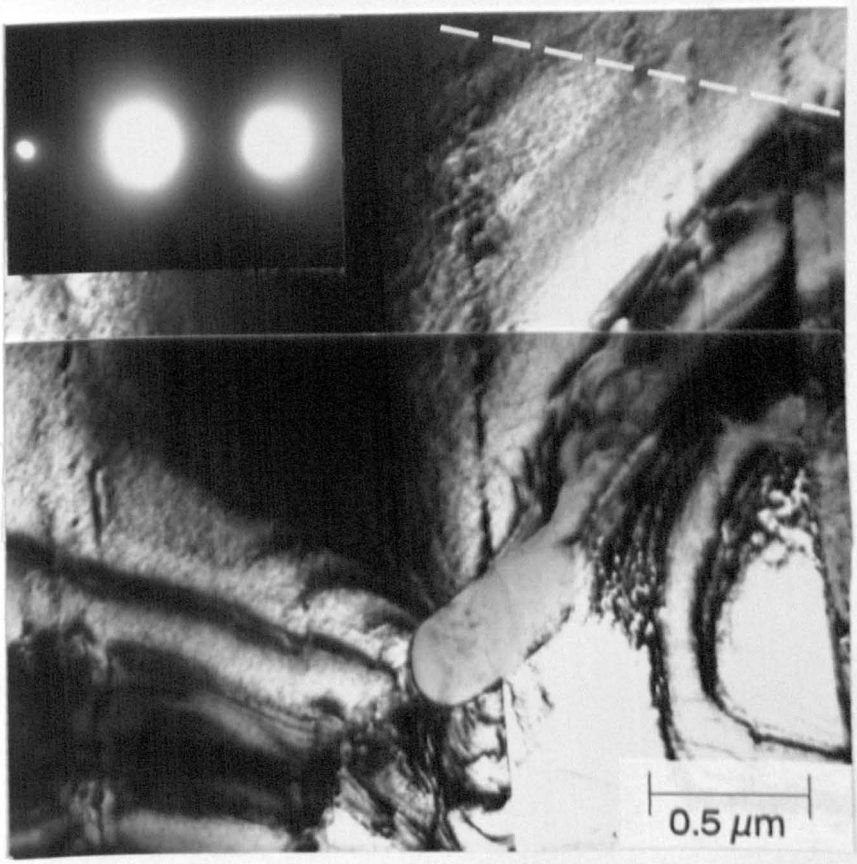

Figure 6.55 T.E.M. montage from which the slip bands in the primary-α grain adjacent to the β-particle were identified as basal slip. The microcrack in the adjacent primary-α is indicted and lies parallel to the basal slip. B = close to $[1\bar{2}10]$, g = [0002].

Figure 6.56 Dark field T.E.M. montage of crack tip furthest from fatigue surface. B = close to $[1\bar{2}12]$, $\underline{g} = [20\bar{2}0]$. The angle of the fatigue surface is indicated.

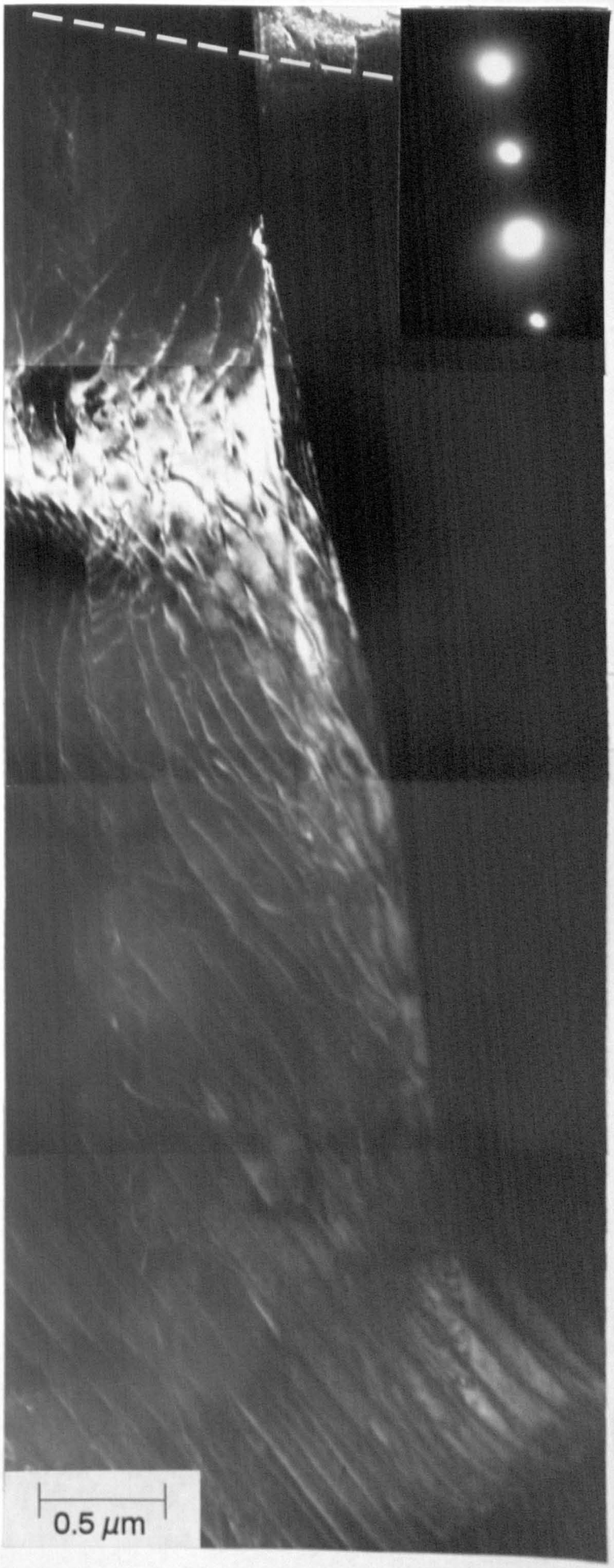
0.5 μm

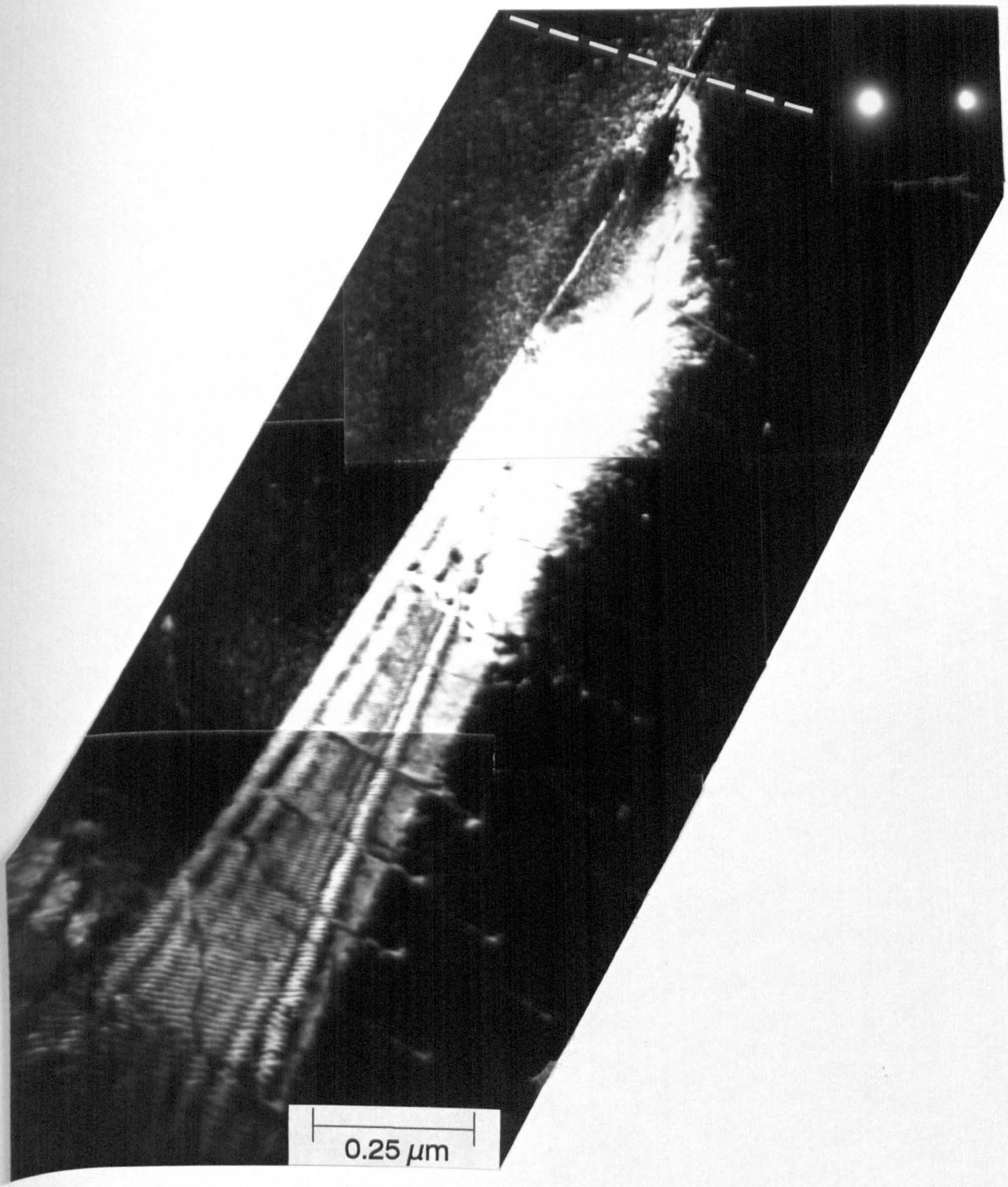

Figure 6.57 Dark field T.E.M. montage showing Moiré fringes which occurred ahead of the crack tip. B = close to $[0\bar{1}11]$, g = $[\bar{1}101]$. The angle of the fatigue surface is indicated.

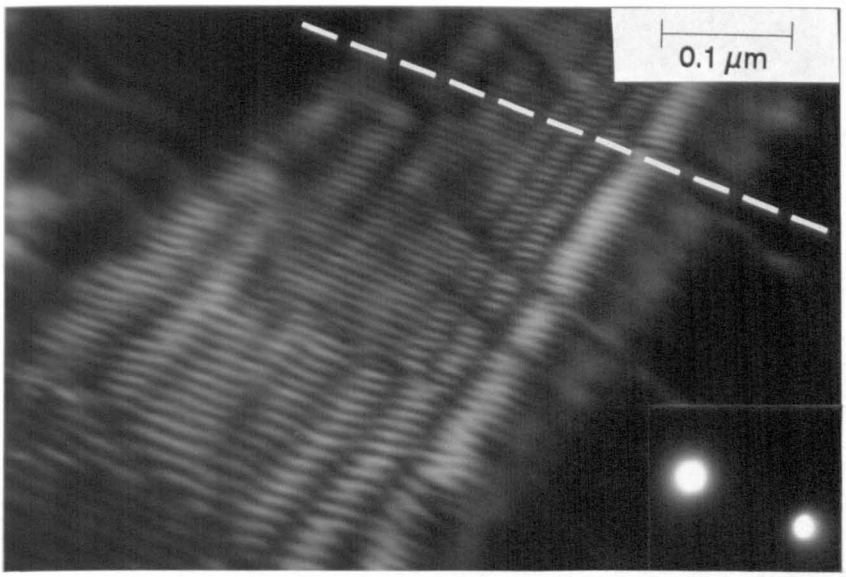

Figure 6.58 High magnification T.E.M. micrograph of the Moiré fringes shown in Figure 6.57. B = close to $[0\bar{1}11]$, g = $[\bar{1}101]$. The angle of the fatigue surface is indicated.

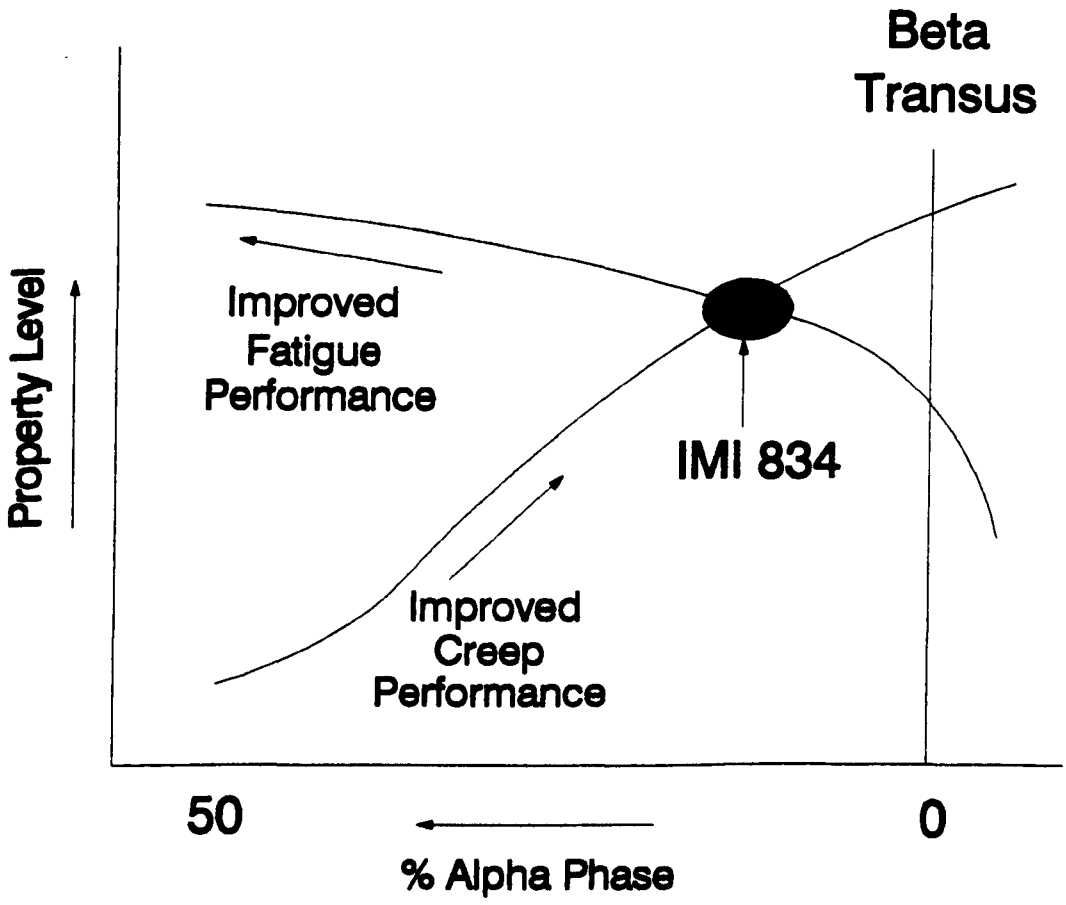

Figure 7.1 Effect of alpha and beta phase proportions on the creep and fatigue properties of IMI 834 (schematic) [9].

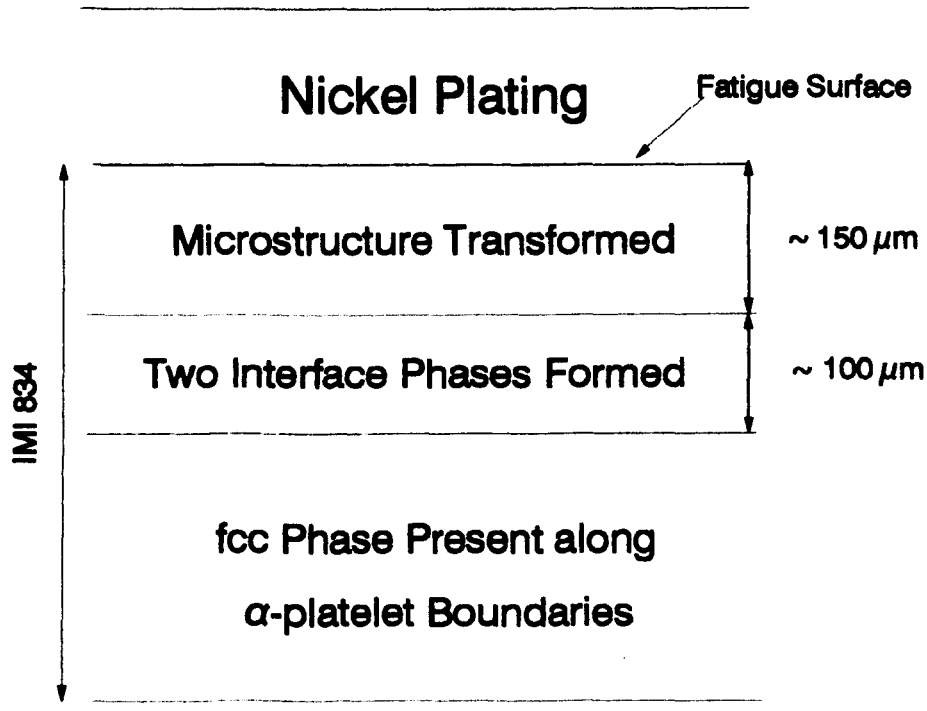

Figure 7.2 Schematic diagram illustrating the effect of the nickel plating process on the thin foil microstructure of IMI 834.

Figure 7.3 (A) Comparison of room temperature S-N data generated for IMI 834 by various workers [131, 190, 192, 204] with data from the present investigation. All specimens were solution treated at 1030°C for 2 hours prior to different cooling rates and ageing times listed below. The R ratios and frequencies used during testing are also listed.

Present; oil quench, 2 hrs 700°C, R = 0.1, f = 5.0 Hz
[204]; 350°C/min, 2 hrs 700°C, R = 0, f = 0.3 Hz
[192]; oil quench, 2 hrs 700°C, R = 0, f = 0.25 Hz
[190]; 450°C/min, 2 hrs 700°C, R = 0.1, f = 0.3 Hz
[131]; oil quench, 2 hrs 700°C, R = 0.1, f = 0.3 Hz

Figure 7.3 (B) Comparison of the S-N data as a function of the 0.2% proof stress. The 0.2% proof stress determined in each investigation was different.

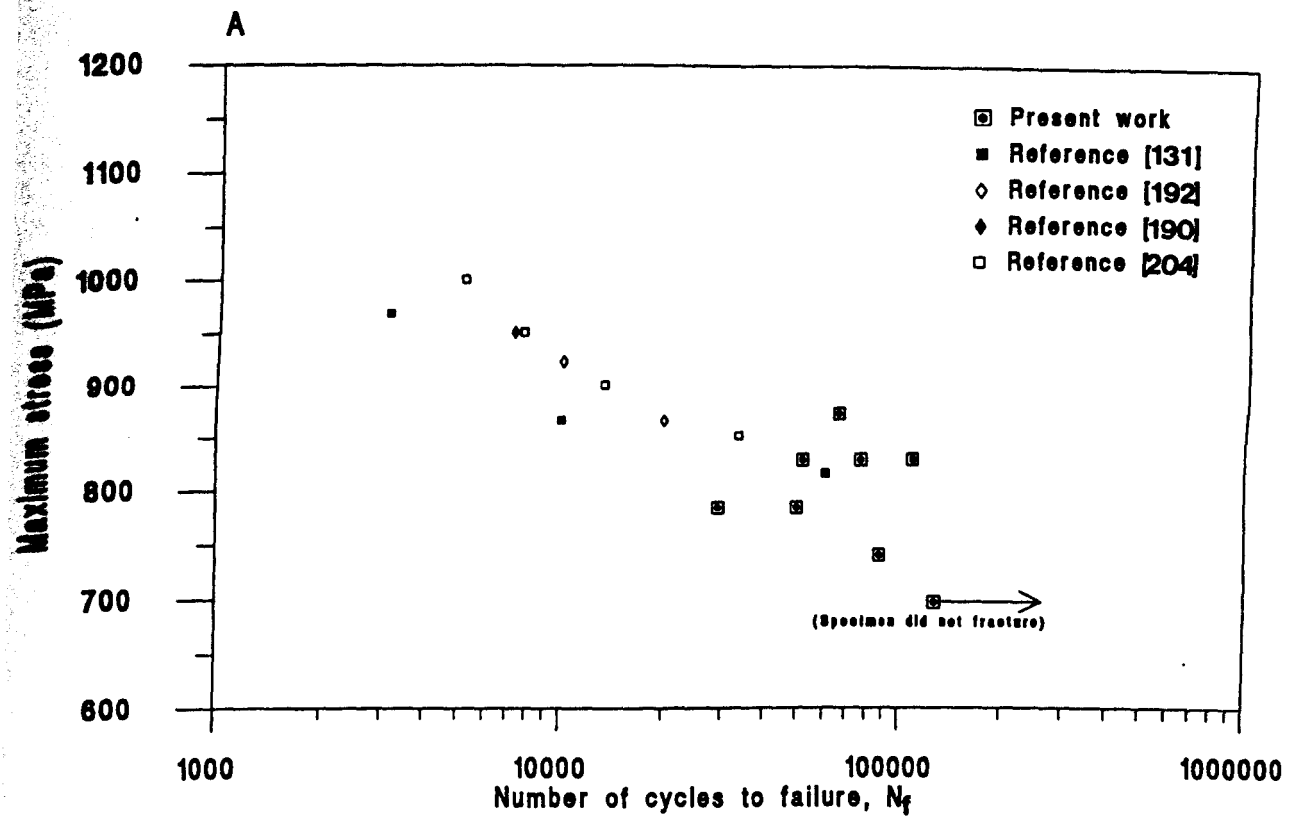
A
Maximum stress (MPa)
1200
1100
1000
900
800
700
600
1000
10000
100000
1000000
Number of cycles to failure, N_f
Present work
Reference [131]
Reference [192]
Reference [190]
Reference [204]
(Specimen did not fracture)

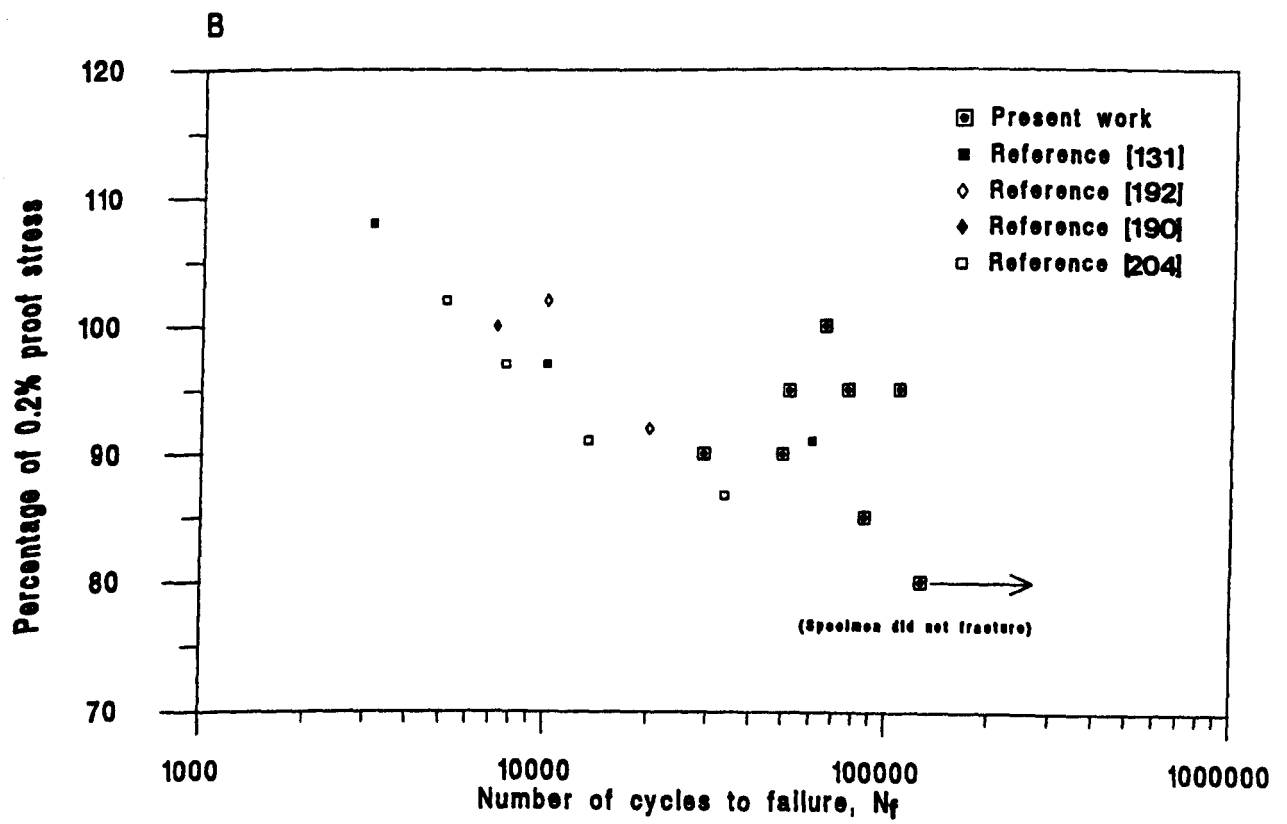
B
Percentage of 0.2% proof stress
120
110
100
90
80
70
1000
10000
100000
1000000
Number of cycles to failure, N_f
Present work
Reference [131]
Reference [192]
Reference [190]
Reference [204]
(Specimen did not fracture)

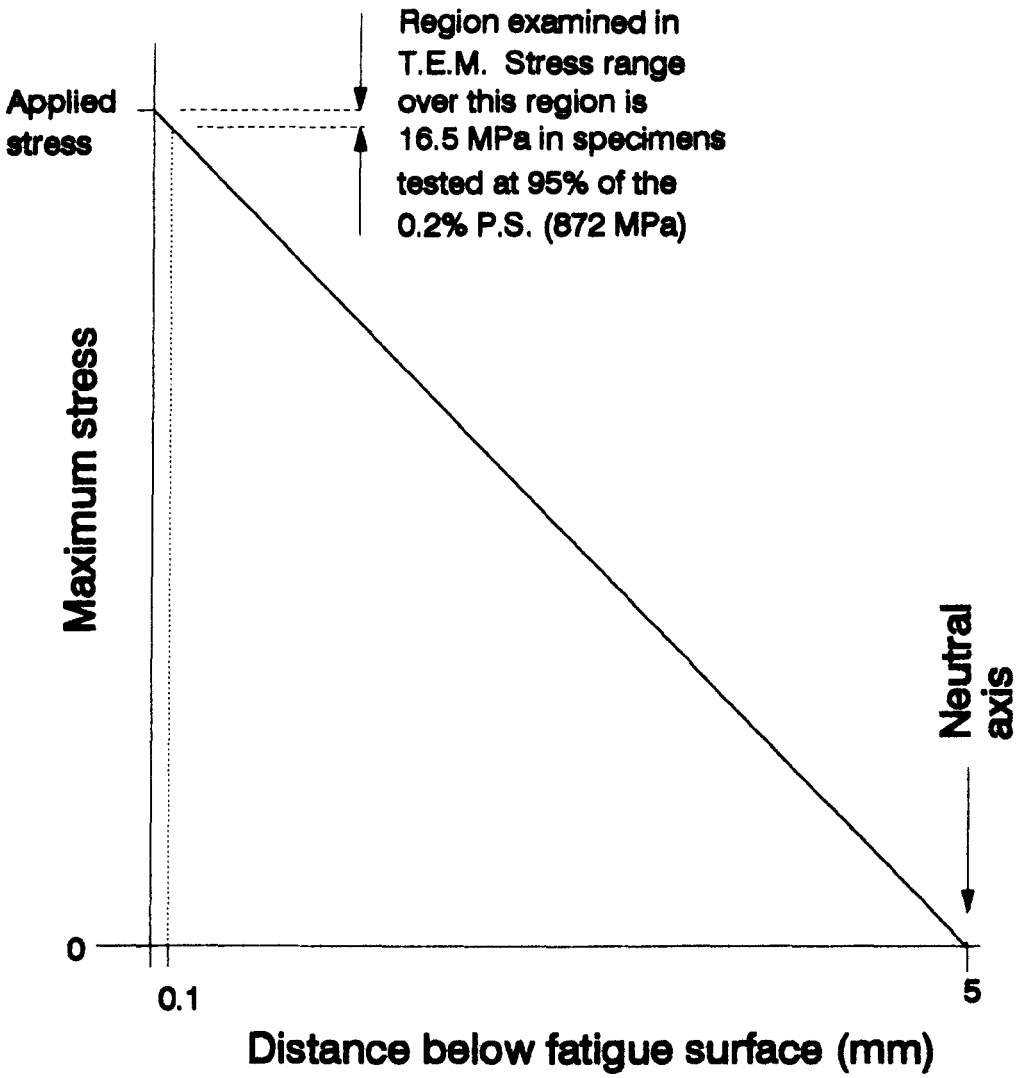

Figure 7.4 Stress profile through the specimen thickness illustrating the drop in stress that occurs over the area of interest in the present investigation (100 microns).

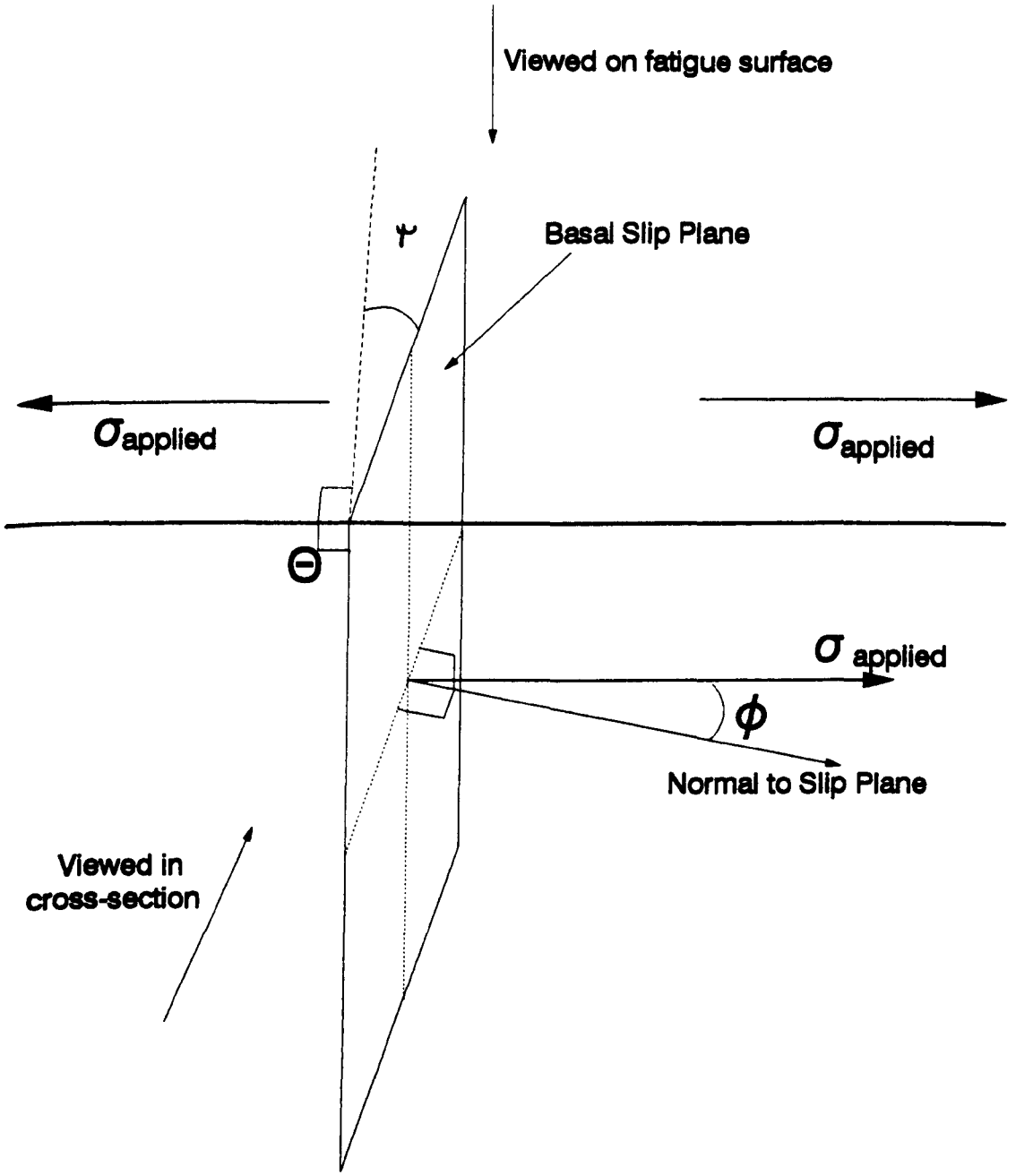

Figure 7.5 Schematic representation of the orientation of basal slip when Θ (the angle between the fatigue surface and the basal slip band) is close to 90°. Ψ = the angle between the normal to the applied stress direction and basal slip band on the fatigue surface. In this example the resolved tensile stress on the basal plane is high.

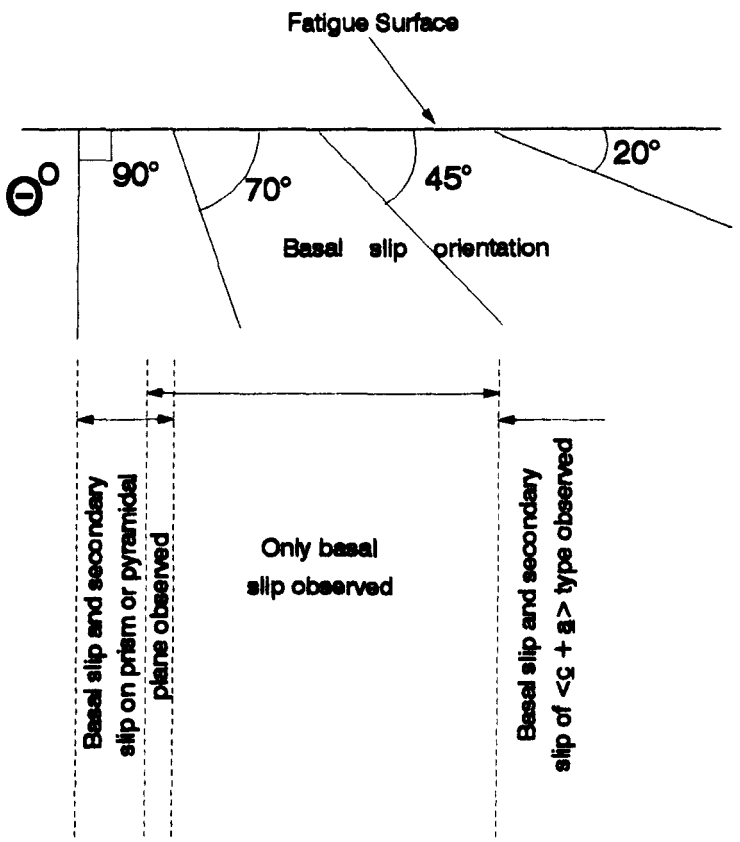

Figure 7.6 Basal slip orientation observed in primary-α grains in cross-sectional foils. The occurrence of secondary slip systems on the prismatic and pyramidal planes is also indicated.

Figure 7.7 Schematic diagram illustrating the suggested mechanism of fatigue crack initiation in IMI 834. (A) Two adjacent, similarly orientated primary-α grains are crossed by slip with a high resolved shear stress (*i.e.* θ = close to 45°). Crack initiation occurs at a sub-surface primary-α/transformed-β grain boundary. (B) Slip in a primary-α grain occurs at a high angle to the fatigue surface (*i.e.* θ = close to 90°), where the tensile shear stress acting to open up a crack along the slip band is high. Crack initiation is most likely to occur if a combination of (A) and (B) are present *i.e.* two adjacent primary-α grains, at or close to the fatigue surface are both orientated such that the angle of the basal slip is between 45° and 80° to the fatigue surface.

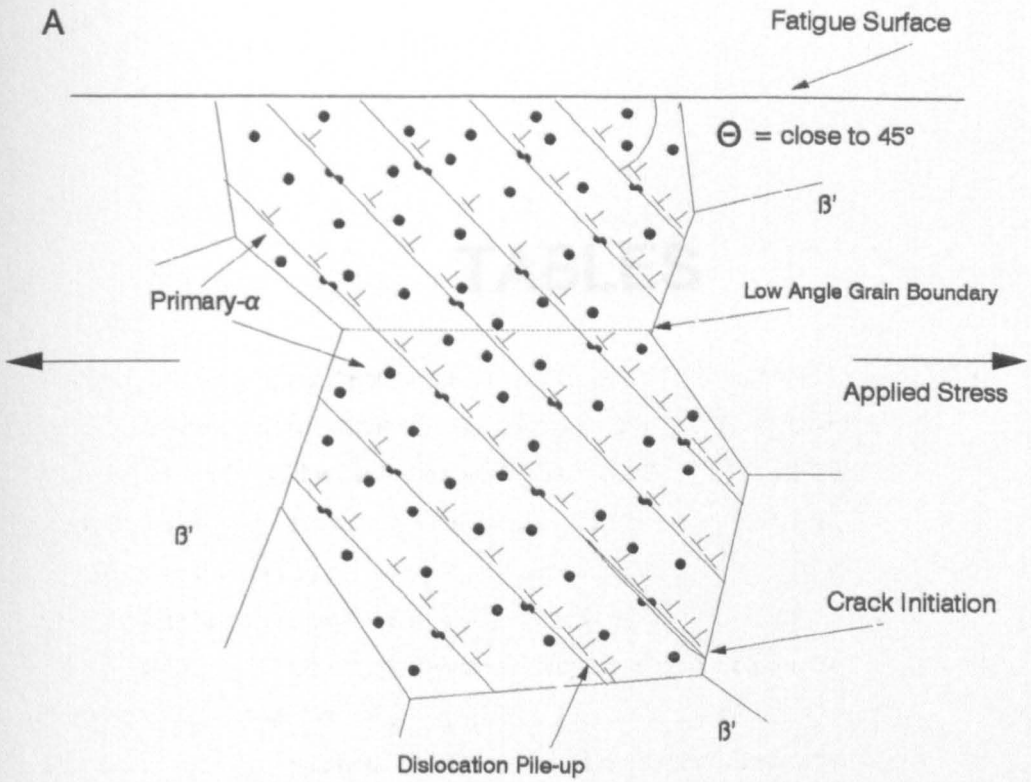
A
Fatigue Surface
Θ = close to 45°
β'
Primary-α
Low Angle Grain Boundary
Applied Stress
β'
Crack Initiation
β'
Dislocation Pile-up

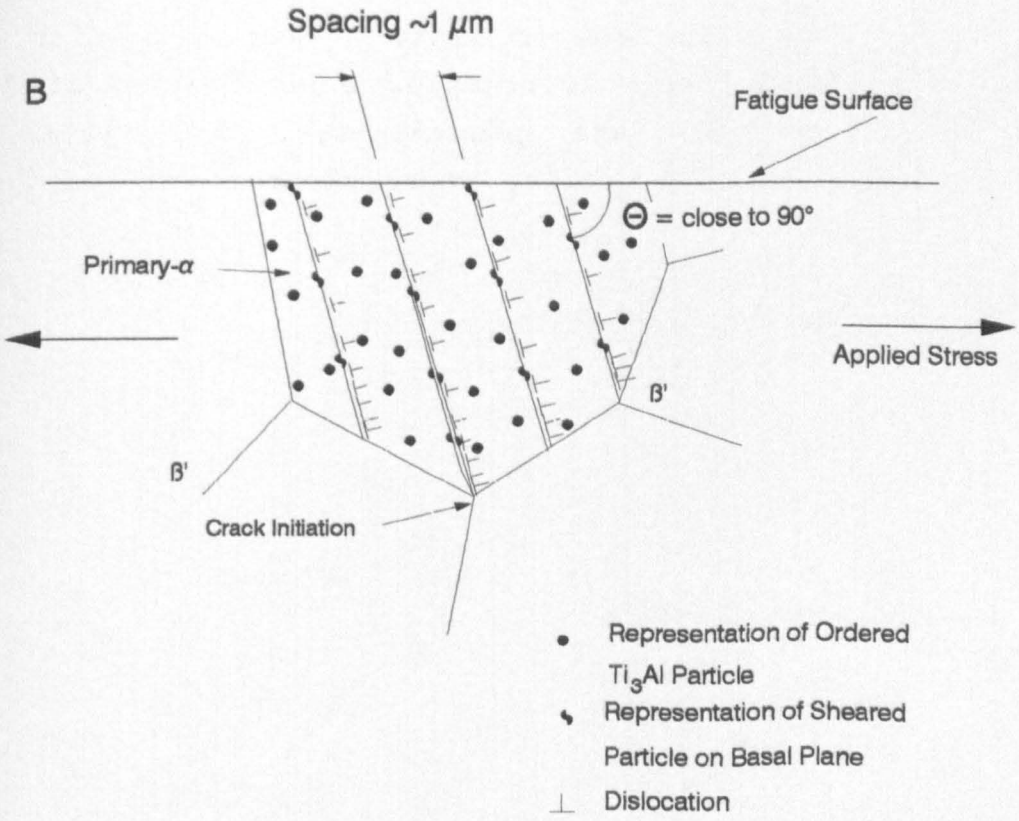
Spacing ~1 μm
B
Fatigue Surface
Θ = close to 90°
Primary-α
Applied Stress
β'
β'
Crack Initiation
Representation of Ordered
Ti3Al Particle
Representation of Sheared
Particle on Basal Plane
Dislocation

TABLES

Alloy Designation	IMI 318 Ti-6-4	IMI 550	IMI 551	Ti-6246	Ti-6242
Year of Introduction	1954	1958	1958	1966	1967
β-transus °C	995	975	1050	940	995
Maximum Temp. °C	325	400		450	450
wt% Al	6	4	4	6	6
wt% Sn	-	2	4	2	2
wt% Zr	-	-	-	4	4
wt% Mo	-	4	4	6	2
wt% Nb	-	-	-	-	-
wt% V	4	-	-	-	-
wt% Si	-	0.5	0.5	-	-
wt% C	-	-	-	-	-

Table 2.1 (A) Temperature range and chemical composition of high temperature α+β titanium alloys.

Alloy Designation	Ti-811	IMI 679	Ti-6242	IMI 685	Ti 6242S	IMI 829	Ti-1100	IMI 834
Year of Introduction	1958	1959	1967	1969	1974	1976	1980's	1983
β-transus °C	1038	954	995	1020	995	1020	1015	1045
Maximum Temp. °C	400	450	450	520	520	550	593	600
wt% Al	8	2.3	6	6	6	5.6	6	5.8
wt% Sn	-	11	2	-	2	3.5	2.75	4
wt% Zr	-	5	4	5	4	3	4	3.5
wt% Mo	1	1	2	0.5	2	0.25	0.4	0.5
wt% Nb	-	-	-	-	-	1	-	0.7
wt% V	1	-	-	-	-	-	-	-
wt% Si	-	0.2	-	0.25	0.1	0.3	0.45	0.35
wt% C	-	-	-	-	-	-	-	0.06

Table 2.1 (B) Temperature range and chemical composition of high temperature near-α titanium alloys.

Alloy Processing	Prior β grain size (μm)	Colony size (μm)	α-platelet size (μm)
α+β (980°C) Air Cool	5*	7	0.4
β (1052°C) Air Cool	300	3.7	0.4
β (1052°C) Controlled Air Cool	250	60	0.6
β (1052°C) Furnace Cool	370	120	1.2

* primary-α grain size

Table 2.2 The effect of cooling rate on the prior-β grain, colony and α-platelet sizes in Ti-6242-Si. Air cooling, controlled air cooling and furnace cooling were carried out at 10°C/s, 0.5°C/s and 0.1°C/s respectively. Taken from Cho *et al*. [39].

Ref.	a (nm)	Phase	Orientation Relationship(s)
73	0.426	M	$(0001)_\alpha // (110)_{fcc}; [11\bar{2}0]_\alpha // [111]_{fcc}$
75	0.433	M	$(0001)_\alpha // (001)_{fcc}; <11\bar{2}0>_\alpha // <110>_{fcc}$
71	0.436	M	$(0001)_\alpha // (111)_{fcc} // (110)_\beta;$ $<11\bar{2}0>_\alpha // <\bar{1}10>_{fcc} // <\bar{1}11>_\beta$
		S,hcp	$(10\bar{1}0)_\alpha // (1010)_p; <0001>_\alpha // <\bar{1}2\bar{1}3>_p$
70	0.426	M	$(0002)_\alpha // (111)_{fcc} // (110)_\beta;$ $[11\bar{2}0]_\alpha // [110]_{fcc} // [111]_\beta$
72	0.435	M	$[0001]_\alpha // [110]_\beta // [001]_{fcc};$ $(1\bar{2}10)_\alpha // (1\bar{1}\bar{1})_\beta // (\bar{1}10)_{fcc}$
		S	One variant obeyed the above relationship.
79	0.440	M	$(1\bar{1}0)_{fcc} // (1\bar{1}00)_\alpha; [001]_{fcc} // [0001]_\alpha$
80		S	$(111)_{fcc} // (0001)_\alpha; [1\bar{1}0]_{fcc} // [11\bar{2}0]_\alpha$
81	-	M	$(001)_{fcc} // (0001)_\alpha; [110]_{fcc} // [11\bar{2}0]_\alpha$
		S	$(111)_{fcc} // (0001)_\alpha; [110]_{fcc} // [11\bar{2}0]_\alpha$
		hcp	$\{10\bar{1}1\}$ twin related to α phase
82	0.434	S	-----
83	-	M	$(110)_{fcc} // (1\bar{1}00)_\alpha; [001]_{fcc} // [0001]_\alpha$
		S	$(111)_{fcc} // (0001)_\alpha; [1\bar{1}0]_{fcc} // [11\bar{2}0]_\alpha$
		hcp	$\{10\bar{1}1\}$ twin related to α phase
78	0.420	S	$\{111\}_{fcc} // (0001)_\alpha // \{110\}_\beta;$ $<110>_{fcc} // <1\bar{2}10>_\alpha // <111>_\beta$
84	0.425	S	$\{001\}_{fcc} // (0001)_\alpha // \{110\}_\beta;$ $<110>_{fcc} // <11\bar{2}0>_\alpha // <111>_\beta$
85	0.453	M	$(1\bar{1}0)_{fcc} // (1\bar{1}00)_\alpha // (1\bar{1}2)_\beta;$ $[001]_{fcc} // [0001]_\alpha // [1\bar{1}0]_\beta$ $[110]_{fcc} // [11\bar{2}0]_\alpha // [1\bar{1}\bar{1}]_\beta$
		S	$(111)_{fcc} // (0002)_\alpha // (110)_\beta;$ $[1\bar{1}0]_{fcc} // [11\bar{2}0]_\alpha // [1\bar{1}\bar{1}]_\beta$
86	0.430	M	$\{011\}_\beta // (0001)_\alpha // \{111\}_{ML} // \{111\}_{SL};$ $<11\bar{1}>_\beta // <1\bar{2}10>_\alpha // <10\bar{1}>_{ML} // <10\bar{1}>_{SL}$
		S	$\{011\}_\beta // (0001)_\alpha // \{001\}_{ML} // \{111\}_{SL};$ $<11\bar{1}>_\beta // <1\bar{2}10>_\alpha // <10\bar{1}>_{ML} // <10\bar{1}>_{SL}$

M = Monolithic Phase
S = Striated Phase
hcp = Hexagonal close packed structure

Table 2.3 Lattice parameters and orientation relationships suggested for the interface phases. Data was taken from the references indicated in the table.

Mechanical Properties	Microstructure	
	(α+β) processed (equiaxed)	β-processed (lenticular)
Tensile Strength	Good	Moderate
Ductility	High	Low
Creep Resistance	Low	High
Fracture Toughness	Low	High
F.C.I.R.*	High	Low
F.C.P.R.**	Low	High

* Fatigue Crack Initiation Resistance

** Fatigue Crack Propagation Resistance

Table 2.4 Comparison of the mechanical properties of near-α and α+β alloys [4, 32].

Cooling Rate (K/min)	UTS (MPa)	
	Room Temperature	510°C
1	905	585
37	985	665
400	1045	700
700	1055	760
2000	1245	925

Table 2.5 Effect of cooling rate on the tensile strength of a near-α alloy, Ti-6242-Si at room temperature and 510°C [99].

hcp metal	a (nm)	c (nm)	c/a*	ratio of interplanar spacings $(10\bar{1}0)/(0001)$
Cadmium	0.297	0.561	1.886	0.92
Zinc	0.266	0.494	1.856	0.94
--	--	--	1.732	1.00
Cobalt	0.250	0.406	1.623	1.06
Magnesium	0.320	0.520	1.623	1.07
Zirconium	0.323	0.515	1.593	1.09
Titanium	0.295	0.468	1.587	1.09
Beryllium	0.228	0.358	1.568	1.10

* measured at room temperature

Table 2.6 Lattice parameters, c/a ratios and interplanar spacings in some hcp metals [107].

Reference	Interstitial Content (wt%)	Slip Planes Identified	CRSS (kg/mm²)	Ratio of CRSS
Levine [124]	100 ppm*	{10$\bar{1}$0}	2.0	1.0
		(0001)	8.0	4.0
Churchman [109]	0.01 (O + N)	{10$\bar{1}$0}	2.1	1.0
		(0001)	6.3	3.0
		{10$\bar{1}$1}	-	-
Churchman [109]	0.1 (O + N)	{10$\bar{1}$0}	9.19	1.0
		(0001)	10.90	1.1
		{10$\bar{1}$1}	9.90	1.2
Rosi *et al.* [111]	0.06 to 0.09 (O + N)	{10$\bar{1}$0} -- {10$\bar{1}$1}	Prism slip Predominant	
Anderson *et al.* [112]	0.03 (O + N) 0.05 C	{10$\bar{1}$0} (0001) --	4.5 to 6.5** 10.9 to 13.5**	1.0 2.0
Williams & Eppelsheimer [110]		{10$\bar{1}$0} (0001) {10$\bar{1}$1}		1.12 1.10 1.00

* 50 ppm O, 25 ppm N and 40 ppm C analysed.

** Range of values obtained from crystals of different length and composition.

Table 2.7 Slip modes, critical resolved shear stresses (CRSS) and ratio of CRSS observed in commercial purity titanium of different interstitial contents. Data was taken from the references indicated in the table.

Alloy	Heat Treatment	% cycle life loss in dwell tests*	Al** Equiv.	Mo*** Equiv.
IMI 318	α + β	16	6.42	4.00
IMI 318	β	20	6.42	4.00
IMI 550	α + β	0	8.30	3.00
IMI 550	β	20	8.30	3.00
IMI 679	α + β	37	8.23	1.00
IMI 685	β	43	8.27	0.50
IMI 829	β	43	8.37	0.75
Ti-6242S	α + β	65	8.66	2.00
Exp. Alloy	α + β	75	9.17	0.85

* Dwell tests were carried out at 20°C and at the stress for each alloy which gave failure in 15000 cycles (about 95% of the 0.2% Proof Stress in each case).

** Al equivalent (wt%)

$Al^* = \%Al + \%Sn/3 + \%Zr/6 + 10(\%O + 2\%N + \%C)$

*** Mo equivalent (wt%)

$Mo^* = \%Mo + 3\%V/4 + \%Nb/2$

Table 2.8 Comparison by Neal [45] of the percentage loss in fatigue life of continuous fatigue tests versus tests with a two minute dwell on load. Alloys of different heat treatment and composition are compared with their aluminium (α-stabiliser) and molybdenum (β-stabiliser) equivalents [45]. Note; exp. alloy = an experimental alloy similar in Al* to IMI 834.

SPECIMEN NUMBER	A (%)	b_{ave} (mm)	d_{ave} (mm)	F_{max}* (kN)	F_{mean}* (kN)
TA1	80	9.980	9.963	13.16	7.24
TA6	85	10.002	9.980	14.06	7.74
TA3	90	10.003	9.999	14.96	8.23
TA5	90	10.010	10.006	14.98	8.24
TA4	95	10.018	9.989	15.77	8.68
TD2	95	9.991	10.007	15.78	8.69
TE2	95	10.022	9.989	15.77	8.68
TD3	95	9.994	10.004	15.77	8.68
TE3	95	9.999	10.023	15.84	8.71
TA2	100	10.039	9.991	16.64	9.15

* Calculated from the formulae given in section 3.2.2 and Appendix 2 using the measured value of the 0.2% P.S. for the tangential specimens of 872 x 10^6 N.

Table 3.1 Fatigue test data. F_{max} and F_{mean} values for tangential specimens of average breadth, b, and average depth, d. Parameters required for fatigue testing at A% of the 0.2% P.S. (872 x 10^6 N).

Surface	Fatigue	Fracture	Axial	Total	Percentage
Number of points in primary-α	520	495	494	1509	(16.77)
Number of points in trans.-β	2371	2380	2367	7118	(79.09)
Number in both α + β	109	125	139	373	(4.14)
Total in primary-α	574.5	557.5	563.5	1695.5	**18.84%**
Total in trans.-β	2425.5	2442.5	2436.5	7304.5	**81.16%**

Table 4.1 Table showing the point counting data which was used to calculate the volume fraction of the primary-α and the transformed-β phases. The number of points which occurred in the primary-α, transformed-β and on the boundary between these phases (both) was determined by counting 3000 points on each of the three orthogonal surfaces (denoted fatigue, fracture and axial). The number of points that fell at a boundary was halved and this number was added to the number counted in each of the phases to obtain the total number of points falling in each phase. Analysis of the ratios yielded the volume fraction of the primary-α and transformed-β phases.

{hkl}	{hkil}	d (nm)
{010}	$\{10\bar{1}0\}$	0.2555
{002}	{0002}	0.2343
{011}	$\{10\bar{1}1\}$	0.2244
{012}	$\{10\bar{1}2\}$	0.1727
{110}	$\{1\bar{2}10\}$	0.1475
{103}	$\{10\bar{1}3\}$	0.1333
{200}	$\{20\bar{2}0\}$	0.1278
{112}	$\{1\bar{2}12\}$	0.1248
{201}	$\{20\bar{2}1\}$	0.1233
{004}	{0004}	0.1172

Table 4.2 Planes and d spacings for α titanium, $\underline{a}$ = 0.2951 nm, $\underline{c}$ = 0.4686 nm.

{hkl}	d (nm)
{011}	0.2308
{002}	0.1632
{112}	0.1333
{022}	0.1154
{013}	0.1032
{222}	0.0942

Table 4.3 Planes and d spacings for the retained-β phase, $\underline{a}$ = 0.3264 nm.

{hkil}	2θ (degrees)	Relative Peak Intensity		
		Axial Surface	Fatigue Surface	Fracture Surface
$10\bar{1}0$	41.01	20.0	19.8	11.3
0002	44.92	4.8	15.0	18.8
$10\bar{1}1$	47.02	100.0	100.0	100.0
$10\bar{1}2$	62.44	21.4	12.5	5.6
$1\bar{2}10$	74.72	14.4	8.7	4.6
$10\bar{1}3$	84.37	16.8	18.8	6.2
$20\bar{2}0$	88.92	1.3	1.1	0.5
$1\bar{2}12$	91.65	11.3	10.8	8.0
$20\bar{2}1$	93.10	3.8	5.1	4.0
0004	99.59	0.3	1.8	1.2
011_β	45.65	-	-	1.1

Table 4.4 Relative intensities of X-ray peaks from the three orthogonal surfaces. The values are based on the intensity of the $\{10\bar{1}1\}_\alpha$ peak being set to 100 in each case. Cobalt radiation with $\lambda = 0.179021$ nm was used between $2\theta = 40°$ and $100°$.

{hkil}	Experimental d Spacings (nm)	Calculated d* Spacings (nm)
$10\bar{1}0$	0.609	0.609
$11\bar{2}0$		0.352
0001	0.336	0.360
$10\bar{1}1$	0.305	0.310
$20\bar{2}0$	0.300	0.304
$11\bar{2}1$	0.257	0.251
$20\bar{2}1$	0.238	0.232
$21\bar{3}0$		0.230
$30\bar{3}0$	0.203	0.234
$21\bar{3}1$	0.198	0.194
0002	0.168	0.180

* Assuming calculated lattice parameters $\underline{a}$ = 0.703 nm and $\underline{c}$ = 0.360 nm.

Table 4.5 Electron diffraction analysis of titanium-zirconium silicides in IMI 834. The experimental and calculated d spacings are listed with the corresponding {hkil} indices.

Foil Preparation Technique	State of Foil	Observed Effect in Thin Foil
Electropolished (section 3.3.5.1)	Fatigued & Unfatigued	No additional phases observed at the α-plate-let boundaries or across the α-platelet width.
Back-thinned (section 3.3.5.2)	Fatigued & Unfatigued	
Dimpled + Electropolished (section 3.3.5.4)	Unfatigued	No additional phases observed in the thin foils.
Dimpled + Ion-beam Milled (section 3.3.5.4)	Unfatigued	A phase of 0.1 to 0.5 μm wide was observed along some of the α-platelet boundaries.
Electropolished + Ion-beam Milled (section 3.3.5.4)	Unfatigued	A phase of 0.1 to 0.5 μm wide was observed along some of the α-platelet boundaries.
Cross-sectional Foils (Ni plated) (section 3.3.5.3)	Fatigued	A phase was observed at the boundaries of the α-platelets. A second phase was also observed as acicular bands about 0.1 μm wide across the width of the α-platelets in some regions.

Table 5.1 Comparison of the effects of foil preparation techniques on the occurrence of phases at the α-platelet boundaries in the thin foil microstructure of IMI 834.

{hkl}	d (nm)
{111}	0.251
{002}	0.217
{022}	0.153
{113}	0.131
{222}	0.125
{004}	0.109
{331}	0.100
{420}	0.097

Table 5.2 Planes and d spacings for the fcc interface phase. Lattice parameter, $\underline{a}$ = 0.434 nm.

Specimen Number	0.2% P.S. (MPa)	U.T.S. (MPa)	E* (GPa)
TD1	872	992	117
TC7	872	994	116
TC13	927	1056	120
OR11B	880	1003	118
IR5B	880	1012	114

* Young's Modulus, calculated from the gradient of the stress-strain curves. $E_{average}$ = 117 GPa.

Table 6.1 Values of the 0.2% proof stress (P.S.), ultimate tensile strength (U.T.S.) and Young's modulus, E, obtained from tensile test specimens taken from tangential and radial positions in the compressor disc section.

Specimen Number	% P.S	σ_{max} (MPa)	Fatigue Lifetime N_f, at 5 Hz
TA1	80	698	126880*
TA6	85	741	86543
TA3	90	785	29040
TA5	90	785	49308
TA4	95	828	76290
TD2	95	828	108300
TD3	95	828	51500
TA2	100	872	65500

* Specimen did not fail.

Table 6.2 Fatigue lifetime/number of cycles to failure, N_f, of tangential specimens tested between 80 and 100% of the 0.2% P.S.

Specimen Number	Percent of 0.2% P.S.	$\Delta\sigma$ (MPa) (Eqn. 6.2)	a (mm)*	ΔK ($MPam^{1/2}$)
TA6	85	393.4	2.05	31.6
TA3	90	381.4	2.30	32.4
TA5	90	346.1	2.55	31.0
TD2	95	298.2	3.00	28.9
TA4	95	328.0	2.80	30.8
TE2	95	447.3	2.00	35.5

* a = the crack depth at which the transition occurred.

Table 6.3 Determination of ΔK for the transition from a facetted fracture surface to a ductile surface appearance for specimens in which the fatal crack initiated at a non-corner site on the fatigue surface of the test piece. A value of $Y = 1$ was used in equation 6.1 for the determination of ΔK. $\Delta\sigma$ was calculated according to equation 6.2.

Zone (B) Close to	Band Width (μm)	g Vector	Dislocation Contrast* A	B	C	Figure Number	φ°**
[0001]	1.05	$[10\bar{1}0]$	1	0	1	-	-
[0001]	1.05	$[2\bar{1}\bar{1}0]$	1	1	1	6.19B	-
[0001]	1.05	$[\bar{1}100]$	0	1	1	-	-
[0001]	1.05	$[1\bar{2}10]$	1	1	1	6.20A	-10
[0001]	1.05	$[01\bar{1}0]$	1	1	0	-	-
$[0\bar{1}12]$	0.95	$[\bar{2}110]$	1	1	1	6.20B	49
$[1\bar{2}13]$	0.90	$[01\bar{1}1]$	1	1	0	6.20C	-37
$[1\bar{2}13]$	0.90	$[1\bar{1}0\bar{1}]$	0	1	1	6.20D	15
$[1\bar{2}13]$	0.90	$[10\bar{1}0]$	1	0	1	6.20E	-
$[2\bar{4}23]$	0.63	$[10\bar{1}0]$	1	0	1	-	-
$[2\bar{4}23]$	0.63	$[01\bar{1}2]$	1	1	0	-	-
$[2\bar{4}23]$	0.63	$[\bar{1}102]$	0	1	1	6.20F	6

* Dislocations in contrast = 1
Invisible dislocations = 0

** ϕ = angle between $\underline{g}$ and u′, the projected direction of the dislocation marked B, in Figures 6.20A-D and 6.20F (see Figure 6.21). + = clockwise, - = anticlockwise.

Table 6.4 Beam directions, B, corresponding widths of slip band, $\underline{g}$ vectors and contrast of dislocations A, B and C, used to determine the slip plane and Burgers vectors of dislocations of the slip band in Figures 6.19B and 6.20A to 6.20F.

Zone (B) Close to	Band Width (μm) Band 1	Band 2	g Vector	Figure Number	ϕ_1°*	ϕ_2°*
$[1\bar{2}10]$	0.05	0.42	$[\bar{1}011]$	6.24	-72	-28
$[2\bar{4}23]$	0.25	0.26	$[11\bar{2}2]$	-	0	44
$[1\bar{2}13]$	0.40	0.08	$[10\bar{1}0]$	6.26A	-36	8
$[0\bar{1}12]$	0.43	0.05	$[2\bar{1}\bar{1}0]$	6.26B	-56	-20
$[1\bar{1}01]$	0.33	0.25	$[11\bar{2}0]$	-	-27	20
$[1\bar{1}00]$	0.02	0.50	$[11\bar{2}0]$	6.26C	-42	0

* ϕ = angle between g and u', the projected direction of slip bands 1 and 2 (see Figures 6.27 and 6.28A to C)
+ = clockwise rotation - = anticlockwise rotation

Table 6.5 Beam directions, B, corresponding widths of slip bands and g vectors used to determine the planes of slip bands marked 1 and 2 in Figures 6.25 and 6.26A to 6.26C. See stereographic projections, Figures 6.27 and 6.28A to C for determination of the slip planes (1 and 2) by trace analysis. Band 1 was activated at 90° to the fatigue surface and band 2 was activated at 40° to the fatigue surface.

Zone (B) Close to	Band Width (μm) Band 1	Band 2	g Vector	Figure Number
$[1\bar{2}10]$	0.0	-	[0002]	-
$[1\bar{2}10]$	0.1	0.4	$[\bar{1}01\bar{1}]$	-
$[1\bar{2}13]$	0.4	0.3	$[011\bar{1}]$	-
$[1\bar{1}01]$	0.35	0.20	$[11\bar{2}0]$	-
$[2\bar{2}01]$	0.2	0.25	$[11\bar{2}0]$	-
$[1\bar{1}00]$	0.1	0.25	$[11\bar{2}0]$	6.29

Table 6.6 Beam directions, B, corresponding widths of slip bands and g vectors used to determine the planes of the slip bands in Figure 6.29.

Closest Zone*	° from (0001)	° from $\{11\bar{2}0\}$	° from $\{10\bar{1}0\}$	Number of Grains with this Orientation Analysed
(0001)	0	90.0	90.0	0
$\{1\bar{2}16\}$	27.9	62.1	74.3	0
$\{10\bar{1}4\}$	24.6	68.9	65.4	0
$\{10\bar{1}2\}$	42.5	54.2	47.5	1
$\{1\bar{2}13\}$	46.6	43.4	51.0	8
$\{4\bar{5}16\}$	54.5	39.7	36.9	0
$\{10\bar{1}1\}$	61.4	40.5	28.6	5
$\{2\bar{4}23\}$	64.7	25.3	38.4	0
$\{1\bar{5}43\}$	70.3	22.4	44.6	2
$\{1\bar{2}11\}$	72.5	17.5	34.5	1
$\{20\bar{2}1\}$	75.0	33.3	15.0	1
$\{5\bar{7}23\}$	75.0	15.8	44.4	2
$\{30\bar{3}1\}$	79.7	31.6	10.3	1
$\{11\bar{2}0\}$	90.0	0.0	30.0	7
$\{10\bar{1}0\}$	90.0	30.0	0.0	4

* Orientation within 5° of the specified closest zone.

Table 6.7 Orientations of grains close to the fatigue surfaces of cross-sectional thin foils analysed at 0° tilt. See also Figure 6.36.

Zone (B) Close to	Width of Band, Y, at 60° to Boundary	g Vector	Figure Number
$[\bar{1}2\bar{1}6]$	0.088 μm	$[10\bar{1}0]$	-
[0001]	0.040 μm	$[10\bar{1}0]$	6.41A
$[1\bar{2}16]$	0.082 μm	$[10\bar{1}0]$	-
$[1\bar{2}13]$	0.130 μm	$[10\bar{1}0]$	-
$[1\bar{2}13]$	0.160 μm	$[10\bar{1}1]$	6.40
$[2\bar{4}23]$	0.210 μm	$[10\bar{1}0]$	6.41B

Table 6.8 Beam directions, B, corresponding widths of slip band and g vectors used to determine the plane of the slip band, Y, in Figure 6.40. See Figures 6.41A and 6.41B.

Element (wt%)	Nominal	Present Investigation	33	90	190	32
Al	5.8	5.81	5.82	5.88	5.84	5.78
Sn	3.5	3.78	4.46	4.71	4.01	4.54
Zr	4.0	3.39	3.96	3.96	3.52	4.05
Nb	0.70	0.70	0.73	0.70	0.70	0.70
Mo	0.50	0.45	0.54	0.50	0.53	0.52
Si	0.35	0.32	0.35	0.38	0.33	0.44
Fe	<0.02	<0.02	0.02	0.02	0.015	0.020
C	0.06	0.06	0.05	0.05	0.05	0.055
O_2 (ppm)	1100	885	1150	660	0.1 wt%	0.10 wt%
N_2 (ppm)	40	23	30	60	30	0.002 wt%
H_2 (ppm)	-	-	-	55	-	-
Al*	9.41	9.14	9.68	9.39	9.32	9.56

Table 7.1 Comparison of the chemical composition of IMI 834 from different investigations. The aluminium equivalent, Al*, was calculated using the formula of Rosenberg (equation 2.4, section 2.2.5.1).

Element	Composition of Phase in Atomic %			
	Primary-α	α-platelets	Platelet Boundaries	
			Silicides	Retained-β
Al	12.8 ± 0.8	11.6 ± 1.7	5.9	8.48
Sn	2.3 ± 0.2	2.4 ± 0.2	2.6	2.28
Zr	2.5 ± 0.2	2.3 ± 0.2	16.5	1.66
Nb	0.4 ± 0.1	0.5 ± 0.1	0.45	1.44
Mo	0.3 ± 0.1	0.3 ± 0.04	0.37	4.16
Si	1.4 ± 0.3	1.2 ± 0.2	17.93	4.27
Ti	bal.	bal.	bal.	bal.

Table 7.2 Scanning Transmission Electron Microscope (STEM) analysis of the composition of the primary-α, α-platelet, silicide and retained-β phases in IMI 834 (Cast HR 32609) [191].

Solution Treatment, Ageing Treatment + Reference	Cooling Rate/ Medium. (°C per minute)	Microstructure
2 hrs at 1010°C + 2 hrs at 625°C [190]	2000	20% primary-α + fine, lamellar transformed-β
2 hrs at 1015°C + 2 hrs at 700°C [168]	OQ	25% primary-α + fine, lamellar transformed-β
2 hrs at 1020°C + 2 hrs at 700°C [32]	OQ	12-15% primary-α + fine lamellar transformed-β
2 hrs at 1030°C + 2 hrs at 625°C [190]	2000	6% primary-α + fine, lamellar transformed-β
2 hrs at 1030°C + 2 hrs at 625°C [190]	350	15% primary-α + coarse lamellar transformed-β
2 hrs at 1030°C + 2 hrs at 625°C [190]	200	18% primary-α + coarse lamellar transformed-β
2 hrs at 1030°C + 2 hrs at 700°C [190]	2000	6% primary-α + fine, lamellar transformed-β
2 hrs at 1028°C + 2 hrs at 700°C [168]	OQ	15% primary-α + fine, lamellar transformed-β
2 hrs at 1030°C + 2 hrs at 700°C *	OQ	19% primary-α + fine, lamellar transformed-β
2 hrs at 1030°C + 2 hrs at 700°C [190]	350	15% primary-α + coarse lamellar transformed-β
2 hrs at 1044°C + 2 hrs at 700°C [168]	OQ	6% primary-α + fine, lamellar transformed-β

* Present Investigation

Table 7.3 Effect of heat treatment and cooling rate on the microstructure of IMI 834 [32, 168, 190]. OQ = oil quenched from processing temperature.

Technique	U/F*	Effect Observed in IMI 834	Effect Observed in Literature
Electro-polished/ Back-thinned	F&U F&U	No additional phases observed under the given conditions.	IFP observed as thin foil artefact along the α-platelet boundaries [81, 83-85, 89].
Dimpled + Electro-polished	U	No additional phases observed in thin foils.	-------
Dimpled + Ion-beam-Milled	U	A phase 0.1-0.5 mm wide was present along some of the platelet boundaries.	Ion-beam milling is said to prevent any IFP formation [81, 83, 89].
Electro-polished + Ion-beam-Milled	U	A phase was present along some of the platelet boundaries.	-------
Cross-sectional foils (Ni plated). (3.3.5.3)	F	Phase present along α-platelet boundaries. A second phase is also present as acicular bands across the α-platelets.	-------

* U = unfatigued foil specimen,
F = fatigued foil specimen.

Table 7.4 A comparison of the effects of thin foil preparation techniques observed in the present investigation with those made in the literature.

Reference	Processing Treatment*	0.2% P.S. (MPa)	U.T.S. (MPa)	
Present work (Table 6.1)	1030°C 2 hrs, oil quench 700°C 2hrs	872	993	(Tangential)
		880	1008	(Radial)
Dowson *et al.* [168, 169]	1028°C 2 hrs, oil quench 700°C 2 hrs	981	1069	
Borchert & Daeubler [190]	1030°C 2 hrs, oil quench 700°C 2 hrs	950	--	
Cope & Hill [32]	1020°C 2 hrs, oil quench 700°C 4 hrs	933	1060	
Smith [203]	1025°C 2 hrs, oil quench	979	1053	(Tangential)
		943	1096	(Radial)
	625°C 2 hrs	910	1030	(Target)
Neal [31]	1035°C 2 hrs, oil quench 625°C 2 hrs	905	1035	

* First temperature = solution treatment temperature, Second temperature = ageing temperature.

Table 7.5 Comparison of room temperature properties of IMI 834 compressor disc specimens by different workers [31, 32, 168, 169, 190, 203]. 0.2% P.S. = Proof stress, U.T.S. = ultimate tensile stress.

Heat* Treatment	v/o Primary-α	Primary-α GS (μm)**	Prior-β GS (μm)**	0.2% P.S. (MPa)	U.T.S. (MPa)
2 hrs at 1100°C	0	-	650	1025	1115
1/2 hr at 1100°C	0	-	420	1000	1100
2 hrs at 1044°C	5	16	120	984	1073
2 hrs at 1028°C	15	19	60	981	1069
2 hrs at 1015°C	25	22	46	976	1063
2 hrs at 1030°C***	18.8	35	66	872	993

* All material received a 2 hour ageing treatment at 700°C following the solution treatment and oil quenching quoted.

** GS = Grain Size

*** Present investigation

Table 7.6 Heat treatment conditions, microstructural characteristics and mechanical properties of IMI 834 studied by Dowson *et al.* [168, 169]. Also tabulated are the results of the present investigation.